



IntechOpen

Porosity

Process, Technologies and Applications

Edited by Taher Hcine Ghrib



POROSITY - PROCESS, TECHNOLOGIES AND APPLICATIONS

Edited by **Taher Hcine Ghrib**

Porosity - Process, Technologies and Applications

<http://dx.doi.org/10.5772/intechopen.68404>

Edited by Taher Hcine Ghrib

Contributors

Amir Khan, Gul Zaman, Obaid Algehtani, J. Angel Menéndez Díaz, María Canal-Rodriguez, Ana Arenillas, Tetsuo Umegaki, Naoki Toyama, Yoshiyuki Kojima, Anders Neramoen, Yi Long, Ning Wang, Yujie Ke, Ahmed Niameh Mehdy Alhusseney, Adel Gharib Nasser, Nabeel Al-Zurfi, Patrik Nemec, Zine El Abiddine Fellah, Claude Depollier, Mohamed Fellah, Erick Ogam, F.G. Mitri, Ana Paula Carvalho, Ana Sofia Mestre, Farshid Karbassian

© The Editor(s) and the Author(s) 2018

The rights of the editor(s) and the author(s) have been asserted in accordance with the Copyright, Designs and Patents Act 1988. All rights to the book as a whole are reserved by INTECHOPEN LIMITED. The book as a whole (compilation) cannot be reproduced, distributed or used for commercial or non-commercial purposes without INTECHOPEN LIMITED's written permission. Enquiries concerning the use of the book should be directed to INTECHOPEN LIMITED rights and permissions department (permissions@intechopen.com).

Violations are liable to prosecution under the governing Copyright Law.



Individual chapters of this publication are distributed under the terms of the Creative Commons Attribution 3.0 Unported License which permits commercial use, distribution and reproduction of the individual chapters, provided the original author(s) and source publication are appropriately acknowledged. If so indicated, certain images may not be included under the Creative Commons license. In such cases users will need to obtain permission from the license holder to reproduce the material. More details and guidelines concerning content reuse and adaptation can be found at <http://www.intechopen.com/copyright-policy.html>.

Notice

Statements and opinions expressed in the chapters are those of the individual contributors and not necessarily those of the editors or publisher. No responsibility is accepted for the accuracy of information contained in the published chapters. The publisher assumes no responsibility for any damage or injury to persons or property arising out of the use of any materials, instructions, methods or ideas contained in the book.

First published in London, United Kingdom, 2018 by IntechOpen

eBook (PDF) Published by IntechOpen, 2019

IntechOpen is the global imprint of INTECHOPEN LIMITED, registered in England and Wales, registration number: 11086078, The Shard, 25th floor, 32 London Bridge Street

London, SE19SG – United Kingdom

Printed in Croatia

British Library Cataloguing-in-Publication Data

A catalogue record for this book is available from the British Library

Additional hard and PDF copies can be obtained from orders@intechopen.com

Porosity - Process, Technologies and Applications

Edited by Taher Hcine Ghrib

p. cm.

Print ISBN 978-1-78923-042-0

Online ISBN 978-1-78923-043-7

eBook (PDF) ISBN 978-1-83881-318-5

We are IntechOpen, the first native scientific publisher of Open Access books

3,400+

Open access books available

109,000+

International authors and editors

115M+

Downloads

151

Countries delivered to

Our authors are among the
Top 1%

most cited scientists

12.2%

Contributors from top 500 universities



WEB OF SCIENCE™

Selection of our books indexed in the Book Citation Index
in Web of Science™ Core Collection (BKCI)

Interested in publishing with us?
Contact book.department@intechopen.com

Numbers displayed above are based on latest data collected.
For more information visit www.intechopen.com



Meet the editor



Taher Hcine Ghrib is currently an associate professor and an aggregated teacher in physics at the College of Sciences, Dammam of Imam Abdulrahman Bin Faisal University, Saudi Arabia. He obtained his habilitation degree in physics at the Faculty of Science in 2017 in Tunisia. He prepared his thesis in Tunisia that covers an “investigation of the thermally treated steel by the photothermal deflection technique” and presented it in 2008. He obtained his aggregation degree in physics and chemistry at the Preparatory Institute for Scientific and Technical Studies of El Marsa in 2001 in Tunisia. He also worked as a course teacher of physics. He worked on steel and metal alloys in his thesis and demonstrated a very practical method for measuring the mechanical properties of steels such as hardness by measuring the thermal conductivity by means of mathematical models and experimental nondestructive measurements. Almost all of his works are published in numerous publications in various journals and books. Now, he is specialized in nano- and porous materials and thin films of metals, perovskites, and alloys. He is involved in the Empowering Tunisian Renewable Energy Research Activities (ETRERA) project, of which the object is to realize a fuel cell of high-electrical performance. He has also led many scientific projects in Saudi Arabia.

Contents

Preface XI

Section 1 Porous Materials 1

Chapter 1 **Porous Silicon 3**
Farshid Karbassian

Chapter 2 **Nanoporous Carbon Synthesis: An Old Story with Exciting New Chapters 37**
Ana S. Mestre and Ana P. Carvalho

Chapter 3 **Carbon Xerogels: The Bespoke Nanoporous Carbons 69**
María Canal-Rodríguez, J. Angel Menéndez and Ana Arenillas

Section 2 Porosity Controlling and Measurement 91

Chapter 4 **Controlled Porosity in Thermochromic Coatings 93**
Ning Wang, Yujie Ke and Yi Long

Chapter 5 **Ultrasound Measuring of Porosity in Porous Materials 111**
Zine El Abiddine Fellah, Mohamed Fellah, Claude Depollier, Erick Ogam and Farid G. Mitri

Chapter 6 **Unsteady Magnetohydrodynamic Flow of Jeffrey Fluid through a Porous Oscillating Rectangular Duct 125**
Amir Khan, Gul Zaman and Obaid Algahtani

Section 3 Porosity Effect on the Materials Properties 139

Chapter 7 **Porous Structures in Heat Pipes 141**
Patrik Nemec

- Chapter 8 **High-Porosity Metal Foams: Potentials, Applications, and Formulations 181**
Ahmed Niameh Mehdy Alhusseney, Adel Gharib Nasser and Nabeel M J Al-zurf
- Chapter 9 **Porosity Evolution during Chemo-Mechanical Compaction 201**
Anders Nermoen
- Chapter 10 **Role of Interparticle Space in Hollow Spheres of Silica-Based Solid Acids on Their Acidic Properties and Activity for Hydrolytic Dehydrogenation of Ammonia Borane 221**
Tetsuo Umegaki, Toyama Naoki and Yoshiyuki Kojima

Preface

Given their practical importance in improving the general or specific properties, the porosity in materials has been extensively investigated and prepared in the recent decades with various techniques. The preparation techniques can be mechanical, chemical, or electrical, such as electrical discharge machining (EDM) and electrochemical anodization process. Several scientists have been oriented toward the production of well-spaced and well-organized nanometric and micrometric pores, which constitute a technological revolution useful for a wide variety of applications. Nowadays, numerous studies have been focused on the effect of porosity by exploring the effect of pore size, shape, and density with the goal to enhance some surface or volume properties, such as heat capacity, thermal conductivity, gap energy, optical absorption, optical emissivity, and mechanical hardness. Several techniques are used in the characterizations of the porous materials, such as scanning electron microscopy (SEM); atomic force microscopy (AFM); transmission electron microscopy (TEM); X-ray diffraction (XRD) for the imaging and structural characterization; and the photoluminescence (PL), ultraviolet-visible (UV-VIS), and infrared (IR) spectroscopy for the optical characterization.

The purpose of this book is to present various techniques for the production of pores on the surface and the volume of different materials; to investigate the influence of some parameters, such as the anodizing current, the annealing temperature, the heating time, the chemical composition and concentration, and the nature of some additive and deposited thin layers on the total properties; and to give more ways to use them in different fields.

Taher Hcine Ghrib
College of Science of Dammam
Imam Abdulrahman Bin Faisal University
Dammam, Saudi Arabia

Porous Materials

Porous Silicon

Farshid Karbassian

Additional information is available at the end of the chapter

<http://dx.doi.org/10.5772/intechopen.72910>

Abstract

Porous silicon is a sponge-like structure of monocrystalline silicon which although accidentally discovered, soon became one of the most well-researched silicon structures. Its properties and applications have been the main subject of several books and more than a dozen review articles. However, a survey of porous silicon fabrication methods has not been published even though more than 20 different routes have been developed to synthesize this material. This chapter briefly discusses the properties of porous silicon, describes its fabrication methods, and introduces its applications.

Keywords: porous silicon, fabrication, synthesis, preparation method, etching

1. Introduction

Porous silicon, solid silicon with voids therein, is one of the most important porous materials with a wide range of applications from batteries and fuel cells to drug delivery and diagnostics [1–3]. Although optoelectronics, especially light emission, has been porous silicon's primary area of interest for the last 25 years, the material has recently found its way to cosmetics, consumer care, nutrition, and food industry. The preparation of porous silicon is rather simple and inexpensive. It can be performed by several methods depending on the desired structure and properties. It shows highly tunable structural, mechanical, optical, electrical, thermal, emissive, and physiochemical properties. Some of its properties like luminescence and medical biodegradability are direct consequences of nanoscale porosification and are not observed in bulk silicon.

2. Properties of porous silicon

Porous silicon structures, like other porous materials, are classified by their dominant pore dimensions. Structures with pore dimensions below 2 nm and above 50 nm are called microporous

and macroporous silicon, respectively; those lie between are called mesoporous silicon. Due to the extremely rich details with respect to the range of variations in pore size, shape, orientation, branching, interconnection, and distribution, morphology is the least quantifiable aspect of this material. **Figure 1** schematically demonstrates the four different morphological aspects of porous silicon and their variations, and **Figure 2** shows cross-sectional SEM micrographs of different porous silicon structures.

Various morphologies and different pore dimensions give porous silicon extremely diverse structural, mechanical, optical, electrical, thermal, emissive, physiochemical, and biochemical properties. **Table 1** compares the properties of mesoporous silicon with those of bulk silicon. As the structure and surface chemistry of porous silicon can be precisely controlled during properly chosen fabrication process and appropriate post-fabrication treatment, the material's properties can be tuned according to the desired application. Tuning of porous silicon properties can be performed by manipulating its structural parameters, altering its surface chemistry, or impregnating other materials [4].

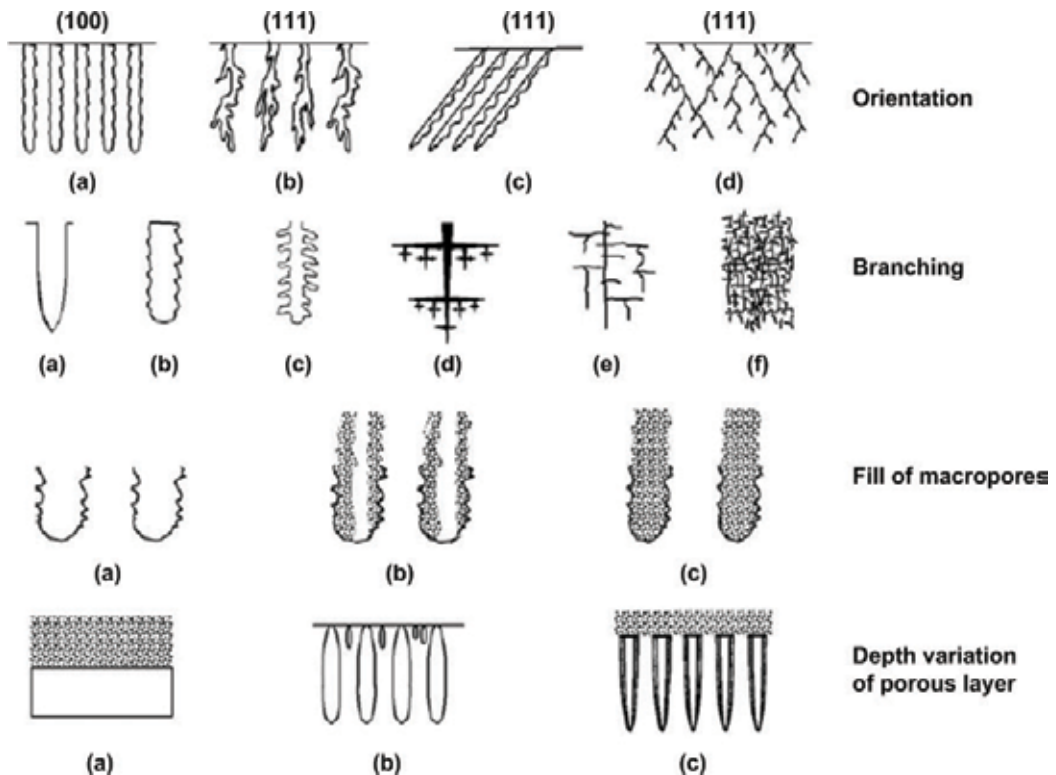


Figure 1. Morphological characteristics of porous silicon; Orientation: (a) aligned to $\langle 100 \rangle$ direction and source of holes, (b) roughly aligned to source of holes, (c) partially aligned to $\langle 100 \rangle$ direction and source of holes, (d) aligned only to $\langle 100 \rangle$ direction; branching: (a) smooth pore walls, (b) branches shorter than diameter, (c) second level branches only, (d) dendritic branches, (e) main pores with second and third level branches, (f) dense, random and short branches; fill of macropores: (a) unfilled, (b) partially filled with microporous Si, (c) fully filled with microporous Si; depth variation of the porous layer: (a) single layer of microporous Si, (b) single layer of macroporous Si with smaller pores near the surface, (c) a layer of microporous Si on top of macroporous Si (Macropores may be filled by microporous Si.) [5].

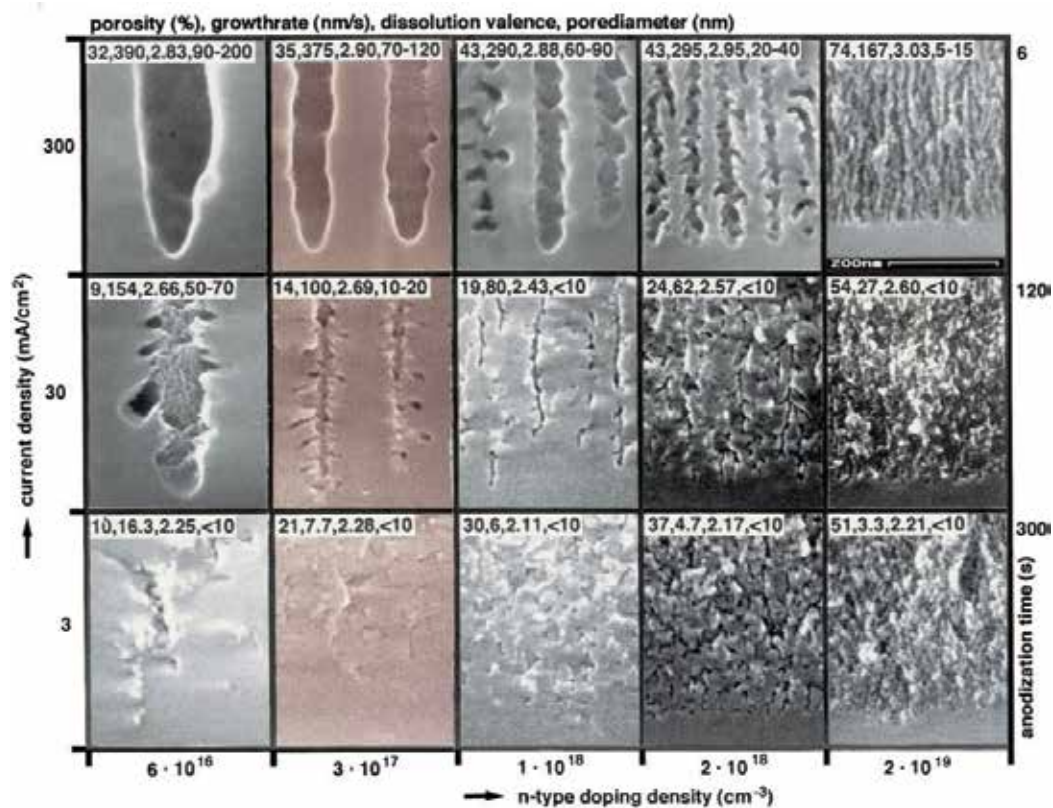


Figure 2. Cross-sectional SEM micrographs of various porous silicon structures formed by anodic etching [6].

	Property	Bulk silicon	Mesoporous silicon
Structural	Porosity	—	20–95%
	Density	2.33 g/cm ³	0.12–1.9 g/cm ³
	Pore size (diameter)	—	2–50 nm
	Surface area	—	100–800 m ² /g
	Lattice structure	Diamond	Diamond
Mechanical	Young's modulus	160 GPa	1–100 GPa
	Hardness	11.5 GPa	0.2–10 GPa (layer) 0.05–1 GPa (composite)
	Yield strength	7 GPa	—
	Fracture toughness	0.6 MPam ^{1/2}	—
Optical	Bandgap	1.1 eV	1.1–3.2 eV
	Infrared refractive index	3.5	1.1–3.0
	Color	Gray	All colors (layer) Brown-yellow (particle)
	Reflectivity (500–1000 nm)	10–35%	0.1–10%

	Property	Bulk silicon	Mesoporous silicon
Electrical	Resistivity	10^{-2} – 10^3 Ωcm	10^3 – 10^{12} Ωcm
	Free electron mobility	1350 cm^2/Vs	0.1–30 cm^2/Vs
	Hole mobility	480 cm^2/Vs	2–6 cm^2/Vs
	Dielectric constant	11.5	2–8
Thermal	Conductivity	150 W/mK	0.03–20 W/mK
	Melting point	1414°C	800–1414°C
	Specific heat	0.7 J/gK	—
	Diffusivity	0.8 cm^2/s	—
Emissive	PL wavelength	1000–1200 nm	400–1300 nm
	PL efficiency	10^{-6}	0.01–0.23 (films) 0.01–0.6 (suspensions)
	EL efficiency	10^{-8}	0.01–0.1
Physiochemical	Isoelectric point	pH 1.6–2.5	pH 1.6–7.7
	Zeta potential (pH 7)	–(45–70) mV	—
	Surface wettability	5–96°	<0.5–167°
Biochemical	Medical biodegradability	—	Months (implants) Days (microparticles) Hours (nanoparticles)

Table 1. Tunable properties of mesoporous silicon in comparison with those of bulk silicon [4].

3. Fabrication of porous silicon

Since 1956 that porous silicon was discovered, more than 20 methods have been developed to fabricate porous silicon structures. These methods can be divided into two categories: top-down and bottom-up. In the top-down approach, clusters of a monocrystalline silicon wafer are removed to generate voids in an almost perfect crystal, and form a porous structure. This approach relies on chemical and/or physical removal of the atoms from a silicon wafer. The result would be a chip-based porous silicon layer. In contrary, bottom-up approach relies on putting silicon clusters together in such a way that while establishing a crystalline form, leaves empty spaces behind so that a porous structure can be synthesized. These approaches usually lead to porous silicon powders. In this section, all fabrication routes introduced for preparation of porous silicon will be discussed; however, it should be noted that among about 20 fabrication routes, less than a dozen has attracted attention.

3.1. Anodic etching

Before chemical mechanical polishing became dominant, electropolishing was used for planarization of silicon wafers. In electropolishing, a silicon wafer is placed in an electrochemical

cell as the anode, a platinum electrode is utilized as the cathode, and hydrofluoric acid as the electrolyte. Passing electric current through the silicon wafer leads to dissolution of silicon atoms and removal of surface roughness if a critical current density (J_{PSL}) is exceeded. In 1956, something went wrong during an electropolishing process at Bell Labs, and the current in the cell reduced leaving a matt black, brown, or red layer on the surface of the wafer [7]. For more than a decade, it was believed that the matt dark layer formed on the silicon surface was a sub-fluoride (SiF_2)_x grown during the anodic dissolution. Later, it was proposed that the dark film was a dissolution/precipitation product resulted from a two-step disproportionation reaction. Finally, in 1969, it was discovered that the layer indeed has a porous structure formed by dissolution of silicon atoms in an electrochemical etching process [5].

Anodic etching, which is also called electrochemical etching, has been the most common method for the fabrication of porous silicon over the last 60 years. During these years, three electrochemical cell configurations have been utilized for the formation of porous silicon: lateral cell, single cell, and double cell. Lateral cell, which is the simplest electrochemical cell used for anodic etching of silicon, is shown in **Figure 3(a)**. Silicon wafer about to be etched serves as the anode, platinum or any other conducting material resistant to hydrofluoric acid, like graphite, serves as the cathode electrode, and the cell body is made of acid-resistant polymers like PTFE. As the wafer is soaked in HF, any silicon surface that is exposed to the electrolyte is porosified as long as the current density remains below the critical value ($J < J_{PSL}$). The main advantages of the lateral cell are its simplicity and ability to anodize silicon-on-insulator (SOI) wafers. Its drawback is the nonuniformity in both porosity and thickness of the resulting layer. This inhomogeneity is due to a lateral potential drop across the wafer which leads to nonuniform current density and therefore nonuniform porosity and thickness [8].

The second configuration, single cell, shown in **Figure 3(b)**, is the most common electrochemical cell used for porosification of silicon wafers. In order to provide uniform current density inside the silicon wafer, a back-side contact is used for the anode and the wafer is sealed so that only its front-side could be exposed to the electrolyte. Using this single cell configuration, acceptable porosity and thickness uniformity can be achieved for low resistivity silicon wafers. However, high resistivity wafers need high dose B or P ion implantation and subsequent annealing on their back-side to provide appropriate electrical contact to the external circuit. This implantation and subsequent annealing steps might be even followed by deposition of a thin layer of metal. Single cell configuration provides simultaneous control over porosity and thickness of the porous silicon film. Moreover, illumination which is necessary for n-type silicon wafers, can be easily performed in this cell. Using chemical pumps to circulate the electrolyte further improves the uniformity and minimizes the attachment of hydrogen bubbles to the silicon surface [9].

The last configuration, double cell, is designed to optimize the uniformity of porous silicon layer. It is composed of two half-cells separated by the silicon wafer about to be etched as illustrated in **Figure 3(c)**. Large platinum electrodes which are immersed in both half-cells serve as anode and cathode. The electric current flows from one half-cell to the other through the wafer. Hence, the front-side and back-side of the wafer act as local anode and local cathode. Chemical pumps are used to circulate the electrolyte between the half-cells to prevent any decrease in the local concentration of the electrolyte and remove the hydrogen bubbles. Here, electrolytic contact to the wafer reduces the nonuniformities associated with the back-side metal contact in

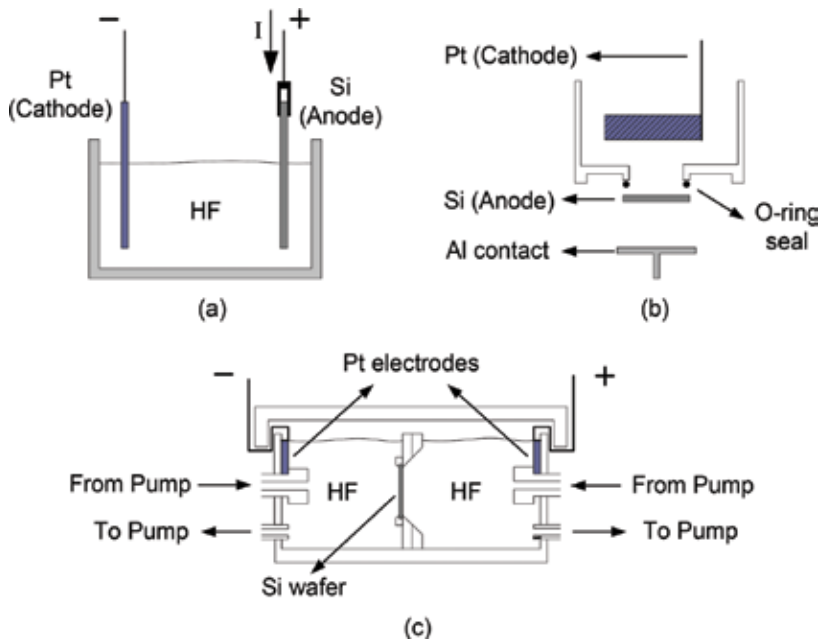


Figure 3. Electrochemical cell configurations used for the fabrication of porous silicon: (a) lateral cell, (b) single cell, and (c) double cell [8, 10].

the single cell approach. It also resolves the necessity of metallization in high resistivity wafers. By contrast, the equipment setup is complicated in comparison to the other electrochemical cells used for porosification [10]. In this configuration, if anodic etching under illumination is needed, the cell body should be made of transparent acid-resistant materials like PMMA.

The dissolution of silicon atoms by anodic etching can be controlled by either the current or the voltage of the electrochemical cell. Generally, constant current is preferred due to reproducibility and better controllability of porosity and thickness of the porous layer [11]. In the dissolution process, hydrogen gas is freed. The generated hydrogen bubbles are attached to the surface for some time preventing the electro-active species to reach the surface and interrupt the dissolution process. Addition of a surfactant like ethanol or methanol improves the penetration of the electrolyte into the pores and minimizes the hydrogen bubbles evolution [9]. Besides aqueous, ethanolic, or methanolic HF electrolytes, porous silicon can also be formed in the mixture of HF with metal oxides like manganese(IV) oxide MnO_2 , or certain organic compounds like acetonitrile CH_3CN and dimethylformamide (DMF).

Depending on the fact that electrochemical cell works either in electropolishing regime ($J > J_{\text{PSL}}$) or porosification ($J < J_{\text{PSL}}$), the charge transfer reactions that lead to the removal of the surface silicon atom, could be a tetravalent or divalent mechanism respectively. **Figure 4** illustrates the divalent mechanism which leads to formation of porous silicon structures. In situ spectroscopy of silicon samples immersed in HF-based solutions has shown that the silicon surface is passivated by Si–H bonds [12]. As the Si–F bond (6 eV) is much stronger than the Si–H bond (3.5 eV), the possibility that the surface had been passivated by fluorine and then Si–F bonds

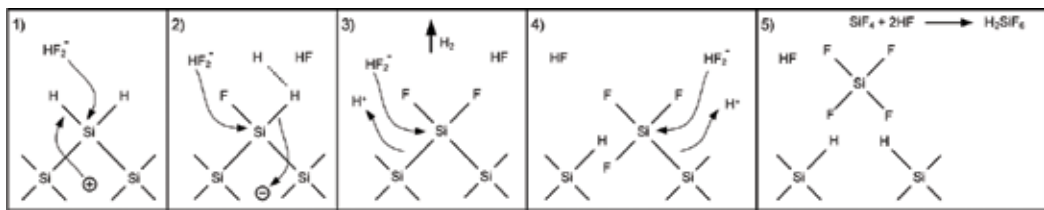
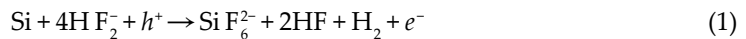


Figure 4. Divalent electrochemical dissolution of a silicon atom in hydrofluoric acid solution [13].

were replaced by the Si–H ones, is ruled out. This led to the conclusion that if a surface silicon atom establishes a bond to a fluorine atom, it is immediately removed from the surface and the surface is passivated by hydrogen [13]. The dissolution of a surface atom begins when a hole traveling inside the silicon wafer reaches the interface of silicon and electrolyte (stage 1). At this point a bifluoride (HF_2^-) ion from the solution could attack Si–H bonds replacing one with a Si–F bond. Since the electronegativity of hydrogen is close to that of silicon, Si–H bonds are effectively unpolarized; therefore, they could not be influenced by bifluoride anions unless a hole was present. After the first Si–F bond established, due to its polarizing effect, another bifluoride anion attacks the silicon atom releasing a hydrogen molecule as depicted in stage 3 of the figure. The polarization induced by the Si–F groups lowers the electron density of the silicon back-bonds and facilitates the dissolution of the loosely bounded silicon atom by HF. After the removal of a silicon atom, the remaining surface passivates with hydrides again (stage 5). The overall reaction in the divalent process can be summarized as Eq. (1):



If the dissolved silicon atom was removed from a microscopically flat surface, its removal leaves a microroughness. This small topographical alteration changes the distribution of the electric field which increases the probability of presence of the holes. Hence, the etch rate at microroughness becomes greater than the surrounding flat areas. Accordingly, surface roughness increases and eventually a porous structure is formed.

Anodic etching is the most common method for the fabrication of chip-based n-type and p-type porous silicon. All classes of porosity can be realized by anodic etching with proper control over the porosity and thickness. Although there has been success in integration of anodically etched porous silicon structures with electronic circuitry, this fabrication method is not compatible with standard ULSI technology [14].

3.2. Stain etching

Shortly after observation of the matt dark layer on silicon wafer which had been subjected to electrochemical etching, when the porous nature of the material were still unknown, similar structures were realized by electroless chemical etching of silicon in mixture of hydrofluoric acid and concentrated nitric acid solution [15]. Due to the stains formed on the surface of the silicon wafer as a result of electroless chemical dissolution (**Figure 5**), this method became known as stain etching.

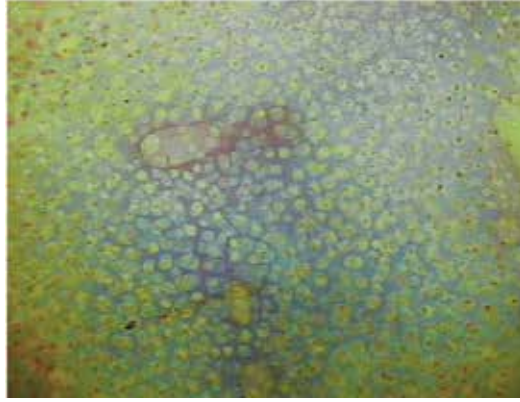
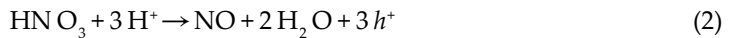


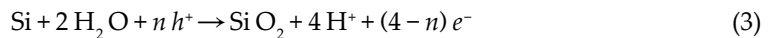
Figure 5. The stains formed on the silicon surface after being subjected to electroless chemical etching.

Although an external potential is not applied to the silicon wafer to be etched by this route, dissolution of silicon atoms has a localized electrochemical mechanism. Indeed, sites of the silicon surface temporarily act as local cathode and local anode. Complex charge transfer reactions taking place between these local electrodes lead to the removal of an atom at the local anode site. Few moments later, these local electrode sites will no longer have their previous roles; they might become neutral areas or might even turn into new local electrodes; yet, it is probable that a local anode site will become a local electrode again. When a silicon atom is removed from the surface, the resulting microroughness attracts the electric charge carriers passing by. If this charge carrier was a hole, the site would act as a local anode again. Continuation of this local electrochemical process leads to formation of a porous layer. Due to the electrochemical mechanism of stain etching, holes do have a critical role in the removal of silicon atoms and formation of pores, as they do in the anodic etching of silicon. Hence, p-type silicon which has at least thousands of holes in every cubic micrometers can be easily porosified, while n-type silicon which has negligible holes usually needs illumination.¹ Incident photons with proper energy ($h\nu > E_g$) generate holes in the n-type silicon and promote stain etching.

The reaction in the local cathode consists of a series of complicated reaction pathways that lead to the reduction of HNO_3 , generation of NO , and injection of holes into the silicon. The first stage of these reaction pathways is the formation of HNO_2 which is the rate-limiting step of overall reaction. The cathode reaction can be summarized as Eq. (2):



If the injected holes do not recombine with free electrons of the silicon wafer, they could attach to a silicon atom, which then turns to be a local anode and oxidized as depicted by Eq. (3):

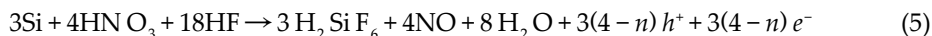


¹Stain etching under illumination should not be confused with photoetching which will be discussed in the following subsection.

The oxidized silicon atom is then removed by hydrofluoric acid (Eq. (4)), and the residual protons (H^+) at the anode site react with HNO_3 and repeat the cycle.



The overall reaction can be written as Eq. (5):



where n being the average number of holes needed to remove one silicon atom [16].

Although porous silicon formation by stain etching usually occurs in HF/ HNO_3 solution, the mixture of hydrofluoric acid with other compounds such as sodium nitrite $NaNO_2$, chromium(VI) oxide CrO_3 , iron(III) chloride $FeCl_3$, and potassium iodate KIO_3 can also lead to formation of porous silicon structures [17–19]. The reaction pathways that lead to the dissolution of silicon atoms are similar to those that occur in HF/ HNO_3 solution. The strong oxidizing agent of the solution oxidizes silicon atoms and the oxidized atoms are removed by HF, forming a soluble complex. It is also possible to use acetic acid as a surfactant. It does not participate in the chemical reactions; it only dilutes the solution and decreases the surface tension so that better wetting and a smoother surface would be achieved [16].

Stain etching is the simplest, most straightforward, and most inexpensive way to fabricate porous silicon. It almost needs nothing but a plastic beaker. It can be used to prepare porous silicon on a SOI wafer in which buried oxide layer makes electrochemical etching difficult. The main disadvantage of this method is that there is an upper limit (about 1.5 μm) for the thickness of the porous silicon layer.

3.3. Photoetching

Fabrication of mesoporous silicon by photoetching has been introduced in 1993 [20]. In the proposed method, silicon wafer is immersed in the aqueous HF solution under illumination of He-Ne laser as shown in **Figure 6**. Although coherent light sources have usually been utilized, photoetching can also be performed by incoherent sources such as Xe lamps and W lamps [21, 22]. Due to the built-in electric field existed in silicon, near its interface with the solution, formation of porous structures by this method is restricted to n-type silicon substrates. Indeed, illumination of both n-type and p-type silicon with proper photon energies ($h\nu > E_g$), breaks the Si–Si bonds and generates free electron/hole pairs. The charge carriers generated near the surface are drifted by the built-in electric field, but the direction of the built-in electric field is different for n-type and p-type silicon. In the n-type silicon, holes are pushed toward the surface where they can facilitate the removal of a nearby silicon atom, while the opposite direction of the built-in electric field in p-type silicon wafers drives the holes away. Hence, photoetching can only remove silicon atoms from the n-type silicon wafers.²

²It should be noted that it is not impossible to prepare p-type porous silicon by photoetching; however, the rate of the process is extremely disappointing [23].

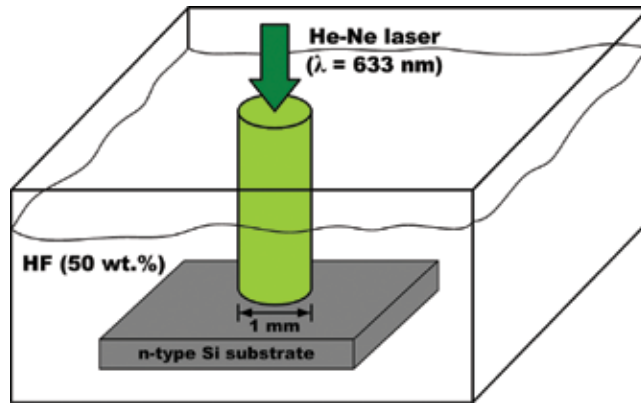


Figure 6. Porous silicon formation by photoetching.

Porosification of silicon also depends on the wavelength of the incident light. If the energy of the incident photons is less than the silicon bandgap ($h\nu < E_g$), the photons are not absorbed by the wafer and the light travels through the material. In this case, neither free electron/hole pairs are generated, nor dissolution of silicon atoms takes place. In contrast, if the energy of the photons is greater than the bandgap of silicon, the light is absorbed and generated holes facilitate the dissolution of silicon atoms and formation of porous structures. Nevertheless, the formation of porous structures does not necessarily lead to the formation of a porous layer. Indeed, the porous layer cannot be formed unless porous structures survive and porosification continues. If the energy of the incident photons is less than the bandgap of the fabricated porous structures, the light reaches the underlying substrate and generates free electron/hole pairs there (**Figure 7(a)**). Generated holes are then promote the removal of silicon atoms; therefore, porosification continues and the porous layer is formed. However, if the energy of the photons is not only greater than the bandgap of silicon but also greater than that of porous silicon structures, photons are absorbed in the porous structures and lead to their removal (**Figure 7(b)**).

Figure 8(a) shows a micrograph of a porous structure formed in HF solution under illumination of the He-Ne laser beam for 60 minutes. Part (b) of this figure depicts the relation of

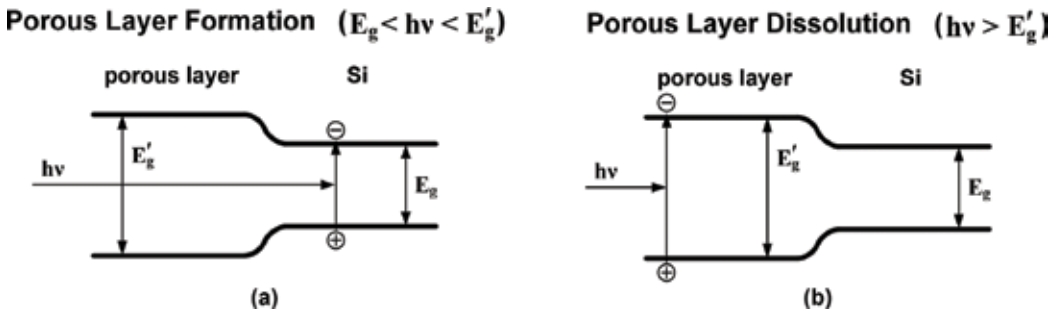


Figure 7. Formation of porous silicon layer depends on the energy of incident photons: (a) porosification continues and a porous layer is formed, and (b) porous structures are dissolved once being formed [20].

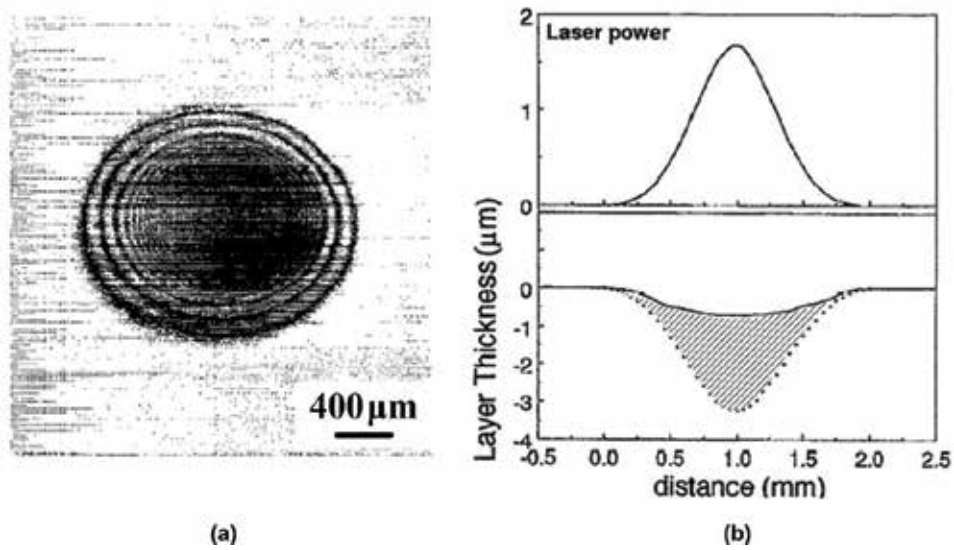


Figure 8. Porous silicon layer synthesized by photoetching: (a) micrograph, (b) relation between the power distribution of the incident beam and the synthesized porous layer [20].

optical-power distribution of the incident laser beam and the synthesized porous layer. The dip at the center shows the complete removal of silicon atoms and the marked area illustrates the porous region. It is observed that the thickness of the porous layer linearly increases with the photoetching duration regardless of the crystal orientation of the specimen [20]. Addition of a mild oxidizing agent like H_2O_2 or I_2 to the HF solution leads to stable formation of porous layers in much shorter periods of time [24].

In addition to the aqueous HF solution, porous silicon structures have been photoetched using aqueous solutions of sodium fluoride NaF and potassium fluoride KF [25]. The chemical reactions lead to the removal of silicon atoms are almost the same. For instance, potassium fluoride dissociates into K^+ and F^- ions. Due to negligible solubility of F^- , the dissociation of KF would be as follows:



The holes, generated by illumination, dehydrogenates the surface silicon atoms and facilitate the establishment of surface Si–F bonds. The atoms are then attacked by bifluoride anions and removed leading to formation of the porous layer.

It should be noted that stain etching can also be performed under illumination in which the incident light generates free electron/hole pairs and increases the etch rate. However, such a photo-assisted chemical dissolution of silicon should not be considered photoetching unless the solution was unable to dissolve silicon by itself and the light was the key factor. However, this classification has not always been followed and photo-assisted stain etching processes were incorrectly addressed photoetching [18, 19, 26].

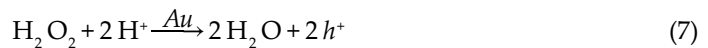
Photoetching can be utilized for the realization of porous silicon on SOI wafers, micromachined wafers and wafers with microelectronic circuitry [24]. If HF solution is used, instead of NaF and KF solutions, the technique does not introduce any metallic impurities to the substrate. One of the main limitations of this route is that it only works for n-type silicon wafers. The other is the nonuniform thickness of the realized porous layer.

3.4. Metal-assisted etching

The authors of first reports on the fabrication of porous silicon by metal-assisted etching were not aware of the catalyst role in porous silicon formation mechanism and gave incorrect speculations for the appearance of the pores [27]. It was discovered later that the catalytic behavior of metallic nanoparticles is the key factor in realization of porous silicon layers in this technique. Here, metal catalysts such as Al, Ag, Au, Pd, Pt, Fe, or Au-Pd alloy are deposited and patterned on the surface of the silicon wafer. The wafer is then immersed in a solution consisting of hydrofluoric acid and a mild oxidizing agent. The oxidizing agents used in metal-assisted etching are not strong like those utilized in stain etching, so that silicon dissolution only takes place in the presence of the metal catalyst. While hydrogen peroxide H_2O_2 is the most common oxidizing agent in metal-assisted etching of silicon, porosification can also be performed using sodium persulfate $Na_2S_2O_8$, iron(III) nitrate $Fe(NO_3)_3$, potassium dichromate $K_2Cr_2O_7$, and potassium permanganate $KMnO_4$ [28–30]. The metallic nanoparticle absorbs an electron and injects a hole into the silicon substrate. This hole injection facilitates the oxidation of a nearby silicon atom at the surface. The oxidized silicon atom is then attacked by bifluoride ions and dissolved by a divalent charge transfer reaction.

One way to perform metal-assisted etching is to deposit and pattern metal catalysts and then immerse the predeposited specimen in the etchant consisting of HF and the oxidizing agent. The other way is to immerse the bare silicon wafer in a solution composed of HF and certain metal salts such as silver nitrate $AgNO_3$, potassium tetrachloroaurate(III) $KAuCl_4$, and potassium hexachloroplatinate(IV) K_2PtCl_6 [30, 31]. Here, metal catalysts are precipitated on the silicon surface, and initiate the dissolution process.

Similar to anodic etching, stain etching, and photoetching discussed in the previous subsections, holes have a key role in dissolution of silicon atoms in the metal-assisted etching. For instance, in gold-assisted porous silicon formation in HF/ H_2O_2 solution, holes necessary for silicon atoms removal are generated from the reduction of hydrogen peroxide. Due to the enormous difference between the electrochemical potential of hydrogen peroxide and silicon, H_2O_2 injects few holes into the valence band of silicon even in the absence of a metal catalyst. Since silicon atoms removal in HF-based solutions stems from the presence of holes near the silicon surface, dissolution of silicon wafers is possible in the HF/ H_2O_2 solution; however, the etch rate is only few nanometers per hour [13]. The presence of gold catalytically promotes the reduction of H_2O_2 and significantly increases the number of injected holes as depicted in Eq. (7):



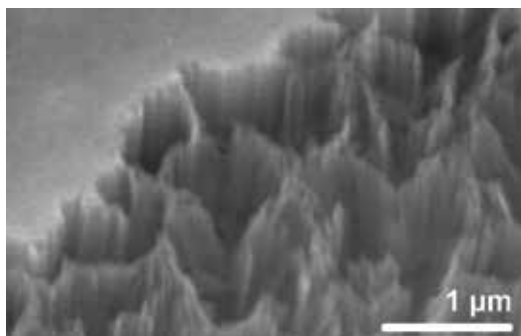
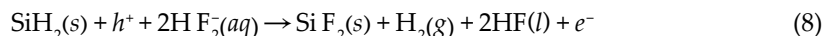


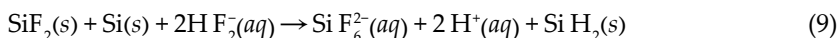
Figure 9. An SEM image of a sample subjected to metal-assisted etching after selective lithographic patterning. Only regions coated with the metal catalyst were etched [32].

The injected holes accelerate the silicon atoms removal by a practical etch rate. **Figure 9** demonstrates an SEM image of a sample in which the gold catalyst layer was selectively removed prior to be immersed in HF/H₂O₂ solution. While significant etching occurred in the metal-coated area of the wafer, there has not been any visible dissolution in the uncoated regions.

The dissolution of the silicon atom after hole injection is a divalent charge transfer reaction in which the surface Si—H bonds are replaced by Si—F bonds as depicted in Eq. (8):



The silicon atom is then removed as a result of bifluoride ions attack:



By proper adjustment in the ratio of oxidizing agent to hydrofluoric acid, it is possible to control the class of porosity and fabricate mesoporous and macroporous structures [32]. As porous silicon formation only takes place in the area coated with the metal catalysts, any desirable pattern for the porous area can be easily achieved. The introduction of metallic impurities to the substrate is the main disadvantage of metal-assisted etching.

3.5. Vapor etching

In 1999, Bessaïs and his colleagues observed that porous silicon can be fabricated on top of a solar cell structure if the device is being sprayed by HF droplets [33]. The dissolution of silicon atoms was attributed to the low velocity of HF droplets initiating the idea of etching silicon with low velocity HF/HNO₃ droplets that later became known as vapor etching. **Figure 10** schematically demonstrates the experimental setup used for preparation of porous silicon by vapor etching [34]. The polypropylene container partially filled with HF/HNO₃ solution is placed in a thermostatic bath. The silicon substrate is positioned inside the container's lid, a few centimeters above the liquid level. The lid must be sealed so that the empty space above the solution level becomes saturated with acid vapor. As the temperature

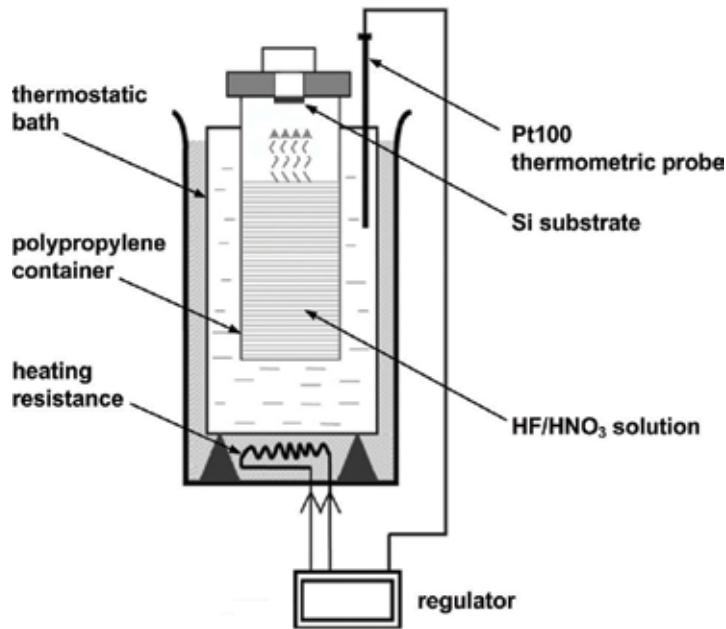


Figure 10. Schematic illustration of vapor etching setup used for porous silicon fabrication [34].

increases, supersaturation leads to the formation of droplets on the container walls and the silicon surface. In case of extremely rough silicon surfaces, the droplets will attach and form a liquid film which destroys the porous layer [34].

In order to achieve homogenous porous layers, the kinetics of the process and hence the determining factors, i.e., concentration and temperature of the solution as well as duration of vapor exposure, must be controlled. Increasing either the HNO₃ content of the solution or the temperature of the process significantly increases the etch rate. For temperatures between 20 and 30°C, the etch rate is rather low and homogenous porous layers can be achieved by exposure times up to 30 min. However, increasing the temperature to 40°C leads to speedy condensation of droplets on the silicon surface and destruction of porous layers unless the exposure time remains below 20 min. At 60°C and beyond, the speed of condensation is so fast that porous layers can only be synthesized in exposure times less than 2 min.

The vapor etching method is rather simple and inexpensive. It can be used for preparation of luminescent silicon structures and antireflection coatings in solar cells where thin layers of porous silicon are required. The concentration of the solution, temperature, and duration of the vapor etching process have to be controlled precisely or ammonium hexafluorosilicate (NH₄)₂SiF₆ and Si/SiO_x nanoparticles will be formed instead of porous silicon [35]. The method is unable to produce highly porous structures as the condensation of the droplets leads to the formation of a liquid film on the surface, which in turn results in the removal of the porous layer. The area of specimen should be chosen small in comparison to the diameter of the container or the uniformity in porosity and thickness will be lost.

3.6. Reactive-ion etching

Chemically stable mesoporous and macroporous silicon structures can be formed as a result of a maskless sequential reactive-ion etching (RIE) of silicon wafers using H_2 , O_2 , and SF_6 plasma [36]. The sequential process is composed of one etching and two passivation subsequences: oxidation and fluorination, as depicted in **Figure 11**. In the etching subsequence, SF_6 ions and radicals of the plasma remove the silicon atoms by a combination of chemical and physical etching mechanisms. During the oxidation subsequence, a very thin oxide layer is formed on the surface of the pores as a result of their exposure to the O_2 plasma. In the following subsequence, fluorination, the dangling bonds of the silicon/oxide interface are replaced by Si–F bonds, transforming the thin oxide layer into a stable SiO_xF_y passivating film. Formation of this SiO_xF_y layer stabilizes the chemical properties of the final porous structure, which always been the inevitable weakness of porous silicon structures formed by HF-based processes [37]. The porous silicon structures evolve by the repetition of these three subsequences.

By proper adjustment of the gases flow rates, plasma powers, durations of the subsequences, and repetition, it is possible to tailor the porosity and thickness of the mesoporous or macroporous material [36]. Since the fabrication process is performed at room temperature, it can be used as a post-fabrication treatment, which is very important in a technological point of view.

3.7. Spark erosion

Spark erosion that later became known as spark processing is another top-down porous silicon fabrication route introduced in the early 1990s [38]. This method can be used to prepare not only porous silicon but also other porous materials such as As, Bi, Ge, GaAs, Sb, Se,

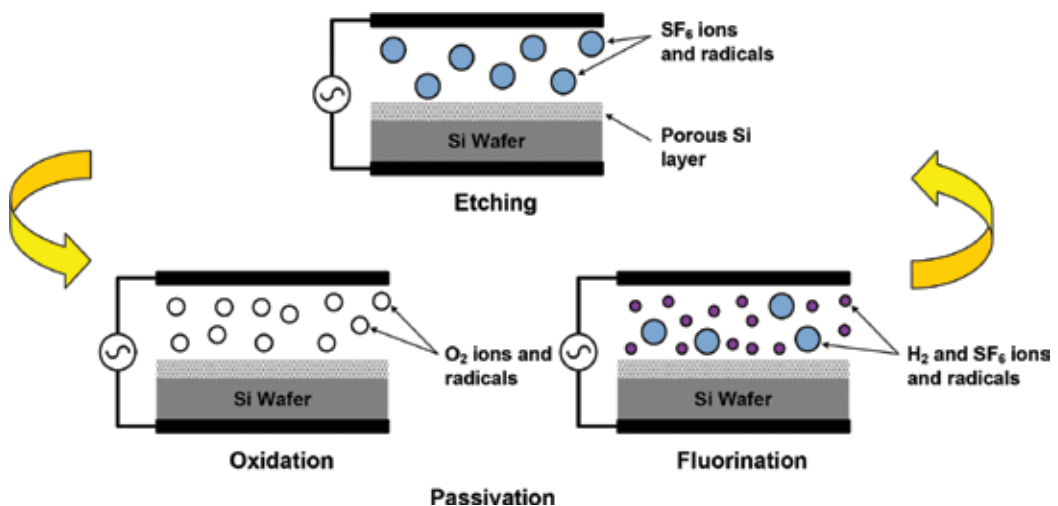


Figure 11. The sequential RIE process to synthesize porous silicon is composed of one etching and two passivation subsequences (oxidation and fluorination) [36].

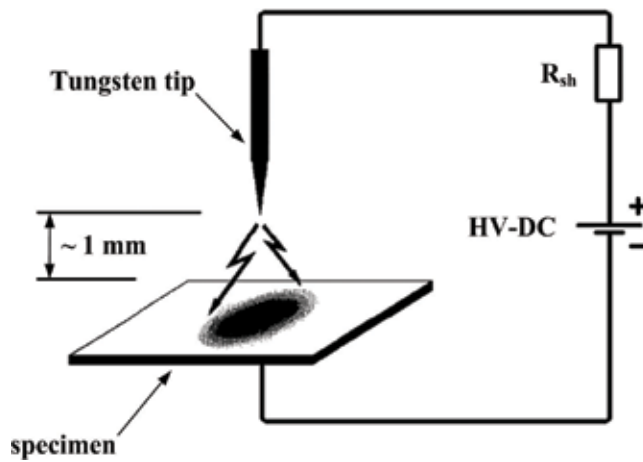


Figure 12. Schematic illustration of porous silicon formation by spark erosion [39].

Sn, and Te [39]. As demonstrated in **Figure 12**, the silicon substrate is placed near a tip and eroded by sparks for at least several hours so that porous structures are formed on its surface. Spark erosion does not involve any chemical reactions in the dissolution of silicon atoms and the removal mechanism is purely physical. The discharges between the tip and the silicon substrate ionize the gaseous environment and the silicon surface is then eroded due to the colliding ions. During their first studies, Hummel and his colleagues used silicon tips and performed spark erosion in pure N_2 to prevent unwanted impurities entering the specimen [38]. However, later studies showed that using a tungsten tip or performing the erosion in air does not increase the impurity level of the substrates [40]. The voltage used for spark processing is in the range of several kilovolts; the currents flow during erosion are in the range of tens of milliamperes; and the average time interval between the sparks is few milliseconds [41]. Although in spark processing chip-based porous silicon structures are formed, the method is incompatible with standard fabrication technology. Moreover, the nonuniform thickness of the porous layer is inevitable in this technique.

3.8. Laser-induced plasma erosion

Another physical process that has been utilized to remove silicon atoms and synthesize porous layers is the generation of the air optical breakdown plasma near a silicon target which its surface is about to be porosified. As depicted in **Figure 13**, optical breakdown is initiated by focusing a pulsed TEA CO_2 laser beam (wavelength of $10.6\ \mu m$, pulse energy of 1 J, and repetition rate of 3 Hz) by a Fresnel lens near the silicon target. The intensity of the laser used by Kabashin and Meunier was not enough to initiate the optical breakdown; however, the presence of the silicon target reduces the threshold of the optical breakdown and generates a high temperature plasma ($10^4\ K$) with intense currents ($10^6\ A$) [42]. Apparently, light action and contact of the silicon surface with such a plasma lead to localized melting, evaporation, vapor redeposition, recrystallization, erosion of silicon surface, and formation of the porous silicon layer [42].

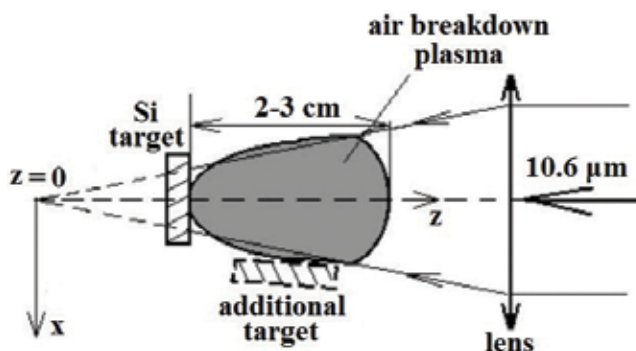


Figure 13. Schematic illustration of the experimental setup used for laser-induced plasma erosion (The additional target shown in the figure was used for control tests and was not necessary for porous silicon formation.) [42].

Using laser-induced plasma erosion, luminescent mesoporous silicon has been prepared on both p-type and n-type silicon wafers regardless of the dopant type or concentration of the silicon wafers. The porosity of the layers is typically between 40 and 70% with thicknesses up to 500 nm. However, the thickness of the porous region shows significant nonuniformity. The area of the porous region varies between hundreds of micrometers and several millimeters depending on the position of the silicon target with respect to the focal plane of the lens.

3.9. Oxidation of Rochow reaction byproduct

Macroporous silicon powders can be synthesized by acid washing and oxidation of Rochow reaction byproducts. Metallurgical-grade silicon powders are ground with Cu-based particles to form a contact mass. The obtained material then reacts with chloromethane CH_3Cl to produce organosilicon compounds (Rochow reaction³). The waste contact mass byproduct is composed of unreacted silicon, metal compounds, and deposited carbon. Recovering the metal components by acid washing leaves porous Si/C composite as depicted in **Figure 14**. Such a porous Si/C composite has been successfully used as the anode in lithium-ion batteries [44]. Porous silicon can be obtained by oxidation of the Si/C composite in air at 400°C for 1 h.

3.10. Ion implantation

Macroporous silicon structures can be fabricated by low-energy high-dose ion implantation of silver into monocrystalline silicon wafers without any thermal annealing process [45]. The implantation is carried out at the energy of 30 keV and doses above $1 \times 10^{16} \text{ cm}^{-2}$. Pore formation is presumably driven by microexplosion and voids clustering. It is believed that microexplosion initiates a void and lowers the energy required for the formation of nearby voids; the neighboring voids then cluster to minimize the dangling bonds density [45, 46]. The fabricated porous layer has an average pore size of about 120 nm. It has been observed that during ion implantation, silver atoms are agglomerated inside the pore walls forming nanoparticles with dimen-

³Rochow reaction is the most common route to synthesize organosilane monomers in the chemical industry [43].

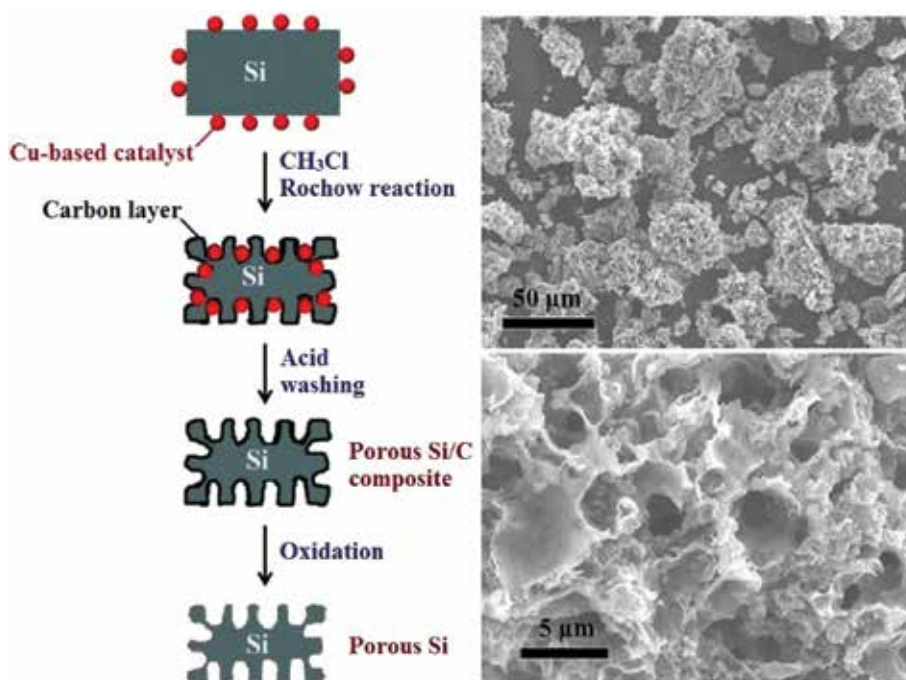


Figure 14. Synthesis and SEM micrographs of porous Si/C composite synthesized by acid washing of Rochow reaction byproduct [44].

sions between 5 and 10 nm. Although the electromagnetic coupling between localized surface plasmon of silver nanoparticles and porous silicon structures promotes the optical behavior of the material, the presence of metallic nanoparticle is undesirable in other application areas.

3.11. Plasma hydrogenation

This method has been introduced in 2005 for the fabrication of luminescent microporous and mesoporous silicon [47, 48]. In contrast to the fabrication routes already discussed in this chapter, plasma hydrogenation is a bottom-up approach. It starts with the deposition of a thin amorphous silicon (a-Si) layer with a thickness of about 200 nm. The amorphous layer is deposited by physical vapor deposition techniques like evaporation [47, 48] or sputtering [49, 50] instead of chemical vapor deposition to increase the number of voids. Later, the specimens are placed in a DC plasma-enhanced chemical vapor deposition (DC-PECVD) setup to be exposed to DC hydrogen plasma as illustrated in **Figure 15**. After the hydrogenation, a thermal annealing step is performed. It is believed that hydrogen radicals of the plasma replace the dangling bonds of the amorphous silicon layer during the hydrogenation step; then, in the annealing step, the silicon surface is depassivated and H_2 is exhausted from the specimen. The energy freed from breaking Si–H bonds promotes the rearrangement of silicon atoms of the specimen and a porous crystalline structure is formed [51]. Although porous silicon can be realized by performing one hydrogenation followed by one annealing step, breaking the process duration into three consecutive repetition of hydrogenation and annealing steps provide more controllability over the properties of the synthesized porous layer. This fabrication process is

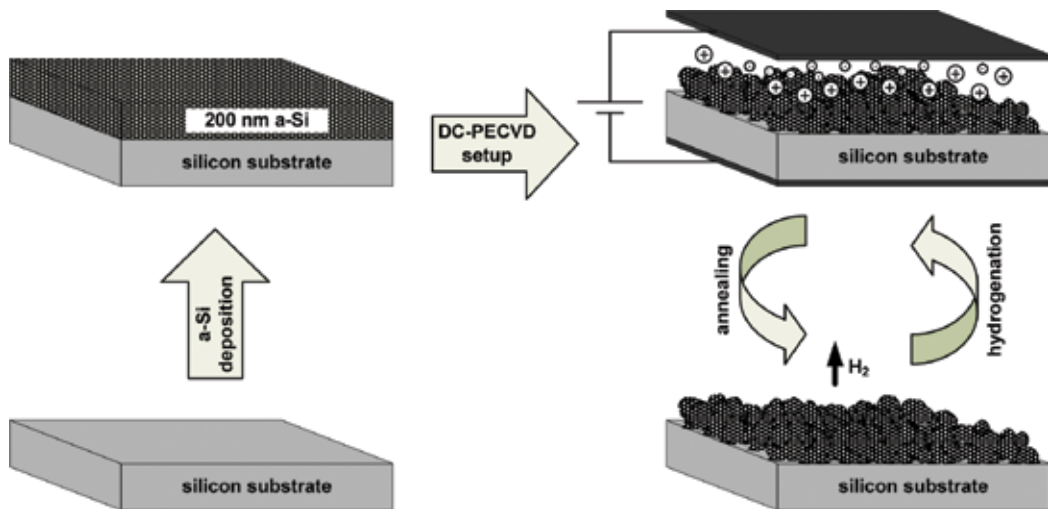


Figure 15. Schematic illustration of fabrication process of porous silicon by plasma hydrogenation.

fully compatible with standard ULSI technology. Moreover, as it is a low-temperature process (below 400°C), it can be considered as a post-fabrication treatment to implement luminescent porous silicon devices on a chip with microelectronic circuitry. The limitation of this fabrication route is that only thin layers of porous silicon can be synthesized.

3.12. Laser ablation

Another bottom-up approach to realize porous silicon is collecting laser-ablated silicon clusters [52]. In this technique, a silicon target is irradiated with a pulsed laser beam in a vacuum chamber as illustrated in **Figure 16**. The laser-ablated silicon clusters are collected by placing the substrate in the vicinity of the target where the ablation plume could reach. The substrate is usually heated to increase adhesion of the porous layer. It is also rotated to increase the uniformity of the deposited film. The porosity and thickness of the porous silicon layer can be controlled by the power of the incident laser, the distance between the substrate and the target, and duration of the ablation. This technique has not attracted much attention for chip-based applications due to its incompatibility with standard technology.

3.13. High-density plasma deposition of silicon

Mesoporous silicon structures can be fabricated by deposition of high void density crystalline silicon films using low-temperature high-density plasma. An electron cyclotron resonance (ECR)-PECVD tool with hydrogen diluted silane at about 100°C has been utilized for the preparation of thin films composed of nanoscale silicon columns in a void matrix [53]. Porous layers has been realized in the pressure ranges between 5 and 12 mTorr corresponding to microwave power between 640 and 340 W. Formation of the porous structure stems from low mobility and therefore low diffusion length of the deposition species compared to the average distance between the physisorption sites. The low mobility of deposition species can be attributed to the low substrate temperature as well as the low kinetic energy of the impinging ions

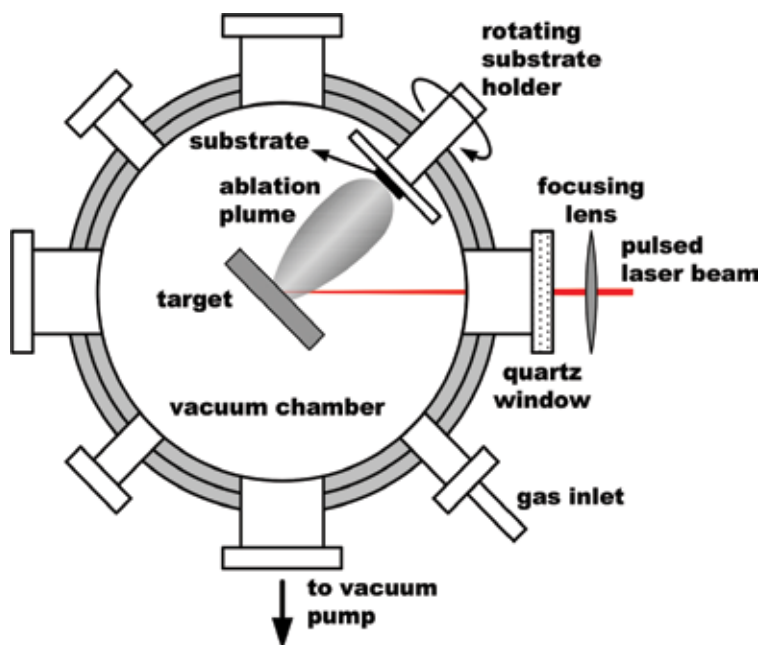


Figure 16. Schematic illustration of the laser ablation setup.

of the ECR plasma (< 50 eV) [53]. Moreover, H radicals of the plasma also have a major role in the formation of the structure. Although the deposition process is performed at low temperatures, ECR plasma has high concentrations of H radicals which promote the crystallinity of the structure. The strained regions between the crystallites cannot withstand the severe H radical etching, leading to the formation of a void volume.

Using high-density plasma deposition, uniform porous layers up to $1\ \mu\text{m}$ can be realized on silicon wafers, glass and plastic substrates as well as metal foils. Increasing the plasma power lowers the void fraction of the layer and decreases the porosity. Similarly, increasing the substrate temperature also decreases the porosity. By controlling substrate temperature and microwave power, porosities between 25 and 90% can be achieved by this bottom-up method. The obtained porous silicon layers show luminescence in the red portion of the spectrum and are sensitive to water vapor.

3.14. Oblique-angle deposition

Porous amorphous silicon has been fabricated by oblique-angle deposition, aka glancing-angle deposition, using electron-beam evaporation [54, 55] or magnetron sputtering [56]. Oblique-angle deposition is performed by positioning the substrate at a steep angle with respect to the vapor flux in order to achieve geometric shadowing. As schematically shown in **Figure 17**, random growth fluctuation on the substrate surface produces shadow regions where incident vapor flux cannot reach. As deposition continues, areas of larger height variation preferentially grow. Hence, an array of oriented nanorods is formed leaving pores behind. By controlling the vapor flux incident angle during deposition, the porosity can be tailored [57]. The pores of the material realized by oblique-angle physical vapor evaporation techniques are

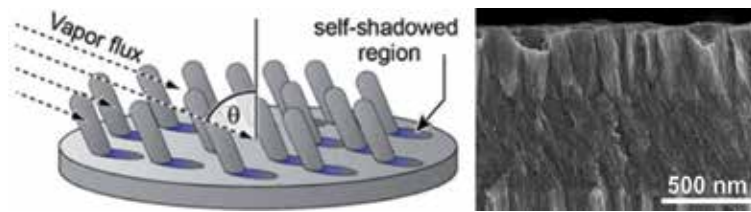


Figure 17. Schematic illustration of the oblique-angle deposition process and a cross-sectional SEM image of the obtained porous silicon layer [56, 57].

enclosed by the surrounding amorphous silicon matrix. Such structures spoil the available enormous surface area of porous silicon and restrict applications of the material. Indeed, this fabrication route has mainly been used to prepare antireflection coatings in solar cells.

3.15. Unidirectional solidification of molten silicon

Another method for realization of porous silicon is unidirectional solidification of molten silicon in hydrogen ambient. As schematically illustrated in **Figure 18**, high-purity silicon pieces are placed in an alumina crucible and inductively heated in the hydrogen atmosphere. The setup is then tilted and the molten is poured into a specifically designed mold [58]. The sidewalls of the mold are made of molybdenum and its bottom is made of copper which can be cooled down by circulated water. Due to the significant difference of thermal conductivities and heat capacities of the sidewalls and the bottom of the mold, unidirectional solidification can take place in the vertical direction. Both melting and solidification steps were performed in a constant pressure of hydrogen. It is believed that hydrogen dissolves in the molten and generates pores during solidification. Porosity and average pore size of the ingot change from 10 to 34% and 100 to 300 μm , respectively, depending on the hydrogen pressure alteration from 1 to 0.1 MPa.

Using unidirectional solidification of molten silicon in hydrogen atmosphere, porous cylindrical silicon ingots, 25 mm in diameter and about 30 mm in height, with elongated spheroidal “lotus-type” pores have been fabricated (**Figure 19**). The average pore size in the obtained ingots is at least two orders of magnitude greater than that of porous silicon structures realized by other fabrication routes.

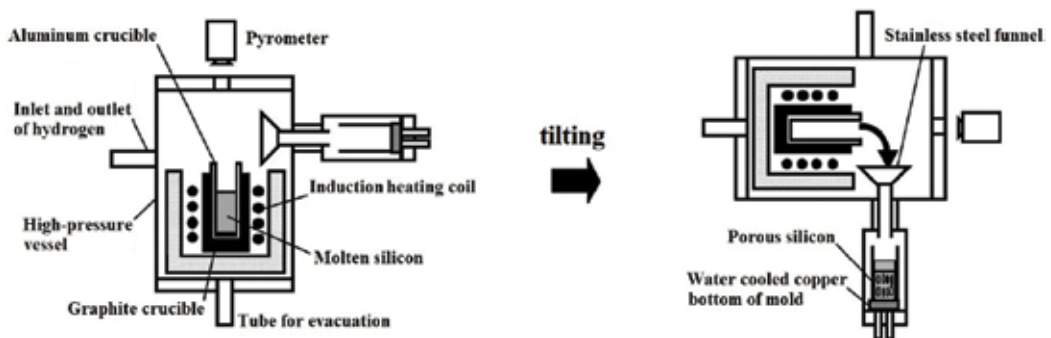


Figure 18. Setup used for preparation of porous silicon by unidirectional solidification of molten silicon [58].

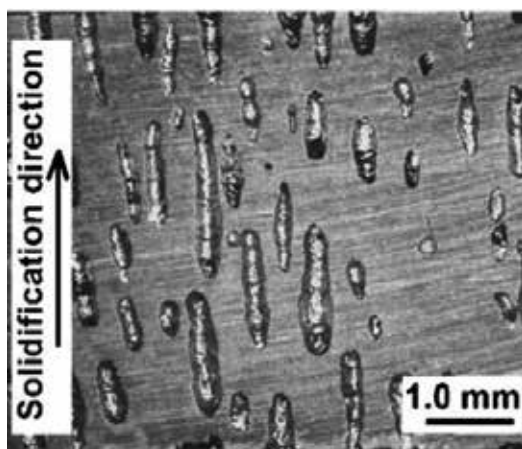
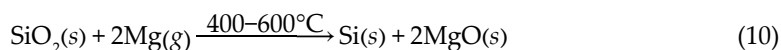


Figure 19. Cross-sectional SEM micrograph of a typical porous silicon ingot prepared by unidirectional solidification of molten silicon [58].

3.16. Porous silica reduction

Reduction of porous silica is another bottom-up route to synthesize porous silicon structures [59, 60]. This preparation method is utilized when inexpensive products are required as low-cost silica feedstocks like sand, living plants, and agricultural wastes can be used. As silica reduction generally occurs by magnesium vapor at moderate temperatures, this fabrication process is called magnesiothermic reduction of silica (Eq. (10)).



However, the reduction can also take place using other reducing agents, e.g., lithium, sodium, aluminum, and calcium [61–64]. The reaction pathway of Eq. (10) is then followed by acid leaching to remove the metal oxide byproduct and obtain porous silicon. The pore size and morphology of the synthesized porous silicon strongly depends upon morphology and moisture content of the feedstock, thermal budget of the process, and byproduct size distribution. In addition to metallothermic porous silica reduction, porous silicon synthesis has also been performed by mechanochemical reduction of SiO powder [60].

Porous silica reduction is a simple route for the realization of porous silicon. All classes of porosity can be achieved by this method. However, it is important to precisely control the process to prevent formation of magnesium silicate instead of silicon. Sintering and reintroduction of oxygen, especially in highly porous products, are also issues [63, 65].

3.17. Dealloying

Using dealloying of Al-Si eutectic system, thin layers of mesoporous silicon with ultrahigh density of cylindrical pores with an average diameter of 5 to 13 nm have been realized [66]. The Al-Si system is deposited by sputtering of an $\text{Al}_{0.56}\text{Si}_{0.44}$ target with Ar pressure of 0.1 Torr at low temperatures (below 100°C). Cylindrical pores are generated as a result of combination of nanoscale phase separation of the Al-Si system during deposition and subsequent removal of Al cylinders

by chemical etching. Indeed, by appropriate choosing of deposition parameters, especially the deposition rate, it is possible to control the structural development of Al-Si system that occurs at the surface during the film growth at low temperatures. Accordingly, by controlling the nanoscale phase separation through deposition parameters, Fukutani et al. have successfully fabricated Al nanocylinders surrounded by an amorphous silicon matrix [66]. Removing the Al cylinders by immersing the specimen in concentrated sulfuric acid solution for 24 h, a porous amorphous silicon layer with cylindrical pores is obtained (**Figure 20**). A subsequent annealing step at 800°C in H₂ atmosphere for 1 h crystallizes the porous material without any visible alteration in the average size and density of the pores [67]. Further studies are needed to determine the controllability over the shape and orientation of the pores generated by this method.

3.18. Laser-induced silane decomposition

Laser-induced decomposition of silane has been used to prepare high porosity mesoporous structures composed of silicon nanocrystals [68]. Nanocrystals have been synthesized by pulsed CO₂ laser-induced decomposition of SiH₄ in a complex apparatus illustrated in **Figure 21**. The setup consists of three vacuum chambers: a source chamber containing the flow reactor, a differential chamber encasing the chopper for size selection, and an ultrahigh vacuum (UHV) chamber that contains the time-of-flight mass spectrometer. The “source chamber” is indeed a laser-driven CVD reactor where silicon clusters are produced by pulsed CO₂ laser pyrolysis of SiH₄. The reaction products are extracted perpendicularly to both the gas flow and the CO₂ laser beam through a conical nozzle projected into the reaction zone. The extracted nanocrystals are then skimmed into a low-pressure vacuum chamber (differential chamber); they form a “molecular beam” of non-interacting clusters. The beam passes through the slits of a rotating chopper, synchronized with the pulsed pyrolysis laser and can be vertically moved from outside. The chopper is used to preselect a small portion of the initially broad cluster pulse to narrow the cluster size distribution. Immediately behind the chopper, is a sample holder that can be moved into the cluster beam to collect the nanocrystals. Thus, silicon particles with preselected size can be deposited on the substrate. If the sample holder is moved out of the path of the beam, the silicon nanoparticles enter the UHV detector chamber equipped with a time-of-flight mass spectrometer [68, 69]. Pores are automatically formed when nanocrystals are collected by the substrate. This fabrication route has not attracted much attention due to the complexity of the apparatus and poor adhesion of the porous layer.

3.19. Electrodeposition

Porous silicon structures can also be synthesized by galvanic deposition, also known as immersion plating. Addition of sodium hexafluorosilicate Na₂SiF₆ to dilute hydrofluoric acid concen-

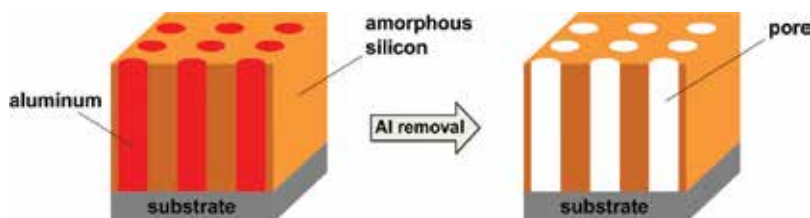


Figure 20. Fabrication of cylindrical pores by dealloying of Al-Si eutectic system and subsequent Al removal (The porous amorphous silicon structure can be crystallized by performing a thermal annealing process.) [67].

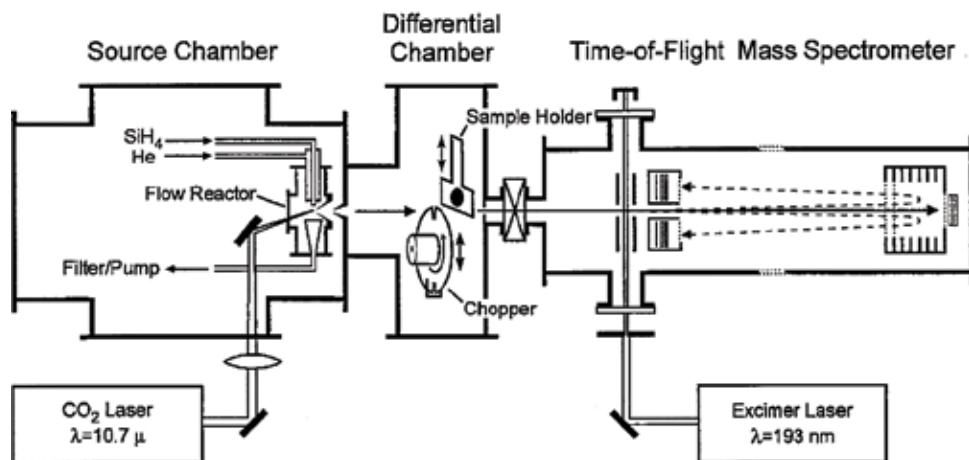
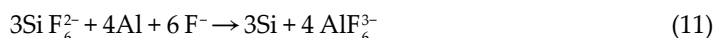


Figure 21. Schematic illustration of the apparatus used for realization of porous silicon layers by laser-induced decomposition of silane [69].

trated with nitric acid solution leads to galvanic deposition of mesoporous silicon layers on metallic substrates like pure aluminum or aluminum alloy [70]. The reaction pathway of this electrodeposition process is as follows:



in which aluminum reduces Si F_6^{2-} to silicon and forms a porous film on the substrate surface. The obtained porous layer has an amorphous structure with pore sizes between 3 and 8 nm [70]. In addition to the limited pore size achievable by electrodeposition, this bottom-up synthesis has a slow rate. Indeed, a 12- μm -thick layer is grown in 6 h. Additionally, the layer has a poor adhesion to the substrate.

3.20. Mechanical synthesis

Porous silicon structures can also be formed by compacting and sintering of silicon powder [71]. This fabrication method usually consists of a top-down stage in which silicon powder is formed and a bottom-up pressing process followed by sintering. Silicon powder is usually synthesized by grinding monocrystalline silicon wafers or polycrystalline silicon pieces by a high-energy ball mill. The milling reactor and balls can be made of either hardened steel or ceramic materials. The duration of the milling process might vary from several minutes to a few days depending on the desired particle size, degree of amorphization, agglomeration, and stress of the synthesized powder. Although high-energy ball milling is now extensively used to prepare silicon powder, the material can also be synthesized by precipitation of silicon from silane, especially when high purity powder is required [72]. Silicon powder is then pressed so that a porous green body is formed. The typical compaction pressure varies between 50 and 1000 MPa and uniaxial or isostatic pressing can be applied [73]. As milling and pressing stages generate highly defective silicon matrix, high-temperature treatment is necessary to release the strain and remove the defects. This high-temperature treatment also promotes a transition from amorphous to crystalline structure. The following sintering stage leads to porous matrices with

typical porosities up to 30%. The limited porosity is the inevitable consequence of the pressure and high temperature of the sintering stage. Indeed, as sintering enhances the strength and density of the material, porosity significantly decreases. However, it is possible to further increase the porosity of the sinter by performing an extra stage of electrochemical or stain etching [73].

All classes of porosity can be realized by mechanical synthesis. Porosity of the sinter can be tailored by tuning compaction pressure and sintering temperature. The method is capable of forming large porous silicon matrices which is impossible by top-down fabrication routes [74]. However, in addition to the limited porosity, lack of control over the morphology of the pores is the main disadvantage of mechanical synthesis. Moreover, high defect density and a great number of impurities of the mechanically made matrix are also important issues. The high compressive stress during ball-powder-ball collisions in the ball milling stage changes the Si–Si bond length, inflicts amorphization, and introduces a great number of defects [75]. Although the structure recrystallizes and most defects are removed during high-temperature treatment, the final product has still significantly higher density of defects and unwanted impurities in comparison to other porous silicon fabrication methods.

3.21. Annealing of ultrathin films of amorphous silicon

Ultrathin low porosity silicon membranes can be fabricated by rapid thermal annealing of predeposited ultrathin amorphous silicon layers [76]. The fabrication process is schematically shown in **Figure 22**. It starts with thermal oxidation in which 500 nm layers of SiO₂ are grown on both sides of the wafer. These oxide layers are not required for porous silicon formation and grown so that the membrane can be realized. After removing the front-side and patterning the back-side oxide layers, a three layer stack of 20 nm SiO₂/15 nm amorphous silicon/20 nm SiO₂ is deposited on the front-side of the wafer. The structure is then placed in a rapid thermal annealing setup and exposed to high temperature (770°C) for 30 s. As a result

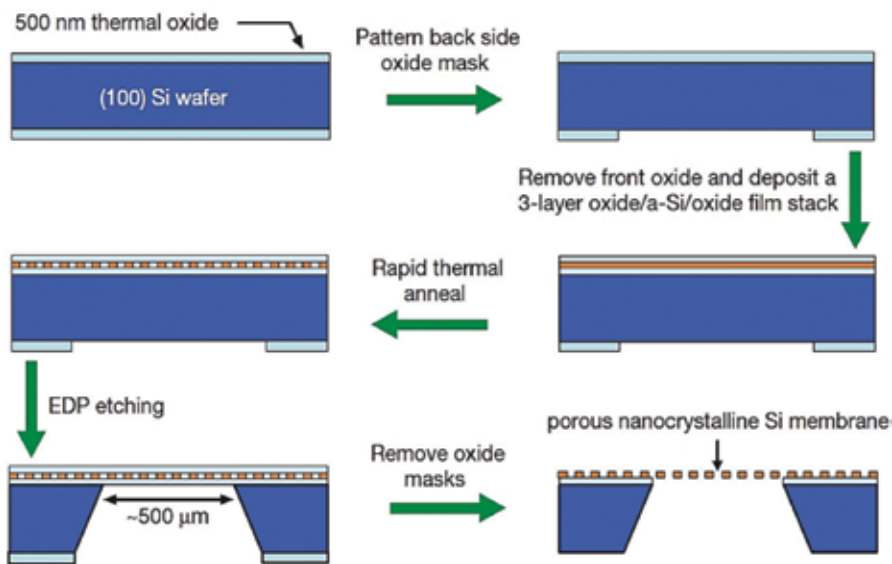


Figure 22. Fabrication process of porous nanocrystalline silicon membranes for ultrafiltration [76].

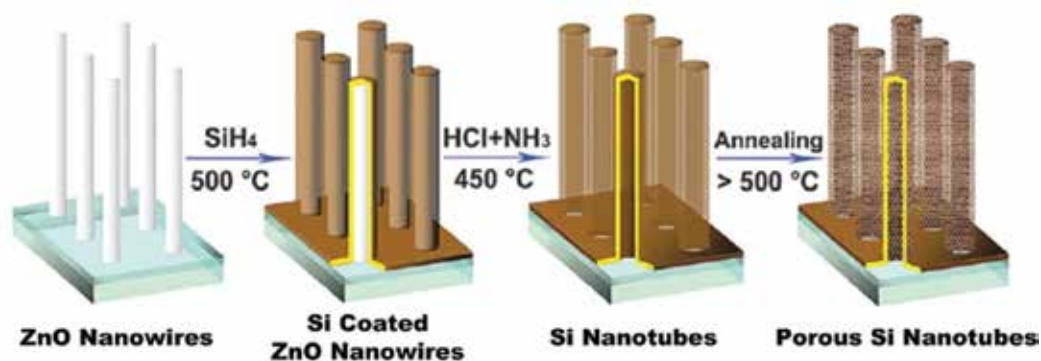


Figure 23. Fabrication of porous silicon nanotubes by using ZnO nanowire templates [77].

of high temperature annealing, nanocrystals nucleate leaving voids behind. Then, the voids span the molecularly thin membrane to create pores. Finally, the membrane is fabricated by anisotropic etching of the back-side of the wafer with ethylenediamine pyrocatechol (EDP) and removal of the protecting oxide layers. This method can only be used for the fabrication of ultrathin layers of porous silicon which is applicable for ultrafiltration. The porosity of the layers cannot exceed 7% and the pore sizes ranges only between 5 and 55 nm.

3.22. Using sacrificial template

As depicted in **Figure 23**, firstly, an array of ZnO nanowires is grown on the substrate. The specimen is then placed in a CVD reactor in which silane is used to form a silicon coating around the ZnO nanowires. The thickness of the over-coating silicon shell, which can be determined by the duration of the silane exposure, is extremely crucial for the formation of porous silicon. Indeed, only silicon sidewall thicknesses of about 12 nm or less finally lead to porous nanotubes. The temperature of the CVD process determines the crystallinity of the silicon over-coating layer. Deposition at 500°C results in amorphous silicon, while formation of crystalline shells requires at least 600°C. In order to remove the ZnO template and form silicon nanotubes, the sample is heated up to 450°C at the presence of ammonium chloride NH_4Cl . Ammonium chloride sublimates and decomposes into ammonia and hydrogen chloride gas. The latter reacts with ZnO creating ZnCl_2 liquid which is then converted into zinc amide species in the presence of ammonia. If the sidewall would be less than 12 nm, a further thermal annealing process porosifies the nanotubes. Porosification has been attributed to a strain-influenced mechanism [77]. The pore sizes of the obtained structure ranges from 5 to 10 nm. These porous nanotubes can be used for therapeutic applications due to their solubility in water at room temperature.

4. Applications

Due to its high chemical reactivity and rapid oxidation, porous silicon was being utilized for device isolation. By the end of the 1980s, porous silicon had also been used for other purposes like the realization of SOI substrates and the formation of a buffer layer in epitaxial growth of compound semiconductors on silicon substrates. However, it was only after the discovery of

strong photoluminescence in porous silicon that the material attracted broad attention. Since then porous silicon has been used for the fabrication of gas sensors, humidity sensors, biosensors, light emitting structures, optical waveguides, distributed Bragg reflectors, Fabry-Pérot resonators, photonic crystals, flat panel displays, optical and acoustic filters, ultrasound generators, and many other devices. Even though optoelectronics has remained the main research area of porous silicon, recently, the material has found application in other areas like medicine, diagnostics, cosmetics, consumer care, and nutrition. In contrast to the conventional chip-based applications, these new areas rely on porous silicon powders and independent structures. In this section, we briefly discuss the application domains of porous silicon and the reader is encouraged to refer to the literature dedicated to porous silicon applications (for example, see [78]).

4.1. Optic and optoelectronic applications

Since Canham's report on strong photoluminescence in porous silicon at room temperature in 1990 [79], the material has attracted broad attention. Indeed, most of the knowledge we now have about this material is due to the interest arose from this observation. Although bulk silicon is a poor emitter of light due to its indirect bandgap, quantum confinement effect makes radiative transition possible in porous silicon. Accordingly, light emitting devices, luminescing in the infrared, visible, and ultraviolet part of the spectrum have been fabricated. There has also been success in integrating porous silicon LEDs with electronic components offering hope for the realization of silicon-based monolithic optoelectronic integrated circuits.

Several optical components have also been realized by porous silicon. For instance, optical waveguides have been prepared using alternating low porosity and high porosity porous silicon layers. In such a structure, light would be trapped inside the low porosity layer which has a higher refractive index in comparison to the adjacent low refractive index layers due to total internal reflection. Based upon the thickness and refractive indices of the layers, the waveguide would support up to several number of propagating modes. Although the light is guided inside the low porosity layer, decaying fields existed in the adjacent layers facilitate coupling of light into and out of the waveguide. Photonic crystals, optical resonators, and diffraction gratings are among other optical applications of porous silicon.

4.2. Electronic applications

Gas sensing, gettering, lithium-ion batteries, and solar cells antireflection coatings are the main application areas of porous silicon in the field of electronics. The large amount of surface area makes porous silicon a promising candidate for realization of gas sensors. Almost a dozen structures have been proposed for porous silicon gas sensors based on alteration of the electrical and optical characteristics of the material in presence of more than 50 chemical species. Porous silicon has also been utilized as an anode in lithium-ion batteries. These anodes not only have more capacity than conventional anodes used in lithium-ion batteries but also are devoid of mechanical instability due to the expansion/contraction problem of bulk silicon with lithiation and delithiation process. Another electronic application area of porous silicon is gettering, i.e., deportation of impurities from active regions of the electronic devices. The great deal of surface area in porous silicon absorbs the impurities and makes the material suitable as a getter medium. Finally, porous silicon is an appropriate candidate to be used as antireflection coatings in solar cells due to its tunable refractive index.

4.3. Medical and diagnostics applications

Both chip-based and independent porous silicon structures have been utilized for medical and diagnostics applications. Biosensors have been realized to detect proteins, enzymes, and antibodies. For instance, porous silicon has been used to measure the prostate-specific antigen (PSA) in order to diagnose prostate cancer. Brachytherapy, insertion of radioactive implants directly into the target tissue, has also used this material to treat cancer. In this technique a medical radioisotope is placed in a porous silicon capsule and injected into the tissue requiring destruction. Meanwhile, biodegradable porous silicon is under preclinical test for drug delivery. The material's tunable pore size and modifiable surface chemistry make tunable drug load and release possible and therefore put porous silicon forward as a potential candidate for this carrier technology. Finally, porous silicon can be considered for tissue engineering due to its desirable properties. In this regenerative medicine, a temporary biodegradable scaffold is implanted in the body so that the tissue could heal itself around it. Accordingly, the scaffold should be made from a biocompatible material that could be easily synthesized, formed and controllably dissolved.

Author details

Farshid Karbassian

Address all correspondence to: f.karbassian@gmail.com

Science and Technology Park, University of Tehran, Tehran, Iran

References

- [1] Thakur M, Issacson M, Sinsabaugh SL, Wong MS, Biswal SL. Gold-coated porous silicon films as anodes for lithium ion batteries. *Journal of Power Sources*. 2012;**205**:426-432. DOI: 10.1016/j.jpowsour.2012.01.058
- [2] Jaouadi M, Dimassi W, Gaidi M, Chtourou R, Ezzaouia H. Nanoporous silicon membrane for fuel cells realized by electrochemical etching. *Applied Surface Science*. 2012;**258**(15):5654-5658. DOI: 10.1016/j.apsusc.2012.02.050
- [3] Anglin EJ, Cheng L, Freeman WR, Sailo MJ. Porous silicon in drug delivery devices and materials. *Advanced Drug Delivery Reviews*. 2008;**60**(11):1266-1277. DOI: 10.1016/j.addr.2008.03.017
- [4] Canham L. Tunable properties of porous silicon. In: Canham L, editor. *Handbook of Porous Silicon*. Switzerland: Springer; 2014. pp. 201-206
- [5] Zhang XG. Morphology and formation mechanisms of porous silicon. *Journal of the Electrochemical Society*. 2004;**151**(1):C69-C80. DOI: 10.1149/1.1632477
- [6] Lehmann V, Stengl R, Luigart A. On the morphology and the electrochemical formation mechanism of mesoporous silicon. *Materials Science and Engineering B*. 2000;**69-70**:11-22. DOI: 10.1016/S0921-5107(99)00286-X

- [7] Uhler A Jr. Electrolytic shaping of germanium and silicon. *Bell System Technical Journal*. 1959;**35**(2):333-347
- [8] Halimaoui A. Porous silicon formation by anodisation. In: Canham L, editor. *Properties of Porous Silicon*. UK: INSPEC; 1997. pp. 12-22
- [9] Fauchet PM et al. Light-emitting porous silicon: Materials science, properties, and device applications. *IEEE Journal of Selected Topics in Quantum Electronics*. 1995;**1**(4):1126-1139. DOI: 10.1109/2944.488691
- [10] Jung KH, Shih S, Kwong DL. Development in luminescent porous Si. *Journal of the Electrochemical Society*. 1993;**140**(10):3046-3064. DOI: 10.1149/1.2220955
- [11] Korotcenkov G, Cho BK. Silicon porosification: State of the art. *Critical Reviews in Solid State and Materials Sciences*. 2010;**35**(3):153-260. DOI: 10.1080/10408436.2010.495446
- [12] Niwano M, Miura T, Kimura Y, Tajima R, Miyamoto N. Real-time, in situ infrared study of etching of Si(100) and (111) surfaces in dilute hydrofluoric acid solution. *Journal of Applied Physics*. 1996;**79**(7):3708-3713. DOI: 10.1063/1.361203
- [13] Lehmann V. *Electrochemistry of Silicon: Instrumentation, Science, Materials and Applications*. Germany: Wiley-VCH; 2002
- [14] Fauchet PM. Progress toward nanoscale silicon light emitters. *IEEE Journal of Selected Topics in Quantum Electronics*. 1998;**4**(6):1020-1028. DOI: 10.1109/2944.736103
- [15] Fuller CS, Ditzenberger JA. Diffusion of donor and acceptor elements in silicon. *Journal of Applied Physics*. 1956;**27**(5):544-553. DOI: 10.1063/1.1722419
- [16] Shih S, Jung KH, Hsieh TY, Sarathy J, Campbell JC, Lockwood DJ. Photoluminescence and formation mechanism of chemically etched silicon. *Applied Physics Letters*. 1992;**60**(15):1863-1865. DOI: 10.1063/1.107162
- [17] Fathauer RW, George T, Ksendzov A, Vasquez RP. Visible luminescence from silicon wafers subjected to stain etches. *Applied Physics Letters*. 1992;**60**(8):995-997. DOI: 10.1063/1.106485
- [18] Xu YK, Adachi S. Properties of light-emitting porous silicon photoetched in aqueous HF/FeCl₃ solution. *Journal of Applied Physics*. 2007;**101**(10):103509. DOI: 10.1063/1.2733752
- [19] Xu YK, Adachi S. Properties of light-emitting porous silicon formed by stain etching in HF/KIO₃ solution under light illumination. *Journal of Applied Physics*. 2008;**103**(10):103512. DOI: 10.1063/1.2924423
- [20] Noguchi N, Suemune I. Luminescent porous silicon synthesized by visible light irradiation. *Applied Physics Letters*. 1993;**62**(12):1429-1431. DOI: 10.1063/1.108650
- [21] Zhang Z, Lerner MM, Alkel T III, Keszler DA. Formation of a photoluminescent surface on n-Si by irradiation without an externally applied potential. *Journal of the Electrochemical Society*. 1993;**140**(6):L97-L98. DOI: 10.1149/1.2221655
- [22] Tomioka S, Miazaki T, Adachi S. Porous silicon formation by photoetching in HF/H₂O₂ solution using incoherent light source. *Japanese Journal of Applied Physics*. 2007;**46**(8A):5021-5024. DOI: 10.1143/JJAP.46.5021

- [23] Andersen OK, Frello T, Veje E. Photoinduced synthesis of porous silicon without anodization. *Journal of Applied Physics*. 1995;**78**(10):6189-6192. DOI: 10.1063/1.360564
- [24] Adachi S. Porous silicon formation by photoetching. In: Canham L, editor. *Handbook of Porous Silicon*. Switzerland: Springer; 2014. pp. 67-74
- [25] Tomioka K, Adachi S. Strong and stable ultraviolet emission from porous silicon prepared by photoetching in aqueous KF solution. *Applied Physics Letters*. 2005;**87**(25):251920. DOI: 10.1063/1.2149157
- [26] Xu YK, Adachi S. Light-emitting porous silicon formed by photoetching in aqueous HF/KIO₃ solution. *Journal of Physics D: Applied Physics*. 2006;**39**(21):4572-4577. DOI: 10.1088/0022-3727/39/21/011
- [27] Dimova-Malinovska D, Sendova-Vassileva M, Tzenov N, Kamenova M. Preparation of thin porous silicon layers by stain etching. *Thin Solid Films*. 1997;**297**(1-2):9-12. DOI: 10.1016/S0040-6090(96)09434-5
- [28] Megouda N, Hadjersi T, Piret G, Boukherroub R, Elkechai O. Au-assisted electroless etching of silicon in aqueous HF/H₂O₂ solution. *Applied Surface Science*. 2009;**255**(12):6210-6216. DOI: 10.1016/j.apsusc.2009.01.075
- [29] Chartier C, Bastide S, Lévy-Clément C. Metal-assisted chemical etching of silicon in HF-H₂O₂. *Electrochimica Acta*. 2008;**53**(17):5509-5516. DOI: 10.1016/j.electacta.2008.03.009
- [30] Peng K et al. Fabrication of single-crystalline silicon nanowire by scratching a silicon surface with catalytic metal particles. *Advanced Functional Materials*. 2006;**16**(3):387-394. DOI: 10.1002/adfm.200500392
- [31] Qu Y et al. Electrically conductive and optically active porous silicon nanowires. *Nano Letters*. 2009;**9**(12):4539-4543. DOI: 10.1021/nl903030h
- [32] Karbassian F, Mousavi BK, Rajabali S, Talei R, Mohajerzadeh S, Asl-Soleimani E. Formation of luminescent silicon nanowires and porous silicon by metal-assisted electroless etching. *Journal of Electronic Materials*. 2014;**43**(4):1271-1279. DOI: 10.1007/s11664-014-3051-3
- [33] Saadoun M, Ezzaouia H, Bessaïs B, Boujmil MF, Bennaceur R. Formation of porous silicon for large-area silicon solar cells: A new method. *Solar Energy Materials & Solar Cells*. 1999;**59**(4):377-385. DOI: 10.1016/S0927-0248(99)00057-4
- [34] Saadoun M et al. Vapour-etching-based porous silicon: A new approach. *Thin Solid Films*. 2002;**405**(1-2):29-34. DOI: 10.1016/S0040-6090(01)01757-6
- [35] Saadoun M et al. Formation of luminescent (NH₄)₂SiF₆ phase from vapour etching-based porous silicon. *Applied Surface Science*. 2003;**210**(3-4):240-248. DOI: 10.1016/S0169-4332(03)00152-1
- [36] Karbassian F, Rajabali S, Chimeh A, Mohajerzadeh S, Asl-Soleimani E. Luminescent porous silicon prepared by reactive ion etching. *Journal of Physics D: Applied Physics*. 2014;**47**(38):385103. DOI: 10.1088/0022-3727/47/38/385103

- [37] Cullis AG, Canham LT, Calcott PDJ. The structural and luminescence properties of porous silicon. *Journal of Applied Physics*. 1997;**82**(3):909-965. DOI: 10.1063/1.366536
- [38] Hummel RE, Chang S-S. Novel technique for preparing porous silicon. *Applied Physics Letters*. 1992;**61**(16):1965-1967. DOI: 10.1063/1.108331
- [39] Ludwig MH, Hummel RE, Stora M. Luminescence of spark-processed materials. *Thin Solid Films*. 1995;**255**(1-2):103-106. DOI: 10.1016/0040-6090(94)05631-M
- [40] Chang S-S, Kurokawa S, Sakai A. Luminescence properties of spark-processed Si in air, O₂, and N₂ with low pressure. *Applied Surface Science*. 2006;**252**(12):4048-4054. DOI: 10.1016/j.apsusc.2005.04.054
- [41] Stora ME, Hummel RE. Variation of spark-processing parameters on the photoluminescence properties of spark-processed silicon. *Journal of Physics and Chemistry of Solids*. 2002;**63**(9):1655-1668. DOI: 10.1016/S0022-3697(01)00250-5
- [42] Kabashin AV, Meunier M. Fabrication of photoluminescent Si-based layers by air optical breakdown near the silicon surface. *Applied Surface Science*. 2002;**186**(1-4):578-582. DOI: 10.1016/S0169-4332(01)00690-0
- [43] Rochow EG. The direct synthesis of organosilicon compounds. *Journal of the American Chemical Society*. 1945;**67**(6):963-965. DOI: 10.1021/ja01222a026
- [44] Zhang Z et al. Scalable synthesis of interconnected porous silicon/carbon composites by the Rochow reaction as high-performance anodes of lithium ion batteries. *Angewandte Chemie, International Edition*. 2014;**53**(20):5165-5169. DOI: 10.1002/anie.201310412
- [45] Stepanov AL, Trifonov AA, Osin YN, Valeev VF, Nuzhdin VI. Fabrication of nanoporous silicon by Ag⁺-ion implantation. *Nanoscience and Nanoengineering*. 2013;**1**(3):134-138. DOI: 10.13189/nn.2013.010302
- [46] Darby BL et al. Insights for void formation in ion-implanted Ge. *Thin Solid Films*. 2011;**519**(18):5962-5965. DOI: 10.1016/j.tsf.2011.03.040
- [47] Abdi Y, Hashemi P, Karbassian F, Nayeri FD, Behnam A, Mohajerzadeh S, Koohsorkhi J, Robertson MD, Arzi E. Fabrication of nano-crystalline porous silicon on Si substrates by a plasma enhanced hydrogenation technique. In: *Mater. Res. Soc. Symp. Proc.*; March–April 2005; San Francisco, CA. Vol. 862. pp. A19.1.1-A19.1.6. DOI: 10.1557/PROC-862-A19.1
- [48] Abdi Y, Derakhshandeh J, Hashemi P, Mohajerzadeh S, Karbassian F, Nayeri F, Arzi E, Robertson MD, Radamson H. Light-emitting nano-porous silicon structures fabricated using a plasma hydrogenation technique. *Materials Science and Engineering B*. 2005;**124-125**:483-487. DOI: 10.1016/j.mseb.2005.08.090
- [49] Jamei M, Karbassian F, Mohajerzadeh S, Abdi Y, Hashemi P, Robertson M, Yuill S. Silicon nanocrystals fabricated by a novel plasma enhanced hydrogenation technique suitable for light emitting devices. In: *Mater. Res. Soc. Symp. Proc.*; Nov. 2006; Boston, MA. Vol. 958. DOI: 10.1557/PROC-0958-L07-05

- [50] Jamei M, Fallah B, Mohajerzadeh S, Karbassian F, Abdi Y, Koohsorkhi J, Robertson MD, Yuill S. Fabrication of light emitting diodes using nano-porous silicon thin films. In: *Nanotech Proc.*; May 2007; Santa Clara, CA. Vol. 1. pp. 177-180
- [51] Jamei M, Karbassian F, Mohajerzadeh S, Abdi Y, Robertson MD, Yuill S. The preparation of nanocrystalline silicon by plasma-enhanced hydrogenation for the fabrication of light-emitting diodes. *IEEE Electron Device Letters*. 2007;**28**(3):207-210. DOI: 10.1109/LED.2007.891260
- [52] Savin DP, Roizin YO, Demchenko DA, Mugeński E, Sokólska I. Properties of laser ablated porous silicon. *Applied Physics Letters*. 1996;**69**(20):3048-3050. DOI: 10.1063/1.116835
- [53] Kalkan AK, Bae S, Li H, Hayes DJ, Fonash SJ. Nanocrystalline Si thin films with arrayed void-column network deposited by high density plasma. *Journal of Applied Physics*. 2000;**88**(1):555-561. DOI: 10.1063/1.373695
- [54] Beydaghyan G, Kaminska K, Brown T, Robbie K. Enhanced birefringence in vacuum evaporated silicon thin films. *Applied Optics*. 2004;**43**(28):5343-5349. DOI: 10.1364/AO.43.005343
- [55] Jang SJ, Song YM, Yeo CI, Park CY, Lee YY. Highly tolerant a-Si distributed Bragg reflector fabricated by oblique angle deposition. *Optical Materials Express*. 2011;**1**(3):451-457. DOI: 10.1364/OME.1.000451
- [56] Godinho V et al. A new bottom-up methodology to produce silicon layers with a closed porosity nanostructure and reduced refractive index. *Nanotechnology*. 2013;**24**(27):275604. DOI: 10.1088/0957-4484/24/27/275604
- [57] Poxson DJ et al. High-performance antireflection coatings utilizing nanoporous layers. *MRS Bulletin*. 2011;**36**(6):434-438. DOI: 10.1557/mrs.2011.110
- [58] Nakahata T, Nakajima H. Fabrication of lotus-type porous silicon by unidirectional solidification in hydrogen. *Materials Science and Engineering A*. 2004;**384**(1-2):373-376. DOI: 10.1016/j.msea.2004.07.004
- [59] Bao Z et al. Chemical reduction of three-dimensional silica micro-assemblies into micro-porous silicon replicas. *Nature*. 2007;**446**(7132):172-175. DOI: 10.1038/nature05570
- [60] Zheng Y, Yang J, Wang J, NuLi Y. Nano-porous Si/C composites for anode material of lithium-ion batteries. *Electrochimica Acta*. 2007;**52**(19):5863-5867. DOI: 10.1016/j.electacta.2007.03.013
- [61] Yasuda K, Nohira T, Ogata YH, Ito Y. Direct electrolytic reduction of solid silicon dioxide in molten LiCl-KCl-CaCl₂ at 773 K. *Journal of the Electrochemical Society*. 2005;**152**(11):D208-D212. DOI: 10.1149/1.2042910
- [62] Wang J-F et al. Amorphous silicon with high specific surface area prepared by a sodio-thermic reduction method for supercapacitors. *Chemical Communications*. 2013;**49**(44):5007-5009. DOI: 10.1039/c3cc41967c

- [63] Canham L. Porous silicon formation by porous silica reduction. In: Canham L, editor. Handbook of Porous Silicon. Switzerland: Springer; 2014. pp. 85-92
- [64] Nohira T, Yasuda K, Ito Y. Pinpoint and bulk electrochemical reduction of insulating silicon dioxide to silicon. *Nature Materials*. 2003;**2**(6):397-401. DOI: 10.1038/nmat900
- [65] Banerjee HD, Sen S, Acharya HN. Investigations on the production of silicon from rice husks by the magnesium method. *Materials Science and Engineering*. 1982;**52**(2):173-179. DOI: 10.1016/0025-5416(82)90046-5
- [66] Fukutani K, Tanji K, Motoi T, Den T. Ultrahigh pore density nanoporous films produced by the phase separation of eutectic Al-Si for template-assisted growth of nanowire arrays. *Advanced Materials*. 2004;**16**(16):1456-1460. DOI: 10.1002/adma.200400268
- [67] Fukutani K, Ishida Y, Aiba T, Miyata H, Den T. Characterization of nanoporous Si thin films obtained by Al-Si phase separation. *Applied Physics Letters*. 2005;**87**(25):253112. DOI: 10.1063/1.2149292
- [68] Voigt F, Brüggemann R, Unold T, Huiskens F, Bauer GH. Porous thin films grown from size-selected silicon nanocrystals. *Materials Science and Engineering: C*. 2005;**25**(5-8): 584-589. DOI: 10.1016/j.msec.2005.06.035
- [69] Huiskens F, Hofmeister H, Kohn B, Laguna MA, Paillard V. Laser production and deposition of light-emitting silicon nanoparticles. *Applied Surface Science*. 2000;**154-155**:305-313. DOI: 10.1016/S0169-4332(99)00476-6
- [70] Krishnamurthy A, Rasmussen DH, Suni IL. Galvanic deposition of Nanoporous Si onto 6061 Al alloy from aqueous HF. *Journal of the Electrochemical Society*. 2011;**158**(2):D68-D71. DOI: 10.1149/1.3521290
- [71] Greskovich C, Rosolowski JH. Sintering of covalent solids. *Journal of the American Ceramic Society*. 1976;**59**(7-8):336-343. DOI: 10.1111/j.1151-2916.1976.tb10979.x
- [72] Möller H-J, Welsch G. Sintering of ultrafine silicon powder. *Journal of the American Ceramic Society*. 1985;**68**(6):320-325. DOI: 10.1111/j.1151-2916.1985.tb15233.x
- [73] Jakubowicz J. Porous silicon formation by mechanical means. In: Canham L, editor. Handbook of Porous Silicon. Switzerland: Springer; 2014. pp. 93-102
- [74] Jakubowicz J, Smardz K, Smardz L. Characterization of porous silicon prepared by powder technology. *Physica E*. 2007;**38**(1-2):139-143. DOI: 10.1016/j.physe.2006.12.017
- [75] Unifantowicz P, Vaucher S, Lewandowska M, Kurzydłowski KJ. Structural changes of silicon upon high-energy milling investigated by Raman spectroscopy. *Journal of Physics: Condensed Matter*. 2008;**20**(2):025205. DOI: 10.1088/0953-8984/20/02/025205
- [76] Striemer CC, Gaborski TR, McGrath JL, Fauchet PM. Charge- and size-based separation of macromolecules using ultrathin silicon membranes. *Nature*. 2007;**445**(7129):749-753. DOI: 10.1038/nature05532

- [77] Huang X, Gonzalez-Rodriguez R, Rich R, Gryczynski Z, Coffey JL. Fabrication and size dependent properties of porous silicon nanotube arrays. *Chemical Communications*. 2013;**49**(51):5760-5762. DOI: 10.1039/c3cc41913d
- [78] Canham L, editor. *Handbook of Porous Silicon*. Switzerland: Springer; 2014. pp. 731-1008
- [79] Canham LT. Silicon quantum wire array fabricated by electrochemical and chemical dissolution of wafers. *Applied Physics Letters*. 1990;**57**(10):1046-1048. DOI: 10.1063/1.103561

Nanoporous Carbon Synthesis: An Old Story with Exciting New Chapters

Ana S. Mestre and Ana P. Carvalho

Additional information is available at the end of the chapter

<http://dx.doi.org/10.5772/intechopen.72476>

Abstract

Activated carbons are key materials in technological applications of multidisciplinary fields (e.g. adsorption, separation, and catalytic processes). The extensive use of these materials results from the combination of a well-developed pore network (micropores or micro + mesopores) along with the presence of heteroatoms (e.g. oxygen, nitrogen, and sulfur). The large scale production of nanoporous carbons is a well-established process since the first patents date from the beginning of the twentieth century. Conventional activation methodologies are divided between physical, using steam or CO₂, and chemical, being KOH, ZnCl₂, and H₃PO₄ the most commonly reported oxidizing agents. Due to the paucity of operational parameters that can be changed or added in the production of activated carbons, there is still room for R&D. In this chapter, both conventional and innovative synthetic processes are reviewed to offer an up-to-date picture regarding raw materials, carbonization step, activation process, and other approaches. Conventional activation of gels and chars obtained by novel approaches (i.e. sol-gel method, hydrothermal carbonization (HTC), and acid-mediated carbonization) and more innovative strategies (i.e. variations of HTC process, carbonization of organic salts and ionothermal approaches) are addressed. Textural, surface chemistry and morphological properties of the derived porous carbons were reviewed and critically rationalized.

Keywords: nanoporous carbon materials, carbon precursors, conventional synthesis, innovative synthesis, pore size distribution, heteroatom doping, morphology

1. Historic perspective

Carbon is the main element of the entire world's flora, and its atomic structure allows unique bonding possibilities leading to various structures with distinct properties. As consequence, carbon materials are used for so long that it is hard to determine the very first moment.

At the beginning, carbon was used in the form of charcoal that consists of carbonized wood, coal or partially devolatilized coals, and also carbon black obtained by incomplete burning of vegetable oil. After centuries of use of these man-made forms of carbon, the discovery of the processes to perform the activation of charcoal allowed to greatly improve the properties and performances of carbon materials. These new materials where pores (voids) are enclosed by carbon atoms are known as activated carbons or active carbons and, more recently, also named as nanoporous carbons.

The oldest known man-made carbon forms—charcoal and carbon black—were used in the Stone Age as a black color pigment for cave painting [1]. For example, charcoal was used as color pigment to draw the black lines of the illustrations in the Cave of Altamira (Spain) that represents the apogee of Paleolithic cave painting art developed across Europe, from 35,000 to 11,000 BC. At about 8,000 BC, charcoal was used in metal production [1]. In 3,750 BC, the Egyptians and Sumerians used it in the reduction of copper, tin, and zinc minerals in the bronze manufacturing process and also as smokeless fuel [2–4]. The first proof of the medicinal use of carbons was found in an Egyptian papyrus, dated of 1,550 BC, where it is reported the use of charcoal for the adsorption of odors from putrefying wounds and also to treat problems of the intestinal tract [5, 6]. The therapeutic value of carbon was later explored by the Greeks (Hippocrates, ca. 460–370 BC) and Romans (Pliny the Elder, AD 23–79) in the treatment of various diseases, including food poisoning, epilepsy, chlorosis, and anthrax [1, 7]. Hippocrates also recommended that the water should be filtered with carbonized wood before its consumption, so as to eliminate bad flavor and odor [8]. Also, Hindu documents from 450 BC mention the use of sand and charcoal filters for drinking water purification [5, 6]. Recent studies also concluded that in Phoenicians ships (460 BC) drinking water was stored in carbonized wood barrels to keep it fresh, a practice that was continued until the eighteenth century. In 157 AD, a medical treatise from Claudius Galvanometer indicated the use of carbons of both vegetable and animal origin for the treatment of various diseases [9]. A Sanskrit document (AD 200) recommended that after being stored in copper vessels and exposed to sunlight, water should be filtrated with coal [6]. This is most probably one of the earliest manuscripts describing the degradation of contaminants from water to assure its disinfection.

It was only during the eighteenth century that the mechanisms underlying the properties of charcoals started to be recognized. In 1773, Scheele measured the adsorptive properties of charcoals from distinct sources using various gases; a decade later, Lowitz studied the abilities of charcoals to adsorb odors from wounds [7, 9]. This author published results regarding the adsorption of a range of organic vapors and also studied systematically the adsorption in various aqueous solutions, namely in the decolorization of contaminated tartaric acid solutions. The discussion of the contribution of charcoals to control odors from gangrenous ulcers was made by Kehl, in 1793, who also discovered that charcoal from animal origin (animal tissues) could be used to remove color from solution, including from sugar solutions [7, 9]. The introduction of carbon materials in industrial processes took place in England, in 1794, when wood charcoals were applied as bleaching agents in the processing of sugar. By that time, the method for preparing the wood charcoals was kept a secret [9]. In 1805, the first large-scale sugar refining facility was introduced in France by Gruillon, working with ground and washed wood char [9]. Between 1805 and 1808, Delessert demonstrated the effectiveness

of charcoal for decolorizing sugar-beet liquor contributing for the growth of this industry in France [9]. In 1808, all European sugar refineries were using charcoal as a decolorizer [9]. The discovery of bone-derived char as a more efficient raw sugar syrups decolorizing agent was made by Figuier in 1811, and quickly the sugar industry replaced wood charcoal by this improved material [5, 9]. The regeneration of bone-derived char by heating was discovered in 1811, and sometime later granular bone-derived char started to be produced, thus enabling an easier regeneration [9]. In 1815, the majority of sugar refining facilities were using granular bone-derived char [9]. The dependence of the decolorizing properties on the char's source, the thermal processing and particle size was demonstrated by Bussy in 1822 [9]. He also produced a carbon material with higher decolorizing ability than bone-derived char by heating blood with potash, being this the first recorded example of an "activated carbon" material obtained by thermal and chemical processes [5, 9].

The first large-scale application in gas phase took place in 1854 [8], with the installation of carbon filters in London sewage ventilation systems. In 1872, carbon filters were also used in the masks of the chemical industry workers for preventing the inhalation of mercury vapors.

Besides thousands of years of history, and the already large range of applications for charcoals, it was only in the beginning of the twentieth century that one of the most outstanding abilities of carbon materials was explored: the possibility of enclosing a huge porosity into the carbon material structure. This "revolution" was due to the discoveries of Raphael von Ostrejko that, between 1900 and 1903, patented two different methods for the industrial activation of charcoal and the production of activated carbon materials [10]. This set of patents mentions the bases of the chemical activation process (carbonization of lignocellulosic materials with metallic chlorides) and of the thermal or physical activation (slight gasification of chars with water vapor or carbon dioxide at elevated temperatures) and also the specific equipment for thereof. The factory for full-scale activated carbon production was built by that time in Ratibor, now named Raciborz (Poland), and still operates, being so the world's oldest industrial activated carbon manufacturing plant [10, 11].

Although sugar industry was the first to apply activated carbons, in this case for whitening purposes, the starting point for the great development in the production and application of activated carbons was undoubtedly World War I, when these materials were used in gas masks [7, 8]. The production and search for new activated carbons has been boosted decade after decade due to their fundamental role in various technological applications which are related to, namely, restricted environmental regulations, recovery of valuable chemical compounds, and catalysts support [8, 12–14].

Nowadays, the driving forces for the research in nanoporous carbons are related with the properties of the most recent carbon materials: fullerenes [15], carbon nanotubes [16] and graphene [17]. However, the excellent properties of these novel carbon forms also fostered the interest in the traditional porous carbons and, in the recent years, a considerable number of studies searching for new synthetic approaches have been published. The main objective is the preparation of highly porous materials with controlled porosity, and often also with tuned surface chemistry, to present enhanced behavior as, for example, electrode materials for supercapacitors.

2. Properties of nanoporous carbons

Describing nanoporous carbon materials as carbon structures with enclosed porosity is correct but it is somewhat incomplete since properties, as for example, surface chemistry, chemical composition, morphology or electrical conductivity are also essential to understand their potential and performance in a given application.

Regarding the physical properties of nanoporous carbon materials, porosity is undoubtedly the most important one. IUPAC defines *nanopores* as pores with apertures up to around 100 nm and, according to their size, *nanopores* are classified as follows [18]:

- *Micropores*—pores with width less than 2 nm
- *Mesopores*—pores with width between 2 and 50 nm
- *Macropores*—pores with width greater than 50 nm

Due to their relevance for the adsorption process, micropores can be further distinguished between *narrow micropores* (i.e. *ultramicropores*) with width <0.7 nm and *wide micropores* (i.e. *supermicropores*) with width between 0.7 and 2 nm [18].

The limits for this pore classification were suggested by nitrogen adsorption-desorption data at -196°C [18] and rely on the fact that each pore size range corresponds to different pore filling mechanisms disclosed by the isotherm profile [19]. Micropore filling is regarded as a primary physisorption process and occurs at low relative pressures. Firstly, at very low relative pressure, adsorption occurs in the ultramicropores where due to the close vicinity of pore walls there is an overlapping of the adsorption forces favoring the enhancement of the adsorbent-adsorbate interaction, this process is termed “primary micropore filling.” After this initial filling in the most energetic sites, the cooperative adsorbate-adsorbate interactions inside the supermicropores become more relevant (secondary process) occurring up to relative pressures ≈ 0.15 [18]. In mesopores, the physisorption comprises three stages: monolayer adsorption (i.e. all adsorbate molecules are in contact with the surface of the adsorbent) followed by consecutive adsorbate layers (multilayer adsorption) and finishing with capillary condensation [18]. The adsorption onto mesopores commonly presents a hysteresis loop [19]. The macropores are so wide that do not allow capillary condensation since behave as an open space (cannot be characterized by nitrogen adsorption whose maximum relative pressure occurs near the unity) [19].

In nanoporous carbons, the porosity results from the voids between the randomly cross-linked graphite-like crystallites that constitute the structure of the carbon skeleton, from the consumption of less organized carbonaceous matter and also from the removal of reactive carbon atoms in the crystallite during activation process (**Figure 1**). Surface area and pore size distribution (PSD) are the physical properties that will greatly influence the performance of nanoporous carbons in a given process. These parameters are commonly obtained from the analysis of nitrogen adsorption isotherm at -196°C . The surface area (apparent surface area for microporous materials) is commonly obtained applying the Brunauer-Emmett-Teller (BET) equation. Regarding

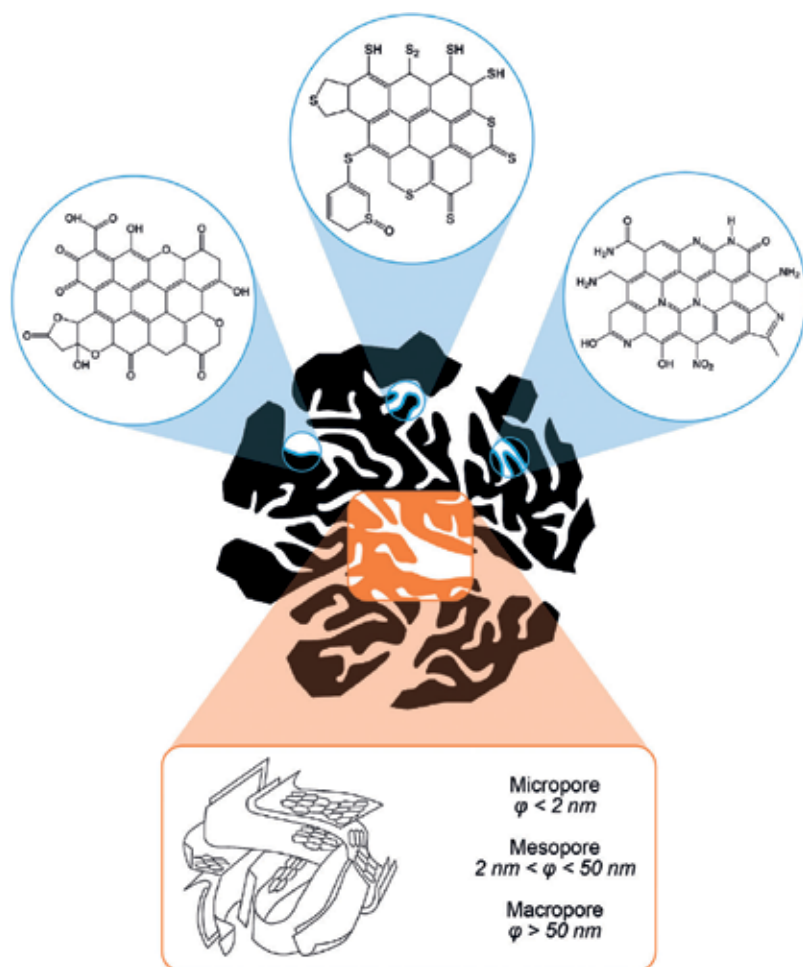


Figure 1. Schematic representation of pore structure (bottom rectangle) and surface chemistry—oxygen, nitrogen, and sulfur groups (top circles)—in nanoporous carbons.

the PSD, there are various mathematic models available, being those using the Non-Local Density Functional Theory (NLDFT) the most advanced ones. The use of nitrogen as adsorptive at -196°C has however diffusional limitations in ultramicroporous carbon materials; thus, for an accurate characterization of the micropore network, carbon dioxide adsorption at 0°C has been repeatedly proposed as a better alternative to nitrogen [20–22]. Besides the limitation of nitrogen for the characterization of ultramicropores, it is known that, due to its quadrupole moment, nitrogen molecule orientation during adsorption will be dependent on the surface chemistry of the adsorbent [18, 22]. To overcome this issue, other adsorptive gases like argon or krypton can be used.

Carbon atoms are the major element of nanoporous carbon skeleton but the elemental composition of these materials also includes hydrogen and oxygen and, depending on the precursor, preparation route and post-synthesis functionalization may also have nitrogen,

sulfur or phosphorus containing groups. These heteroatoms are mainly located at the edges of the basal planes due to the presence of unsaturated carbon atoms that are highly reactive. **Figure 1** summarizes the most relevant oxygen, nitrogen, and sulfur-containing surface groups that may be present in the surface of nanoporous carbon materials, being important to mention that oxygen surface groups are, by far, the most common ones. These materials may also contain inorganic matter, sometimes attaining 20% (wt.), being this ash content mainly inherited from the carbon precursor [12].

The elemental composition and type of surface groups of a nanoporous carbon influence its performance in both gaseous and liquid phase processes, due to specific interactions with the adsorptive and also the solvent in the case of adsorption from solution. Properties like hydrophobicity/hydrophilicity or acid/base behavior are highly dependent on the surface chemistry of these materials. Carbons are in general hydrophobic, but the presence of increasing amounts of oxygen surface functionalities favors the adsorption of water molecules due to the formation of hydrogen bonds and, consequently, its wettability. This ability of porous carbon materials may be advantageous, or not, depending on the desired application. For example, in the impregnation of carbon supports with catalysts in aqueous phase, a high wettability will increase the impregnation degree; but in the adsorption of organic compounds from diluted aqueous solutions, higher wettability may lead to the formation of water molecule clusters that hinder the diffusion of the target compounds towards the adsorption active sites (the same being valid for gas streams purification).

Regarding acid/base character, nanoporous carbons are considered amphoteric materials due to the presence of both acid and basic sites in their surface. Thus, depending on the amount and strength of all the surface groups, the materials may present net acid, basic or neutral surfaces. The surface chemistry of nanoporous carbons can be assessed through numerous techniques, and the best way to get a good characterization is to employ complementary techniques and combine the analysis of the results. For example, Boehm and potentiometric titrations provide qualitative and quantitative information on the surface of the nanoporous carbons, while temperature programmed desorption (TPD) detects more oxygen groups than Boehm titration, although with less quantitative information. On the other hand, X-ray photoelectron spectroscopy (XPS) and diffuse reflectance infrared spectroscopy (DRIFT) provide qualitative information about the surface of the nanoporous carbons [23].

Other properties of nanoporous carbon materials that may play important roles in specific applications are the morphology (powdered (PAC) and granular (GAC) forms are the most common ones), electrical conductivity, hardness and density.

For more specific information regarding properties of nanoporous carbon materials and characterization methods, several reference texts are available [8, 21, 23–27].

3. Nanoporous carbon synthesis

There are a large range of carbon-rich precursors namely from vegetable (e.g. wood, fruit shells, stones or peels) or petrochemical origin that can be successfully transformed into activated carbons. However, the economically viable large-scale production of activated carbons

requests the use of raw materials that gather high availability and constancy with high density and hardness, low inorganic content and, last but not the least, low cost. Thus, commercially available activated carbons are mainly produced from coal (i.e. lignite, sub-bituminous, bituminous and anthracite), coconut shell charcoal and wood charcoal. The raw material is a key issue for activated carbon producers since the development of the porous network occurs by consumption of the (char)coal precursor and the preparation yields can reach values as low as 10% (wt.). Consequently, assuring the supply of high quality precursors at a cost-effective price is of paramount importance to control the quality of the final material and the production cost. In 2015, the global activated carbon market was valued by Markets and Markets at USD 4.74 billion corresponding to 2743.7 kton being expected to continue to growth, mainly driven by more stringent government regulations to assure human and environmental protection. As already mentioned, (char)coal is the most important raw material for activated carbon producers but they are not the major (char)coal consumer. In fact, activated carbons are only a “by-product” of (char)coal production, which have the energy sector as major market (mainly for metallurgical, industrial and cooking fuel) that actually controls demand and prices. This reality, allied to the fact that most of raw materials came from the Asian continent, and that external factors (e.g. natural disasters) may compromise the quality, availability and cost of (char)coal, continues to drive the research for finding new, and more sustainable, raw materials and preparation routes for activated carbon production.

Conventional methods for activated carbon production request the use of high temperature kilns where, under a controlled atmosphere, the carbon-rich raw materials are transformed into nanoporous carbons. There are numerous procedures for the production of activated carbons, although the great majority of synthetic routes published and patents registered worldwide, including those allowing nowadays industrial production, fall in two major categories: the selective gasification of raw materials’ carbon atoms (physical or thermal activation), and the co-carbonization of the precursor with oxidizing and/or dehydrating agents (chemical activation). The number of steps requested for the production of activated carbons depends on the characteristics of the raw material, morphological specifications of the final product, and on the type of activation. A general process flowsheet is presented in **Figure 2**.

The most commonly used **pre-treatments** are those aiming to obtain a given particle size or shape, washing steps for dirt removal and/or for the reduction of the inorganic content (i.e. acid washing) and pre-oxidation to prevent fluidization of coking coal during carbonization [8, 12]. The raw material can be crushed and sieved to obtain powdered or granular particles with specific dimensions. Milling, binder addition and briquetting are other common options when working with precursors presenting low volatile content (e.g. medium-high rank coals,

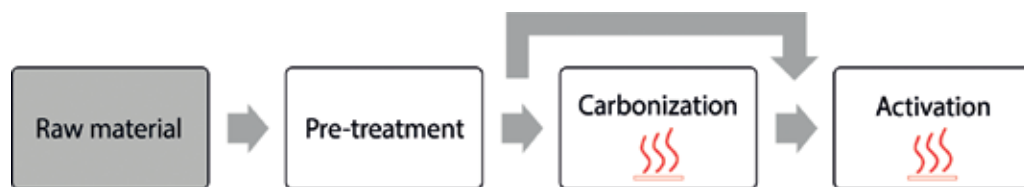


Figure 2. General flowsheet for conventional physical (thermal) and chemical activation processes.

volatiles <20–30% (wt.)). To assure an efficient diffusion of the activating agent to all the individual coal particles of the briquette, it is common to mill and subsequently briquette the particles to obtain granular materials with a well-developed network of transport pores (i.e. meso and macropores) [8]. Direct activation of granular coal with low volatile content will not allow an uniform activation of the granules due to the incipient network of transport pores.

Physical or thermal activation is generally made in two consecutive heating steps: carbonization under inert atmosphere (usually nitrogen) to devolatilize the raw material, followed by activation that consists in the partial gasification of the obtained char with oxidizing agents (i.e. steam, carbon dioxide or a mixture of both) leading to the formation of the porous network. While the carbonization usually occurs at temperatures between 400 and 600°C, the gasification requests temperatures ranging from 800 to 1000°C. Depending on the raw material, it is also possible to avoid the carbonization step and proceed directly to the thermal activation. Activation with CO_2 must occur in conditions that assure chemical control (slow activation rate—days) instead of diffusional control which is faster but leads to external particle burning and, consequently, to poor porosity development [8]. The reactions of steam and carbon dioxide with carbon are endothermic, thus thermal activation needs external energy supply to maintain the requested high temperature. Oxygen (or air) is not commonly used as oxidizing agent since its reaction with carbon is highly exothermic and fast, being difficult to control and assure porosity development instead of particle consumption [8, 12, 24]. Due to this and to the safety issues related to the temperature control, oxygen activation is scarcely used. However, low amounts of oxygen (or air) can be added during thermal activation with steam or carbon dioxide to help maintaining the high temperatures by reacting with the gases produced during activation (i.e. CO and H_2) [24]. This approach has the advantage of lowering the pressure of CO and H_2 , both inhibiting gases for the activation, and increasing the partial pressure of the activating agent [24].

Chemical activation usually requests only one heating step: the raw material is mixed with an activating agent (e.g. ZnCl_2 , H_3PO_4 , KOH) and is further treated under controlled atmosphere at temperatures from 400 to 900°C, depending on the selected activating agent. The solid product obtained need to be exhaustively washed with water to remove the chemicals and dried before storage. In this process, the mechanism of pore formation is dependent on the chemical agent: zinc chloride promotes the removal of water molecules from the lignocellulosic structures of the raw material while phosphoric acid combines chemically with them [24]. In none of these processes, the selective removal of carbon atoms occurs. With potassium hydroxide, the process is more complex since there is the disintegration of the structure followed by intercalation of the metallic potassium [24, 28, 29] into the “graphitic” laminar structure, breaking down particles and limiting granular activated carbons synthesis. Simultaneously, there is also some gasification of carbon atoms due to reaction with CO_2 and H_2O , resulting from the redox reaction of carbon with potassium compounds [30]. During carbonization (i.e. heat treatment under inert atmosphere), the lignocellulosic precursor losses volume by contraction, but when chemical activation is applied there is incorporation of the activating reagent inside the particles inhibiting the expected contraction, that is, the activating agent may behave as a template for the formation of the microporosity [24]. In fact, in 2004, Molina-Sabio and Rodríguez-Reinoso [30] published an enlightening research that allowed to conclude that the dehydration of the carbon precursor (i.e. peach stones) by ZnCl_2

occurs along with templating by the activating agent, thus justifying the porosity evolution with the amount of ZnCl_2 impregnated.

Chemical activation has advantages over physical process related with the use of a single heating step and lower temperatures, usually higher yields, shorter activation time (hours) and higher surface area and pore volumes. All these add-ons came with a price since this activation process is more corrosive (e.g. ZnCl_2 or KOH) than the physical one, and activating agents can be hazardous for the environment (i.e. ZnCl_2 and H_3PO_4). Also, regardless the activating agent, a time-consuming washing step is needed to remove chemicals from the newly formed pore network and, if possible, to recover the activating agent. Actually, ZnCl_2 use is declining due to the environmental issues associated with zinc residues [12], low recovery efficiencies, corrosion problems and presence of residual zinc in final carbon [8].

Zinc chlorine and phosphoric acid lead to higher activation yields ($\approx 40\%$) compared to physical activation since the use of these compounds inhibit the formation of tar and other by-products formed in physical activation [12]. In the case of potassium hydroxide, the more complex activation mechanism gathering K intercalation in carbon lattice and gasification allows to prepare activated carbon with a large range of yields depending on the precursor: from 80 and 70% [31–33] to values, as low as, 20–10% [34–36]. KOH allows obtaining superactivated carbons (over $3000 \text{ m}^2 \text{ g}^{-1}$) when high KOH /precursor weight ratios (i.e. between 2 and 4) are used.

Table 1 gathers information regarding the most suitable precursors for the commonly used activating agents, as well as, the type of porosity obtained, and the effect of experimental conditions on the pore size distribution. It is important to emphasize that the effect of experimental conditions on pore size distribution presented in **Table 1** is a general trend; thus, for an in-depth knowledge of the effect of activating agent and experimental conditions on the porous characteristics of a given raw material, a comprehensive study is always needed.

The above-mentioned precursors and activating agents are those more representative for industrial scale production of activated carbons. However, regarding the production of specialty carbons (low volume processes) and for research works, the number of options increases exponentially. Regarding raw materials, hard biomass residues like shells and stones allow to obtain high quality PACs or GACs; phenol formaldehyde polymers yield high surface area porous carbons, while polyacrylonitrile (PAN), acrylonitrile textile or rayon are adequate to synthesize activated carbon fibers or cloths [24]. When aiming nitrogen doped materials, for example for the adsorption of sulfur species, the use of polymers containing nitrogen (e.g. PAN) is a common synthetic route. In what concerns activating agents, besides ZnCl_2 , H_3PO_4 and KOH , alkali hydroxides and salts (e.g. NaOH , K_2CO_3 , Na_2CO_3) and metal chlorides (e.g. AlCl_3 , FeCl_3 , NH_4Cl , CuCl_2) can also be used [24].

At industrial scale, steam activation continues to be the most widely used method to produce activated carbons. The advantages of steam activation are related with the fact that does not request post-activation work-up, namely a final washing step, is less expensive and has less environmental constraints than the chemical activation. Besides, for precursors with less than 10% of ash, carbon materials with surface areas of $1000 \text{ m}^2 \text{ g}^{-1}$ can be easily obtained with activation yields of 50% [8], thus allowing a good compromise between production cost and porosity development.

Type of activation	Activating agent	Appropriate precursors	Porosity	General trend of experimental conditions on pore size distribution (PSD)
Physical	CO ₂	Coals and, in less extend, hard lignocellulosic materials	Micro	- High activation degree leads to high volume of micropores with similar pore size distribution (PSD)
	Steam	Coals and, in less extend, hard lignocellulosic materials	Micro (+ meso)	- Widening of PSD with increase in activation degree - Micro + mesopore networks are obtained at high activation degree (yield 20%) and/or high activation temperatures
Chemical	ZnCl ₂	Lignocellulosic materials (high volatile and oxygen content)	Micro + meso	- Uniform microPSD that widens to the border of micro/mesopore with the increase of Zn/precursor ratio
	H ₃ PO ₄	Lignocellulosic materials (high volatile and oxygen content)	Micro + meso	- PSD mainly in the border of micro/mesopore and dependent on heat treatment temperature (<450°C)
	KOH	High rank coals (low volatile and high carbon content)	Micro	- KOH/precursor ratio has more influence on adsorption capacity and PSD than activation temperature - Increase of KOH/precursor ratio widens pores from narrow to large micropores and, in less extend, to small mesopores; also hinders the granular morphology (particle disintegration leads to powders)

Table 1. Appropriate precursors, kinetic of activation, and type of porosity usually obtained for the most common activating agents (information gathered from reference literature [8, 12, 24, 29]).

In general, the above-described activating methodologies produce activated carbons with wide pore size distributions, so the need for carbon materials with more regular porosity prompted the research on the synthesis of ordered mesoporous carbons (OMCs) by applying hard or soft templating approaches. The advantages of OMCs over conventional activated carbons are related with the ordered and hierarchical pore network, but their multi-step preparation procedures are time consuming, use hazardous chemicals to remove the inorganic templates and, consequently, have very low atomic economy and high production costs. This class of nanostructured materials is out of the scope of the present chapter since the first works were published in the late 1990s, and comprehensive reviews are available in the literature, providing a broad overview and up-to-date information on synthesis and properties of this class of porous carbon materials [37–39]. In the following, the recent developments regarding new synthesis approaches—i.e. precursors, activating agent and routes—for preparing nanoporous carbon materials are presented.

3.1. Conventional activation of gels and chars obtained by novel approaches

As already mentioned, classical preparation of activated carbons usually requests an initial thermochemical process (carbonization) to remove other elements than carbon and transform

the raw material (i.e. coal or biomass) in a carbon-rich material (charcoal) that will be subsequently activated to improve the pore network. This thermochemical conversion is particularly important when using biomass whose carbon content usually is between 30 and 50% (wt.) [25]. However, the need for more specialized porous carbon materials, as well as the growing interest in developing more sustainable and greener processes, has prompted the research community to explore alternatives to the conventional carbonization step which, in some cases, also allow to make feasible the use of novel precursors.

In the category of alternative methods to obtain carbon-rich materials for further activation *via* conventional methodologies, processes as distinct as sol-gel polymerization reaction, hydrothermal carbonization (HTC) and acid-mediated carbonization (AMC) can be grouped. While sol-gel process involves the use of synthetic compounds—resorcinol and formaldehyde—as reagents for the polycondensation reaction in the presence of a catalyst, both HTC and AMC are mainly applied to transform biomass into a coal-like material.

The first resorcinol-formaldehyde organic gel was synthesized by Pekala in 1989 being the aqueous polycondensation performed under alkaline conditions [40]. One of the major advantages of this process is its flexibility since the main properties of the gel can be tuned during the synthesis and drying process. The synthesis starts with the formation of the wet gel and, during this step, the most important parameters controlling the properties of the final gel are the precursors' concentration, the catalyst type and concentration and the time and temperature of curing [41]. After drying, aerogels (supercritical drying), xerogels (subcritical drying), and cryogels (freeze drying) can be obtained. The drying procedure is one of the most important steps regarding the porous properties of the organic gel and is also crucial when the preparation of a thermally stable carbon gel is foreseen. The organic gels are mainly mesoporous materials thus if the preparation of a micro + mesoporous material is envisaged a thermochemical step involving carbonization and/or activation must be considered. The first works focused on the carbonization and activation of organic gels were published during the 1990s, and nowadays, these methodologies continue to be studied to better tune the pore network of these materials and explore novel applications.

A great advantage of conventional activation of organic gels over the previously mentioned carbon precursors is the possibility of coupling the mesopore network of the organic gels with micropores created during carbonization or activation step. Tamon et al. studied the effect of carbonization on the porous properties of aerogels and cryogels proving that both precursors preserved the mesoporous structure after the thermal treatment and that cryogels are more prone to develop micropores [42]. Regarding activation, literature data reveal that the gasification of aerogels with CO₂ allows retaining the mesopore network of the organic gels and increasing the volume of micropores [43, 44]. Moreno-Castilla and co-workers reported the activation of a mesoporous aerogel with CO₂ showing that for a 22% burn-off the increase and widening of the precursor micropore network practically did not change the mesopore structure [44]. In a recent work, Ania and co-workers [45] evaluated the effect of carbonization and activation (physical and chemical) of xerogels which, due to their drying in subcritical conditions, may suffer stronger changes upon thermal treatment. In fact, both carbonization and CO₂ activation lead to the increase of the micropore volume at the expense of a severe

decrease in the mesopore volume and shrinkage of the average pore size. However, under controlled experimental conditions (i.e. impregnation methodology and temperature), the chemical activation of the xerogel with KOH or K_2CO_3 allowed to suppress the shrinkage and structural collapse, forming a micropore structure associated with the enlargement and/or preservation of the mesopore network of the pristine xerogel [45]. For further discussion and information regarding the control of the properties of resorcinol-formaldehyde organic and carbon gels, the reader can refer to the reviews by Al-Muhtaseb and co-workers [41, 46].

Hydrothermal carbonization (HTC) is probably one of the most promising alternatives to conventional carbonization of biomass, as it is clearly shown by the ever-increasing number of publications focused in this process since the beginning of the twentieth century. HTC is inspired in the natural processes of coal formation that take millions years and request temperature and pressure in a nonoxidizing atmosphere to transform biomass into a carbon-rich material. Interestingly, the first research work on HTC was published in 1913 by Friedrich Bergius, a Nobel Laureate in recognition of his studies regarding carbon-water reactions at high pressure and mild temperature to successfully produce H_2 by avoiding CO generation [47]. When performing the experiments, Bergius noticed that when peat was used as carbon source the solid residue obtained had an elemental composition similar to that of coal, leading him to investigate the HTC decomposition of plant-based compounds into coal-like materials [48]. As reported in [49], with the exception of the works by Berl and Schmidt (1932) and van Krevelen et al. (1960), the interest in the solid carbon materials obtained from HTC process was forgotten until the work published by Wang et al. [50] in 2001. These authors reported the synthesis of carbon spheres from sugar under hydrothermal conditions (190°C and self-generated pressure in a high-pressure vessel). HTC is a cost effective and eco-friendly process; since to convert biomass into carbon-rich materials, it uses water as solvent, mild temperatures, self-generated pressure and occurs in few hours with no CO_2 emission. Since 2001, the interest in this carbonization process has been exponentially increasing, and in 2016, around 400 papers mentioning hydrothermal carbonization were published, and the works focusing in this process received more than 11,000 citations (source Web of Science, Sept 2017). Some advantages of HTC-derived materials, commonly known as hydrochars, over charcoals obtained by conventional carbonization is their high content in oxygenated groups and the possibility of morphological control (e.g. spherical morphology).

Hydrochars have an incipient pore network; thus, conventional activation has been commonly employed to obtain specialized nanoporous carbon materials, mainly regarding surface functionalization, morphology features and ultrahigh surface areas and pore volumes. The use of hydrochars as activated carbon precursors was first reported by Zhao et al. [51] aiming to prepare a nitrogen-containing porous carbon material to be used as supercapacitor. The authors performed HTC of D-glucosamine (carbon source) and the hydrochar containing 6.7% of nitrogen was further activated with KOH allowing to obtain a nitrogen-doped porous carbon with a BET area of $600\text{ m}^2\text{ g}^{-1}$.

As it can be clearly seen in the overview of hydrochar-derived activated carbons presented in **Table 2**, the great majority of studies concerning hydrochar activation used KOH as activating agent, mainly because, in general, this oxidizing agent allows obtaining the most developed microporosities reaching BET surface areas higher than $3000\text{ m}^2\text{ g}^{-1}$. It is also interesting to notice that there are studies reporting the use of hydrochars for the synthesis of micro + mesoporous

Activating agent	Carbon precursor	BET area (m ² g ⁻¹)	Observations	Ref.
ZnCl ₂	<i>Salix psammophila</i>	839–1308		[68]
	Coconut shell (+ H ₂ O ₂)	1652–1744	V _{Meso} /V _{Total} = 50–60%	[52]
	Sewage sludge	417–519	V _{Meso} /V _{Total} = 53–66% and N,S-doped	[53]
	Tobacco stem	297–1347		[69]
H ₃ PO ₄	Glucose, sucrose	1750–2120	Spherical particles	[60]
	Rattan sawdust (<i>Calamus gracilis</i>)	1151		[70]
KOH	D-Glucosamine	600	N-doped	[51]
	Glucose	1283	Spherical particles	[59]
	Starch, cellulose, sawdust	1260–2850		[71]
	Furfural, glucose, starch, cellulose, eucalyptus sawdust	1200–2370		[72]
	Potato starch, eucalyptus sawdust (+ melamine)	3280–3420	V _{Meso} /V _{Total} = 50–55% and N-doped	[56]
	Cellulose, potato starch, eucalyptus sawdust	2125–2967		[73]
	Glucose, cellulose, rye straw	891–2250	Controlled PSD	[58]
	Spruce and corncob hydrolysis products	2220–2300		[74]
	Hazelnut	1700		[75]
	Paper pulp mill sludge	1470–2980	Sponge-like particles	[76]
	Sucrose	1169–2431	Controlled PSD	[35]
	Glucose, sucrose	1312–3152		[60]
	Jujum grass, <i>Camellia japonica</i>	1050–3537		[77]
	Bagasse waste + sewage sludge	2296	Hierarchical porosity	[78]
	Sucrose	1635–3036		[79]
	Sucrose	1534		[80]
	Tobacco rods	1761–2115	V _{Meso} /V _{Total} = 79–89% and N-doped	[54]
	Eucalyptus sawdust, <i>Paeonia lactiflora</i> (flowering plant) <i>Sargassum fusiforme</i> (seaweed)	1202–2783		[81]
	Tobacco stem	217–501		[69]
	Microalgae (<i>Spirulina platensis</i>) + glucose	1260–2370	N-doped	[63]
	Algae (<i>Nannochloropsis salina</i>) + glucose	747–1538	N-doped	[62]
NaOH	Glucose, sucrose	532–2129	Spherical particles	[60]
	Palm date seed	1282		[82]
	Rattan stalks (<i>Lacosperma secundiflorum</i>)	1135	V _{Meso} /V _{Total} = 72%	[55]

Activating agent	Carbon precursor	BET area (m ² g ⁻¹)	Observations	Ref.
K ₂ CO ₃	Sucrose	694–1375	Spherical particles and controlled PSD	[35]
	<i>Salix psammophila</i>	964–1469		[68]
	Golden shower pods	812–903		[83]
	Tobacco stem	355–553		[69]
CO ₂	Pinewood sawdust and rice husk	292–569		[84]
	Sunflower stem, walnut shells, olive stones	379–438		[85]
	Glucose, sucrose	923–2555	Spherical particles	[60]
Steam	Starch (+ acrylic acid)	785–1148	Spherical particles with blackberry morphology	[61]
	Sucrose	814	Spherical particles	[35]
Air	Sunflower stem, walnut shells, olive stones	213–434		[85]
—	Bamboo shoots (+ H ₂ SO ₄ conc.)	972	V _{Meso} /V _{Total} = 46–54% and N-doped	[57]

V_{Meso} and V_{Total} microporous and total pore volume, respectively; PSD, pore size distribution.

Table 2. Overview of the properties of hydrochar-derived activated carbons (2010–2017).

materials *via* chemical activation with zinc chloride [52, 53] or hydroxides [54–56], with the mesopore volume corresponding to at least 50% of the total pore volume, i.e. textural characteristics that are not easy to obtain by the most conventional carbonization + activation process. A recent work reports the preparation of an N-doped nanoporous carbon with similar volumes of micro and mesopores and a BET area near 1000 m² g⁻¹ by using HTC of bamboo shoots in the presence of water and 0.5 cm³ of H₂SO₄ followed by the carbonization of the obtained hydrochar, so in the absence of any activating agent [57]. The work by Fuertes and Sevilla enables the synthesis of superactivated porous carbons with 50% of mesopores by adding melamine during the HTC process, thus the final materials also present 1.3–1.7% of nitrogen [56]. Besides opening the possibility of preparing mesoporous carbon materials, the use of hydrochars as activated carbon precursors also allows better control of the micropore size distribution [34, 35, 58].

When starting from simple carbohydrates, the use of HTC followed by activation may enable preparing carbons with spherical morphology (diameters in the micrometer range) and smooth surfaces [34, 35, 59, 60]. It is also possible to obtain a nanoporous carbon material with spherical shape, but with blackberry morphology, by adding acrylic acid to starch during the HTC step [61].

The use of water as solvent constitutes a major advantage of HTC over convention carbonization that requests dry biomass. In fact, HTC makes feasible the use of wet biomass as is the case of algae [62, 63] or sewage sludge [53] that after being carbonized can be activated to obtain a carbon material with well-developed pore structure and also heteroatom-rich surface (i.e. nitrogen and sulfur). HTC is, in fact, a valuable process when envisaging heteroatom-doped carbon materials, since if precursors with nitrogen and/or sulfur—e.g. glucosamine, algae, sewage

sludge, tobacco rods or bamboo shoots—were selected this methodology allows retaining higher percentages of heteroatoms compared to conventional carbonization, and thus assures relevant amounts of these atoms after the activation step [53, 54, 57, 62, 63].

Following a somewhat different approach, White et al. reported the preparation of nitrogen-doped carbogel materials by reacting glucose and ovalbumin (secondary biomass precursor) in HTC conditions [64]. The novelty was the saturation of the monolithic hydrochar with ethanol followed by extraction under supercritical conditions, resembling the last step of the synthesis of organic aerogels. The final material was obtained after carbonization (350–900°C). When using 550°C, a material with an interconnected 3D pore system, BET area of 476 m² g⁻¹ and 5–7% (wt.) nitrogen content was obtained.

Very recently, Sevilla et al. proposed an alternative to KOH activation of biomass-derived hydrochars by using potassium oxalate (K₂C₂O₄) and melamine to obtain N-doped superactivated carbons with high yields (40–46%) [65]. The materials attained BET areas near 3000 m² g⁻¹, presenting mainly micropores (70%) and nitrogen content between 0.5 and 0.9% irrespectively the amount of melamine used. Although the mixture of potassium oxalate/melamine is presented by the authors as an alternative to the corrosive KOH, it is important to highlight that this synthesis route is restricted for lab-scale (under restricted security conditions) since the KCN present in the solid will generate dangerous toxic vapors of HCN during the washing with HCl.

For a deeper overview regarding the HTC process and derived carbon materials, a recent book chapter by Titirici et al. [48] and a minireview [66] are recommended, and for deeper analysis on hydrochar-derived activated carbons, the following review [67] can be consulted.

Acid-mediated carbonization (AMC) is so far the less studied alternative method to obtain a carbon-rich material. However, considering that acid catalysis is a common practice to extract sugars from lignocellulosic biomass [86] and that, as just discussed, sugars can be successfully used as activated carbon precursors (i.e. *via* HTC followed by activation), this process must also be explored. This methodology allows processing largely available and hopefully low cost biomass residues. Moreover, AMC occurs at atmospheric pressure and, in some cases, at low temperature ($\approx 100^\circ\text{C}$) allowing processing carbon precursors that do not gather the adequate properties to be carbonized through the conventional process or by HTC. In fact, AMC is able to maximize the availability of cellulose and hemicellulose in carbon precursors with high inorganic content (e.g. rice husk) [87, 88] and is also efficient for producing carbon-rich materials from liquid carbon precursors, as is the case of glycerol [89]. Depending on the acid catalyst used (e.g. H₂SO₄ and/or H₃PO₄), the obtained oxygen-rich chars also contain relevant amounts of sulfur or phosphorus groups, thus enhancing the reactivity for subsequent activation and allowing to join a well-developed pore network with heteroatom doping in the final activated carbon.

Wang et al. evaluated sulfuric acid hydrolysis of rice husk followed by the dehydration, polymerization and carbonization of the sugars to yield chars, which can be named as acid-chars. These materials were activated with H₃PO₄ [87, 88] and KOH [88] to produce nanoporous carbons with BET areas higher than 2400 m² g⁻¹, and in the case of phosphoric acid activation, materials with micro + mesopore networks. In 2010, the authors reported the effect of H₂SO₄ concentration during carbonization step, as well as the reaction temperature and time onto the

yield of the obtained acidchar that attained 32% (wt.) for the reaction at 95°C during 10 h when 72% H_2SO_4 solution was used in both hydrolysis and carbonization [88]. Regarding the effect of the H_2SO_4 concentration (42–72%) during acid carbonization onto the textural properties of the activated carbon obtained by H_3PO_4 activation, the authors concluded that although acidchars prepared under distinct acid concentrations present similar elemental analysis, the BET area and pore volumes increase as the concentration of the H_2SO_4 decreases [87]. These findings were rationalized by the authors considering that high H_2SO_4 concentrations promote the aggregation of carbon nanoparticles during carbonization, limiting the uniform H_3PO_4 impregnation of the particles and consequently the development of the pore network in the inner particle [87].

In a recent publication, Cui and Atkinson [89] systematically investigated liquid glycerol AMC using various acid catalysts (i.e. H_2SO_4 , H_3PO_4 , HCl and CH_3COOH) aiming to study the effect of the acid carbonization conditions onto the textural properties of glycerol-derived nanoporous carbon materials obtained by subsequent physical activation with steam and CO_2 . The AMC of glycerol was made under nitrogen between 400 and 800°C, and the highest carbonization yields were obtained at 400°C for 10:3 volumetric mixtures glycerol:acid (30% yield for H_2SO_4 and 50% yield for H_3PO_4). Upon activation, materials with BET area values ranging between 990 and 2470 $\text{m}^2 \text{g}^{-1}$ and tailored porosity were obtained. The H_3PO_4 -char originated micro + mesoporous carbon materials with the volume of mesopores being more than 50% of the total porosity regardless the physical activating agent and the amount of acid during the AMC, while the steam activation of the H_2SO_4 -char lead to materials with 40–44% mesopore volume, and the CO_2 activation only 22–25% mesopore volume. The elemental analysis of the nanoporous carbon materials obtained by H_2SO_4 carbonization revealed the presence of 0.35–0.71% of sulfur and the materials carbonized with H_3PO_4 and activated with CO_2 attained even higher heteroatom doping with phosphorus content between 2.04 and 4.34%.

3.2. Other strategies to synthesize nanoporous carbons

3.2.1. Variations of hydrothermal carbonization (HTC) process

In parallel with the studies centered in the activation of hydrochars, in the last few years, the scientific community also started to explore new synthesis routes to obtain a porous structure during the HTC step, being prepared porous carbons with BET surface areas up to 700 $\text{m}^2 \text{g}^{-1}$. The methodologies proposed avoid the need of further thermal or chemical activation, may enable the synthesis of heteroatom-doped solids [90] and can also allow the synthesis of hierarchical materials [91].

Fechler et al. reported the synthesis of porous carbon materials with BET areas between 425 and 672 $\text{m}^2 \text{g}^{-1}$ through HTC (180°C overnight) of glucose mixed with several eutectic salt mixtures (i.e. $\text{LiCl}/\text{ZnCl}_2$, $\text{NaCl}/\text{ZnCl}_2$, and KCl/ZnCl_2) in the presence of a small amount of water [90]. The authors proved that both the amount of water added and the salt composition are determinant for the successful synthesis of materials, which are formed by very small particles aggregation, identical to aerogels. The use of the eutectic mixture $\text{LiCl}/\text{ZnCl}_2$ originated the carbon materials with the highest surface area. When 2-pyrrol-carboxyaldehyde was added as co-reagent of the mixture glucose and ZnCl_2 , a material with 3% of nitrogen and BET area of 576 $\text{m}^2 \text{g}^{-1}$ was obtained. Fellingner et al. used glucose as carbon source and borax ($\text{Na}_2\text{B}_4\text{O}_7$) as

both catalyst and structure-directing agent to prepare hierarchical structured carbogels under HTC conditions [91]. Further carbonization under nitrogen at 550 or 1000°C allowed to obtain a carbon material with a BET area of 614 m² g⁻¹ and 70% of mesopore volume.

3.2.2. Carbonization of organic salts

In 2010, Zhou and co-workers developed mesoporous carbons by the carbonization of organic salts (magnesium and barium citrates) evaluating the influence of the temperature of the thermal treatment (600–800°C) [92]. In the case of magnesium salt, BET areas up to 2322 m² g⁻¹ were attained, and the increase of temperature resulted in a progressive increase of the mesopore volume percentage (from 50 to 100%). The barium citrate-derived materials are mainly mesoporous (>90%) and, independently of the temperature, pores between 10 and 20 nm are obtained. Calcium citrate was tested by other authors who reported the paramount importance of temperature in the textural properties of the mesoporous carbons [93].

Atkinson and Rood proposed the use of dichloroacetates of alkaline metals as carbon precursors for the synthesis of nanoporous carbons, being the pore networks, once again, dependent on the cation [94]. The pore structure is produced by fast pyrolysis (15 s to 7 min) under nitrogen flow at temperatures between 300 and 1100°C, and materials attained BET areas of 740 m² g⁻¹. This methodology allowed the synthesis of microporous materials when lithium salt was used and micro + mesoporous solids for the other two metals. In the same research line, Xu and co-workers reported the pyrolysis of EDTA salts to obtain nitrogen-doped porous carbons with BET areas reaching 1800 m² g⁻¹ and porosity characteristics dependent on the thermal treatment temperature (higher the temperature, higher the mesopore volume) [95, 96].

The protocol of organic salts carbonization was extended to gluconates and alginates along with citrates to understand the mechanism of the porosity development [97–99]. The results shown that the textural properties of the porous carbon materials obtained by this methodology are heavily dependent on the type of the cation in the organic salt: while potassium salts originate essentially microporous solids, for sodium and calcium the amount of mesopores is also relevant [98]. In the case of calcium citrate-derived material, the development of the mesoporosity was attributed to the formation of CaO nanoparticles, which act as endotemplates during the carbonization. It was also shown that the nature of the organic salt has a great impact on the morphology, with sodium gluconate leading to the formation of large carbon nanosheets, while sodium citrate originates sponge-like particles. The synthesis of nitrogen-doped porous carbons was also explored by mixing potassium gluconate with melamine, which allowed to obtain a microporous material gathering 22.9% of nitrogen with 660 m² g⁻¹ of BET area [97]. The endotemplate approach on the carbonization of organic salts was further explored with iron, calcium and zinc citrates [99]. The carbonization of these nonalkali organic salts produces mesoporous materials with BET areas between 950 and 1610 m² g⁻¹ and distinct pore size distributions: monomodal distribution centered at 11 nm for calcium citrate, bimodal distribution centered at 9 and 20 nm for iron citrate, and bimodal distribution centered at 3 and 10 nm for iron citrate. These carbons can be post-functionalized by heat treatment in the presence of melamine to obtain materials gathering high BET area and mesopore volume with high nitrogen content (8–9%).

3.2.3. Ionothermal approaches

The synthesis of porous carbon materials *via* ionothermal concept derives from the methodologies proposed in 2004 by Morris and co-workers to prepare zeolite analogues (i.e. inorganic materials) using ionic liquids or eutectic mixtures as both solvents and inorganic structure directing agents (templates) [100]. The ionothermal approach is analogous to hydrothermal and solvothermal processes, where the solvents are predominantly molecular (water or nonaqueous solvents, respectively) but, as the name means, it refers to processes occurring in ionic solvents (e.g. ionic liquids or eutectic mixtures) [100]. The low vapor pressure of the ionic solvents is a great advantage of ionothermal reaction over the hydrothermal or solvothermal concepts, since it allows avoiding the safety concerns connected with the high pressures required to prevent molecular solvent evaporation [101].

The preparation of carbon materials following the ionothermal principles is reported in the literature as both ionothermal and molten salt synthesis processes. Nowadays, there is still not a generally accepted terminology for these processes what turns difficult to understand the classifications and underlying procedures followed by the distinct authors. In fact, the use of ionothermal/molten salt process can be linked either to the preparation of carbon materials with incipient porosity obtained at temperatures $\approx 200^\circ\text{C}$ (ionothermal carbonization—ITC) [102] or to the preparation of porous carbons by a two-step process including the previously mentioned ITC followed by a thermal treatment of the ionothermal derived carbon at high temperatures (attaining 1000°C or more) [103, 104]. Ionothermal/molten salt process is also considered in the case where the mixture of the carbon precursor and the ionic solvent is directly thermally treated at high temperature [105, 106].

The first studies reporting the preparation of porous carbon materials through ionothermal process used ionic liquids as carbon precursors. In 2009, Lee et al. synthesized N-doped materials (2–3%) with BET area values between 640 and $780\text{ m}^2\text{ g}^{-1}$, and the authors demonstrated the influence of the ionic liquid nature on the development of mainly microporous or micro + mesoporous materials [107]. In a further work, the authors report a similar process for obtaining materials with up to 17% of nitrogen content, although with lower porosity development [108]. In 2010, other approach of the same research group gathered an ionic liquid with simple carbohydrates allowing to obtain carbon materials with a highly developed mesopore network after treatment at only 200°C during 20 h in a nonpressurized chamber [102]. Xie et al. reported the synthesis of magnetic hierarchical porous carbons by using several carbohydrates and an iron containing ionic liquid, and the authors proposed that the ionic liquid has a triple role: salt template, solvent and catalyst [103].

In the subsequent research in ionothermal approaches (**Table 3**), the introduction of salts as co-reagents became common and generally accepted as a hard template route. Zinc chloride is by far the most frequently reported salt, used alone or in mixtures (eutectic or not) with other salts. This strategy allowed to synthesize porous carbons with ultrahigh surface area (easily around $2000\text{ m}^2\text{ g}^{-1}$), hierarchical structure and high heteroatom doping (i.e. nitrogen (>5%) and sulfur). All these features are of fundamental importance for boosting the application of these materials in energy storage processes. Actually, in the great majority of publications, the authors report high performance of the ionothermal-derived porous carbons as supercapacitors. While initially nitrogen-containing ionic liquids were used as carbon precursors [109–111], along the years, the number of studies exploring carbohydrates, or even biomass, as carbon source has increased [105, 106, 112–120].

Reagents	Thermal treatment	BET area (m ² g ⁻¹)	Observations	Ref.
Imidazolium-based ionic liquids	800 °C (N ₂) 1 h	640–780	Micropores or micro + mesopores depending of ionic liquid used 2–3% N-doping	[107]
Imidazolium-based ionic liquids	800 °C (N ₂) 1 h	<100	11.4–17.6% N-doping	[108]
Ionic liquid + glucose or fructose	160–200°C, 2–20 h, open air	6–288	Micro + mesopores	[102]
Glucose, fructose, xylose, or starch + iron containing ionic liquid	180°C 24 h	44–155	Hierarchical pores and magnetic	[103]
	Autoclave + 750°C (N ₂) 4 h	160–404	Ionic liquid triple role: salt template, solvent, catalyst	
N-containing and N,B-containing ionic liquids + eutectic salt mixtures (alkaline metal and zinc chlorides)	1000°C or 1400°C (N ₂)	1100–2000	5% N-doping 6% N + 6% B double doping Pore network dependent on salt mixture and amount	[109]
Glucose, cellulose, or lignin + eutectic salt mixture (KCl/ZnCl ₂)	1000°C (N ₂) linear or two-step regime	866–2025	$V_{\text{Meso}}/V_{\text{Total}} = 63\text{--}92\%$	[112]
Glucose + molten salt LiCl/KCl + activating oxysalts (KOH, NaBO ₂ , K ₂ CO ₃ , KNO ₃ , KH ₂ PO ₄ , K ₂ SO ₄ or KClO ₃)	600–1300°C (N ₂)	997–1912	Oxysalt influences morphology $V_{\text{Meso}}/V_{\text{Total}} = 21\text{--}52\%$ oxysalt dependent	[113]
Glucose, cellulose, or sugar cane bagasse + metal free ionic liquids	200°C 24 h (autoclave) + 600–900°C (N ₂)	16–627	2.8–6.6% N-doping Micro + mesopores	[104]
Peanut shell + salt mixtures (Na ₂ CO ₃ /K ₂ CO ₃ , Li ₂ CO ₃ /Na ₂ CO ₃ /K ₂ CO ₃ , CaCl ₂ , CaCl ₂ /NaCl)	850°C (N ₂) 1 h	316–408		[120]
Imidium ionic liquid + eutectic salt mixture (KCl/ZnCl ₂)	850°C (N ₂) 2 h	1056	2.8% N-doping and 5.16% S-doping	[110]
Imidazolium ionic liquid + salt mixture (NaCl/ZnCl ₂)	1000°C (N ₂) 2 h	1410–1770	3.7–4.5% N-doping	[111]
Molten ZnCl ₂ + common organic solvents (e.g. ethanol, acetonitrile, dimethylsulfoxide, glycerol)	550 °C Schlenck-type reactor	750–1650	14% N-doping or 13% S-doping Aerogel, nanosheet or hyperbranch morphology dependent on solvent	[121]
ZnCl ₂ + glucose or glucosamine dissolved in H ₂ O (+ 2-thiophenecarboxylic acid (TCA))	900–1000°C (N ₂)	881–1246	Hierarchical pores N,S-doping (5.6% N and 1.8%S) Carbon aerogels	[122]
Glucose and melamine + eutectic salt mixture (LiCl/KCl)	550–1000°C 5 h (N ₂)	387–1190	6–24% N-doping	[106]

Reagents	Thermal treatment	BET area (m ² g ⁻¹)	Observations	Ref.
Melamine and terephthalaldehyde + salt mixture (KCl/ZnCl ₂)	700°C (N ₂) 2 h	426–1992		[114]
Glucose, cellulose, lignin (+ melamine) + eutectic salt mixture (KCl/ZnCl ₂)	800 °C (N ₂) two-step regime	1273–1834	11.9% N-doping $V_{\text{Meso}}/V_{\text{Total}} = 69.2\text{--}97.5\%$	[115]
Glucose + eutectic and noneutectic salt mixture (KCl/ZnCl ₂)	350°C 2 h + 900°C 1 h (N ₂)	1000–2160	$V_{\text{Meso}}/V_{\text{Total}} > 50\%$	[105]
Phloroglucinol + glyoxylic acid + pluronic F127 + H ₂ O + salts (LiCl, NaCl, KCl); pH control	600–900°C (Ar)	535–1815	$V_{\text{Meso}}/V_{\text{Total}} = 15\text{--}60\%$	[123]
Lignin from beech wood + nitration + eutectic salt mixture (KCl/ZnCl ₂)	850°C	1381–1589	5.3–6.1% N-doping	[117]
Adenine + eutectic and noneutectic salt mixture (NaCl/ZnCl ₂)	900 °C (N ₂) 1 h	1770–2900	5.9–7.7% N-doping Pore structure dependent on NaCl proportion (micro + mesopores)	[116]
Tofu + LiCl/KCl + LiNO ₃	850°C (Ar) 2 h	1200	1.54–4.72% N-doping Micropores	[119]
Wheat straws + salt mixture (LiCl/KCl) + LiNO ₃	650–850°C (N ₂) 2 h	1067	4.28% N-doping	[118]

Table 3. Chronological overview of porous carbon synthesis by ionothermal approaches (2009–2017).

More elaborated synthesis schemes have been reported, as is the case of the work developed by Chang et al. [121] where organic solvents were added dropwise to molten ZnCl₂ at 550°C. By changing the solvent, the authors were able to obtain nitrogen (14%) or sulfur (13%) doped porous carbons with different morphologies (i.e. aerogel, nanosheets or hyperbranch). There are also reports on ITC of biomass with nitrogen-containing ionic liquid followed by conventional KOH activation to yield nitrogen doping up to 1.59% and apparent surface areas of 2838 m² g⁻¹ [124]. The ionothermal approach is actually a powerful route to synthesize porous carbon materials with valuable graphene-like (2D) structures [125–128].

It is also possible to found reports on highly mesoporous carbon materials obtained by ZnCl₂-mediated ionothermal/molten salt synthesis [129–131]. Although these routes are presented as novel synthesis procedures, the high mesopore volumes reported are most probably the result of the complex ZnCl₂ activation mechanism when very high amount of ZnCl₂ is added. As it was previously mentioned, the behavior of chemical activating agents as templates during carbonization cannot be disregarded, and for the particular case on ZnCl₂, the results obtained by Molina-Sabio and Rodríguez-Reinoso [30] allowed the authors to conclude that this chemical acts as template for the creation of porosity. So, although new materials are being produced under “novel” synthesis procedures with appealing names, in some cases, the experimental route and underlying mechanism for pore creation seems to be the one accepted for conventional chemical activation.

For more information regarding the preparation of porous carbon materials *via* ionothermal/molten salt approaches and also their main applications, several review works are available in the literature [132–136].

4. Conclusion

The technological relevance of porous carbon materials continues to prompt the scientific community and companies to explore alternative routes to the conventional methods, in order to develop specialized materials or improve the production process (e.g. optimizing energy costs and minimizing wastes).

The great majority of conventional and innovative processes allowing the synthesis of porous carbons involve heat treatments at moderate-to-high temperatures for carbonization to occur and subsequent formation of the porous carbon skeleton. In the case of chemical activation or ionothermal/molten salt processes, a washing step with water or 10% HCl is required to remove chemical compounds clog the porosity.

Conventional methods are based on a solid and structured carbon material and therefore activation occurs by gasification, selective oxidation of the most reactive carbon atoms and heteroatoms or intercalation processes. Thus, the conventional methodologies are considered top-down processes. Regarding innovative approaches both top-down and bottom-up routes are reported in the literature. HTC or ionothermal reactions promote a top-down process when the carbon precursor is a biomass, but is a bottom-up route when discrete entities (e.g. carbohydrates or ionic liquids) are the starting materials. The acid-mediated degradation of biomass is a top-down route that converts biomass in a carbohydrate-rich acid liquor that is carbonized in a bottom-up approach. Some of the advantages of these novel approaches over the conventional ones are related to the possibility of producing highly porous carbon materials with easier pore size distribution tuning, high amounts of heteroatoms in the surface, and fine control of morphology (e.g. sponge-like, aerogel-like, spherical, sheets (2D)). In light of a more sustainable and circular economy, it is also relevant that some of the novel synthetic approaches (e.g. HTC) allow enabling future large-scale production based on high moisture containing biomass residues and even liquids (e.g. glycerol).

The driving force for the development of new porous carbons throughout these non-conventional methods is the search for high performing materials for electrochemical applications and energy storage, which request hierarchically porous structures ideally doped with electron-rich nonmetallic elements (e.g. nitrogen, sulfur) to increase the conductivity.

The carbon atom is a versatile element that since the Stone Age has reinvented itself. So, the overlook of this chapter allows to predict that in the near future the number of novel synthesis routes to feed the demand for even more specialized porous carbons will continue to increase. This may occur by revisiting synthesis routes established for other classes of materials or by the discovery of completely novel processes.

Acknowledgements

The authors thank Fundação para a Ciência e Tecnologia (FCT), Portugal, for financial support to CQB through the strategic project UID/MULTI/00612/2013. ASM thanks the financial support of FCT for the Post-doc grant SFRH/BPD/86693/2012. J. Conceição is acknowledged for the illustration of **Figure 1**.

Author details

Ana S. Mestre and Ana P. Carvalho*

*Address all correspondence to: ana.carvalho@fc.ul.pt

Centro de Química e Bioquímica, Faculdade de Ciências, Universidade de Lisboa, Lisboa, Portugal

References

- [1] Jäger H, Frohs W, Collin G, von Sturm F, Vohler O, Nutsch G. Carbon, 1. General. Ullmann's Encyclopedia of Industrial Chemistry. Weinheim, Germany: Wiley-VCH Verlag GmbH & Co. KGaA; 2010. DOI: 10.1002/14356007.a05_095.pub2
- [2] Greenwood NN, Earnshaw A. Chemistry of the Elements. 2nd ed. Butterworth-Heinemann Elsevier: Oxford, UK; 2006
- [3] Przepiórski J. Activated carbon filters and their industrial applications. In: Bandosz TJ, editor. Activated Carbon Surfaces in Environmental Remediation. New York: Elsevier; 2006. pp. 421-474. DOI: 10.1016/S1573-4285(06)80018-9
- [4] Derbyshire F, Jagtoyen M, Thwaites M. Porosity in Carbons. London: Edward Arnold; 1995
- [5] Çeçen F. Activated carbon. In: Kirk-Othmer Encyclopedia of Chemical Technology. John Wiley & Sons, Inc.; 2014. pp. 1-34. DOI: 10.1002/0471238961.0103200902011105.a01.pub3
- [6] Çeçen F. Water and wastewater treatment: Historical perspective of activated carbon adsorption and its integration with biological processes. In: Çeçen F, Aktaş Ö, editors. Activated Carbon for Water and Wastewater Treatment. Weinheim, Germany: Wiley-VCH Verlag GmbH & Co. KGaA; 2011. pp. 1-11. DOI: 10.1002/9783527639441.ch1
- [7] Dąbrowski A. Adsorption—From theory to practice. Advances in Colloid and Interface Science. 2001;**93**(1-3):135-224. DOI: 10.1016/S0001-8686(00)00082-8
- [8] Menéndez-Díaz JÁ, Martín-Gullón I. Types of carbon adsorbents and their production. In: Bandosz TJ, editor. Activated Carbon Surfaces in Environmental Remediation. New York: Elsevier; 2006. pp. 1-48. DOI: 10.1016/S1573-4285(06)80010-4

- [9] University of Kentucky, Center for Applied Energy Research, web information; Available from: "<http://www.caer.uky.edu/carbon/history/carbonhistory.shtml>" (Accessed: 2017-05-15)
- [10] Ostrejko R. (British Patent 14,224, 1900; French Patent 304,867, 1901; German Patent 136,792, 1901; US Patent 739,104) 1903. Available from: <http://speicyte.wix.com/raphael-von-ostrejko> [Accessed: 2017-07-05]
- [11] Bandoz TJ. Nanoporous carbons: Looking beyond their perception as adsorbents, catalyst supports and Supercapacitors. *The Chemical Record*. 2016;**16**(1):205-218. DOI: 10.1002/tcr.201500231
- [12] Rodríguez-Reinoso F, Sepúlveda-Escribano A. Porous carbons in adsorption and catalysis. In: Nalwa HS, editor. *Handbook of Surfaces and Interfaces of Materials*. San Diego: Academic Press; 2001. pp. 309-355
- [13] Rodríguez-Reinoso F, Sepúlveda-Escribano A. Carbon as Catalyst Support. *Carbon Materials for Catalysis*. Hoboken, NJ, USA: John Wiley & Sons, Inc.; 2008. pp. 131-155. DOI: 10.1002/9780470403709.ch4
- [14] Figueiredo JL, Pereira MFR. Carbon as Catalyst. *Carbon Materials for Catalysis*. Hoboken, NJ, USA: John Wiley & Sons, Inc.; 2008. pp. 177-217. DOI: 10.1002/9780470403709.ch6
- [15] Kroto HW, Heath JR, O'Brien SC, Curl RF, Smalley RE. C60: Buckminsterfullerene. *Nature*. 1985;**318**(6042):162-163. DOI: 10.1038/318162a0
- [16] Iijima S. Helical microtubules of graphitic carbon. *Nature*. 1991;**354**(6348):56-58. DOI: 10.1038/354056a0
- [17] Novoselov KS, Geim AK, Morozov SV, Jiang D, Zhang Y, Dubonos SV, Grigorieva IV, Firsov AA. Electric field effect in atomically thin carbon films. *Science*. 2004;**306**(5696):666-669. DOI: 10.1126/science.1102896
- [18] Thommes M, Kaneko K, Neimark AV, Olivier JP, Rodríguez-Reinoso F, Rouquerol J, Sing KSW. Physisorption of gases, with special reference to the evaluation of surface area and pore size distribution (IUPAC technical report). *Pure and Applied Chemistry*. 2015;**87**(9-10):1051-1069. DOI: 10.1515/pac-2014-1117
- [19] Gregg SJ, Sing KSW. *Adsorption, Surface Area and Porosity*. 2nd ed. London: Academic Press Inc.; 1982. DOI: 10.1002/bbpc.19820861019
- [20] Sing KSW, Rouquerol F, Llewellyn P, Rouquerol J. 9—Assessment of microporosity. In: *Adsorption by Powders and Porous Solids*. 2nd ed. Oxford: Academic Press; 2014. pp. 303-320. DOI: 10.1016/B978-0-08-097035-6.00009-7
- [21] Choma J, Jaroniec M. Characterization of nanoporous carbons by using gas adsorption isotherms. In: Bandoz TJ, editor. *Activated Carbon Surfaces in Environmental Remediation*. New York: Elsevier; 2006. pp. 107-158. DOI: 10.1016/S1573-4285(06)80012-8
- [22] KSW S. 10—Adsorption by active carbons. In: *Adsorption by Powders and Porous Solids*. 2nd ed. Oxford: Academic Press; 2014. pp. 321-391. DOI: 10.1016/B978-0-08-097035-6.00010-3

- [23] Bandosz TJ, Ania CO. Surface chemistry of activated carbons and its characterization. In: Bandosz TJ, editor. *Activated Carbon Surfaces in Environmental Remediation*. New York: Elsevier; 2006. pp. 159-229. DOI: 10.1016/S1573-4285(06)80013-X
- [24] Marsh H, Rodríguez-Reinoso F. *Activated Carbon*. Oxford: Elsevier; 2006
- [25] Bansal RC, Donnet J-B, Stoeckli R. *Active Carbon*. New York: Marcel Dekker; 1988
- [26] Bandosz TJ. *Activated Carbon Surfaces in Environmental Remediation*. 1st ed. New York: Elsevier Ltd; 2006
- [27] Bottani EJ, Tascón JMD. *Adsorption by Carbons*. Oxford: Elsevier Ltd.; 2008
- [28] Hu Z, Vansant EF. Synthesis and characterization of a controlled-micropore-size carbonaceous adsorbent produced from walnut shell. *Microporous Materials*. 1995;**3**(6):603-612. DOI: 10.1016/0927-6513(94)00067-6
- [29] Wang J, Kaskel S. KOH activation of carbon-based materials for energy storage. *Journal of Materials Chemistry*. 2012;**22**(45):23710-23725. DOI: 10.1039/C2JM34066F
- [30] Molina-Sabio M, Rodríguez-Reinoso F. Role of chemical activation in the development of carbon porosity. *Colloids and Surfaces A: Physicochemical and Engineering Aspects*. 2004;**241**(1):15-25. DOI: 10.1016/j.colsurfa.2004.04.007
- [31] Lota G, Centeno TA, Frackowiak E, Stoeckli F. Improvement of the structural and chemical properties of a commercial activated carbon for its application in electrochemical capacitors. *Electrochimica Acta*. 2008;**53**(5):2210-2216. DOI: 10.1016/j.electacta.2007.09.028
- [32] Kunowsky M, Marco-Lozar JP, Cazorla-Amorós D, Linares-Solano A. Scale-up activation of carbon fibres for hydrogen storage. *International Journal of Hydrogen Energy*. 2010;**35**(6):2393-2402. DOI: 10.1016/j.ijhydene.2009.12.151
- [33] Wang J, Yang X, Wu D, Fu R, Dresselhaus MS, Dresselhaus G. The porous structures of activated carbon aerogels and their effects on electrochemical performance. *Journal of Power Sources*. 2008;**185**(1):589-594. DOI: 10.1016/j.jpowsour.2008.06.070
- [34] Mestre AS, Freire C, Pires J, Carvalho AP, Pinto ML. High performance microspherical activated carbons for methane storage and landfill gas or biogas upgrade. *Journal of Materials Chemistry A*. 2014;**2**(37):15337-15344. DOI: 10.1039/C4TA03242J
- [35] Mestre AS, Tyszkó E, Andrade MA, Galhetas M, Freire C, Carvalho AP. Sustainable activated carbons prepared from a sucrose-derived hydrochar: Remarkable adsorbents for pharmaceutical compounds. *RSC Advances*. 2015;**5**(25):19696-19707. DOI: 10.1039/C4RA14495C
- [36] Mestre AS, Pires J, Nogueira JMF, Carvalho AP. Activated carbons for the adsorption of ibuprofen. *Carbon*. 2007;**45**(10):1979-1988. DOI: 10.1016/j.carbon.2007.06.005
- [37] Enterría M, Figueiredo JL. Nanostructured mesoporous carbons: Tuning texture and surface chemistry. *Carbon*. 2016;**108**:79-102. DOI: 10.1016/j.carbon.2016.06.108
- [38] Lee J, Kim J, Hyeon T. Recent progress in the synthesis of porous carbon materials. *Advanced Materials*. 2006;**18**(16):2073-2094. DOI: 10.1002/adma.200501576

- [39] Ma TY, Liu L, Yuan ZY. Direct synthesis of ordered mesoporous carbons. *Chemical Society Reviews*. 2013;**42**(9):3977-4003. DOI: 10.1039/c2cs35301f
- [40] Pekala RW. Organic aerogels from the polycondensation of resorcinol with formaldehyde. *Journal of Materials Science*. 1989;**24**(9):3221-3227. DOI: 10.1007/bf01139044
- [41] ElKhatat AM, Al-Muhtaseb SA. Advances in tailoring resorcinol-formaldehyde organic and carbon gels. *Advanced Materials*. 2011;**23**(26):2887-2903. DOI: 10.1002/adma.201100283
- [42] Tamon H, Ishizaka H, Yamamoto T, Suzuki T. Preparation of mesoporous carbon by freeze drying. *Carbon*. 1999;**37**(12):2049-2055. DOI: 10.1016/S0008-6223(99)00089-5
- [43] Rasines G, Macias C, Haro M, Jagiello J, Ania CO. Effects of CO₂ activation of carbon aerogels leading to ultrahigh micro-meso porosity. *Microporous Mesoporous Materials*. 2015;**209**:18-22. DOI: 10.1016/j.micromeso.2015.01.011
- [44] Fairén-Jiménez D, Carrasco-Marín F, Moreno-Castilla C. Porosity and surface area of monolithic carbon aerogels prepared using alkaline carbonates and organic acids as polymerization catalysts. *Carbon*. 2006;**44**(11):2301-2307. DOI: 10.1016/j.carbon.2006.02.021
- [45] Gomis-Berenguer A, García-González R, Mestre AS, Ania CO. Designing micro- and mesoporous carbon networks by chemical activation of organic resins. *Adsorption*. 2017;**23**(2):303-312. DOI: 10.1007/s10450-016-9851-4
- [46] Al-Muhtaseb SA, Ritter JA. Preparation and properties of resorcinol-formaldehyde organic and carbon gels. *Advanced Materials*. 2003;**15**(2):101-114. DOI: 10.1002/adma.200390020
- [47] James LK. Nobel Laureates in Chemistry, 1901-1992 (History of Modern Chemical Sciences). 1st ed. American Chemical Society and the Chemical Heritage Foundation; 1993
- [48] Marinovic A, Pileidis FD, Titirici M-M. Chapter 5. Hydrothermal Carbonisation (HTC): History, State-of-the-Art and Chemistry. *Porous Carbon Materials from Sustainable Precursors*. The Royal Society of Chemistry; 2015. pp. 129-55. DOI: 10.1039/9781782622277-00129
- [49] Sevilla M, Fuertes AB. Chemical and structural properties of carbonaceous products obtained by hydrothermal carbonization of saccharides. *Chemistry—A European Journal*. 2009;**15**(16):4195-4203. DOI: 10.1002/chem.200802097
- [50] Wang Q, Li H, Chen L, Huang X. Monodispersed hard carbon spherules with uniform nanopores. *Carbon*. 2001;**39**(14):2211-2214. DOI: 10.1016/s0008-6223(01)00040-9
- [51] Zhao L, Fan LZ, Zhou MQ, Guan H, Qiao SY, Antonietti M, Titirici MM. Nitrogen-containing hydrothermal carbons with superior performance in supercapacitors. *Advanced Materials*. 2010;**22**(45):5202-5206. DOI: 10.1002/adma.201002647
- [52] Jain A, Jayaraman S, Balasubramanian R, Srinivasan MP. Hydrothermal pre-treatment for mesoporous carbon synthesis: Enhancement of chemical activation. *Journal of Materials Chemistry A*. 2014;**2**(2):520-528. DOI: 10.1039/C3TA12648J

- [53] Liu TT, Li Y, Peng NN, Lang QQ, Xia Y, Gai C, Zheng QF, Liu ZG. Heteroatoms doped porous carbon derived from hydrothermally treated sewage sludge: Structural characterization and environmental application. *Journal of Environmental Management*. 2017;**197**:151-158. DOI: 10.1016/j.jenvman.2017.03.082
- [54] Zhao YQ, Lu M, Tao PY, Zhang YJ, Gong XT, Yang Z, Zhang GQ, Li HL. Hierarchically porous and heteroatom doped carbon derived from tobacco rods for supercapacitors. *Journal of Power Sources*. 2016;**307**:391-400. DOI: 10.1016/j.jpowsour.2016.01.020
- [55] Islam MA, Ahmed MJ, Khanday WA, Asif M, Hameed BH. Mesoporous activated carbon prepared from NaOH activation of rattan (*Lacosperma secundiflorum*) hydrochar for methylene blue removal. *Ecotoxicology and Environmental Safety*. 2017;**138**:279-285. DOI: 10.1016/j.ecoenv.2017.01.010
- [56] Fuertes AB, Sevilla M. High-surface area carbons from renewable sources with a bimodal micro-mesoporosity for high-performance ionic liquid-based supercapacitors. *Carbon*. 2015;**94**:41-52. DOI: 10.1016/j.carbon.2015.06.028
- [57] Chen XF, Zhang JY, Zhang B, Dong SM, Guo XC, Mu XD, Fei BH. A novel hierarchical porous nitrogen-doped carbon derived from bamboo shoot for high performance supercapacitor. *Scientific Reports*. 2017;**7**:7362-7372. DOI: 10.1038/s41598-017-06730-x
- [58] Falco C, Marco-Lozar JP, Salinas-Torres D, Morallón E, Cazorla-Amorós D, Titirici MM, Lozano-Castelló D. Tailoring the porosity of chemically activated hydrothermal carbons: Influence of the precursor and hydrothermal carbonization temperature. *Carbon*. 2013;**62**(0):346-355. DOI: 10.1016/j.carbon.2013.06.017
- [59] Li M, Li W, Liu S. Hydrothermal synthesis, characterization, and KOH activation of carbon spheres from glucose. *Carbohydrate Research*. 2011;**346**(8):999-1004. DOI: 10.1016/j.carres.2011.03.020
- [60] Romero-Anaya AJ, Ouazzine M, Lillo-Ródenas MA, Linares-Solano A. Spherical carbons: Synthesis, characterization and activation processes. *Carbon*. 2014;**68**(0):296-307. DOI: 10.1016/j.carbon.2013.11.006
- [61] He CL, Liu YL, Xue ZP, Zheng MT, Wang HB, Xiao Y, Dong HW, Zhang HR, Lei BF. Simple synthesis of carboxylate-rich porous carbon microspheres for high-performance supercapacitor electrode materials. *International Journal of Electrochemical Science*. 2013;**8**(5):7088-7098
- [62] Yuan B, Wang J, Chen Y, Wu X, Luo H, Deng S. Unprecedented performance of N-doped activated hydrothermal carbon towards C_2H_6/CH_4 , CO_2/CH_4 , and CO_2/H_2 separation. *Journal of Materials Chemistry A*. 2016;**4**(6):2263-2276. DOI: 10.1039/C5TA08436A
- [63] Sevilla M, Falco C, Titirici MM, Fuertes AB. High-performance CO_2 sorbents from algae. *RSC Advances*. 2012;**2**(33):12792-12797. DOI: 10.1039/C2ra22552b
- [64] White RJ, Yoshizawa N, Antonietti M, Titirici MM. A sustainable synthesis of nitrogen-doped carbon aerogels. *Green Chemistry*. 2011;**13**(9):2428-2434. DOI: 10.1039/c1gc15349h

- [65] Sevilla M, Ferrero GA, Fuertes AB. Beyond KOH activation for the synthesis of superactivated carbons from hydrochar. *Carbon*. 2017;**114**:50-58. DOI: 10.1016/j.carbon.2016.12.010
- [66] Fang J, Zhan L, Ok YS, Gao B. Minireview of potential applications of hydrochar derived from hydrothermal carbonization of biomass. *Journal of Industrial and Engineering Chemistry*. 2018;**57**:15-21. DOI: 10.1016/j.jiec.2017.08.026
- [67] Jain A, Balasubramanian R, Srinivasan MP. Hydrothermal conversion of biomass waste to activated carbon with high porosity: A review. *Chemical Engineering Journal*. 2016;**283**:789-805. DOI: 10.1016/j.cej.2015.08.014
- [68] Zhu X, Liu Y, Qian F, Zhou C, Zhang S, Chen J. Role of hydrochar properties on the porosity of hydrochar-based porous carbon for their sustainable application. *ACS Sustainable Chemistry & Engineering*. 2015;**3**(5):833-840. DOI: 10.1021/acssuschemeng.5b00153
- [69] Chen RF, Li LQ, Liu Z, Lu MM, Wang CH, Li HL, Ma WW, Wang SB. Preparation and characterization of activated carbons from tobacco stem by chemical activation. *Journal of the Air & Waste Management Association*. 2017;**67**(6):713-724. DOI: 10.1080/10962247.2017.1280560
- [70] Adebisi GA, Chowdhury ZZ, Abd Hamid SB, Ali E. Equilibrium isotherm, kinetic, and thermodynamic studies of divalent cation adsorption onto *Calamus gracilis* sawdust-based activated carbon. *BioResources*. 2017;**12**(2):2872-2898. DOI: 10.15376/biores.12.2.2872-2898
- [71] Sevilla M, Fuertes AB. Sustainable porous carbons with a superior performance for CO₂ capture. *Energy & Environmental Science*. 2011;**4**(5):1765-1771. DOI: 10.1039/C0ee00784f
- [72] Sevilla M, Fuertes AB, Mokaya R. High density hydrogen storage in superactivated carbons from hydrothermally carbonized renewable organic materials. *Energy & Environmental Science*. 2011;**4**(4):1400-1410. DOI: 10.1039/C0ee00347f
- [73] Wei L, Sevilla M, Fuertes AB, Mokaya R, Yushin G. Hydrothermal carbonization of abundant renewable natural organic chemicals for high-performance supercapacitor electrodes. *Advanced Energy Materials*. 2011;**1**(3):356-361. DOI: 10.1002/aenm.201100019
- [74] Falco C, Sieben JM, Brun N, Sevilla M, van der Maehlen T, Morallon E, Cazorla-Amorós D, Titirici MM. Hydrothermal carbons from hemicellulose-derived aqueous hydrolysis products as electrode materials for supercapacitors. *ChemSusChem* 2013;**6**(2):374-382. DOI: 10.1002/cssc.201200817
- [75] Unur E. Functional nanoporous carbons from hydrothermally treated biomass for environmental purification. *Microporous and Mesoporous Materials*. 2013;**168**(0):92-101. DOI: 10.1016/j.micromeso.2012.09.027
- [76] Wang HL, Li Z, Tak JK, Holt CMB, Tan XH, Xu ZW, Amirkhiz BS, Hayfield D, Anyia A, Stephenson T, Mitlin D. Supercapacitors based on carbons with tuned porosity derived from paper pulp mill sludge biowaste. *Carbon*. 2013;**57**:317-328. DOI: 10.1016/j.carbon.2013.01.079

- [77] Coromina HM, Walsh DA, Mokaya R. Biomass-derived activated carbon with simultaneously enhanced CO₂ uptake for both pre and post combustion capture applications. *Journal of Materials Chemistry A*. 2016;**4**(1):280-289. DOI: 10.1039/C5TA09202G
- [78] Feng HB, Hu H, Dong HW, Xiao Y, Cai YJ, Lei BF, Liu YL, Zheng MT. Hierarchical structured carbon derived from bagasse wastes: A simple and efficient synthesis route and its improved electrochemical properties for high-performance supercapacitors. *Journal of Power Sources*. 2016;**302**:164-173. DOI: 10.1016/j.jpowsour.2015.10.063
- [79] Hao S-W, Hsu C-H, Liu Y-G, Chang BK. Activated carbon derived from hydrothermal treatment of sucrose and its air filtration application. *RSC Advances*. 2016;**6**(111):109950-109959. DOI: 10.1039/C6RA23958G
- [80] Bedin KC, Martins AC, Cazetta AL, Pezoti O, Almeida VC. KOH-activated carbon prepared from sucrose spherical carbon: Adsorption equilibrium, kinetic and thermodynamic studies for methylene blue removal. *Chemical Engineering Journal*. 2016;**286**:476-484. DOI: 10.1016/j.cej.2015.10.099
- [81] Balahmar N, Al-Jumaily AS, Mokaya R. Biomass to porous carbon in one step: Directly activated biomass for high performance CO₂ storage. *Journal of Materials Chemistry A*. 2017;**5**(24):12330-12339. DOI: 10.1039/c7ta01722g
- [82] Islam MA, Tan IAW, Benhouria A, Asif M, Hameed BH. Mesoporous and adsorptive properties of palm date seed activated carbon prepared via sequential hydrothermal carbonization and sodium hydroxide activation. *Chemical Engineering Journal*. 2015;**270**:187-195. DOI: 10.1016/j.cej.2015.01.058
- [83] Tran HN, You SJ, Chao HP. Fast and efficient adsorption of methylene green 5 on activated carbon prepared from new chemical activation method. *Journal of Environmental Management*. 2017;**188**:322-336. DOI: 10.1016/j.jenvman.2016.12.003
- [84] Liu Z, Zhang F-S. Removal of copper(II) and phenol from aqueous solution using porous carbons derived from hydrothermal chars. *Desalination*. 2011;**267**(1):101-106. DOI: 10.1016/j.desal.2010.09.013
- [85] Román S, Valente Nabais JM, Ledesma B, González JF, Laginhas C, Titirici MM. Production of low-cost adsorbents with tunable surface chemistry by conjunction of hydrothermal carbonization and activation processes. *Microporous and Mesoporous Materials*. 2013;**165**(0):127-133. DOI: 10.1016/j.micromeso.2012.08.006
- [86] Harmer MA, Fan A, Liauw A, Kumar RK. A new route to high yield sugars from biomass: Phosphoric-sulfuric acid. *Chemical Communications*. 2009;**(43)**:6610-6612. DOI: 10.1039/B916048E
- [87] Wang L, Guo Y, Zou B, Rong C, Ma X, Qu Y, Li Y, Wang Z. High surface area porous carbons prepared from hydrochars by phosphoric acid activation. *Bioresource Technology*. 2011;**102**(2):1947-1950. DOI: 10.1016/j.biortech.2010.08.100
- [88] Wang L, Guo Y, Zhu Y, Li Y, Qu Y, Rong C, Ma X, Wang Z. A new route for preparation of hydrochars from rice husk. *Bioresource Technology*. 2010;**101**(24):9807-9810. DOI: 10.1016/j.biortech.2010.07.031

- [89] Cui Y, Atkinson JD. Tailored activated carbon from glycerol: Role of acid dehydrator on physiochemical characteristics and adsorption performance. *Journal of Materials Chemistry A*. 2017;**5**(32):16812-16821. DOI: 10.1039/C7TA02898A
- [90] Fechler N, Wohlgemuth S-A, Jaker P, Antonietti M. Salt and sugar: Direct synthesis of high surface area carbon materials at low temperatures via hydrothermal carbonization of glucose under hypersaline conditions. *Journal of Materials Chemistry A*. 2013;**1**(33):9418-9421. DOI: 10.1039/C3TA10674H
- [91] Fellingner TP, White RJ, Titirici MM, Antonietti M. Borax-mediated formation of carbon aerogels from glucose. *Advanced Functional Materials*. 2012;**22**(15):3254-3260. DOI: 10.1002/adfm.201102920
- [92] Zhou J, Yuan X, Xing W, Si WJ, Zhuo SP. Capacitive performance of mesoporous carbons derived from the citrates in ionic liquid. *Carbon*. 2010;**48**(10):2765-2772. DOI: 10.1016/j.carbon.2010.04.004
- [93] Zhou QQ, Chen XY, Wang B. An activation-free protocol for preparing porous carbon from calcium citrate and the capacitive performance. *Microporous Mesoporous Materials*. 2012;**158**:155-161. DOI: 10.1016/j.micromeso.2012.03.031
- [94] Atkinson JD, Rood MJ. Preparing microporous carbon from solid organic salt precursors using in situ templating and a fixed-bed reactor. *Microporous Mesoporous Materials*. 2012;**160**:174-181. DOI: 10.1016/j.micromeso.2012.05.008
- [95] Xu B, Duan H, Chu M, Cao GP, Yang YS. Facile synthesis of nitrogen-doped porous carbon for supercapacitors. *Journal of Materials Chemistry A*. 2013;**1**(14):4565-4570. DOI: 10.1039/c3ta01637d
- [96] Xu B, Zheng DF, Jia MQ, Cao GP, Yang YS. Nitrogen-doped porous carbon simply prepared by pyrolyzing a nitrogen-containing organic salt for supercapacitors. *Electrochimica Acta*. 2013;**98**:176-182. DOI: 10.1016/j.electacta.2013.03.053
- [97] Fuertes AB, Ferrero GA, Sevilla M. One-pot synthesis of microporous carbons highly enriched in nitrogen and their electrochemical performance. *Journal of Materials Chemistry A*. 2014;**2**(35):14439-14448. DOI: 10.1039/c4ta02959c
- [98] Sevilla M, Fuertes AB. A general and facile synthesis strategy towards highly porous carbons: Carbonization of organic salts. *Journal of Materials Chemistry A*. 2013;**1**(44):13738-13741. DOI: 10.1039/c3ta13149a
- [99] Ferrero GA, Sevilla M, Fuertes AB. Mesoporous carbons synthesized by direct carbonization of citrate salts for use as high-performance capacitors. *Carbon*. 2015;**88**:239-251. DOI: 10.1016/j.carbon.2015.03.014
- [100] Cooper ER, Andrews CD, Wheatley PS, Webb PB, Wormald P, Morris RE. Ionic liquids and eutectic mixtures as solvent and template in synthesis of zeolite analogues. *Nature*. 2004;**430**(7003):1012-1016. DOI: 10.1038/nature02860
- [101] Taubert A, Li Z. Inorganic materials from ionic liquids. *Dalton Transactions*. 2007;(7):723-727. DOI: 10.1039/B616593A

- [102] Lee JS, Mayes RT, Luo HM, Dai S. Ionothermal carbonization of sugars in a protic ionic liquid under ambient conditions. *Carbon*. 2010;**48**(12):3364-3368. DOI: 10.1016/j.carbon.2010.05.027
- [103] Xie ZL, White RJ, Weber J, Taubert A, Titirici MM. Hierarchical porous carbonaceous materials via ionothermal carbonization of carbohydrates. *Journal of Materials Chemistry*. 2011;**21**(20):7434-7442. DOI: 10.1039/c1jm00013f
- [104] Zhang PF, Gong YT, Wei ZZ, Wang J, Zhang ZY, Li HR, Dai S, Wang Y. Updating biomass into functional carbon material in ionothermal manner. *ACS Applied Materials & Interfaces*. 2014;**6**(15):12515-12522. DOI: 10.1021/am5023682
- [105] Pampel J, Denton C, Feller T-P. Glucose derived ionothermal carbons with tailor-made porosity. *Carbon*. 2016;**107**:288-296. DOI: 10.1016/j.carbon.2016.06.009
- [106] Yu ZF, Wang XZ, Song XD, Liu Y, Qiu JS. Molten salt synthesis of nitrogen-doped porous carbons for hydrogen sulfide adsorptive removal. *Carbon*. 2015;**95**:852-860. DOI: 10.1016/j.carbon.2015.08.105
- [107] Lee JS, Wang XQ, Luo HM, Baker GA, Dai S. Facile ionothermal synthesis of microporous and mesoporous carbons from task specific ionic liquids. *Journal of the American Chemical Society*. 2009;**131**(13):4596-4597. DOI: 10.1021/ja900686d
- [108] Lee JS, Wang XQ, Luo HM, Dai S. Fluidic carbon precursors for formation of functional carbon under ambient pressure based on ionic liquids. *Advanced Materials*. 2010;**22**(9):1004-1007. DOI: 10.1002/adma.200903403
- [109] Fechner N, Feller T-P, Antonietti M. "Salt templating": A simple and sustainable pathway toward highly porous functional carbons from ionic liquids. *Advanced Materials*. 2013;**25**(1):75-79. DOI: 10.1002/adma.201203422
- [110] Cui ZT, Wang SG, Zhang YH, Cao MH. A simple and green pathway toward nitrogen and sulfur dual doped hierarchically porous carbons from ionic liquids for oxygen reduction. *Journal of Power Sources*. 2014;**259**:138-144. DOI: 10.1016/j.jpowsour.2014.02.084
- [111] Elumeeva K, Fechner N, Feller TP, Antonietti M. Metal-free ionic liquid-derived electrocatalyst for high-performance oxygen reduction in acidic and alkaline electrolytes. *Materials Horizons*. 2014;**1**(6):588-594. DOI: 10.1039/c4mh00123k
- [112] Ma Z, Zhang H, Yang Z, Zhang Y, Yu B, Liu Z. Highly mesoporous carbons derived from biomass feedstocks templated with eutectic salt ZnCl_2/KCl . *Journal of Materials Chemistry A*. 2014;**2**(45):19324-19329. DOI: 10.1039/C4TA03829K
- [113] Liu XF, Antonietti M. Molten salt activation for synthesis of porous carbon nanostructures and carbon sheets. *Carbon*. 2014;**69**:460-466. DOI: 10.1016/j.carbon.2013.12.049
- [114] Su SJ, Lai QX, Liang YY. Schiff-base polymer derived nitrogen-rich microporous carbon spheres synthesized by molten-salt route for high-performance supercapacitors. *RSC Advances*. 2015;**5**(75):60956-60561. DOI: 10.1039/c5ra07628e

- [115] Ma Z, Zhang H, Yang Z, Ji G, Yu B, Liu X, Liu Z. Mesoporous nitrogen-doped carbons with high nitrogen contents and ultrahigh surface areas: Synthesis and applications in catalysis. *Green Chemistry*. 2016;**18**(7):1976-1982. DOI: 10.1039/C5GC01920F
- [116] Pampel J, Feller TP. Opening of bottleneck pores for the improvement of nitrogen doped carbon electrocatalysts. *Advanced Energy Materials*. 2016;**6**(8):6-13. DOI: 10.1002/Aenm.201502389
- [117] Graglia M, Pampel J, Hantke T, Feller TP, Esposito D. Nitro lignin-derived nitrogen-doped carbon as an efficient and sustainable electrocatalyst for oxygen reduction. *ACS Nano*. 2016;**10**(4):4364-4371. DOI: 10.1021/acs.nano.5b08040
- [118] Yang F, Sun LL, Xie WL, Jiang Q, Gao Y, Zhang W, Zhang Y. Nitrogen-functionalization biochars derived from wheat straws via molten salt synthesis: An efficient adsorbent for atrazine removal. *Science of the Total Environment*. 2017;**607**:1391-1399. DOI: 10.1016/j.scitotenv.2017.07.020
- [119] Ouyang T, Cheng K, Gao YY, Kong SY, Ye K, Wang GL, Cao DX. Molten salt synthesis of nitrogen doped porous carbon: A new preparation methodology for high-volumetric capacitance electrode materials. *Journal of Materials Chemistry A*. 2016;**4**(25):9832-9843. DOI: 10.1039/c6ta02673g
- [120] Yin H, Lu B, Xu Y, Tang D, Mao X, Xiao W, Wang D, Alshawabkeh AN. Harvesting capacitive carbon by carbonization of waste biomass in molten salts. *Environmental Science & Technology*. 2014;**48**(14):8101-8108. DOI: 10.1021/es501739v
- [121] Chang YQ, Antonietti M, Feller TP. Synthesis of nanostructured carbon through Ionothermal carbonization of common organic solvents and solutions. *Angewandte Chemie-International Edition*. 2015;**54**(18):5507-5512. DOI: 10.1002/anie.201411685
- [122] Schipper F, Vizintin A, Ren J, Dominko R, Feller T-P. Biomass-derived heteroatom-doped carbon aerogels from a salt melt sol-gel synthesis and their performance in Li-S batteries. *ChemSusChem*. 2015;**8**(18):3077-3083. DOI: 10.1002/cssc.201500832
- [123] Nita C, Bensafia M, Vaultot C, Delmotte L, Matei Ghimbeu C. Insights on the synthesis mechanism of green phenolic resin derived porous carbons via a salt-soft templating approach. *Carbon*. 2016;**109**:227-238. DOI: 10.1016/j.carbon.2016.08.011
- [124] Liu YC, Huang BB, Lin XX, Xie ZL. Biomass-derived hierarchical porous carbons: Boosting the energy density of supercapacitors via an ionothermal approach. *Journal of Materials Chemistry A*. 2017;**5**(25):13009-13018. DOI: 10.1039/c7ta03639f
- [125] Liu XF, Antonietti M. Moderating black powder chemistry for the synthesis of doped and highly porous graphene nanoplatelets and their use in electrocatalysis. *Advanced Materials*. 2013;**25**(43):6284-6290. DOI: 10.1002/adma.201302034
- [126] Liu XF, Giordano C, Antonietti M. A facile molten-salt route to graphene synthesis. *Small*. 2014;**10**(1):193-200. DOI: 10.1002/smll.201300812

- [127] Zhang PF, Qiao ZA, Zhang ZY, Wan S, Dai S. Mesoporous graphene-like carbon sheet: High-power supercapacitor and outstanding catalyst support. *Journal of Materials Chemistry A*. 2014;**2**(31):12262-12269. DOI: 10.1039/c4ta02307b
- [128] He B, Li WC, Lu AH. High nitrogen-content carbon nanosheets formed using the Schiff-base reaction in a molten salt medium as efficient anode materials for lithium-ion batteries. *Journal of Materials Chemistry A*. 2015;**3**(2):579-585. DOI: 10.1039/c4ta05056h
- [129] Deng X, Zhao BT, Zhu L, Shao ZP. Molten salt synthesis of nitrogen-doped carbon with hierarchical pore structures for use as high-performance electrodes in supercapacitors. *Carbon*. 2015;**93**:48-58. DOI: 10.1016/j.carbon.2015.05.031
- [130] Shang HS, Lu YJ, Zhao F, Chao C, Zhang B, Zhang HS. Preparing high surface area porous carbon from biomass by carbonization in a molten salt medium. *RSC Advances*. 2015;**5**(92):75728-75734. DOI: 10.1039/c5ra12406a
- [131] Kong WX, Zhao F, Guan HJ, Zhao YF, Zhang HS, Zhang B. Highly adsorptive mesoporous carbon from biomass using molten-salt route. *Journal of Materials Science*. 2016;**51**(14): 6793-6800. DOI: 10.1007/s10853-016-9966-8
- [132] Fellingner TP, Thomas A, Yuan JY, Antonietti M. 25th anniversary article: "cooking carbon with salt": Carbon materials and carbonaceous frameworks from ionic liquids and poly(ionic liquid)s. *Advanced Materials*. 2013;**25**(41):5838-5854. DOI: 10.1002/adma.201301975
- [133] Antonietti M, Fechner N, Fellingner TP. Carbon aerogels and monoliths: Control of porosity and nanoarchitecture via sol-gel routes. *Chemistry of Materials*. 2014;**26**(1):196-210. DOI: 10.1021/cm402239e
- [134] Liu XF, Fechner N, Antonietti M. Salt melt synthesis of ceramics, semiconductors and carbon nanostructures. *Chemical Society Reviews*. 2013;**42**(21):8237-8265. DOI: 10.1039/c3cs60159e
- [135] Xie ZL, Su DS. Ionic liquid based approaches to carbon materials synthesis. *European Journal of Inorganic Chemistry*. 2015;**(7)**:1137-1147. DOI: 10.1002/ejic.201402607
- [136] Deng YF, Xie Y, Zou KX, Ji XL. Review on recent advances in nitrogen-doped carbons: Preparations and applications in supercapacitors. *Journal of Materials Chemistry A*. 2016;**4**(4):1144-1173. DOI: 10.1039/c5ta08620e

Carbon Xerogels: The Bespoke Nanoporous Carbons

María Canal-Rodríguez, J. Angel Menéndez and
Ana Arenillas

Additional information is available at the end of the chapter

<http://dx.doi.org/10.5772/intechopen.71255>

Abstract

This chapter focuses on the main features of resorcinol-formaldehyde-based carbon xerogels. The first part of the chapter discusses ways of synthesizing these materials and the different variables involved. Then a review of the ways in which the meso- and macroporosity of organic xerogels can be controlled by adjusting the synthesis conditions is undertaken. Special attention is paid to the pH and components of the precursor solution and how these variables are interrelated with each other. The formation of the microporosity during the carbonization or activation processes that give rise to the carbon xerogels is also briefly discussed. Besides the fact that the porosity of these materials can be tailored during the synthesis, another notable characteristic is that, compared with most porous carbons, they possess a relatively high electrical conductivity, which make them ideal materials for use as electrodes in energy storage devices. Their use in supercapacitors and in lithium ion batteries is addressed in the last part of the chapter.

Keywords: carbon xerogels, designed porosity, electrical conductivity, energy storage, supercapacitors

1. Synthesis of resorcinol-formaldehyde xerogels

The most common way of synthesizing organic gels is via the polymerization reaction between resorcinol (R) and formaldehyde (F), using water as solvent and a basic catalyst as the reaction promoter [1–5]. This polymerization reaction consists of two stages: an addition reaction (**Figure 1**) and a condensation reaction (**Figure 2**).

Resorcinol is a benzyl compound with two hydroxyl groups at positions 1 and 3, which allow formaldehyde to be added at positions 2, 4 and 6 (see **Figure 1**) [6, 7]. In the presence of a basic catalyst, the ionization of the resorcinol occurs through the abstraction of hydroxyl hydrogens, resulting in resorcinol anions. Resorcinol anions are more reactive than resorcinol itself, which

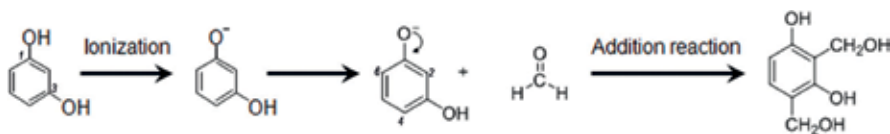


Figure 1. Addition reaction between resorcinol and formaldehyde.

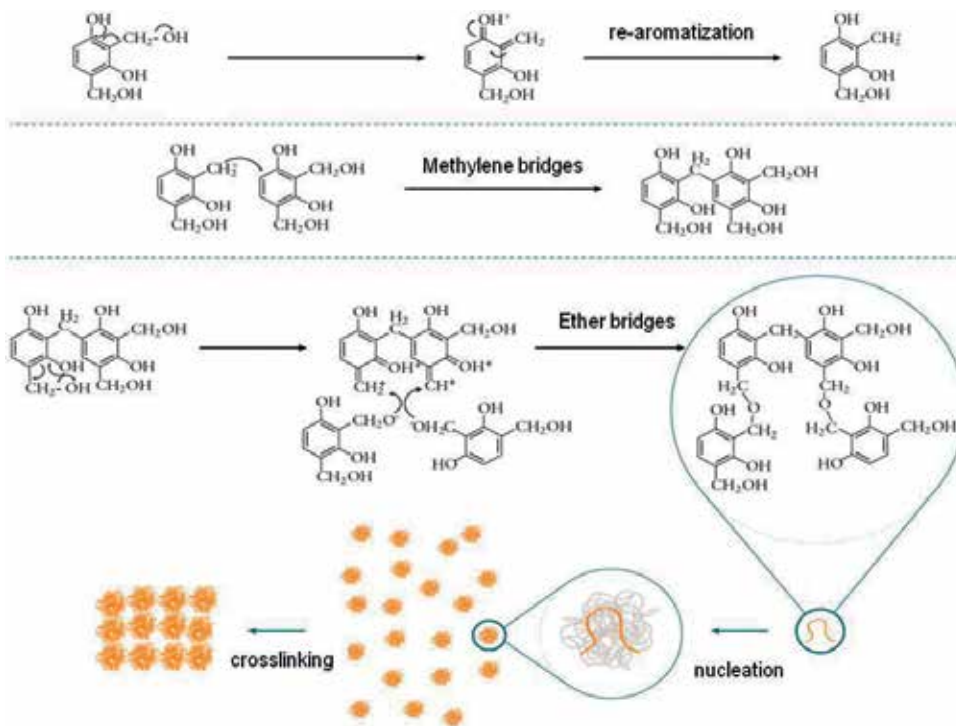


Figure 2. Polycondensation reactions during the synthesis of resorcinol and formaldehyde gels.

favors the addition of formaldehyde leading to the formation of hydroxymethyl derivatives, as shown in **Figure 1** [8, 9]. These hydroxymethyl derivatives are the monomers that are necessary for polymerization to occur. At the same time as the addition reaction, the condensation reaction takes place, in which the hydroxymethyl derivatives lose OH groups to form a benzyl cation (**Figure 2**) [10]. This cation reacts with a benzene ring of another molecule by bonding the rings with methylene and ether bridges [11, 12], giving rise to the formation of polymeric particles, known as nodules. The nodules are aggregated and cross-linked by polymer chains to form a three-dimensional porous network in a liquid medium (**Figure 2**).

The appearance of the nodules decreases the fluidity of the precursor mixture. The time required from the start of the reaction to the point where the solution starts to lose fluidity, i.e., when the gel begins to form, is known as the gelation time, whereas the exact moment at which the gel is obtained is called the gelation point [13]. After reaching this point of gelation, the solid structure that is immersed in the liquid continues to evolve. This stage is called

curing, where the remaining hydroxyl groups continue to undergo polymerization, thereby increasing the number of cross-linkages between the nodules [14].

The formation of the nodules, their growth and cross-linking between polymer chains depend on the concentration of each of the reagents used. The final polymeric structure will depend on the values of these variables. This is of great importance since it is the polymeric structure that determines the physical and chemical properties of the materials and, therefore, their adaptability to the requirements of a specific application.

After the gelation and curing processes, i.e., the polymerization and cross-linking reactions, a stable three-dimensional polymer is obtained. However, the polymer is imbibed in the reaction media. Usually, the steps mentioned above (i.e., polymerization and curing) occur in covered containers [9, 15–17]. This means that all the reaction media or solvent used is covering the polymer, filling all the pores of the structure. The next step of the process is to eliminate the solvent in order to obtain a dry polymer with all its pores available. Three drying methods are found in the literature [4, 6, 18]: (i) supercritical drying, (ii) cryogenic drying and (iii) subcritical drying, giving rise to three different kinds of gel commonly referred to as aerogels, cryogels and xerogels, respectively, (**Figure 3**).

The most common method of solvent elimination is by supercritical drying [8, 12, 14, 16, 19–25]. This method consists in exchanging the solvent used for the synthesis, by CO₂ under supercritical conditions, (i.e. under high values of pressure and temperatures), and then eliminating the CO₂ as a gas simply by changing the operating conditions (i.e., reducing the pressure). If water has been used as the solvent, as in the present case, it must first be replaced by an organic solvent due to the high solubility of the CO₂ in water. The main advantage of this procedure is that the polymeric structure is not subjected to any surface tension forces, as the final solvent, CO₂, is eliminated in gas phase. In this way, the previously tailored porosity is preserved. However, the several solvent exchanges and the high pressures required for the supercritical drying make this option expensive and too long. The gels obtained by this method are known as aerogels.

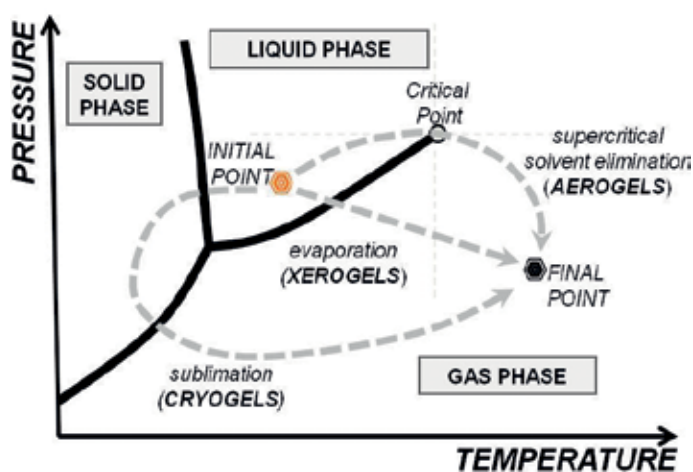


Figure 3. Scheme of different ways of eliminating the solvent during the synthesis of resorcinol-formaldehyde gels.

Under cryogenic drying, the solvent used must be frozen and then eliminated by sublimation. As in the first case, when water is the dissolvent used for the synthesis, before the freezing process, it must be replaced by an organic solvent in order to avoid the formation of ice crystals inside the polymer structure, which would lead to the uncontrolled formation of megalopores or voids [18, 26]. The gels obtained in this drying process have high pore volumes [18] and are known as cryogels. Despite the fact that this procedure is more affordable than supercritical drying, it is still expensive due to the need for using exchanging solvents, very low operating temperatures and numerous long steps.

The performance of the third drying method is based on the direct evaporation of the solvent and the generation of gels known as xerogels. Unlike the two cases mentioned above, under subcritical drying conditions, a liquid-vapor interphase takes place. This interphase generates high superficial tensions that may cause the collapse of the porous structure of the gel. When water is the solvent used during the synthesis of the gel, one possible solution to this problem can be to replace the water by another solvent with less surface tension, such as acetone or cyclohexane. However, some authors [18, 27–32] have demonstrated that a suitable choice of operating conditions during the drying stage minimizes the shrinkage of the gel structure. In other words, the porosity of the gel is preserved without the need for solvent exchanges. For this reason, subcritical drying is the cheapest, easiest and fastest method, and consequently the most upscalable alternative for producing gels on a large scale.

2. Tailoring the meso- and macroporosity

Perhaps the most relevant property of carbon xerogels is that their mesoporosity (i.e., pores with an average size between 2 and 50 nm) and macroporosity (i.e., pores with an average size greater than 50 nm) can be tailored during the synthesis of the organic xerogels by selecting the appropriate synthesis conditions and, above all, by predetermining the characteristics of the precursor solution.

During the gelation stage, the polycondensation of resorcinol and formaldehyde leads to the formation of quasi-spherical nodules (nucleation) that become attached to each other during the curing step (cross-linking). Then, when the solvent is removed, during the drying step, the empty interspaces between the nodules form pores with a size that depends on the size of the nodules formed in the previous stages of the synthesis. A sketch representing the formation of the nodules and the way they cross-link with the pores formed in the resorcinol-formaldehyde (RF) gel is presented in **Figure 4**.

As reported in many studies, the size of the nodules and hence of the mesopores (or macropores) can be varied by changing the synthesis conditions, such as the pH [5, 19, 33–36], type and amount of solvent [6, 37], the concentration of the reactants [6, 20, 37], the type of catalyst [7, 25], the temperature and time of synthesis [25, 28], etc. As there are so many variables involved, the meso- or macroporosity of the xerogels can be tailored with a relatively high degree of precision by adjusting these variables. This is, of course, a great advantage, as it means that it is possible to design specific porous textures for specific applications. However, these variables

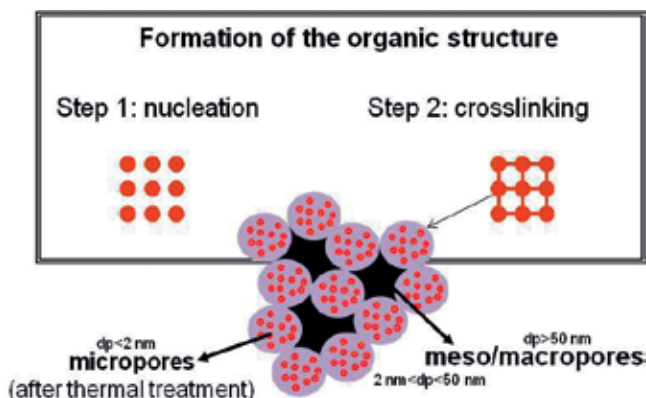


Figure 4. Schematic representation of pore formation in RF xerogel synthesis.

are not independent of each other. Therefore, in order to be able to predict how changes in more than one of them will affect the porosity of the resultant xerogel, it is necessary to know the way in which they are interrelated, which is not a straightforward task [34, 37, 38].

The complexity of the problem can be explained briefly as follows. Resorcinol is responsible for the formation of the nodules or clusters and so the greater the amount of resorcinol that is used, the more the clusters that will be generated, while formaldehyde strengthens the gel by generating a structure that is more branched and/or interconnected. The volume of solvent added affects the distance between the nodules and so the greater the volume of solvent that is used, the more segregated the nodules will be, while the pH influences the speed of the reaction, i.e., the higher the pH is, the faster the resorcinol anions will be formed and consequently more nodules of small size will be created. All of these differences in the polymer structure affect the final porosity of the RF gel. Finally, the type of catalyst and the composition of the formaldehyde solution also influence the porosity formed by the RF gel [34]. However, as mentioned above, it is obvious that the modifications in porosity brought about by changes in the pH of the precursor solution, for example, will not be the same if the amount of solvent also changes. This is exemplified in **Figure 5**, where scanning electron microscope photographs, and the sketches in the insets, show for instance how increasing the pH of the precursor solutions from 5 to 5.8 leads to a polymeric structure with larger nodules (and hence wider pores) if the dilution is increased at the same time from 5.7 to 11.7.

Interestingly, the mesoporosity (or macroporosity) of the organic xerogels is preserved with only slight variations when thermal treatments such as carbonization and/or activation are applied [39]. The meso- or macroporosity of the carbon xerogels that is designed before and formed during the synthesis of the organic xerogel persists in the carbon xerogel, occasionally with a slight shrinkage of the pores when the carbonization or activation temperature is higher than 900°C [40–42]. However, as this shrinkage is a function of the temperature and heating rate, it can easily be predicted. Therefore, by taking this into account, it is possible to predesign the mesoporosity (or macroporosity) of the carbon xerogels before they are produced.

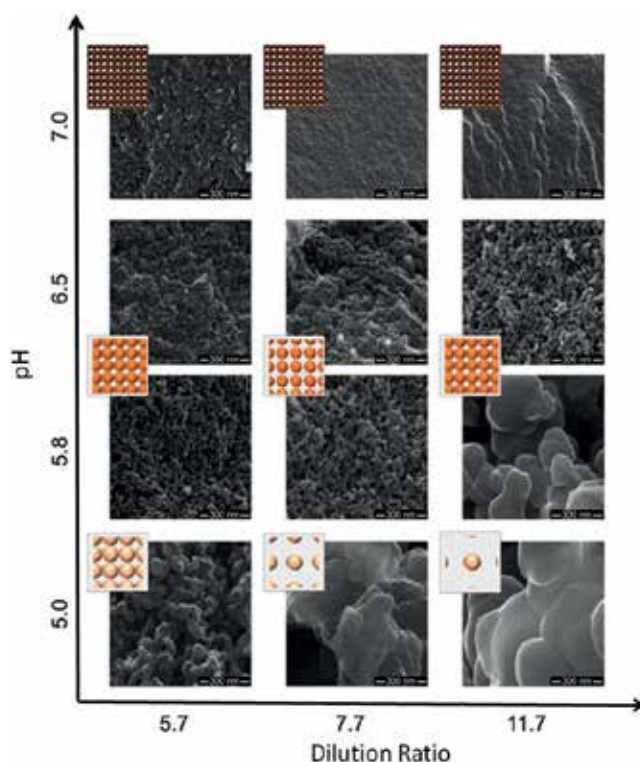


Figure 5. SEM microphotographs of carbon xerogels obtained under different synthesis conditions (adapted from [39]).

3. Tailoring the microporosity

As stated above, mesopores and macropores, which are the voids between the nodules of polymer that make up the organic xerogel polymeric structure, are predetermined during the synthesis of the organic xerogel. However, in order to obtain the carbon xerogel, it is necessary to subject the organic gel to a carbonization process or, in other words, to a thermal treatment in an inert atmosphere. During the carbonization, as the temperature increases, diverse volatile compounds are released from the organic xerogel, while reorganization and condensation reactions occur, leading to a thermally stable material that is mainly composed of carbon with a dominant sp^2 structure. The release of the volatile molecules (mainly H_2 , CO , CO_2 and light hydrocarbons) leaves behind small holes or micropores. This microporosity is allocated to the carbonized nodules that constitute the carbon xerogel. This process is schematized in **Figure 6**.

Although the amount (pore volume) and size of these micropores may differ depending on the carbonization conditions and the type of organic xerogel being carbonized, in practice, for carbonization temperatures between 800 and 1000°C, the microporosity is similar for any carbon xerogel no matter the starting organic xerogel used [9, 27, 30, 43]. However, the microporosity can be modified by performing an activation process, which can be performed either during or after the carbonization. Either chemical activation (with KOH, phosphoric

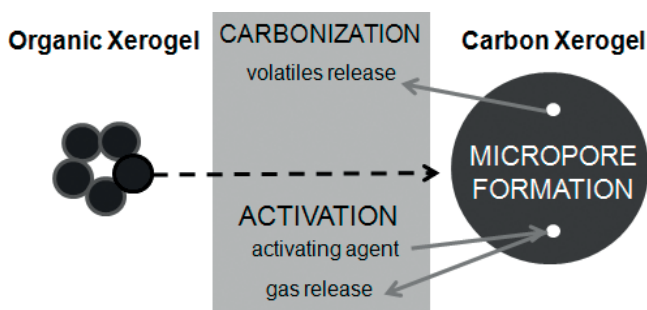


Figure 6. Micropore formation in a carbon xerogel by either carbonization or activation of the organic xerogel.

acid, etc.) or physical activation (with CO₂, steam or both) can be employed [40, 42]. An appropriate selection of the activation process is essential for tailoring the microporosity of the carbon xerogel. Thus, different micropore volume and micropore size distributions can be obtained by varying the xerogel/activating agent ratio, the type of activating agent or the reaction time and temperature [40, 42].

4. Unique exohedral porosity

A particularity of carbon xerogels is their unique porous structure, which completely differs from that of most porous carbons. Thus, carbon xerogels have a hierarchical porous structure that is composed of both micro- and mesopores (or macropores). Moreover, as stated in the previous sections, the size, and to some extent the pore volume, of the larger pores (meso- or macropores) can be tailored during the synthesis of the organic xerogel, whereas the pore volume and the size of the micropores can be predetermined during the carbonization or activation processes that give rise to the carbon xerogels. Consequently, the entire porosity (micro- and meso-/macroporosity) of carbon xerogels can be independently tailored to conform to predetermined specifications.

In addition, most porous carbons have slit-shaped pores, with more or less flat walls, or cylindrical pores, with negative surface curvatures (endohedral). However, the mesopores (or macropores) of carbon xerogels, due to their polymeric structure of interconnected nodules, have a positive surface curvature (exohedral), which is quite unusual for porous carbons (Figure 7).

The exohedral geometry of mesopores may have important implications for some applications where carbon xerogels are used [44], because the heterogeneous interaction of this kind of positive surface with gases or liquids differs from the interactions that occur with other types of carbon surfaces. For example, the positive curvature facilitates double layer formation in electrochemical capacitors, which is the subject of this chapter. The double layer, which is the basis of charge storage in this kind of device, is favored due to the reduced electrical field near to the positive surface, as a result of which the driving force behind counter-ion adsorption and co-ion desorption is decreased [45]. This has a positive influence on energy, but especially on the power density of supercapacitors.

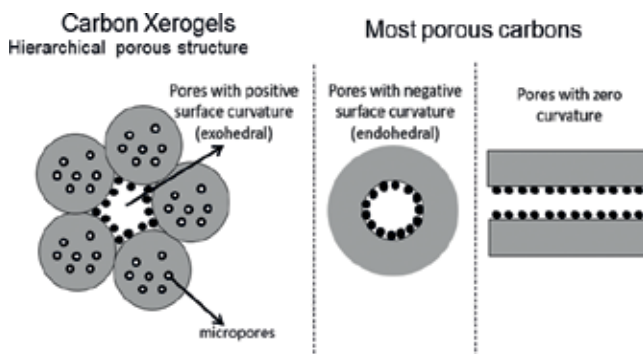


Figure 7. Different kinds of pores according to the curvature of their surface.

5. Combining a high porosity and a high electrical conductivity

Unlike other carbonaceous materials, another remarkable feature of carbon xerogels is that despite being materials with a high porosity they also show low electrical resistivity, i.e., they are good electrical conductors, which are usually opposed characteristics. This is because good electrical conductors are usually materials with ordered carbonaceous structures, with condensed aromatic rings to a greater or lesser extent that have some delocalized π electrons that are free to migrate in the plane, making these kinds of material electrically conductive. This is the case of graphite or graphene [46]. On the other hand, porous materials have disordered structures due to their numerous defects, voids, etc., which are responsible for their high porosity. Such structural defects are not favorable for the movement of the electrons, and therefore porous material is usually synonymous with insulation. In fact, a lot of current research is focused on obtaining the optimal combination of both properties (porosity and electric conductivity) in a single material. The approaches for achieving this involve doping techniques or creating composites of porous materials with highly conductive ones such as carbon nanofibers or graphene. In this way, the resultant composite or doped material retains the porosity of the matrix, but its inherent electrical resistivity is reduced [41, 47–52].

However, even without doping, carbon xerogels have high electrical conductivities of 110 S m^{-1} when their S_{BET} is around $1600 \text{ m}^2 \text{ g}^{-1}$, which is double the electrical conductivity of a commercially activated carbon (50 S m^{-1}) with the same specific area (YP-50F of Kuraray) [41]. This is due to their peculiar carbonaceous structure. On the one hand, as mentioned above, the polymeric structure of carbon xerogels consists of interconnected carbonaceous nodules with the most characteristic porosity between them. These nodules make up the carbonaceous network described in **Figure 2**. Such polycondensed structures are susceptible to ordering due to the effect of temperature resulting in a polymeric structure formed by ordered nodules interconnected with each other. The end product is a very special macroscopically porous material, but ordered at the level of nodules. As a consequence, carbon xerogels differ from active carbons in that they are able to combine a perfect porosity and electrical conductivity. On the other hand, during the carbonization/activation step not only is microporosity generated, but also the carbonaceous structure of the polymeric network undergoes a certain ordering and reorganization due to the high temperatures used (i.e., 1000°C). In fact,

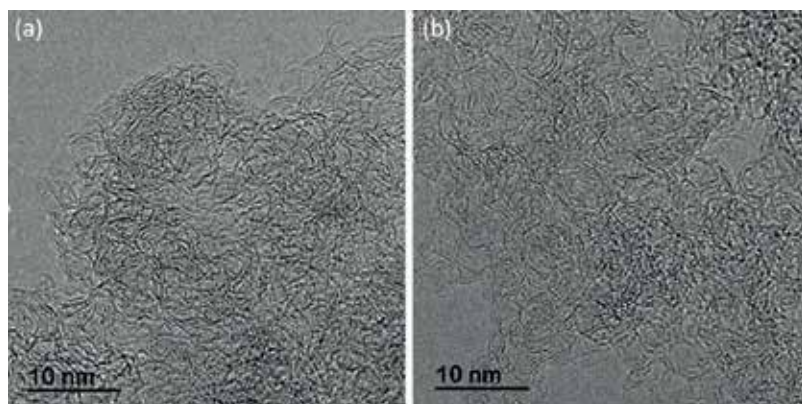


Figure 8. HRTEM images of a carbon xerogel (a) and YP-50F (b).

when carbon xerogels with specific surface areas of $2400 \text{ m}^2 \text{ g}^{-1}$ are produced, i.e., more porous xerogels, their electrical conductivity also increases to ca. 240 S m^{-1} . This is because to obtain a high porosity, the carbonization/activation conditions must be more intense, i.e., more residence time is required. As a result, although extra microporosity is created, the carbon structure has more time to reorganize and order itself.

Figure 8 presents HRTEM images of the nanostructure of a carbon xerogel and YP-50F. As can be seen, both materials are composed of interconnected carbon sheets. Nevertheless, the structure of this carbon xerogel is dense and compact unlike that of YP-50F where there are some voids. According to Canal-Rodríguez et al. [41], these structural differences possibly explain the differences in their electrical conductivity.

This special feature of carbon xerogels, i.e., the combination of a tailored porosity with a high electrical conductivity, makes them perfect candidates for a wide variety of applications in many different areas such as (i) clean energy, i.e., for use as active materials in energy storage devices (this application will be discussed in detail in the following sections) or even in energy generation devices such as fuel cells [53–55]; (ii) environmental issues and better use of natural resources, in water-treatment and in the desalination of brackish water devices that function on the basis of capacitive deionization [56–62]; (iii) biotechnology, where they are used as supports of biomolecules as active materials in sensors [63, 64], etc.

6. Nanoporous carbon xerogels in energy storage

Electrical energy storage is required in numerous applications, not only as a result of the increasing number of electronic devices that we use in our daily life but also as a means to ensure a more rational and sustainable use of energy resources. Thus, there is an increasing demand for more efficient energy storage devices in telecommunications, stand-by power systems, uninterruptible power supply systems, electric/hybrid vehicles, energy recovery systems, burst and regenerative power in industry and transportation, electric grid modulation or as complements to renewable energies.

The specifications for the energy storage devices are given in terms of energy stored ($W\ h$) and power (W) as well as size and weight, cost and durability. The most common electrical energy storage device is the battery. Batteries can store large amounts of energy within relatively small confines of volume and weight. However, the problem with battery systems is their life-span as their energy storage method is based on a chemical process that degrades the components of the battery and reduces the cycling life [65]. Furthermore, the current development of electronic applications demands devices with high power requirements, far beyond the capability of standard batteries. Supercapacitors, also known as electrochemical double layer capacitors (EDLC), store energy via a physical process based on the formation of an electric double layer at the electrode/electrolyte interface [65]. Therefore, the charge/discharge process is very fast and totally reversible with a very low level of degradation of the components. As a consequence, supercapacitors offer a high power density and a very long cycle life.

In general, batteries are used for their relatively high energy density, while supercapacitors are employed for their high power density. Therefore, both devices, if combined, could fulfill complementary functions. Currently both technologies require further optimization of their performance and the incorporation of safer and more cost-effective components. Research and industrial developments for storage devices are currently oriented toward improving energy and power density with new electrode materials, new electrolytes and new electrochemical concepts. Moreover, some research is currently focused on developing hybrid devices where in one electrode energy storage is based on a chemical process, while in the other, it is based on a physical double layer [66, 67].

An EDLC consists of two porous carbon electrodes in contact with the current collector, separated by a porous film and impregnated with an electrolyte solution. When there is an electric potential difference between the electrodes, the electrons in the negatively polarized electrode (anode) are balanced by an equal number of positive cations at the electrode/electrolyte interface, while the storage holes in the positively polarized electrode (cathode) are electrically balanced by the anions from the electrolyte. **Figure 9** shows the scheme of the basic principle of energy storage in this kind of device.

The capacitance of a single electrode (C_e) is proportional to the surface area of the electrode (S) according to Eq. (1),

$$C_e = \varepsilon_0 \varepsilon (S/d) \quad (1)$$

where ε_0 is the vacuum permittivity ($8.854 \cdot 10^{-12} \text{ F m}^{-1}$), ε is the relative permittivity of the dielectric electrolyte used and d is the effective thickness of the double layer. According to this equation, the capacitance of a single electrode will increase as the effective surface area of the electrode increases and the thickness of the double layer decreases (i.e., better contact between electrode and ions of electrolyte). This is the reason for using carbons with well-developed porosity (i.e., a high effective surface area, which means a higher surface area accessible to the electrolyte) as active materials in supercapacitors. Moreover, a greater or lesser ability to accommodate electrolyte ions on the surface of the electrode will also influence the thickness (d) of the double layer. Some studies show that the curvature of the surface (i.e., whether it is positive or negative) will influence the way in which solvated and desolvated ions of the

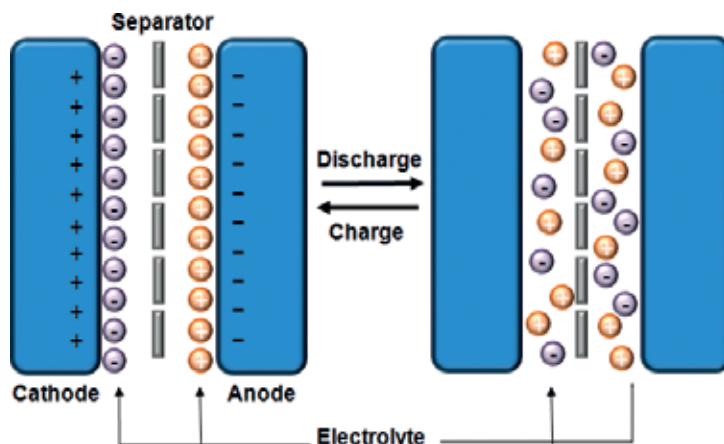


Figure 9. Mechanism of charge/discharge of an electrochemical double layer capacitor.

electrolyte are accommodated [68, 69]. In this respect, exohedral surfaces are more receptive, as it was mentioned above.

For a capacitor, two electrodes are needed, which is the equivalent to two capacitors in series. The resultant capacitance C can be expressed by the following equation Eq. (2),

$$1/C = 1/C_+ + 1/C_- \quad (2)$$

where C_+ and C_- are the capacitance of the cathode and the anode, respectively. Consequently, the difference between the capacitance values of a single electrode or complete capacitor is of great importance because if both electrodes have the same thickness, size, mass and material, the difference between both capacitances (in $F\ g^{-1}$, i.e., the most common parameter employed in the bibliography) will be a factor of four. The maximum energy stored in a supercapacitor (E) is proportional to its capacitance and is given by Eq. (3),

$$E = [C (\Delta E)^2]/2 \quad (3)$$

where ΔE is the operation voltage. The most commonly used operation voltage value is 1 V for aqueous electrolytes and around 2.7 V for organic electrolytes. Higher voltages would lead to the degradation of the components. It is clear that increasing the operation voltage is the most effective way to increase the energy density of a supercapacitor, which is why organic electrolytes are widely used in commercial devices, even though their conductivity, and their capacitance values (see Eq. (1)), are lower. However, the most common organic electrolytes (quaternary ammonium salts in polycarbonate or acetonitrile) have a number of disadvantages that can cause environmental problems; they are highly inflammable and chemically unstable, etc. In order to overcome these problems, research has been oriented toward developing organic electrolytes and ionic liquids, the latter being able to work up to 3.5 V. The wider range of electrolytes available will lead to a correspondingly wider range of porosities in the active material used, which is the topic of this chapter.

As already mentioned and in accordance with Eq. (1), the capacitance of an EDLC is proportional to the surface area of the electrode. However, this surface area is the effective surface area required for the interaction between the electrode-electrolyte, and it might not be the same as, for example, the most common specific surface area values determined by N_2 adsorption-desorption isotherms at -196°C . The presence of microporosity in the electrode is necessary, as micropores are the main contributors to the surface area of the electrode. However, the electrolyte must have access to all the microporosity. Therefore, the presence of feeder pores, i.e., mesopores, is also a determinant. Moreover, the ability to adjust the size of the mesopores to the electrolyte is important in order to favor its movement without penalizing the volumetric capacitance of the electrode. Apart from this, Gogotsi and col. [70] showed that the size of micropores also has a relevant role to play as if this is optimized, the electrolyte ions can be adsorbed in a desolvated or partially desolvated form, thereby minimizing the thickness of the double layer and increasing the capacitance of the electrode (see Eq. (1)). In summary, the ideal electrode will have a very large surface area with the size of micro- and mesopores optimized for the specific electrolyte that is going to be used in the EDLC. Carbon xerogels would appear to be the most suitable candidates for this kind of application, as their micro- and mesoporosity can be tailored to have both the required porosity and a good electrical conductivity.

Clearly, each electrolyte will have different cation and anion sizes. **Table 1** shows some recorded values for the most common electrolytes used in supercapacitors. However, it must be taken into account that these sizes refer to desolvated ions, and it is a known fact that ions move and may be adsorbed in solvated or partially solvated form. Thus, for example, the sizes of TEA^+ and BF_4^- are 0.69 and 0.46 nm, respectively, but the same ions solvated in acetonitrile double that size (i.e., 1.30 and 1.16 nm for TEA^+ and BF_4^- , respectively) [45]. Moreover, new electrolytes are continuously being developed in order to increase the operation voltage of EDLCs and these have a great influence on the maximum energy storage of the device (see Eq. (3)). For these reasons, certain materials susceptible to porosity manipulation, such as carbon xerogels, appear to be the key to future supercapacitor developments.

What is more, there is no general agreement about the optimum micro- and mesopore size, as many factors influence the final performance of the supercapacitor, such as the electrical

	Cation size (nm)	Anion size (nm)
Organic electrolytes		
$(\text{C}_2\text{H}_5)_4\text{N}\cdot\text{BF}_4$, ($\text{TEA}^+\text{BF}_4^-$)	0.69	0.46
$(\text{C}_2\text{H}_5)_3(\text{CH}_3)\text{N}\cdot\text{BF}_4$ ($\text{TEMA}^+\text{BF}_4^-$)	0.65	0.46
Aqueous electrolytes		
H_2SO_4	0.10	0.53
KOH	0.26	0.11
Ionic liquids (<i>long</i> \times <i>wide</i>)		
EMIm BF_4	0.95×0.68	0.52×0.52
EMImTFSI	0.95×0.68	1.13×0.84

Table 1. Desolvated ion sizes for different electrolytes used in supercapacitors [71, 72].

conductivity of the active material, its chemical composition, the technique used to fabricate the electrodes and even the design and engineering aspects involved in the fabrication of the device. Also important is the final application of the supercapacitor: whether it is to be used for energy or power applications or portable or stationary applications (where the volume of the device will be important), etc.

Another factor that has a considerable influence on the capacitance of the supercapacitors is the presence of heteroatoms such as O, N, P or B in the structure of the electrode materials. On the one hand, these surface groups improve the wettability of the electrodes, facilitating contact and diffusion of the aqueous electrolyte in the electrode. On the other hand, if the electrode material has too many surface groups, faradaic reactions are likely to take place (redox reactions). This phenomenon widely known as pseudocapacitance may contribute substantially to increase the total capacitance of the EDLC. However, the presence of some functional groups (e.g., oxygen functional groups) can considerably reduce the electrical conductivity of the active material to the detriment of the overall performance of the supercapacitor, especially in relation to the power supply, as shown below. Moreover, the presence of pseudocapacitance, which is a chemical process, favors the degradation of the components, shortening the life span of the supercapacitor, which is one of the features that distinguishes it from batteries.

The other main feature that distinguishes supercapacitors from batteries is that they are able to supply great power densities. The maximum power density of the supercapacitor also depends on the maximal applicable voltage, see Eq. (4), but it is inversely proportional to the equivalent series resistance (ESR) of the system. The ESR corresponds to the sum of the (i) resistance of the active material used as electrode (i.e., electronic resistance and ionic diffusion resistance), (ii) resistance of the electrolyte selected and (iii) resistance of the assembly of the supercapacitor cell (electrode/current collector contact, type of current collectors and sheet separators, etc.) [41].

$$P = (\Delta E)^2 / (4 \text{ ESR}) \quad (4)$$

Organic electrolytes and ionic liquids have another advantage over aqueous electrolytes that affects the operating voltage of the supercapacitor, namely that they result in higher power density values. In contrast, aqueous electrolytes have considerably higher electrical conductivities, i.e., several orders of magnitude higher, compared to organic and ionic liquids, besides lower viscosities that facilitate their diffusion in the porous structure and the ion movement during charge/discharge process. These characteristics may give higher capacitance values, compensating only partially the lower operating voltage used. It is clear that the properties of the active materials, in terms of porosity and electrical conductivity, will be the key to achieving a high power density, if the same electrolyte and supercapacitor cell configuration are used. Carbon materials with high electrical conductivities combined with an appropriate pore size distribution in order to facilitate ionic diffusion are essential for achieving a first-rate EDLC. Carbon xerogels are able to combine both characteristics, which is not usual in other porous carbons. They have therefore become the most sought-after active materials in supercapacitors.

The most common representation of the relation between the main characteristics of a supercapacitor (i.e., energy and power) is the Ragone plot. **Figure 10** shows the typical Ragone plot where the role of supercapacitors occupying the gap left to be filled by the conventional capacitors and batteries is highlighted. It is clear that the development of new carbon materials,

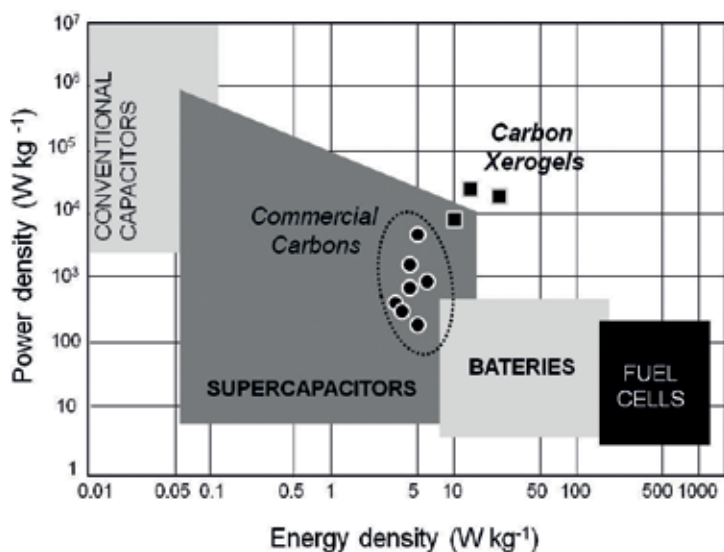


Figure 10. Ragone plot of several active materials and carbon xerogels.

with the appropriate porosity and electrical conductivity for use in supercapacitors, should be focused on the upper right zone of the plot. To this end, carbon xerogel used as an active material offers a truly unique polymeric structure with a high electrical conductivity combined with a modifiable micro- and mesoporosity and therefore optimizable supercapacitor energy and power supply. **Figure 10** shows the location on the Ragone plot of a series of commercial carbons available for the supercapacitor market for use in EDLCs with aqueous electrolyte, in addition to the performances of different carbon xerogels. The advantage of the bespoke nanoporous carbon xerogels discussed in this study is evident.

Batteries are energy storage devices whose performance is based on the conversion of chemical energy into electrical energy via reversible reactions that take place between the anode and cathode electrodes. The working principle is based on the reversible migration of ions from the cathode during the charge stage, after which they migrate through the electrolyte to intercalate into the structure of a carbon-based anode material [73–77]. **Figure 11** shows a schematic representation of a lithium-ion battery.

However, during charging, secondary reactions also take place leading to the formation of a stable passivation layer, known as the solid-electrolyte interface that entraps the ions, reducing the energy storage over time. As a consequence, the service life of batteries is limited. The formation of this layer and the diffusion of the ions through the anode material are complex mechanisms that depend largely on the chemical composition and porous properties of the active material used as anode.

Batteries provide high capacitances, i.e., they supply great energy densities, which is their most advantageous characteristic. However, the chemical process is relatively slow and so, unlike supercapacitors, the main challenge of batteries is to achieve high power densities. Different compounds can be used as electrodes: NaS, Ni-Cd, ion-Li, etc. Graphite is the most commonly used active material as anode material in lithium-ion batteries [1, 73, 78]. Nevertheless, its

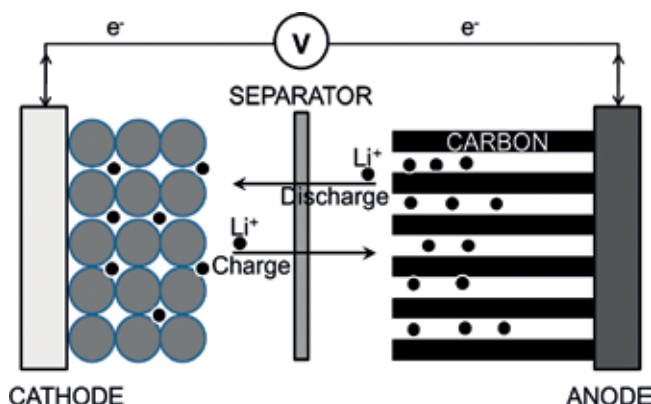


Figure 11. Scheme of the performance of a lithium-ion battery.

maximum specific capacity is limited to 372 mAhg^{-1} , corresponding to one lithium atom per six carbon atoms. Moreover, changes in volume that occur during the successive insertion-deinsertion cycles can cause cell failure when an active material such as graphite is used [1, 73, 78]. One possible remedy is to use alternative materials that combine electrical conductivity, an appropriate porous structure that permits a rapid charge-discharge and free space to accommodate variations in volume. To achieve this combination of properties is no easy task.

Carbon xerogels are porous materials whose porosity can be designed and adapted for use in ion-Li batteries as anodes, or at least to give some light on the mechanisms involved in the reactions occurring inside the carbon anode, which are still unclear [79].

7. Conclusions

Nanoporous carbon xerogels have a great potential in numerous applications since their nanoporosity can be tailored quite accurately. Mesoporosity can be predetermined during the synthesis of the organic xerogel relatively easily by controlling the proportion of each component of the solution precursor. However, the numerous variables involved, i.e., pH and type of catalyst used, degree of dilution, proportion of methanol that comes with the formaldehyde and R/F ratio, require a better knowledge of how their interrelation influences the resulting mesoporosity. The mesoporosity formed in this stage is relatively well preserved during the subsequent carbonization and/or activation processes, during which the microporosity of the carbon xerogel is formed. Depending on the carbonization or activation method selected for obtaining the carbon xerogel, the microporosity can also be tailored. The versatility of these nanoporous carbons makes them suitable for use in numerous applications. Additionally, carbon xerogels possess a good balance between porosity and electrical conductivity, two opposite properties. Thus, high surface area carbon xerogels have an electrical conductivity that is superior to other high surface area carbons. This makes carbon xerogels the ideal materials for use as electrodes in storage devices like supercapacitors where a high surface area and high conductivity are required. The potential of carbon xerogels for serving as electrode in lithium-ion batteries is also currently under investigation with promising results.

Acknowledgements

The authors gratefully acknowledge the financial support of the Ministerio de Economía y Competitividad of Spain, MINECO (Project CTQ2014-54772-P).

Author details

María Canal-Rodríguez, J. Angel Menéndez and Ana Arenillas*

*Address all correspondence to: aapunte@incar.csic.es

INCAR-CSIC, Oviedo, Spain

References

- [1] Kakunuri M, Vennamalla S, Sharma CS. Synthesis of carbon xerogel nanoparticles by inverse emulsion polymerization of resorcinol-formaldehyde and their use as anode materials for lithium-ion battery. *RSC Advances*. 2015;**5**:4747-4753. DOI: 10.1039/c4ra15171b
- [2] Xu J, Wang A, Zhang T. A two-step synthesis of ordered mesoporous resorcinol-formaldehyde polymer and carbon. *Carbon*. 2012;**50**:1807-1816. DOI: 10.1016/j.carbon.2011.12.028
- [3] Haghighi M, Yousefi AA, Mehr MJZ. Nano porous structure of resorcinol-formaldehyde xerogels and aerogels: Effect of sodium dodecylbenzene sulfonate. *Iranian Polymer Journal (English Edition)*. 2012;**21**:211-219. DOI: 10.1007/s13726-012-0023-4
- [4] Elkhatat AM, Al-Muhtaseb SA. Advances in tailoring resorcinol-formaldehyde organic and carbon gels. *Advanced Materials*. 2011;**23**:2887-2903. DOI: 10.1002/adma.201100283
- [5] Taylor SJ, Haw MD, Sefcik J, Fletcher AJ. Gelation mechanism of resorcinol-formaldehyde gels investigated by dynamic light scattering. *Langmuir*. 2014;**30**:10231-10240. DOI: 10.1021/la502394u
- [6] Al-Muhtaseb SA, Ritter JA. Preparation and properties of resorcinol-formaldehyde organic and carbon gels. *Adv Mater*. 2003;**15**:101-114. DOI: 10.1002/adma.200390020
- [7] Job N, Gommès CJ, Pirard R, Pirard JP. Effect of the counter-ion of the basification agent on the pore texture of organic and carbon xerogels. *Journal of Non-Crystalline Solids*. 2008;**354**:4698-4701. DOI: 10.1016/j.jnoncrysol.2008.06.102
- [8] Allahbakhsh A, Bahramian AR. Self-assembled and pyrolyzed carbon aerogels: An overview of their preparation mechanisms, properties and applications. *Nanoscale*. 2015;**7**:14139-14158. DOI: 10.1039/c5nr03855c
- [9] Matos I, Fernandes S, Guerreiro L, Barata S, Ramos AM, Vital J, Fonseca IM. The effect of surfactants on the porosity of carbon xerogels. *Microporous and Mesoporous Materials*. 2006;**92**:38-46. DOI: 10.1016/j.micromeso.2005.12.011

- [10] Rojas-Cervantes ML. Some strategies to lower the production cost of carbon gels. *Journal of Materials Science*. 2016;**50**:1017-1040. DOI: 10.1007/s10853-014-8617-1
- [11] Almazán-Almazán MC, López-Domingo FJ, Domingo-García M, Léonard A, Pérez-Mendoza M, Pirard JP, López-Garzón FJ, Blacher S. Influence of carbon xerogel textural properties on the dynamic adsorption of methyl iodide. *Chemical Engineering Journal*. 2011;**173**:19-28. DOI: 10.1016/j.cej.2011.07.027
- [12] Schwan M, Ratke L. Flexibilisation of resorcinol-formaldehyde aerogels. *Journal of Materials Chemistry A*. 2013;**1**:13462-13468. DOI: 10.1039/c3ta13172f
- [13] Juárez-Pérez EJ, Calvo EG, Arenillas A, Menéndez JA. Precise determination of the point of sol-gel transition in carbon gel synthesis using a microwave heating method. *Carbon*. 2010;**48**:3305-3308. DOI: 10.1016/j.carbon.2010.05.013
- [14] Moreno-Castilla C, Maldonado-Hódar FJ. Carbon aerogels for catalysis applications: An overview. *Carbon*. 2005;**43**:455-465. DOI: 10.1016/j.carbon.2004.10.022
- [15] Zubizarreta L, Arenillas A, Domínguez A, Menéndez JA, Pis JJ. Development of microporous carbon xerogels by controlling synthesis conditions. *Journal of Non-Crystalline Solids*. 2008;**354**:817-825. DOI: 10.1016/j.jnoncrysol.2007.08.015
- [16] Tian HY, Buckley CE, Paskevicius M, Wang SB. Carbon aerogels from acetic acid catalysed resorcinol-furfural using supercritical drying for hydrogen storage. *Journal of Supercritical Fluids*. 2011;**55**:1115-1117. DOI: 10.1016/j.supflu.2010.10.028
- [17] Nagy B, Czakkel O, László K. Novel synthesis route of metal doped resorcinol-formaldehyde polymer xerogels with tuned porosity. *Microporous and Mesoporous Materials*. 2014;**185**:66-71. DOI: 10.1016/j.micromeso.2013.11.004
- [18] Job N, Théry A, Pirard R, Marien J, Kocon L, Rouzaud JN, Béguin F, Pirard JP. Carbon aerogels, cryogels and xerogels: Influence of the drying method on the textural properties of porous carbon materials. *Carbon*. 2005;**43**:2481-2494. DOI: 10.1016/j.carbon.2005.04.031
- [19] Pekala RW. Organic aerogels from the polycondensation of resorcinol with formaldehyde. *Journal of Materials Science*. 1989;**24**:3221-3227. DOI: 10.1007/BF01139044
- [20] Wang F, Yao LF, Shen J, Guan DY, Fang Z. The effect of different ratio in carbon aerogel on pore structure in ambient dry. *Advanced Materials Research*. 2014:450-453
- [21] Wu PD, Zhou B, Du A, Zhang ZH, Wu GM, Shen J. Preparation of carbon aerogels at room temperature using acetonitrile as solvent. *Xinxing Tan Cailiao/New Carbon Materials*. 2012;**27**:462-468
- [22] Wu D, Fu R, Sun Z, Yu Z. Low-density organic and carbon aerogels from the sol-gel polymerization of phenol with formaldehyde. *Journal of Non-Crystalline Solids*. 2005;**351**:915-921. DOI: 10.1016/j.jnoncrysol.2005.02.008
- [23] Horikawa T, Hayashi J, Muroyama K. Controllability of pore characteristics of resorcinol-formaldehyde carbon aerogel. *Carbon*. 2004;**42**:1625-1633. DOI: 10.1016/j.carbon.2004.02.016
- [24] Araby S, Qiu A, Wang R, Zhao Z, Wang CH, Ma J. Aerogels based on carbon nanomaterials. *Journal of Materials Science*. 2016;**51**:9157-9189. DOI: 10.1007/s10853-016-0141-z

- [25] Tamon H, Ishizaka H. Influence of gelation temperature and catalysts on the mesoporous structure of resorcinol-formaldehyde aerogels. *Journal of Colloid and Interface Science*. 2000;**223**:305-307. DOI: 10.1006/jcis.1999.6640
- [26] Kocklenberg R, Mathieu B, Blacher S, Pirard R, Pirard JP, Sobry R, Van Den G. Texture control of freeze-dried resorcinol-formaldehyde gels. *Journal of Non-Crystalline Solids*. 1998;**225**:8-13
- [27] Calvo EG, Juárez-Pérez EJ, Menéndez JA, Arenillas A. Fast microwave-assisted synthesis of tailored mesoporous carbon xerogels. *Journal of Colloid and Interface Science*. 2011;**357**:541-547. DOI: 10.1016/j.jcis.2011.02.034
- [28] Job N, Panariello F, Marien J, Crine M, Pirard JP, Léonard A. Synthesis optimization of organic xerogels produced from convective air-drying of resorcinol-formaldehyde gels. *Journal of Non-Crystalline Solids*. 2006;**352**:24-34. DOI: 10.1016/j.jnoncrysol.2005.11.024
- [29] Zubizarreta L, Arenillas A, Menéndez JA, Pis JJ, Pirard JP, Job N. Microwave drying as an effective method to obtain porous carbon xerogels. *Journal of Non-Crystalline Solids*. 2008;**354**:4024-4026. DOI: 10.1016/j.jnoncrysol.2008.06.003
- [30] Job N, Pirard R, Marien J, Pirard JP. Porous carbon xerogels with texture tailored by pH control during sol-gel process. *Carbon*. 2004;**42**:619-628. DOI: 10.1016/j.carbon.2003.12.072
- [31] Job N, Sabatier F, Pirard JP, Crine M, Léonard A. Towards the production of carbon xerogel monoliths by optimizing convective drying conditions. *Carbon*. 2006;**44**:2534-2542. DOI: 10.1016/j.carbon.2006.04.031
- [32] Czakkel O, Marthi K, Geissler E, László K. Influence of drying on the morphology of resorcinol-formaldehyde-based carbon gels. *Microporous and Mesoporous Materials*. 2005;**86**:124-133. DOI: 10.1016/j.micromeso.2005.07.021
- [33] Lin C, Ritter JA. Effect of synthesis pH on the structure of carbon xerogels. *Carbon*. 1997;**35**:1271-1278. DOI: 10.1016/S0008-6223(97)00069-9
- [34] Rey-Raap N, Angel Menéndez J, Arenillas A. RF xerogels with tailored porosity over the entire nanoscale. *Microporous and Mesoporous Materials*. 2014;**195**:266-275. DOI: 10.1016/j.micromeso.2014.04.048
- [35] Feng Y, Wang J, Ge L, Jiang B, Miao L, Tanemura M. Pore size controllable preparation for low density porous nano-carbon. *Journal of Nanoscience and Nanotechnology*. 2013;**13**:7012-7015. DOI: 10.1166/jnn.2013.8063
- [36] Elkhataat AM, Al-Muhtaseb SA. Advances in tailoring resorcinol-formaldehyde organic and carbon gels. *Advanced Materials*. 2011;**23**:288-2903. DOI: 10.1002/adma.201100283
- [37] Rey-Raap N, Angel Menéndez J, Arenillas A. Simultaneous adjustment of the main chemical variables to fine-tune the porosity of carbon xerogels. *Carbon*. 2014;**78**:490-499. DOI: 10.1016/j.carbon.2014.07.030
- [38] Rey-Raap N, Menéndez JA, Arenillas A. Optimization of the process variables in the microwave-induced synthesis of carbon xerogels. *Journal of Sol-Gel Science and Technology*. 2014;**69**:488-497. DOI: 10.1007/s10971-013-3248-6

- [39] Rey-Raap N, Arenillas A, Menéndez JA. A visual validation of the combined effect of pH and dilution on the porosity of carbon xerogels. *Microporous and Mesoporous Materials*. 2016;**223**:89-93. DOI: 10.1016/j.micromeso.2015.10.044
- [40] Contreras MS, Páez CA, Zubizarreta L, Léonard A, Blacher S, Olivera-Fuentes CG, Arenillas A, Pirard J-P, Job N. A comparison of physical activation of carbon xerogels with carbon dioxide with chemical activation using hydroxides. *Carbon*. 2010;**48**:3157-3168. DOI: 10.1016/j.carbon.2010.04.054
- [41] Canal-Rodríguez M, Arenillas A, Rey-Raap N, Ramos-Fernández G, Martín-Gullón I, Menéndez JA. Graphene-doped carbon xerogel combining high electrical conductivity and surface area for optimized aqueous supercapacitors. *Carbon*. 2017;**118**:291-298. DOI: 10.1016/j.carbon.2017.03.059
- [42] Zubizarreta L, Arenillas A, Pis JJ, Pirard JP, Job N. Studying chemical activation in carbon xerogels. *Journal of Materials Science*. 2009;**44**:6583-6590. DOI: 10.1007/s10853-009-3918-5
- [43] Zhu Y, Hu H, Li W, Zhang X. Resorcinol-formaldehyde based porous carbon as an electrode material for supercapacitors. *Carbon*. 2007;**45**:160-165. DOI: 10.1016/j.carbon.2006.07.010
- [44] Alonso-Buenaposada ID, Arenillas A, Montes-Morán MA, Menéndez JA. Superhydrophobic and breathable resorcinol-formaldehyde xerogels. *Journal of Non-Crystalline Solids*. 2017. DOI: 10.1016/j.jnoncrysol.2017.05.039
- [45] François Béguin VP, Balducci A, Frackowiak E. Carbons and electrolytes for advanced supercapacitors. *Advanced Materials*. 2014;**26**:2219-2251. DOI: 10.1002/adma.201304137
- [46] Pierson HO. *Handbook of Carbon, Graphite, Diamond and Fullerenes Properties, Processing and Applications*. Park Ridge, NJ: Noyes Publications; 1993. p. 61
- [47] Chen TT, Song WL, Fan LZ. Engineering graphene aerogels with porous carbon of large surface area for flexible all-solid-state supercapacitors. *Electrochimica Acta*. 2015;**165**:92-97. DOI: 10.1016/j.electacta.2015.02.008
- [48] Guo K, Song H, Chen X, Du X, Zhong L. Graphene oxide as an anti-shrinkage additive for resorcinol-formaldehyde composite aerogels. *Physical Chemistry Chemical Physics*. 2014;**16**:11603-11608. DOI: 10.1039/C4CP00592A
- [49] Meng FC, Zhang XT, Xu B, Yue SF, Guo H, Luo YJ. Alkali-treated graphene oxide as a solid base catalyst: Synthesis and electrochemical capacitance of graphene/carbon composite aerogels. *Journal of Materials Chemistry*. 2011;**21**:18537-18539. DOI: 10.1039/c1jm13960f
- [50] Hu H, Zhao Z, Wan W, Gogotsi Y, Qiu J. Ultralight and highly compressible graphene aerogels. *Advanced Materials*. 2013;**25**:2219-2223. DOI: 10.1002/adma.201204530
- [51] Yang X, Zhang L, Zhang F, Zhang T, Huang Y, Chen Y. A high-performance all-solid-state supercapacitor with graphene-doped carbon material electrodes and a graphene oxide-doped ion gel electrolyte. *Carbon*. 2014;**72**:381-386. DOI: 10.1016/j.carbon.2014.02.029
- [52] Qian Y, Ismail IM, Stein A. Ultralight, high-surface-area, multifunctional graphene-based aerogels from self-assembly of graphene oxide and resol. *Carbon*. 2014;**68**:221-231. DOI: 10.1016/j.carbon.2013.10.082

- [53] Trefilov AMI, Tiliakos A, Serban EC, Ceaus C, Iordache SM, Voinea S, Balan A. Carbon xerogel as gas diffusion layer in PEM fuel cells. *International Journal of Hydrogen Energy*. 2017;**42**:10448-10454. DOI: 10.1016/j.ijhydene.2017.03.016
- [54] Jin H, Li J, Chen F, Gao L, Zhang H, Liu D, Liu Q. Nitrogen-doped carbon xerogels as novel cathode electrocatalysts for oxygen reduction reaction in direct borohydride fuel cells. *Electrochimica Acta*. 2016;**222**:438-445. DOI: 10.1016/j.electacta.2016.10.196
- [55] Alegre C, Sebastián D, Gálvez ME, Moliner R, Lázaro MJ. Sulfurized carbon xerogels as Pt support with enhanced activity for fuel cell applications. *Applied Catalysis B: Environmental*. 2016;**192**:260-267. DOI: 10.1016/j.apcatb.2016.03.070
- [56] Fathy NA, Attia AA, Hegazi B. Nanostructured activated carbon xerogels for removal of methomyl pesticide. *Desalination and Water Treatment*. 2016;**57**:9957-9970. DOI: 10.1080/19443994.2015.1032362
- [57] Zafra MC, Lavela P, Rasines G, Macías C, Tirado JL. Effect of the resorcinol/catalyst ratio in the capacitive performance of carbon xerogels with potential use in sodium chloride removal from saline water. *Journal of Solid State Electrochemistry*. 2014;**18**:2847-2856. DOI: 10.1007/s10008-014-2548-2
- [58] Omosebi A, Gao X, Landon J, Liu K. Asymmetric electrode configuration for enhanced membrane capacitive deionization. *ACS Applied Materials & Interfaces*. 2014;**6**:12640-12649. DOI: 10.1021/am5026209
- [59] Landon J, Gao X, Kulengowski B, Neathery JK, Liu K. Impact of pore size characteristics on the electrosorption capacity of carbon xerogel electrodes for capacitive deionization. *Journal of the Electrochemical Society*. 2012;**159**:A1861-A1866. DOI: 10.1149/2.007212jes
- [60] Gao X, Omosebi A, Landon J, Liu K. Dependence of the capacitive deionization performance on potential of zero charge shifting of carbon xerogel electrodes during long-term operation. *Journal of the Electrochemical Society*. 2014;**161**:E159-E166. DOI: 10.1149/2.0561412jes
- [61] Gao X, Landon J, Neathery JK, Liu K. Investigation of HNO₃-treated carbon xerogel electrodes for capacitive deionization applications. *ECS Transactions*. 2013;**53**:219-233
- [62] Gao X, Landon J, Neathery JK, Liu K. Modification of carbon xerogel electrodes for more efficient asymmetric capacitive deionization. *Journal of the Electrochemical Society*. 2013;**160**:E106-E112. DOI: 10.1149/2.111309jes
- [63] Li D, Zang J, Zhang J, Ao K, Wang Q, Dong Q, Wei Q. Sol-gel synthesis of carbon xerogel-ZnO composite for detection of catechol. *Materials*. 2016;**9**. DOI: 10.3390/ma9040282
- [64] Dias FS, Tartuci LG, Gorgulho HDF, MacHado WS. Characterization of a carbon xerogel-based sensor for detection of acetone, ethanol, and methanol vapors. *Sensors and Actuators B: Chemical*. 2016;**231**:440-449. DOI: 10.1016/j.snb.2016.03.054
- [65] Shukla AK, Sampath S, Vijayamohanan K. Electrochemical supercapacitors: Energy storage beyond batteries. *Current Science*. 2000;**79**:1656-1661

- [66] Simon P, Naoi K, Kim KB, Brodd RJ, Morita M, Sugimoto W, Park SG. ECS transactions—Electrochemical capacitor and hybrid power batteries 2008—214th ECS meeting: Preface. *ECS Transactions*. 2008;**16**:25-31
- [67] Naoi K, Simon P. New materials and new configurations for advanced electrochemical capacitors. *Electrochemical Society Interface*. 2008;**17**:34-37
- [68] Feng G, Qiao R, Huang J, Dai S, Sumpter BG, Meunier V. The importance of ion size and electrode curvature on electrical double layers in ionic liquids. *Physical Chemistry Chemical Physics*. 2011;**13**:1152-1161. DOI: 10.1039/c0cp02077j
- [69] Huang J, Sumpter BG, Meunier V, Yushin G, Portet C, Gogotsi Y. Curvature effects in carbon nanomaterials: Exohedral versus endohedral supercapacitors. *Journal of Materials Research*. 2010;**25**:1525-1531. DOI: 10.1557/jmr.2010.0195
- [70] Chmiola J, Yushin G, Gogotsi Y, Portet C, Simon P, Taberna PL. Anomalous increase in carbon at pore sizes less than 1 nanometer. *Science*. 2006;**313**:1760-1763. DOI: 10.1126/science.1132195
- [71] Inagaki M, Konno H, Tanaike O. Carbon materials for electrochemical capacitors. *Journal of Power Sources*. 2010;**195**:7880-7903. DOI: 10.1016/j.jpowsour.2010.06.036
- [72] Sillars FB, Fletcher SI, Mirzaeian M, Hall PJ. Variation of electrochemical capacitor performance with room temperature ionic liquid electrolyte viscosity and ion size. *Physical Chemistry Chemical Physics*. 2012;**14**:6094-6100. DOI: 10.1039/c2cp40089h
- [73] Roberts AD, Li X, Zhang H. Porous carbon spheres and monoliths: Morphology control, pore size tuning and their applications as li-ion battery anode materials. *Chemical Society Reviews*. 2014;**43**:4341-4356. DOI: 10.1039/c4cs00071d
- [74] Miranda D, Costa CM, Lanceros-Mendez S. Lithium ion rechargeable batteries: State of the art and future needs of microscopic theoretical models and simulations. *Journal of Electroanalytical Chemistry*. 2015;**739**:97-110. DOI: 10.1016/j.jelechem.2014.12.010
- [75] Wang KX, Li XH, Chen JS. Surface and interface engineering of electrode materials for lithium-ion batteries. *Advanced Materials*. 2015;**27**:527-545. DOI: 10.1002/adma.201402962
- [76] Hu M, Pang X, Zhou Z. Review: Recent progress in high-voltage lithium ion batteries. *Journal of Power Sources*. 2013;**237**:229-242. DOI: 10.1016/j.jpowsour.2013.03.024
- [77] Scrosati B, Garche J. Lithium batteries: Status, prospects and future. *Journal of Power Sources*. 2010;**195**:2419-2430. DOI: 10.1016/j.jpowsour.2009.11.048
- [78] Lee KT, Lytle JC, Ergang NS, Oh SM, Stein A. Synthesis and rate performance of monolithic macroporous carbon electrodes for lithium-ion secondary batteries. *Advanced Functional Materials*. 2005;**15**:547-556. DOI: 10.1002/adfm.200400186
- [79] Rey-Raap N, Piedboeuf MLC, Arenillas A, Menéndez JA, Léonard AF, Job N. Aqueous and organic inks of carbon xerogels as models for studying the role of porosity in lithium-ion battery electrodes. *Materials and Design*. 2016;**109**:282-288. DOI: 10.1016/j.matdes.2016.07.007

Porosity Controlling and Measurement

Controlled Porosity in Thermochromic Coatings

Ning Wang, Yujie Ke and Yi Long

Additional information is available at the end of the chapter

<http://dx.doi.org/10.5772/intechopen.70890>

Abstract

Vanadium dioxide is a promising thermochromic material, seemed as the great candidate for smart window applications. The real application of VO₂ requires high visible transmission (T_{lum}) as well as large solar modulating abilities (ΔT_{sol}), which could not be achieved by pristine VO₂ materials due to the trade-off between T_{lum} and ΔT_{sol} . Here in, the porosity design is thoroughly reviewed from the effect on modulating the thermochromic performance to the porous control and preparation. To begin with, the history, advantages, challenges and approaches to tackle the issues comprised of anti-reflection multilayer structure, nanothermochromism, patterning and porous design is introduced in detail. Then, the effect of porosity on improving the thermochromic performance of VO₂ thin films is demonstrated using the newest experimental and simulation results. In the following, the porous control and structural synthesis, including the polymer-assisted deposition (PAD), freeze-drying, colloidal lithography as well as the dual phase transformation is summarized. Fourthly, the characterization methods, composed of scanning electron microscopy (SEM), transmission electron microscopy (TEM), atomic force microscopy (AFM), X-ray diffraction (XRD), Raman spectroscopy as well as UV-Vis-NIR spectroscopy are demonstrated. Finally, the challenges that the porous design faces and possible approaches to optimize the performance are presented.

Keywords: porosity, vanadium dioxide, thermochromism, smart window, energy saving

1. Introduction

In recent decades, the usage of traditional energy materials, including the oil and the coal meets more and more challenges due to the increase of air pollution, energy shortage and the global warming. Therefore, the concepts of sustainable and environment-friendly production were raised by scientists for energy-saving, and various clean energy technologies have been proposed for industries, for example, fuel cell [1–4], solar cell [5–7] and wind turbines [8–11].

On the other hand, the alternative energy-saving approach is to develop green-energy buildings equipped with state-of-the-art smart windows, for example, electrochromic/thermochromic smart windows [12–17].

Vanadium dioxide (VO_2), as a promising coating material for thermochromic smart windows have been investigated for half a century, since Morin found the intrinsic metal-to-insulator transition (MIT) of VO_2 in 1959 [18]. Below a critical temperature (τ_c) $\sim 68^\circ\text{C}$, VO_2 shows the monoclinic insulating phase ($\text{VO}_2(\text{M})$) with zig-zag V-V chains along the c -axis ($P2_1/c$, V-V separation is 0.262, 0.316 nm) [19]. Above the τ_c , VO_2 is transformed to rutile metallic phase ($\text{VO}_2(\text{R})$) with linear V-V chains along the c -axis ($P4_2/mnm$, V-V separation is 0.288 nm) [19]. The increase of the electrical resistance across the MIT is always in 3–5 orders of magnitude, and the first-order transition could occur simultaneously with the time less than 500 fs [20]. Along with the MIT, the IR transmittance of VO_2 could also be modulated by a large magnitude owing to the change of the optical parameters (refractive 'n' and extinction coefficient 'k') [21]. As a coating material, VO_2 shows the high IR transmittance at the cold state while exhibits the large absorption as well as the strong reflection at the hot state, which gives rise to large IR modulating ability [22–25]. Due to the little difference of optical parameters in the visible region, VO_2 shows the little transmittance difference in the visible region [26–28]. The solar modulating ability especially in the IR region makes VO_2 a promising coating material for thermochromic smart windows.

The VO_2 thermochromic smart windows have various advantages in energy saving. To begin with, the phase transition temperature (τ_c) of VO_2 is close to the room temperature, which cannot be found in other phase transition materials ($\tau_c(\text{V}_2\text{O}_3) = -123^\circ\text{C}$, $\tau_c(\text{V}_2\text{O}_5) = 257^\circ\text{C}$, $\tau_c(\text{V}_6\text{O}_{13}) = -123^\circ\text{C}$, $\tau_c(\text{Ti}_n\text{O}_{2n+1}) = 127\text{--}377^\circ\text{C}$) [27]. Secondly, the τ_c of VO_2 could be further reduced to ambient temperature through doping with other high valence metal cations, for example, W^{6+} [22, 29–33], Mo^{6+} [34–36]. Finally, several synthetic methods, for example, atmospheric pressure CVD [36–40], magnetron sputtering [41–45], sol-gel [35, 46, 47] and hydrothermal assembly [48–50], have been developed to fabricate VO_2 nanostructures for applications. However, for thermochromic applications, VO_2 still meets several challenges. Firstly, it is hard to achieve the high visible transmittance (T_{lum}) and the large solar modulating abilities (ΔT_{sol}) simultaneously, since there is always a tradeoff between the T_{lum} and ΔT_{sol} [51]. Secondly, the thermochromic property is hard to maintain when reducing the τ_c to room temperatures via doping [31]. Finally, the VO_2 coating is not stable in the air [52].

In order to improve the thermochromic performance of VO_2 coating, several interesting strategies, including nanoporosity, nanothermochromism, patterning as well as multilayer structures have been investigated by the scientists. Gao's group reported the enhanced luminous transmittance ($T_{\text{lum}} = \sim 40\%$) and improved thermochromic properties ($\Delta T_{\text{sol}} = \sim 14\%$) of nanoporous VO_2 thin films with low optical constants, and the optical calculations suggested that the further improved performance could be expected by increasing the thin film porosity [53]. Li et al. [54] calculated the nanothermochromics of VO_2 nanocomposite by dispersing VO_2 nanoparticles in the dielectric host, which revealed that the thermochromic performance could be largely enhanced ($T_{\text{lum}} = \sim 65\%$, $\Delta T_{\text{sol}} = \sim 20\%$) with spherical morphologies of the VO_2

nanoparticles in the nanocomposite. Long's group investigated the micropatterning [55] and nanopatterning [51] of VO_2 thin films, which both benefited the VO_2 thin films with improved T_{lum} and ΔT_{sol} . Mlyuka et al. reported the five-layer $\text{TiO}_2/\text{VO}_2/\text{TiO}_2/\text{VO}_2/\text{TiO}_2$ structure, which showed the high T_{lum} (~43%) and the large ΔT_{sol} (~12%). Across the strategies, the nanoporous design showed the advantages in easy-to-handling, low usage of VO_2 materials as well as the thickness control.

2. Enhanced thermochromic properties of VO_2 with porous structure

As is well known, the porous structure could effectively increase the specific area of materials and thus supply large active areas under low loading. On the other hand, the porous design could also reduce the optical constants (refractive index 'n' and the extinction coefficient 'k'), which could benefit the materials with enhanced visible transmittance. The optical calculations of nanoporous VO_2 thin films could be performed with an optical-admittance recursive method, based on the assumption that the optical constants should be linearly dependent on the volume fraction or the 'n' and 'k' is linearly decreased with the porosity. As shown in **Figure 1**, as for the random distributed nanoporous VO_2 thin films (**Figure 1a**), the porous structure gave rise to an obvious decrease of optical constants (n, k) compared with the normal thin film, and the optical calculations revealed the largely enhanced T_{lum} and ΔT_{sol} with increasing the porosity of the thin films.

With respect to the porous structure of VO_2 thin films, there are normally the random distributed and the periodic porous structures. In the random case, as reported by Gao's group [53] and Long's group [57], the thermochromic properties could be enhanced to $T_{\text{lum}} > 40\%$ and $\Delta T_{\text{sol}} > 14\%$. In contrast, for the periodic porous structure, as reported by Xie's group [58] and further developed by Long's group [59, 60], the visible transmittance could be above 46% while maintaining the ΔT_{sol} above 13%. Actually, the periodic nanoporous design is more

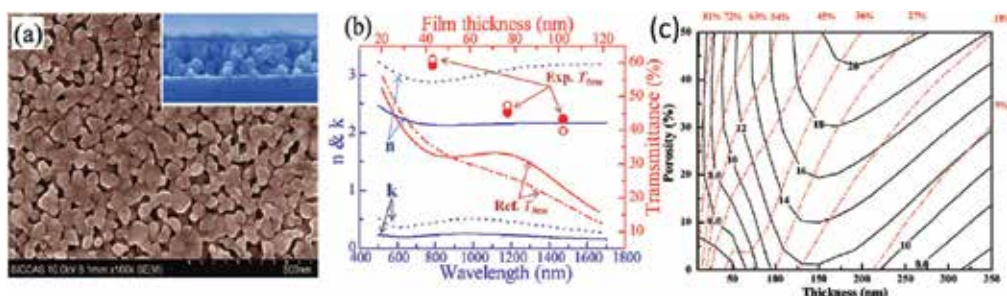


Figure 1. (a) Nanoporous VO_2 thin film. (b) Experimental (solid) and reference (dash) n, k (versus wavelength) and experimental/reference T_{lum} (versus film thickness). Reference data is from Jin et al. [56]. (c) Optical calculations of the nanoporous VO_2 thin films based on an optical-admittance recursive method, where dotted lines and solid lines represent the T_{lum} at insulating state and the ΔT_{sol} , respectively [53].

efficient in controlling the porosity and optimizing the thermochromic properties than the random counterpart, since the porosity could be easily estimated from the structure design.

3. Porous control and synthetic methods

In the nanoporous design for thermochromic VO_2 thin films, there are mainly four different approaches to synthesize and control the porosity, including the polymer assistant deposition (PAD) [53], freeze-drying preparation [57], colloidal lithography assembly [58] as well as the dual-phase transformation [61].

To begin with the PAD, it is a powerful technique to get the continuous nanoporous VO_2 thin films. The polymer used in the PAD process could be cetyltrimethyl ammonium bromide (CTAB) [62], cetyltrimethylammonium vanadate (CTAV) [63], polyvinylpyrrolidone (PVP) [53, 64, 65] or polyethylenimine (PEI) [66, 67]. Take CTAB as an example, when the vanadium precursor was modified by the amphiphilic polymer, the nuclear could be effectively isolated and the nanopores could be formed during the annealing process (**Figure 2**) [62]. It should be noted that the control of the polymer addition is critical to optimize the shape and size of the nanopores.

Freeze-drying is also an efficient way to prepare the nanoporous VO_2 thin films. For a normal sol-gel process, it is hard to get a film with high porosity. When the precursor is frozen and then dried in vacuum, the solvents could sublime and be removed quickly from the structure, which therefore gives rise to the in-situ formation of nanoporous structure (**Figure 3d**). In a typical process for fabricating nanoporous VO_2 thin films with freeze-drying, the V_2O_5 - H_2O_2 -ox (oxalic acid) precursor was firstly dip coated onto fused silica substrates for gelation, and then a pre-freezing process was performed with a following freeze-drying at -80°C and 0.01 mbar [57]. After a post-annealing process under Ar atmosphere at 550°C for 2 h, the nanoporous VO_2 thin films were subsequently obtained (**Figure 3a–c**).

Colloidal lithography assembly is an alternative approach to get the nanoporous VO_2 thin films, especially for the periodic porous design. The close packed monolayer colloidal crystal (MCC) template has been the usual sacrificing template for colloidal lithography assembly, which make it a facile way to prepare the periodic nanoporous structure. In a typical colloidal lithography assembly for nanoporous VO_2 thin films, the polystyrene (PS) MCC template was firstly infiltrated by VOSO_4 solution, then the infiltration with NH_4HCO_3 solution as precipitator was performed to confirm the coating of vanadium source on the template. Finally, the template was picked up by a clean substrate, and then the periodic nanoporous VO_2 thin films were attained though annealing in nitrogen gas [58]. The nanoporous structure could be further modulated by changing the layer number and/or the concentration of the precursor, which could help to optimize the thermochromic properties of the thin films.

More systematically, colloidal lithography was explored to prepare the two-dimensional patterned VO_2 films with tunable periodicity and diverse nanostructures including nanoparticle, nanonet and nanodome arrays [59]. The fabrication process is more flexible via introducing of the plasma etching (PE) technology and controlling the precursor viscosity. They concluded

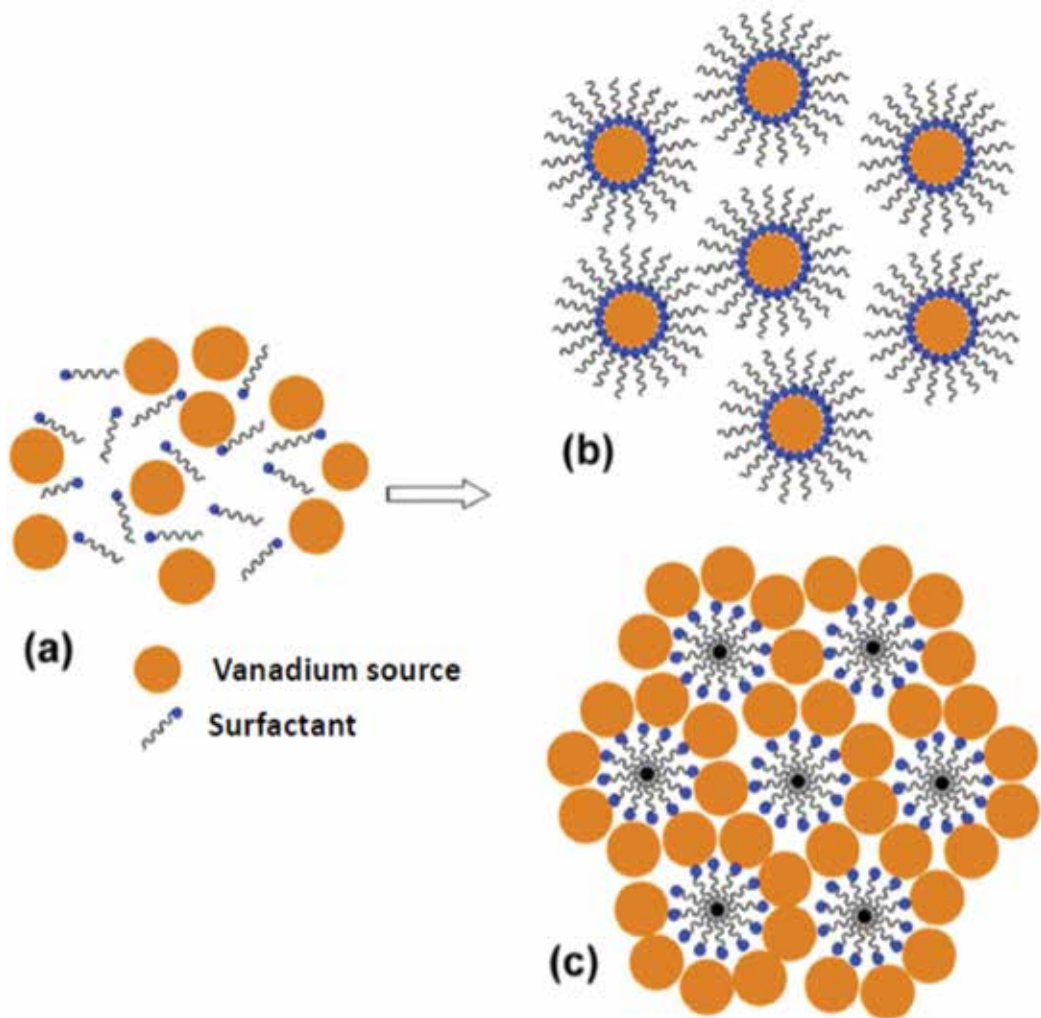


Figure 2. Modification of vanadium precursor by the CTAB. (a) Initial step for adding the CTAB into the vanadium precursor. (b) and (c) Two forms of separation for the nuclear functionalized by the CTAB after strong stirring [62].

the synthesis routes in **Figure 4**. When short PE duration applied, nanoparticle and nanodome arrays are produced using low (Route 1) and high (Route 2) viscosity precursors, respectively. Nanonet arrays are fabricated via prolonging PE duration and using low viscosity precursor (Route 3). Produced two-dimensional patterned VO_2 arrays are highly uniform (**Figure 5**). For the first time, hexagonally patterned VO_2 nanoparticle array with the average diameter down to 60 nm and the periodicity of 160 nm has been fabricated (**Figure 5a**). It is of great interest that such structure gives rise to tunable peak position and intensity of the localized surface plasmon resonance (LSPR) at different temperature. The LSPR was also found a red-shift with increase of the particle size and the media reflective index, respectively, and these results fit well with the tendency calculated using 3D finite-difference time-domain (FDTD). Besides decent thermochemical performance (up to $\Delta T_{\text{sol}} = 13.2\%$ and $T_{\text{lum}} = 46\%$) achieved,

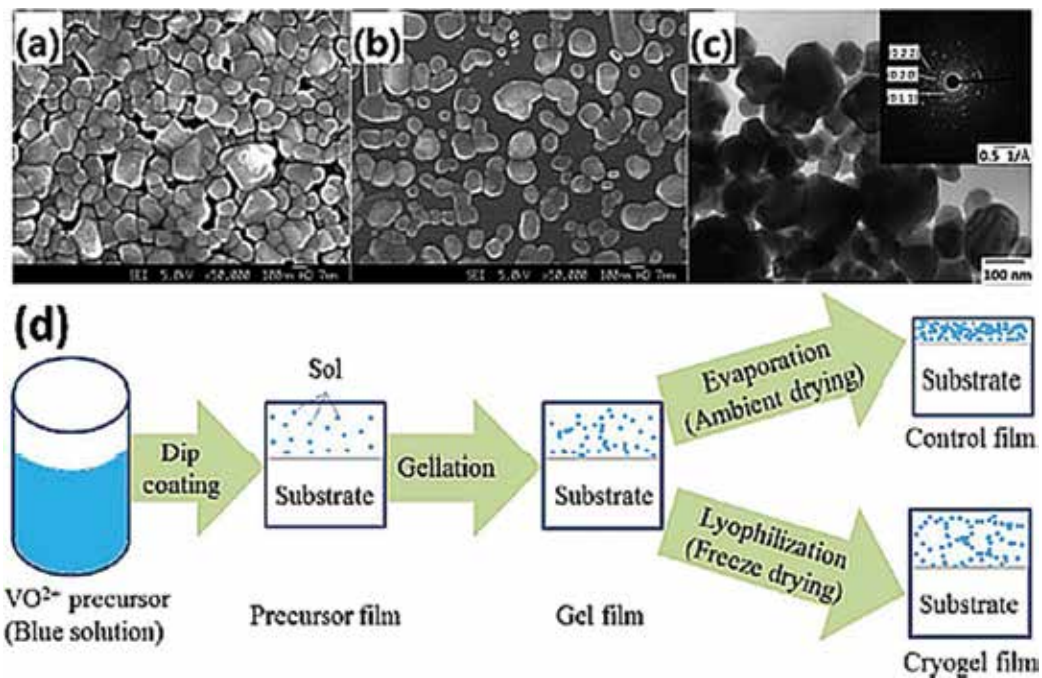


Figure 3. Field-emission scanning electron microscopy (FESEM) image for the freeze-dried nanoporous VO_2 films with 7.5 mL of H_2O_2 (a) and 17.5 mL of H_2O_2 (b) in the precursor. (c) TEM image of (b) and the corresponding SAED (inset). (d) Schematic illustration of the freeze-drying process for the nanoporous design [57].

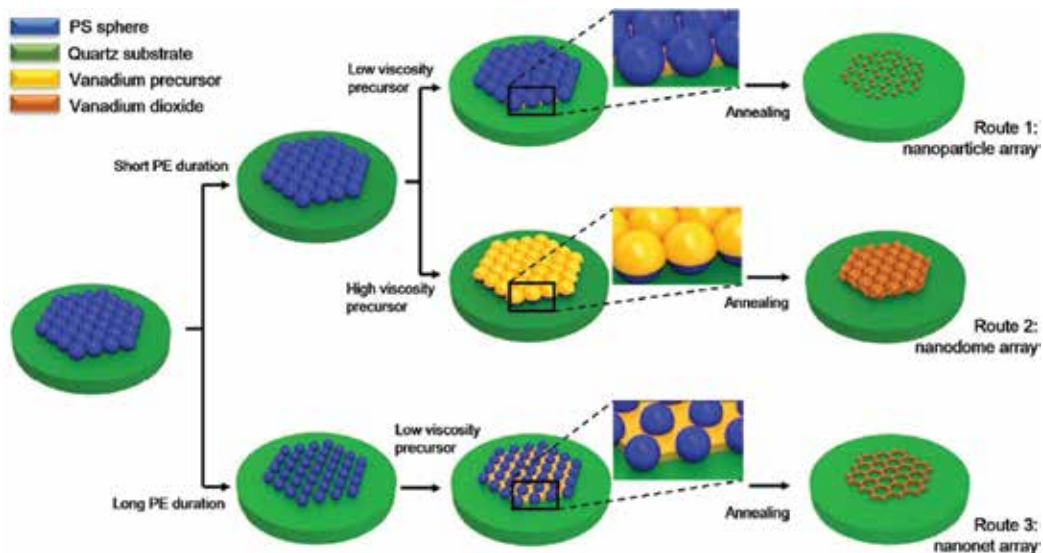


Figure 4. Effect of synthesis conditions on the morphology evolution. Route 1: nanoparticle arrays are prepared via short PE duration and low viscosity precursor; Route 2: nanodome arrays are produced, using high viscosity precursor that can stick on the tops of PS spheres; Route 3, nanonets are fabricated by controlling the interval space between adjacent spheres via long PE duration [59].

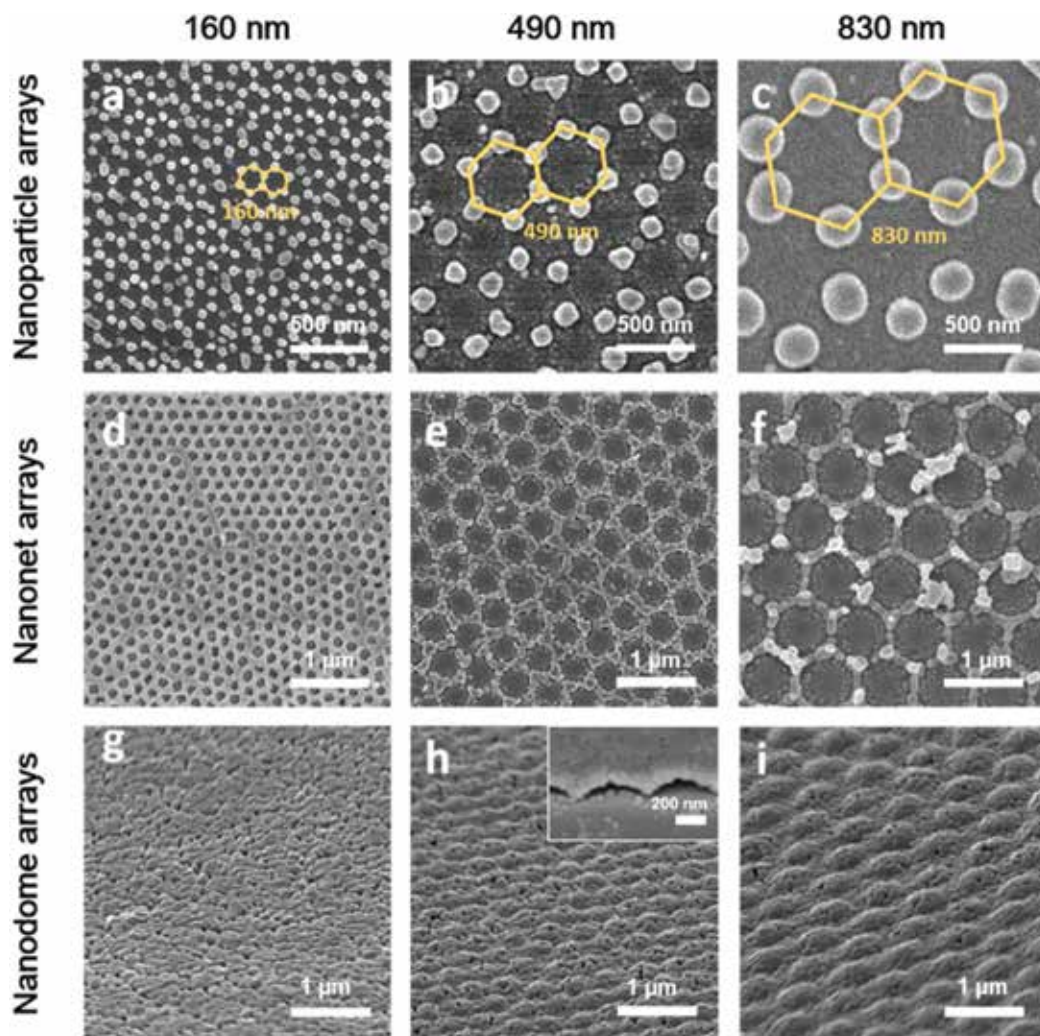


Figure 5. FESEM images of periodic VO_2 films. (a–c) Nanoparticle, (d–f) nanonet, and (g–i) tilted-views of nanodome arrays with periodicity of 160, 490 and 830 nm from left to right, respectively. The insert of (h) is high magnitude tilted-view image of 490 nm periodic nanodome on edge. Yellow hexagons in (a–c) are illustrations for hexagons patterning [59].

the 2D patterned VO_2 films have been demonstrated as an efficient smart thermal radiation filter to remote control the lower critical solution temperature (LCST) behavior of poly N-isopropylacrylamine (PNIPAm) hydrogel. Comparing with template-free method, periodic films produced by nanosphere lithography technique offer more uniform periodicity (less periodic defect) as well as smaller individual nanostructure that is able down to sub-100 nm.

An interesting study using colloidal lithography was to develop photonic structures, consisted of two-dimensional SiO_2 - VO_2 core-shell monolayer (**Figure 6a** and **b**) [60]. The structures with periodicity in visible range are demonstrated with the ability to modulate the visible transmittance by selectively reflecting the light with certain color (**Figure 6c**). Benefiting from

this ability, smart windows based on such structures display controllable appearances as well as good thermochromic performance, which is up to $T_{lum} = 49.6\%$ and $\Delta T_{sol} = 11.0\%$ calculated by 3D FDTD. This statically visible and dynamically near-infrared modulation is further proved by experiments. However, the optimized thermochromic performance is much lower than that in simulation, which is attributed to the sol-gel method where the perfect core-shell structure cannot be produced in experiment as in simulation. Thus, other more controllable methods, such as physical vapor deposition or chemical vapor deposition, could be proposed as a better way for the fabrication of such two-dimensional core-shell structures.

The dual-phase transformation is a newly developed template-free method to prepare the nanoporous VO_2 thin films with ultrahigh visible transmittance. As depicted in **Figure 7**, this method is based on the transformation between the colloids and ionic states stimulated by the moisture. Firstly, the precursor ($VOCl_2 + HCl + H_2O + N_2H_4$) was spin coated onto fused silica substrates, and then the hydrous colloids were formed through water evaporation. After a quick annealing at $300^\circ C$ to solidify the film, and an additional annealing at

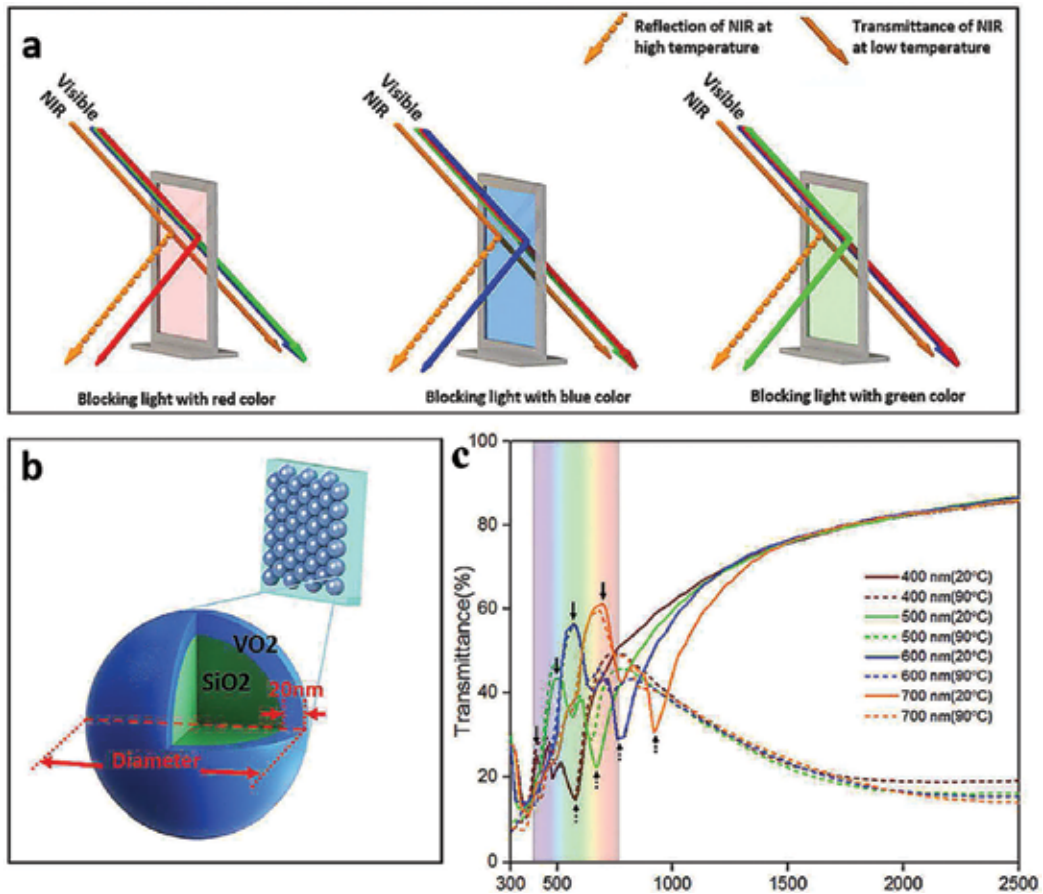


Figure 6. (a) Illustration of how color-changed thermochromic smart window works. (b) Illustration of designed structures for simulation. (c) Calculated transmittance spectrum. The colorful background in (c) denotes the visible spectrum from 370 to 770 nm [60].

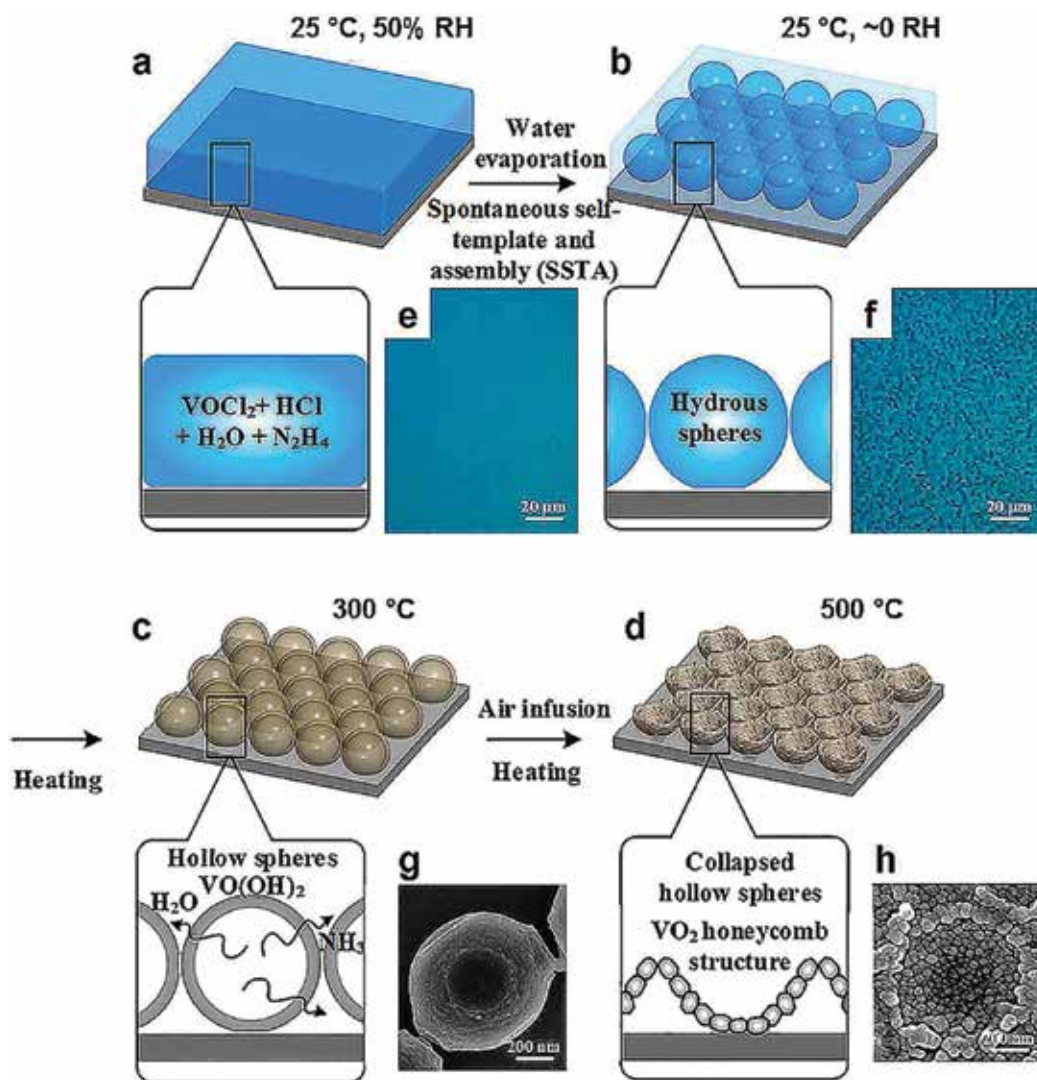


Figure 7. Formation of nanoporous VO_2 thin films through dual phase transformation [61]. (a) Homogeneous, fully solution-based precursor film was deposited at room condition (25 °C, 50% RH). (b) Precursor was spontaneously self-templated and assembled (SSTA) into hydrous sphere arrays after water evaporation in dry nitrogen (25 °C, ~0 RH). (c) Hydrous spheres became hollow $\text{VO}(\text{OH})_2$ spheres after instant heating to 300 °C and (d) finally collapsed to honeycomb structures after being heated at a rate of 2 °C and maintained at 500 °C for 1 h. Microscopic photos of (e) the precursor film and (f) the film after SSTA process. SEM images of (g) captured hollow $\text{VO}(\text{OH})_2$ spheres and (h) final honeycomb structures.

500 °C in N_2 , the honeycomb-like nanoporous VO_2 structures were finally obtained with high visible transmittance ($\sim 700 \text{ nm}$) above 90% as well as a decent solar modulating ability ($\Delta T_{\text{sol}} = \sim 5.5\%$). The critical factor for forming the initial hydrous spheres (colloids) is the ratio control between the HCl and the N_2H_4 [61].

Apart from the above methods, the approaches including, but not limited to the chemical etching [68] and reactive ion etching [69] could also be utilized to produce the VO_2 nanoporous thin films.

4. Characterization

In order to fully characterize the structure and the thermochromic properties of VO₂ nanoporous thin films, the advanced techniques including scanning electron microscopy (SEM), transmission electron microscopy (TEM), atomic force microscopy (AFM), X-ray diffraction (XRD), Raman spectroscopy as well as UV-Vis-NIR spectroscopy could be utilized in the investigation.

With respect to the nanoporous morphology, SEM is a powerful technique to observe the size, shape and the distributions of the nanopores on the surface in a large scale vision, while the details within the pore could be determined using the TEM in a cross-section view. Due to the non-destructive advantage, AFM is also an efficient way to scan the pore distribution on the surface although some artifacts always appear in the AFM images.

Regarding to the thermochromic properties, the VO₂ phase could be firstly confirmed though the XRD and Raman scan, and then the solar modulation ability could be determined with temperature dependent UV-Vis-NIR characterization. As for the XRD, VO₂ (M, P2₁/c) will show the crystalline planes (011)/(-211)/(220)/(022)/(202) at the 2θ positions 28°/37°/55.5°/57.5°/65°, while the VO₂ (R, P4₂/mnm) will show the crystalline planes (110)/(101)/(211)/(220)/(002) at the 2θ positions 28°/37°/55.5°/57.5°/65° [22, 70]. For the Raman scan [58, 71], the VO₂ (M) phase will show the A_g peaks at the Raman shift positions 192/222/302/392/611 cm⁻¹ and the B_g peak at 258 cm⁻¹. In the measurement of thermochromic performance, the transmittance of the normal incidence is recorded at the wavelength range 250–2500 nm at the temperature below and above the τ_c and the integrated luminous transmission (T_{lum} , 380 nm < λ < 780 nm) and the integrated solar modulating abilities (ΔT_{sol} , 250 nm < λ < 2500 nm) could be calculated from the expression

$$T_{lum/sol} = \int \phi_{lum/sol}(\lambda) T(\lambda) d\lambda / \int \phi_{lum/sol}(\lambda) d\lambda \quad (1)$$

where ϕ_{lum} is the standard luminous efficiency function for the photopic vision of human eyes [72], and the ϕ_{sol} is the solar irradiance spectrum for air mass 1.5 (corresponding to the sun standing 37° above the horizon) [73]. ΔT_{sol} is calculated from $T_{sol}(\tau < \tau_c) - T_{sol}(\tau > \tau_c)$.

5. Concluding remarks and outlook

In this chapter, we have elaborated the fabrication of nanoporous VO₂ nanomaterials and the effect of porosity on enhancing the thermochromic properties. Compared with the other property enhancement methods, such as ARC multilayers, biomimetic patterning, nanothermochromism and periodic patterning (**Figure 8**), the porous design shows the advantages in easy-to-handling, low usage of VO₂ materials as well as the thickness control, which could reduce the cost in the real applications. In the fabrication of nanoporous VO₂ thin films, the PAD, freeze-drying as well as the dual-phase transformation are the three main methods for random nanoporous structures, while the colloidal lithography

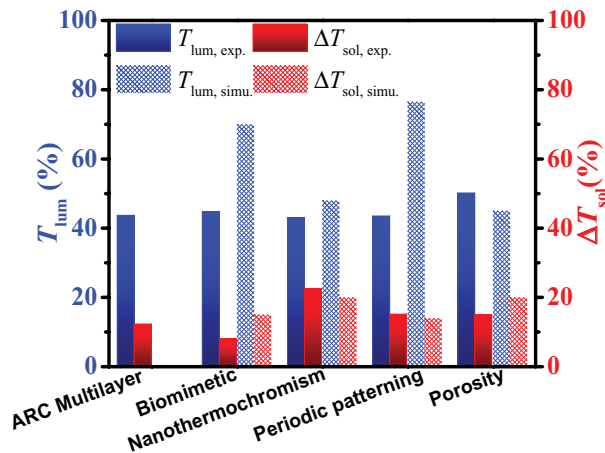


Figure 8. Methods proposed for enhancing the thermochromic performance of VO_2 nanomaterials [55].

with the MCC template is an effective approach for periodic nanoporous structures. The calculations reveal that the nanoporous structure could result in the decrease of optical constants and thus lead to the enhancement of visible transmission while maintain the decent solar modulating abilities.

Although many efforts have been dedicated to optimize the effect of nanoporous structure on enhancing the thermochromic performance of VO_2 thin films, the low visible transmission (<~80%) and the low solar modulating ability (<~30%) restrict the real applications in thermo-chromic smart windows. From the viewpoint of materials design, the periodic nanoporous VO_2 thin films with the periodicity below 100 nm should give rise to the largely enhanced visible transmission as well as the highly reduced scattering, which could greatly improve the thermo-chromic performance for smart window applications.

Acknowledgements

This research is supported by National Research Foundation, Prime Minister's Office, Singapore under its Campus for Research Excellence and Technological Enterprise (CREATE) programme.

Author details

Ning Wang, Yujie Ke and Yi Long*

*Address all correspondence to: longyi@ntu.edu.sg

School of Materials Science and Engineering, Nanyang Technological University, Singapore

References

- [1] Das V, Padmanaban S, Venkitusamy K, Selvamuthukumaran R, Blaabjerg F, Siano P. Recent advances and challenges of fuel cell based power system architectures and control—A review. *Renewable and Sustainable Energy Reviews*. 2017;**73**:10-18. DOI: 10.1016/j.rser.2017.01.148
- [2] Siebel A, Gorlin Y, Durst J, Proux O, Hasché F, Tromp M, et al. Identification of catalyst structure during the hydrogen oxidation reaction in an operating PEM fuel cell. *ACS Catalysis*. 2016;**6**(11):7326-7334. DOI: 10.1021/acscatal.6b02157
- [3] Macauley N, Watson M, Lauritzen M, Knights S, Wang GG, Kjeang E. Empirical membrane lifetime model for heavy duty fuel cell systems. *Journal of Power Sources*. 2016;**336**:240-250. DOI: 10.1016/j.jpowsour.2016.10.068
- [4] Inukai M, Horike S, Itakura T, Shinozaki R, Ogiwara N, Umeyama D, et al. Encapsulating mobile proton carriers into structural defects in coordination polymer crystals: High anhydrous proton conduction and fuel cell application. *Journal of the American Chemical Society*. 2016;**138**(27):8505-8511. DOI: 10.1021/jacs.6b03625
- [5] Lan X, Voznyy O, Kiani A, García de Arquer FP, Abbas AS, Kim G-H, et al. Passivation using molecular halides increases quantum dot solar cell performance. *Advanced Materials*. 2016;**28**(2):299-304. DOI: 10.1002/adma.201503657
- [6] dos Reis Benatto GA, Roth B, Corazza M, Sondergaard RR, Gevorgyan SA, Jorgensen M, et al. Roll-to-roll printed silver nanowires for increased stability of flexible ITO-free organic solar cell modules. *Nanoscale*. 2016;**8**(1):318-326. DOI: 10.1039/c5nr07426f
- [7] Bi D, Xu B, Gao P, Sun L, Grätzel M, Hagfeldt A. Facile synthesized organic hole transporting material for perovskite solar cell with efficiency of 19.8%. *Nano Energy*. 2016;**23**:138-144. DOI: 10.1016/j.nanoen.2016.03.020
- [8] Song D, Yang J, Dong M, Joo YH. Model predictive control with finite control set for variable-speed wind turbines. *Energy*. 2017;**126**:564-572. DOI: 10.1016/j.energy.2017.02.149
- [9] Pahn T, Rolfes R, Jonkman J. Inverse load calculation procedure for offshore wind turbines and application to a 5-MW wind turbine support structure. *Wind Energy*. 2017;**20**(7):1171-1186. DOI: 10.1002/we.2088
- [10] Tummala A, Velamati RK, Sinha DK, Indraj V, Krishna VH. A review on small scale wind turbines. *Renewable and Sustainable Energy Reviews*. 2016;**56**:1351-1371. DOI: 10.1016/j.rser.2015.12.027
- [11] Shen X, Avital E, Paul G, Rezaenia MA, Wen P, Korakianitis T. Experimental study of surface curvature effects on aerodynamic performance of a low Reynolds number airfoil for use in small wind turbines. *Journal of Renewable and Sustainable Energy*. 2016;**8**(5):053303. DOI: 10.1063/1.4963236

- [12] Zhang P, Zhu F, Wang F, Wang J, Dong R, Zhuang X, et al. Stimulus-responsive micro-supercapacitors with ultrahigh energy density and reversible electrochromic window. *Advanced Materials*. 2017;**29**(7):1604491. DOI: 10.1002/adma.201604491
- [13] Zhou Y, Layani M, Boey FYC, Sokolov I, Magdassi S, Long Y. Electro-thermo-chromic devices composed of self-assembled transparent electrodes and hydrogels. *Advanced Materials Technologies*. 2016;**1**(5):1600069. DOI: 10.1002/admt.201600069
- [14] Nakano M, Shibuya K, Ogawa N, Hatano T, Kawasaki M, Iwasa Y, et al. Infrared-sensitive electrochromic device based on VO₂. *Applied Physics Letters*. 2013;**103**(15):153503. DOI: <http://dx.doi.org/10.1063/1.4824621>
- [15] Yang XH, Zhu G, Wang SH, Zhang R, Lin L, Wu WZ, et al. A self-powered electrochromic device driven by a nanogenerator. *Energy & Environmental Science*. 2012;**5**(11):9462-9466. DOI: 10.1039/c2ee23194h
- [16] Granqvist CG, Lansaker PC, Mlyuka NR, Niklasson GA, Avendano E. Progress in chromogenics: New results for electrochromic and thermo-chromic materials and devices. *Solar Energy Materials & Solar Cells*. 2009;**93**(12):2032-2039. DOI: 10.1016/j.solmat.2009.02.026
- [17] Minkin VI. Photo-, thermo-, solvato-, and electrochromic spiroheterocyclic compounds. *Chemical Reviews*. 2004;**104**:2751-2776. DOI: 10.1021/cr020088u
- [18] Morin F. Oxides which show a metal-to-insulator transition at the Neel temperature. *Physical Review Letters*. 1959;**3**(1):34-36. DOI: 10.1103/PhysRevLett.3.34
- [19] Wu C, Feng F, Xie Y. Design of vanadium oxide structures with controllable electrical properties for energy applications. *Chemical Society Reviews*. 2013;**42**(12):5157-5183. DOI: 10.1039/c3cs35508j
- [20] Petrov GI, Yakovlev VV, Squier JA. Nonlinear optical microscopy analysis of ultrafast phase transformation in vanadium dioxide. *Optics Letters*. 2002;**27**(8):655-657. DOI: 10.1364/OL.27.000655
- [21] Wang N, Goh QS, Lee PL, Magdassi S, Long Y. One-step hydrothermal synthesis of rare earth/W-codoped VO₂ nanoparticles: Reduced phase transition temperature and improved thermo-chromic properties. *Journal of Alloys and Compounds*. 2017;**711**:222-228. DOI: 10.1016/j.jallcom.2017.04.012
- [22] Wang N, Duchamp M, Xue C, Dunin-Borkowski RE, Liu G, Long Y. Single-crystalline W-doped VO₂ nanobeams with highly reversible electrical and plasmonic responses near room temperature. *Advanced Materials Interfaces*. 2016;**3**(15):1600164. DOI: 10.1002/admi.201600164
- [23] Wang N, Duchamp M, Dunin-Borkowski RE, Liu S, Zeng X, Cao X, et al. Terbium-doped VO₂ thin films: Reduced phase transition temperature and largely enhanced luminous transmittance. *Langmuir*. 2016;**32**(3):759-764. DOI: 10.1021/acs.langmuir.5b04212

- [24] Wang N, Chew Shun NT, Duchamp M, Dunin-Borkowski RE, Li Z, Long Y. Effect of lanthanum doping on modulating the thermochromic properties of VO₂ thin films. *RSC Advances*. 2016;**6**(54):48455-48461. DOI: 10.1039/c6ra09514c
- [25] Wang N, Liu S, Zeng XT, Magdassi S, Long Y. Mg/W-codoped vanadium dioxide thin films with enhanced visible transmittance and low phase transition temperature. *Journal of Materials Chemistry C*. 2015;**3**(26):6771-6777. DOI: 10.1039/c5tc01062d
- [26] Wang S, Liu M, Kong L, Long Y, Jiang X, Yu A. Recent progress in VO₂ smart coatings: Strategies to improve the thermochromic properties. *Progress in Materials Science*. 2016;**81**:1-54. DOI: 10.1016/j.pmatsci.2016.03.001
- [27] Kiri P, Hyett G, Binions R. Solid state thermochromic materials. *Advanced Materials Letters*. 2010;**1**(2):86-105. DOI: 10.5185/amlett.2010.8147
- [28] Parkin IP, Manning TD. Intelligent thermochromic windows. *Journal of Chemical Education*. 2006;**83**(3):393-400. DOI: 10.1021/ed083p393
- [29] Hu LT, Tao HZ, Chen GH, Pan RK, Wan MN, Xiong DH, et al. Porous W-doped VO₂ films with simultaneously enhanced visible transparency and thermochromic properties. *Journal of Sol-Gel Science and Technology*. 2016;**77**(1):85-93. DOI: 10.1007/s10971-015-3832-z
- [30] Gonçalves A, Resende J, Marques AC, Pinto JV, Nunes D, Marie A, et al. Smart optically active VO₂ nanostructured layers applied in roof-type ceramic tiles for energy efficiency. *Solar Energy Materials & Solar Cells*. 2016;**150**:1-9. DOI: 10.1016/j.solmat.2016.02.001
- [31] Zhu J, Zhou Y, Wang B, Zheng J, Ji S, Yao H, et al. Vanadium dioxide nanoparticle-based thermochromic smart coating: High luminous transmittance, excellent solar regulation efficiency, and near room temperature phase transition. *ACS Applied Materials & Interfaces*. 2015;**7**(50):27796-27803. DOI: 10.1021/acsami.5b09011
- [32] Asayesh-Ardakani H, Nie A, Marley PM, Zhu Y, Phillips PJ, Singh S, et al. Atomic origins of monoclinic-tetragonal (rutile) phase transition in doped VO₂ nanowires. *Nano Letters*. 2015;**15**(11):7179-7188. DOI: 10.1021/acs.nanolett.5b03219
- [33] Huang Z, Chen C, Lv C, Chen S. Tungsten-doped vanadium dioxide thin films on borosilicate glass for smart window application. *Journal of Alloys and Compounds*. 2013;**564**(0):158-161. DOI: 10.1016/j.jallcom.2013.02.108
- [34] Batista C, Ribeiro RM, Teixeira V. Synthesis and characterization of VO₂-based thermochromic thin films for energy-efficient windows. *Nanoscale Research Letters*. 2011;**6**(1):301. DOI: 10.1186/1556-276X-6-301
- [35] Mai LQ, Hu B, Hu T, Chen W, Gu ED. Electrical property of Mo-doped VO₂ nanowire array film by melting-quenching sol-gel method. *The Journal of Physical Chemistry. B*. 2006;**110**(39):19083-19086. DOI: 10.1021/jp0642701
- [36] Manning TD, Parkin IP, Blackman C, Qureshi U. APCVD of thermochromic vanadium dioxide thin films-solid solutions V_{2-x}M_xO₂ (M = Mo, Nb) or composites VO₂: SnO₂. *Journal of Materials Chemistry*. 2005;**15**(42):4560-4566. DOI: 10.1039/b510552h

- [37] Powell MJ, Quesada-Cabrera R, Taylor A, Teixeira D, Papakonstantinou I, Palgrave RG, et al. Intelligent multifunctional VO₂/SiO₂/TiO₂ coatings for self-cleaning, energy-saving window panels. *Chemistry of Materials*. 2016;**28**(5):1369-1376. DOI: 10.1021/acs.chemmater.5b04419
- [38] Drosos C, Vernardou D. Perspectives of energy materials grown by APCVD. *Solar Energy Materials & Solar Cells*. 2015;**140**:1-8. DOI: 10.1016/j.solmat.2015.03.019
- [39] Vernardou D, Louloudakis D, Spanakis E, Katsarakis N, Koudoumas E. Thermochemical amorphous VO₂ coatings grown by APCVD using a single-precursor. *Solar Energy Materials & Solar Cells*. 2014;**128**:36-40. DOI: 10.1016/j.solmat.2014.04.033
- [40] Blackman CS, Piccirillo C, Binions R, Parkin IP. Atmospheric pressure chemical vapour deposition of thermochemical tungsten doped vanadium dioxide thin films for use in architectural glazing. *Thin Solid Films*. 2009;**517**(16):4565-4570. DOI: 10.1016/j.tsf.2008.12.050
- [41] Zheng J, Bao S, Jin P. TiO₂(R)/VO₂(M)/TiO₂(A) multilayer film as smart window: Combination of energy-saving, antifogging and self-cleaning functions. *Nano Energy*. 2015;**11**:136-145. DOI: 10.1016/j.nanoen.2014.09.023
- [42] Yang M, Yang Y, Hong B, Wang L, Luo Z, Li X, et al. Surface-growth-mode-induced strain effects on the metal-insulator transition in epitaxial vanadium dioxide thin films. *RSC Advances*. 2015;**5**(98):80122-80128. DOI: 10.1039/c5ra13490k
- [43] Qian Y, Wenwu L, Jiran L, Zhihua D, Zhigao H, Jian L, et al. Oxygen pressure manipulations on the metal-insulator transition characteristics of highly (0 1 1)-oriented vanadium dioxide films grown by magnetron sputtering. *Journal of Physics D: Applied Physics*. 2013;**46**(5):055310. DOI: 10.1088/0022-3727/46/5/055310
- [44] Ma JW, Xu G, Miao L. Vanadium dioxide thin films deposited on TiO₂ buffer layer for smart thermochemical glazing of windows. In: Li H, Liu YF, Guo M, Zhang R, Du J, editors. *Sustainable Development of Urban Environment and Building Material*, Pts 1-4. Vol. 374-377. Stafa-Zurich: Trans Tech Publications Ltd; 2012. p. 1365-1368
- [45] Huang ZL, Chen SH, Lv CH, Huang Y, Lai JJ. Infrared characteristics of VO₂ thin films for smart window and laser protection applications. *Applied Physics Letters*. 2012;**101**(19):191905. DOI: 10.1063/1.4766287
- [46] Seyfour MM, Binions R. Sol-gel approaches to thermochemical vanadium dioxide coating for smart glazing application. *Solar Energy Materials & Solar Cells*. 2017;**159**:52-65. DOI: 10.1016/j.solmat.2016.08.035
- [47] Warwick MEA, Binions R. Advances in thermochemical vanadium dioxide films. *Journal of Materials Chemistry A*. 2014;**2**:3275-3292. DOI: 10.1039/c3ta14124a
- [48] Yu W, Li S, Huang C. Phase evolution and crystal growth of VO₂ nanostructures under hydrothermal reactions. *RSC Advances*. 2016;**6**(9):7113-7120. DOI: 10.1039/c5ra23898f
- [49] Zhang J, Jin H, Chen Z, Cao M, Chen P, Dou Y, et al. Self-assembling VO₂ nanonet with high switching performance at wafer-scale. *Chemistry of Materials*. 2015;**27**(21):7419-7424. DOI: 10.1021/acs.chemmater.5b03314

- [50] Powell MJ, Marchand P, Denis CJ, Bear JC, Darr JA, Parkin IP. Direct and continuous synthesis of VO₂ nanoparticles. *Nanoscale*. 2015;7(44):18686-18693. DOI: 10.1039/c5nr04444h
- [51] Qian X, Wang N, Li Y, Zhang J, Xu Z, Long Y. Bioinspired multifunctional vanadium dioxide: Improved thermochromism and hydrophobicity. *Langmuir*. 2014;30(35):10766-10771. DOI: 10.1021/la502787q
- [52] Gao YF, Wang SB, Luo HJ, Dai L, Cao CX, Liu YL, et al. Enhanced chemical stability of VO₂ nanoparticles by the formation of SiO₂/VO₂ core/shell structures and the application to transparent and flexible VO₂-based composite foils with excellent thermochromic properties for solar heat control. *Energy & Environmental Science*. 2012;5(3):6104-6110. DOI: 10.1039/c2ee02803d
- [53] Kang L, Gao Y, Luo H, Chen Z, Du J, Zhang Z. Nanoporous thermochromic VO₂ films with low optical constants, enhanced luminous transmittance and thermochromic properties. *ACS Applied Materials & Interfaces*. 2011;3(2):135-138. DOI: 10.1021/am1011172
- [54] Li SY, Niklasson GA, Granqvist CG. Nanothermochromics: Calculations for VO₂ nanoparticles in dielectric hosts show much improved luminous transmittance and solar energy transmittance modulation. *Journal of Applied Physics*. 2010;108(6):063525. DOI: 10.1063/1.3487980
- [55] Lu Q, Liu C, Wang N, Magdassi S, Mandler D, Long Y. Periodical micro-patterned VO₂ thermochromic films by mesh printing. *Journal of Materials Chemistry C*. 2016;4:8385-8391. DOI: 10.1039/c6tc02694j
- [56] Xu G, Jin P, Tazawa M, Yoshimura K. Tailoring of luminous transmittance upon switching for thermochromic VO₂ films by thickness control. *Japanese Journal of Applied Physics*. 2004;43(1):186-187. DOI: 10.1143/jjap.43.186
- [57] Cao X, Wang N, Law JY, Loo SCJ, Magdassi S, Long Y. Nanoporous thermochromic VO₂(M) thin films: Controlled porosity, largely enhanced luminous transmittance and solar modulating ability. *Langmuir*. 2014;30(6):1710-1715. DOI: 10.1021/la404666n
- [58] Zhou M, Bao J, Tao M, Zhu R, Lin Y, Zhang X, et al. Periodic porous thermochromic VO₂(M) films with enhanced visible transmittance. *Chemical Communications*. 2013;49(54):6021-6023. DOI: 10.1039/c3cc42112k
- [59] Ke Y, Wen X, Zhao D, Che R, Xiong Q, Long Y. Controllable fabrication of two-dimensional patterned VO₂ nanoparticle, nanodome, and nanonet arrays with tunable temperature-dependent localized surface plasmon resonance. *ACS Nano*. 2017;11(7):7542-7551. DOI: 10.1021/acsnano.7b02232
- [60] Ke Y, Balin I, Wang N, Lu Q, Yok AIY, White TJ, et al. Two-dimensional, SiO₂/VO₂ photonic crystals with statically visible and dynamically infrared modulated for smart window deployment. *ACS Applied Materials & Interfaces*. 2016;8(48):33112-33120. DOI: 10.1021/acsaami.6b12175
- [61] Liu M, Su B, Kaneti YV, Chen Z, Tang Y, Yuan Y, et al. Dual-phase transformation: Spontaneous self-template surface-patterning strategy for ultra-transparent VO₂ solar modulating coatings. *ACS Nano*. 2017;11(1):407-415. DOI: 10.1021/acsnano.6b06152

- [62] Shi QW, Huang WX, Xu YJ, Zhang YX, Yue F, Qiao S, et al. Synthesis and terahertz transmission properties of nano-porous vanadium dioxide films. *Journal of Physics D: Applied Physics*. 2012;**45**(38):385302(1)-385302(6). DOI: 10.1088/0022-3727/45/38/385302
- [63] Ding S, Liu Z, Li D, Zhao W, Wang Y, Wan D, et al. Tunable assembly of vanadium dioxide nanoparticles to create porous film for energy-saving applications. *ACS Applied Materials & Interfaces*. 2013;**5**(5):1630-1635. DOI: 10.1021/am3023724
- [64] Zhang Z, Gao Y, Luo H, Kang L, Chen Z, Du J, et al. Solution-based fabrication of vanadium dioxide on F:SnO₂ substrates with largely enhanced thermochromism and low-emissivity for energy-saving applications. *Energy & Environmental Science*. 2011;**4**(10):4290. DOI: 10.1039/c1ee02092g
- [65] Du J, Gao Y, Luo H, Kang L, Zhang Z, Chen Z, et al. Significant changes in phase-transition hysteresis for Ti-doped VO₂ films prepared by polymer-assisted deposition. *Solar Energy Materials & Solar Cells*. 2011;**95**(2):469-475. DOI: 10.1016/j.solmat.2010.08.035
- [66] Ji Y, Zhang Y, Gao M, Yuan Z, Xia Y, Jin C, et al. Role of microstructures on the M1-M2 phase transition in epitaxial VO₂ thin films. *Scientific Reports*. 2014;**4**:4854. DOI: 10.1038/srep04854
- [67] Jia QX, McCleskey TM, Burrell AK, Lin Y, Collis GE, Wang H, et al. Polymer-assisted deposition of metal-oxide films. *Nature Materials*. 2004;**3**(8):529-532. DOI: 10.1038/nmat1163
- [68] Huang A, Zhou Y, Li Y, Ji S, Luo H, Jin P. Preparation of V_xW_{1-x}O₂(M)@SiO₂ ultrathin nanostructures with high optical performance and optimization for smart windows by etching. *Journal of Materials Chemistry A*. 2013;**1**(40):12545-12552. DOI: 10.1039/c3ta12232h
- [69] Bai J, Wang D, Nam S-w, Peng H, Bruce R, Gignac L, et al. Fabrication of sub-20 nm nanopore arrays in membranes with embedded metal electrodes at wafer scales. *Nanoscale*. 2014;**6**(15):8900-8906. DOI: 10.1039/c3nr06723h
- [70] Wu C, Zhang X, Dai J, Yang J, Wu Z, Wei S, et al. Direct hydrothermal synthesis of monoclinic VO₂(M) single-domain nanorods on large scale displaying magnetocaloric effect. *Journal of Materials Chemistry*. 2011;**21**(12):4509-4517. DOI: 10.1039/c0jm03078c
- [71] Zhang H, Li Q, Shen P, Dong Q, Liu B, Liu R, et al. The structural phase transition process of free-standing monoclinic vanadium dioxide micron-sized rods: Temperature-dependent Raman study. *RSC Advances*. 2015;**5**(101):83139-83143. DOI: 10.1039/c5ra15947d
- [72] Wyszecki G, Stiles WS. *Color Science: Concepts and Methods, Quantitative Data and Formulae*. 2nd ed. New York: Wiley; 2000
- [73] In ASTM G173-03 Standard Tables of Reference Solar Spectral Irradiances: Direct Normal and Hemispherical on a 37° Tilted Surface, *Annual Book of ASTM Standards*. American Society for Testing and Materials: Philadelphia, PA, USA, 2003; **14**(4)

Ultrasound Measuring of Porosity in Porous Materials

Zine El Abiddine Fellah, Mohamed Fellah,
Claude Depollier, Erick Ogam and Farid G. Mitri

Additional information is available at the end of the chapter

<http://dx.doi.org/10.5772/intechopen.72696>

Abstract

This chapter provides a temporal method for measuring the porosity and the tortuosity of air-saturated porous materials using experimental reflected waves. The direct problem of reflection and transmission of acoustic waves by a slab of porous material is studied. The equivalent fluid model has considered in which the acoustic wave propagates only in the pore-space. Since the acoustic damping in air-saturated porous materials is important, only the reflected waves by the first interface are taken into account, and the multiple reflections are neglected. The study of the sensitivity analysis shows that porosity is much more sensitive than tortuosity to reflection, especially when the incident angle is less than its critical value, at which the reflection coefficient vanishes. The inverse problem is solved using experimental data at a different incidence angle in reflection. Some advantages and perspectives of this method are discussed.

Keywords: porosity, tortuosity, porous material

1. Introduction

Porosity [1–3] is one of the most important parameters for describing the acoustic propagation in porous materials. This parameter intervenes in the propagation phenomena at all frequencies. Porosity is the relative fraction, by volume, of the air contained within the material. Air-saturated porous materials [1, 2, 4] as plastic foams, fibrous or granular materials are of great interest for a wide range of industrial applications. **Figure 1** gives an example of air-saturated porous material commonly used in the sound absorption (passive control). These materials are frequently used in the automotive and aeronautics industries and in the building trade. Beranek [3] has developed an apparatus for measuring the porosity of air saturated porous materials. This device was based on the equation of state for ideal gases at constant temperature i.e., Boyle's law. Porosity can be determined by measuring the change in air pressure occurring with a known change in volume of the chamber containing the sample. In this apparatus, both

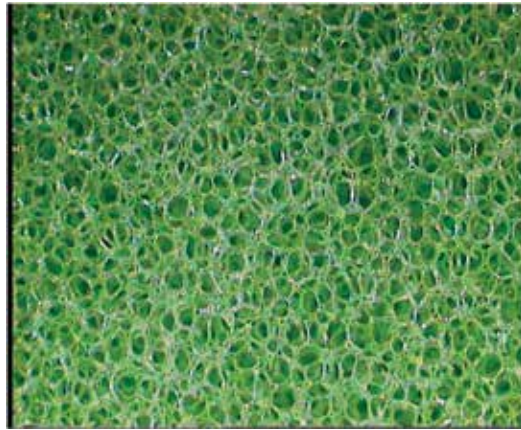


Figure 1. Air saturated plastic foam.

pressure change and volume change are monitored using a U-shaped fluid-filled manometer. Leonard [6] has given an alternate dynamic method for measuring porosity. Other techniques using water as the pore-filling fluid, rather than air, are common in geophysical studies [7, 8]. Mercury has been used as the pore-filling fluid in other applications [9]. However, for many materials, the introduction of liquids into the material is not appropriate. Recently, a similar device to that of Beranek [3], involving the use of an electronic pressure transducer, was introduced by Champoux et al. [10]. This device can be used to measure very slight changes in pressure accurately, and the output can be recorded by a computer.

Generally, the most methods used for measuring the porosity cited previously do not use acoustic waves. Here, we present an ultrasonic method for measuring porosity using ultrasonic reflected waves by the porous material. The direct and inverse problem is solved in the time domain using experimental reflected data. The inverse problem is solved directly in time domain using the waveforms. The attractive feature of a time domain-based approach [11–16] is that the analysis is naturally limited by the finite duration of ultrasonic pressures and is consequently the most appropriate approach for the transient signal.

2. Model

In the acoustics of porous materials, a distinction can be made between two situations depending on whether the frame is moving or not. In the general case (when the frame is moving), as for cancellous bone and rock and all porous media saturated by a liquid, the dynamics of the waves due to the coupling between the solid frame and the fluid are clearly described by the Biot theory [17, 18]. In air-saturated porous media, as plastic foams or fibrous materials that are used in sound absorption, the structure is generally motionless and the waves propagate only in the fluid. This case is described by the model of equivalent fluid, which is a particular case in the Biot model, in which the interactions between the fluid and the structure are taken into account in two frequency response factors: the dynamic tortuosity of the medium

$\alpha(\omega)$ given by Johnson et al. [4] and the dynamic compressibility of the air included in the porous material $\beta(\omega)$ given by Allard and Champoux [5]. In the frequency domain, these factors multiply the density of the fluid and its compressibility, respectively, and represent the deviation from the behavior of the fluid in free space as the frequency increases. In the time domain, they act as operators, and in the high-frequency approximation, their expressions are given by [11]

$$\tilde{\alpha}(t) = \alpha_{\infty} \left(\delta(t) + \frac{2}{\Lambda} \left(\frac{\eta}{\pi \rho_f} \right)^{1/2} t^{-1/2} \right), \quad (1)$$

$$\tilde{\beta}(t) = \left(\delta(t) + \frac{2(\gamma - 1)}{\Lambda'} \left(\frac{\eta}{\pi Pr \rho_f} \right)^{1/2} t^{-1/2} \right). \quad (2)$$

In these equations, $\delta(t)$ is the Dirac function, Pr is the Prandtl number, η and ρ_f are fluid viscosity and fluid density, respectively, and γ is the adiabatic constant. The most important physical parameters of the model are the medium's tortuosity α_{∞} initially introduced by Zwikker and Kosten [2] and viscous and the thermal characteristic lengths Λ and Λ' introduced by Johnson et al. [4] and Allard and Champoux [5]. In this model, the time convolution of $t^{-1/2}$ with a function is interpreted as a semi-derivative operator according to the definition of the fractional derivative of order ν given in Samko et al. [19]

$$D^{\nu}[x(t)] = \frac{1}{\Gamma(-\nu)} \int_0^t (t-u)^{-\nu-1} x(u) du, \quad (3)$$

where $\Gamma(x)$ is the Gamma function.

In this framework, the basic equations of our model can be expressed as follows

$$\rho_f \tilde{\alpha}(t) * \frac{\partial v_i}{\partial t} = -\nabla_i p \quad \text{and} \quad \frac{\tilde{\beta}(t)}{K_a} * \frac{\partial p}{\partial t} = -\nabla \cdot v, \quad (4)$$

where $*$ denotes the time convolution operation, p is the acoustic pressure, v is the particle velocity and K_a is the bulk modulus of the air. The first equation is the Euler equation, the second is a constitutive equation obtained from the equation of mass conservation associated with the behavior (or adiabatic) equation.

In the plane (xoz), the constitutive equation (4) can be written as

$$\begin{aligned} \rho_f \alpha_{\infty} \frac{\partial v_x(x, z, t)}{\partial t} + \frac{2\rho_f \alpha_{\infty}}{\Lambda} \left(\frac{\eta}{\pi \rho_f} \right)^{1/2} \int_0^t \frac{\partial v_x(x, z, t') / \partial t'}{\sqrt{t-t'}} dt' &= -\frac{\partial p(x, z, t)}{\partial x}, \\ \rho_f \alpha_{\infty} \frac{\partial v_z(x, z, t)}{\partial t} + \frac{2\rho_f \alpha_{\infty}}{\Lambda} \left(\frac{\eta}{\pi \rho_f} \right)^{1/2} \int_0^t \frac{\partial v_z(x, z, t') / \partial t'}{\sqrt{t-t'}} dt' &= -\frac{\partial p(x, z, t)}{\partial z}, \\ \frac{1}{K_a} \frac{\partial p(x, z, t)}{\partial t} + \frac{2(\gamma - 1)}{K_a \Lambda'} \left(\frac{\eta}{\pi \rho_f Pr} \right)^{1/2} \int_0^t \frac{\partial p(x, z, t') / \partial t'}{\sqrt{t-t'}} dt' &= -\frac{\partial v_x(x, z, t)}{\partial x} - \frac{\partial v_z(x, z, t)}{\partial z}, \end{aligned} \quad (5)$$

where v_x and v_z are the components of particle velocity along axes x and z . In these equations, the integrals express the fractional derivatives, defined mathematically by convolutions and describe the dispersive nature of the porous material. They take into account the memory effects due to the fluid-structure interactions and to the viscous and thermal losses in the medium.

The problem geometry is shown in **Figure 2**. A homogeneous porous material occupies the region $0 \leq x \leq L$. This medium is assumed to be isotropic and to have a rigid frame. A short sound pulse impinges at oblique incidence on the medium from the left, giving rise to an acoustic pressure field $p(x, z, t)$ and an acoustic velocity field $\mathbf{v}(x, z, t)$ within the material, which satisfies the system of Eq. (5) that can be written as:

$$\rho_f \alpha_\infty \frac{\partial v_x(x, z, t)}{\partial t} + \frac{2\rho_f \alpha_\infty}{\Lambda} \left(\frac{\eta}{\rho_f} \right)^{1/2} D^{1/2}[v_x(x, z, t)] = - \frac{\partial p(x, z, t)}{\partial x}, \quad (6)$$

$$\rho_f \alpha_\infty \frac{\partial v_z(x, z, t)}{\partial t} + \frac{2\rho_f \alpha_\infty}{\Lambda} \left(\frac{\eta}{\rho_f} \right)^{1/2} D^{1/2}[v_z(x, z, t)] = - \frac{\partial p(x, z, t)}{\partial z}, \quad (7)$$

$$\frac{1}{K_a} \frac{\partial p(x, z, t)}{\partial t} + \frac{2(\gamma - 1)}{K_a \Lambda'} \left(\frac{\eta}{\rho_f P_r} \right)^{1/2} D^{1/2}[p(x, z, t)] = - \frac{\partial v_x(x, z, t)}{\partial x} - \frac{\partial v_z(x, z, t)}{\partial z}. \quad (8)$$

In the region $x \leq 0$, the incident pressure wave is given by

$$p^i(x, z, t) = p^i \left(t - \frac{x \cos \theta}{c_0} - \frac{z \sin \theta}{c_0} \right), \quad (9)$$

where c_0 is the velocity of the free fluid ($x \leq 0$); $c_0 = \sqrt{K_a / \rho_f}$.

In the region $0 \leq x \leq L$, the pressure wave is given by

$$p(x, z, t) = p \left(t - \frac{x \cos \theta'}{c'} - \frac{z \sin \theta'}{c'} \right), \quad (10)$$

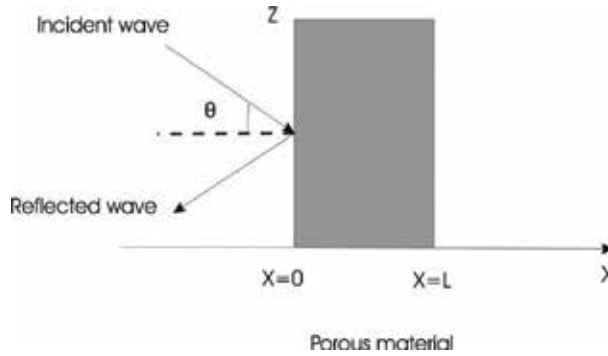


Figure 2. Problem geometry.

where c' is the velocity in the porous material ($0 \leq x \leq L$), and the refraction angle θ' is given by the Descartes-Snell law [27, 28]:

$$\frac{\sin \theta}{c_0} = \frac{\sin \theta'}{c'} \quad (11)$$

To simplify the system of Eq. (5), we can then use the following property

$$\frac{\partial}{\partial z} = -\frac{\sin \theta}{c_0} \frac{\partial}{\partial t}, \quad (12)$$

which implies

$$\frac{\partial v_z}{\partial z} = -\frac{\sin \theta}{c_0} \frac{\partial v_z}{\partial t} \quad \text{and} \quad \frac{\partial p}{\partial z} = -\frac{\sin \theta}{c_0} \frac{\partial p}{\partial t}. \quad (13)$$

From Eqs. (7) and (13), we obtain the relation

$$\frac{\partial v_z}{\partial z} = -\frac{\sin^2 \theta}{c_0^2} \left(\rho_f \alpha_\infty + \frac{2\rho_f \alpha_\infty}{\Lambda} \left(\frac{\eta}{\rho_f} \right)^{1/2} D^{-1/2} \right)^{-1} * \frac{\partial p}{\partial t}. \quad (14)$$

By using Eqs. (6), (8) and (14), the equation systems (6), (7) and (8) can thus be simplified to

$$\rho_f \alpha_\infty \frac{\partial v_x(x, z, t)}{\partial t} + \frac{2\rho_f \alpha_\infty}{\Lambda} \left(\frac{\eta}{\rho_f} \right)^{1/2} D^{1/2} [v_x(x, z, t)] = -\frac{\partial p(x, z, t)}{\partial x}, \quad (15)$$

$$\begin{aligned} \frac{1}{K_a} \frac{\partial p(x, z, t)}{\partial t} + \frac{2(\gamma - 1)}{K_a \Lambda'} \left(\frac{\eta}{\rho_f} \right)^{1/2} D^{1/2} [p(x, z, t)] = \\ -\frac{\partial v_x(x, z, t)}{\partial x} + \frac{\sin^2 \theta}{c_0^2} \left(\rho_f \alpha_\infty + \frac{2\rho_f \alpha_\infty}{\Lambda} \left(\frac{\eta}{\rho_f} \right)^{1/2} D^{-1/2} \right)^{-1} * \frac{\partial p(x, z, t)}{\partial t}. \end{aligned} \quad (16)$$

From Eqs. (15) and (16), we derive the fractional propagation wave equation in the time domain along the x -axis

$$\frac{\partial^2 p(x, z, t)}{\partial x^2} - \frac{1}{c_0^2} (\alpha_\infty - \sin^2 \theta) \frac{\partial^2 p(x, z, t)}{\partial t^2} - \frac{2\alpha_\infty}{K_a} \sqrt{\frac{\rho_f \eta}{\pi}} \left(\frac{1}{\Lambda} + \frac{\gamma - 1}{\sqrt{\text{Pr} \Lambda'}} \right) D^{3/2} [p(x, z, t)] = 0, \quad (17)$$

The solution of the wave Eq. (17) with suitable initial and boundary conditions is by using the Laplace transform. F is the medium's Green function [12, 20] given by

$$F(t, k) = \begin{cases} 0 & \text{if } 0 \leq t \leq k \\ \Xi(t) + \Delta \int_0^{t-k} h(t, \xi) d\xi & \text{if } t \geq k \end{cases} \quad (18)$$

with

$$\Xi(t) = \frac{b'}{4\sqrt{\pi}} \frac{k}{(t-k)^{3/2}} \exp\left(-\frac{b'^2 k^2}{16(t-k)}\right), \quad (19)$$

where $h(\tau, \xi)$ has the following form:

$$h(\xi, \tau) = -\frac{1}{4\pi^{3/2}} \frac{1}{\sqrt{(\tau-\xi)^2 - k^2}} \frac{1}{\xi^{3/2}} \int_{-1}^1 \exp\left(-\frac{\chi(\mu, \tau, \xi)}{2}\right) (\chi(\mu, \tau, \xi) - 1) \frac{\mu d\mu}{\sqrt{1-\mu^2}} \quad (20)$$

and $\chi(\mu, \tau, \xi) = \left(\Delta\mu\sqrt{(\tau-\xi)^2 - k^2} + b'(\tau-\xi)\right)^2 / 8\xi$, $b' = Bc_0^2\sqrt{\pi}$ and $\Delta = b'^2$.

If the incident sound wave is launched in region $x \leq 0$, then the expression of the pressure field in the region on the left of the material is the sum of the incident and reflected fields

$$p_1(x, t, \theta) = p^i\left(t - \frac{x \cos \theta}{c_0}\right) + p^r\left(t + \frac{x \cos \theta}{c_0}\right), \quad x < 0. \quad (21)$$

Here, $p_1(x, t, \theta)$ is the field in the region $x < 0$, p^i and p^r denote the incident and reflected fields, respectively.

The incident and reflected fields are related by the scattering operator (i.e., the reflection operator) for the material. This is an integral operator represented by

$$p^r(x, t, \theta) = \int_0^t \tilde{R}(\tau, \theta) p^i\left(t - \tau + \frac{x \cos \theta}{c_0}\right) d\tau, \quad (22)$$

In Eq. (22), the function \tilde{R} is the reflection kernel for incidence from the left. Note that the lower limit of integration in Eq. (22) is set to 0, which is equivalent to assuming that the incident wavefront impinges on the material at $t = 0$.

Expression of the reflection-scattering operator taking into account the n-multiple reflections in the material is given by

$$\tilde{R}(t, \theta) = \left(\frac{1-E}{1+E}\right) \sum_{n \geq 0} \left(\frac{1-E}{1+E}\right)^{2n} \left[F\left(t, 2n \frac{L}{c}\right) - F\left(t, (2n+2) \frac{L}{c}\right) \right], \quad (23)$$

with

$$E = \frac{\phi \sqrt{1 - \frac{\sin^2 \theta}{\alpha_\infty}}}{\sqrt{\alpha_\infty} \cos \theta}, \quad (24)$$

Generally [21], in air-saturated porous materials, acoustic damping is very important, and the multiple reflections are thus negligible inside the material. So, by taking into account only

the first reflections at interfaces $x = 0$ and $x = L$, the expression of the reflection operator will be given by

$$\tilde{R}(t, \theta) = r(t, \theta) + \mathfrak{R}(t, \theta), \quad (25)$$

with

$$r(t, \theta) = \left(\frac{1-E}{1+E} \right) \delta(t) \quad \text{and} \quad \mathfrak{R}(t, \theta) = -\frac{4E(1-E)}{(1+E)^3} F\left(t, \frac{2L}{c}\right), \quad (26)$$

where $r(t, \theta)$ is the instantaneous response of the porous material corresponding to the reflection contribution at the first interface ($x = 0$). $\mathfrak{R}(t, \theta)$ is equivalent to reflection at the interface $x = L$, which is the bulk contribution to reflection. The part of the wave corresponding to $r(t, \theta)$ is not subjected to dispersion but simply multiplied by the factor $(1-E)/(1+E)$.

The reflection coefficient at the first interface vanishes for a critical angle θ_c

$$r(t, \theta) = 0 \Rightarrow \sin \theta_c = \sqrt{\frac{\alpha_\infty(\alpha_\infty - \phi^2)}{\alpha_\infty^2 - \phi^2}}.$$

Figure 3 shows the variation of the reflection coefficient at the first interface r with the incident angle θ , for a fixed porosity value $\phi = 0.9$, and for different values of tortuosity $\alpha_\infty = 1.99$ (solid line), $\alpha_\infty = 1.75$ (star), $\alpha_\infty = 1.5$ (dashed line), $\alpha_\infty = 1.24$ (dash-dot line) and $\alpha_\infty = 1$ (circle).

Figure 4 shows the variation of r with the incident angle, for a fixed tortuosity of $\alpha_\infty = 1.1$, and for different values of porosity $\phi = 0.99$ (solid line), $\phi = 0.75$ (star), $\phi = 0.50$ (dashed line), $\phi = 0.25$ (dash-dot line) and $\phi = 0.01$ (circle).

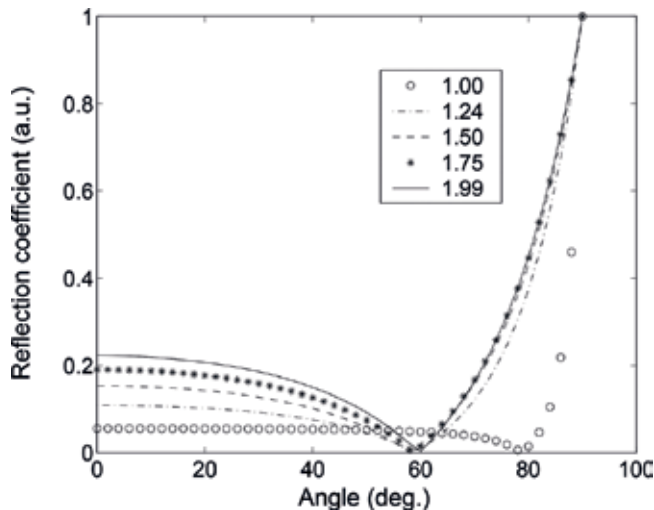


Figure 3. Variation of the reflection coefficient at the first interface r with the incident angle θ , for a fixed porosity value $\phi = 0.9$, and for different values of tortuosity $\alpha_\infty = 1.99$ (solid line), $\alpha_\infty = 1.75$ (star), $\alpha_\infty = 1.5$ (dashed line), $\alpha_\infty = 1.24$ (dash-dot line) and $\alpha_\infty = 1$ (circle).

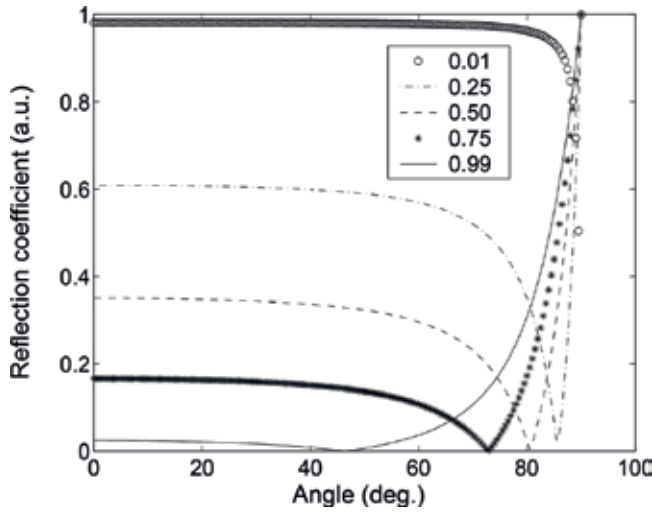


Figure 4. Variation of the reflection coefficient at the first interface with the incident angle, for a fixed tortuosity value $\alpha_{\infty} = 1.1$, and for different values of porosity $\phi = 0.99$ (solid line), $\phi = 0.75$ (star), $\phi = 0.50$ (dashed line), $\phi = 0.25$ (dash-dot line) and $\phi = 0.01$ (circle).

When the incident angle is $\theta < \theta_c$, the reflection coefficient decreases slowly with the incident angle, and when it is $\theta > \theta_c$, the reflection coefficient increases quickly with the angle. It can be seen also from **Figures 2** and **3** that the sensitivity of porosity variation is more important than the sensitivity of tortuosity on the reflection coefficient at the first interface.

3. Inverse problem

The inverse problem is solved using transmitted waves and an estimation of the tortuosity, viscous and thermal characteristic length is given. However, the porosity cannot be inverted in transmission since its sensitivity is low. In this work, we determine porosity and tortuosity by solving the inverse problem for waves reflected by the first interface and by taking into account experimental data concerning all measured incident angles (**Figure 4**). The propagation of acoustic waves in a slab of porous material in the high-frequency asymptotic domain is characterized by four parameters: porosity ϕ , tortuosity α_{∞} , viscous characteristic length Λ , and thermal characteristic length Λ' , the values of which are crucial to the behavior of sound waves in such materials. It is of some importance to work out new experimental methods and efficient tools for their estimation. The basic inverse problem associated with the slab may be stated as follows: from the measurement of the signals transmitted and/or reflected outside the slab, find the values of the medium's parameters. The inverse problem is to find values of parameters ϕ , α_{∞} , which minimize the function:

$$U(\phi, \alpha_{\infty}) = \sum_{\theta_i} \sum_{t_i} [p^r(x, \theta_i, t_i) - r(\theta_i, t_i) * p^i(x, \theta_i, t_i)]^2, \quad (27)$$

where $p^r(x, \theta_i, t_i)$ represents the discrete set of values of the experimental reflected signal for different incident angles θ_i , $r(\theta_i, t_i)$ is the reflection coefficient at the first interface, and $p^i(x, \theta_i, t_i)$ is the experimental incident signal. The term $r(\theta_i, t_i) * p^i(x, \theta_i, t_i)$ represents the predicted reflected signal. The inverse problem is solved numerically by the least-square method.

Let us consider three samples of plastic foam M1, M2, and M3. Their tortuosity and porosity were measured using classical methods [22–31] (**Table 1**). We solved the inverse problem for these samples via waves reflected at the first interface and for different incident angles.

Experiments were performed in air with two broadband Ultrat NCT202 transducers with a 190 kHz central frequency in air and a 6 dB bandwidth extending from 150 to 230 kHz. Pulses of 400 V were provided by a 5052PR panametrics pulser/receiver. An optical goniometer was used to position the transducers. The received signals were amplified to 90 dB and filtered above 1 MHz to avoid high-frequency noise. Electronic interference was removed by 1000 acquisition averages. The experimental setup is shown in **Figure 5**.

Figures 6 and 7 show a variation of the cost function, U , with tortuosity and porosity, for samples M1, M2, and M3, respectively. The reconstructed values of porosity and tortuosity corresponding to the positions of the minima of these cost functions are given in **Table 2**.

Material	M1	M2	M3
Tortuosity	1.1	1.1	1.5
Porosity	0.95	0.99	0.86

Table 1. Measured values of porosity and tortuosity by classical methods [22–31].

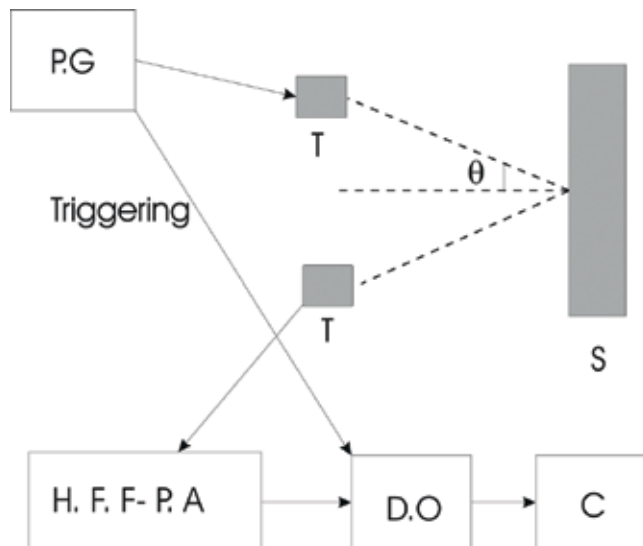


Figure 5. Experimental set-up of the ultrasonic measurements in reflected mode. PG: pulse generator; HFFPA: high-frequency filtering-pre-amplifier; DO: digital oscilloscope; C: computer; T: transducer; S: sample.

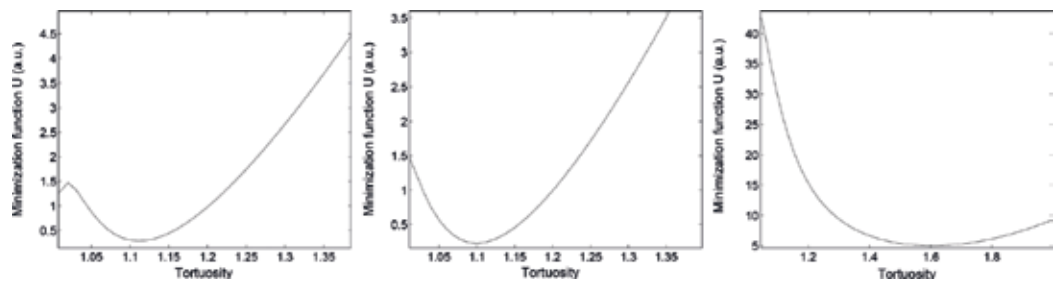


Figure 6. Variation of the cost function U with tortuosity for the plastic foams M1, M2, and M3.

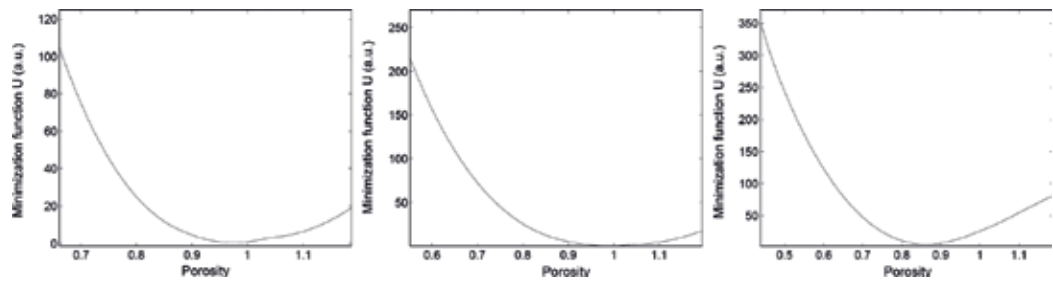


Figure 7. Variation of the cost function U with porosity for the plastic foams M1, M2, and M3.

Material	M1	M2	M3
Tortuosity	1.12	1.1	1.6
Porosity	0.96	0.99	0.85

Table 2. Reconstructed values of porosity and tortuosity by solving the inverse problem.

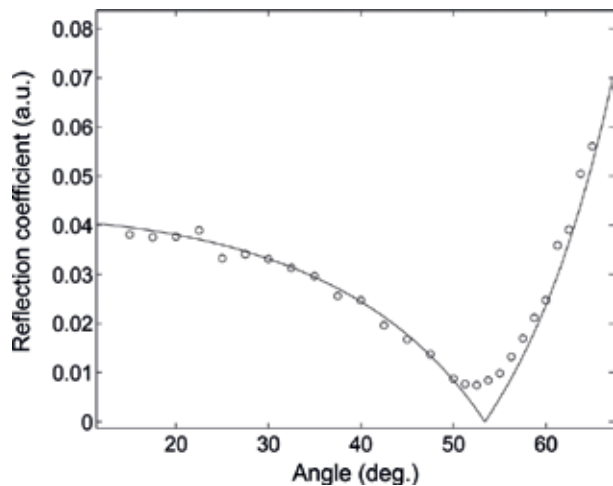


Figure 8. Comparison between simulated reflection coefficient at the first interface using reconstructed values of the porosity and tortuosity (solid line) and experimental data of the reflection coefficient at the first interface (circle) for the plastic foam M1.

A comparison is given in **Figures 8–10**, between simulated reflection coefficient at the first interface using reconstructed values of porosity and tortuosity (solid line) and experimental data of the reflection coefficient at the first interface (circle) for plastic foams M1, M2, and M3, respectively.

The correspondence between experiment and theory is good, which leads us to conclude that this method based on the solution of the inverse problem is appropriate for estimating the porosity and tortuosity of porous materials with a rigid frame. This method is very interesting comparing the classical one using non-acoustic waves.

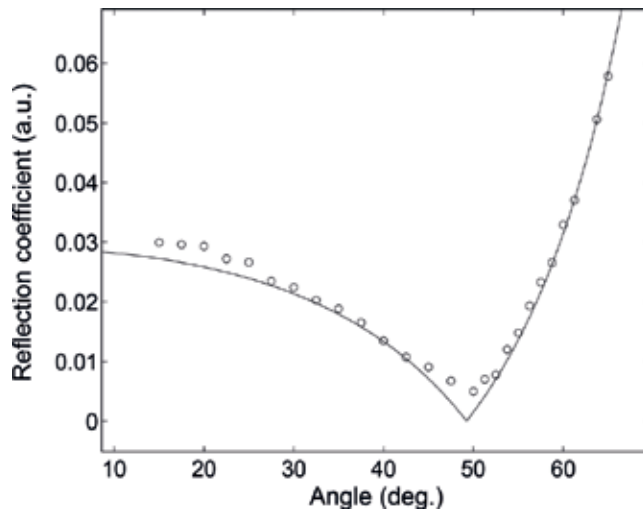


Figure 9. Comparison between simulated reflection coefficient at the first interface using reconstructed values of the porosity and tortuosity (solid line) and experimental data of the reflection coefficient at the first interface (circle) for the plastic foam M2.

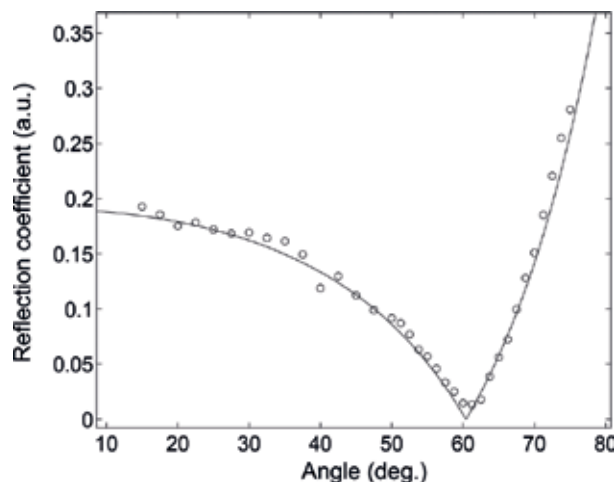


Figure 10. Comparison between simulated reflection coefficient at the first interface using reconstructed values of the porosity and tortuosity (solid line) and experimental data of the reflection coefficient at the first interface (circle) for the plastic foam M3.

4. Conclusion

In this chapter, an inverse determination of porosity and tortuosity is given using experimental reflected acoustic waves at different incidence angles. The inverse problem is solved numerically by the least-square method. The obtained values of porosity and tortuosity are close to those given using classical (non-acoustical) methods. Generally, the tortuosity is inverted easily using transmitted waves, and this is not the case for porosity because of its weak sensitivity in transmitted mode. This method is very interesting from its simplicity and constitutes an alternative to the usual method involving the use of a porosimeter introduced by Beranek [3] and improved by Champoux et al. [10] or the other ultrasonic methods based on transmitted mode.

This method is valuable for porous materials having a rigid frame as air-saturated media, in which the equivalent fluid model is used. However, for liquid-saturated materials as rock or cancellous bone, this method cannot be used and should be adapted using the general Biot model [17, 18]. We hope, in the future, to extend this method to porous media with an elastic frame saturated with viscous fluid, in order to estimate other parameters that play an important role in acoustic propagation.

Author details

Zine El Abiddine Fellah^{1*}, Mohamed Fellah², Claude Depollier³, Erick Ogam¹ and Farid G. Mitri⁴

*Address all correspondence to: fellah@lma.cnrs-mrs.fr

1 LMA, CNRS, UPR 7051, Aix-Marseille Univ, Centrale Marseille, Marseille Cedex 20, France

2 Laboratoire de Physique Théorique, Faculté de Physique, USTHB, Bab-Ezzouar, Algeria

3 LUNAM Université du Maine, UMR CNRS 6613 Laboratoire d'Acoustique de l'Université du Maine, Cedex 09, France

4 Chevron, Santa Fe, New Mexico, United States

References

- [1] Allard JF. *Propagation of Sound in Porous Media: Modeling Sound Absorbing Materials*. London: Chapman and Hall; 1993
- [2] Zwikker C, Kosten CW. *Sound Absorbing Materials*. New York: Elsevier; 1949
- [3] Beranek LL. Acoustic impedance of porous materials. *The Journal of the Acoustical Society of America*. 1942;**13**:248-260
- [4] Johnson DL, Koplik J, Dashen R. Theory of dynamic permeability and tortuosity in fluid-saturated porous media. *Journal of Fluid Mechanics*. 1987;**176**:379-402

- [5] Allard JF, Champoux Y. New empirical equations for sound propagation in rigid frame fibrous materials. *Acoustical Society of America*. 1992;**91**:3346
- [6] Leonard RW. Simplified porosity measurements. *Journal of the Acoustical Society of America*. 1948;**20**:39-34
- [7] Guyon E, Oger L, Plona TJ. Transport properties in sintered porous media composed of two particles sizes. *Journal of Physics D: Applied Physics*. 1987;**20**:1637-1644
- [8] Johnson DL, Plona TJ, Scala C, Psierb F, Kojima H. Tortuosity and acoustic slow waves. *Physical Review Letters*. 1982;**49**:1840-1844
- [9] Van Brakel J, Modry S, Svata M. Mercury porosimetry: State of the art. *Powder Technology*. 1981;**29**:1-12
- [10] Champoux Y, Stinson MR, Daigle GA. Air-based system for the measurement of porosity. *The Journal of the Acoustical Society of America*. 1991;**89**:910-916
- [11] Fellah ZEA, Depollier C. Transient acoustic wave propagation in rigid porous media: A time domain approach. *Journal of the Acoustical Society of America*. 2000;**107**(2):683-688
- [12] Fellah ZEA, Depollier C, Fellah M, Lauriks W, Chpaleon JY. Influence of dynamic tortuosity and compressibility on the propagation of transient waves in porous media. *Wave Motion*. 2005;**41**(2):145-161
- [13] Fellah ZEA, Fellah M, Lauriks W, Depollier C. Direct inverse scattering of transient acoustic waves by a slab of rigid porous material. *Journal of the Acoustical Society of America*. 2003;**113**(1):61-72
- [14] Szabo TL. Time domain wave equations for lossy media obeying a frequency power law. *The Journal of the Acoustical Society of America*. 1994;**96**:491
- [15] Szabo TL. Causal theories and data for acoustic attenuation obeying a frequency power law. *Journal of the Acoustical Society of America*. 1995;**97**:14
- [16] Norton V, Novarini JC. Including dispersion and attenuation directly in time domain for wave propagation in isotropic media. *The Journal of the Acoustical Society of America*. 2003;**113**:3024
- [17] Biot MA. The theory of propagation of elastic waves in fluid-saturated porous solid. I. Low frequency range. *The Journal of the Acoustical Society of America*. 1956;**28**:168
- [18] Biot MA. The theory of propagation of elastic waves in fluid-saturated porous solid. I. Higher frequency range. *The Journal of the Acoustical Society of America*. 1956;**28**:179
- [19] Samko SG, Kilbas AA, Marichev OI. *Fractional Integrals and Derivatives Theory and Applications*. Amsterdam: Gordon and Breach Publishers; 1993
- [20] Fellah ZEA, Fellah M, Lauriks W, Depollier C, Angel Y, Chapelon JY. Solution in time domain of ultrasonic propagation equation in porous material. *Wave Motion*. 2003;**38**: 151-163

- [21] Fellah ZEA, Mitri FG, Depollier C, Berger S, Lauriks W, Chapelon JY. Characterization of porous materials with a rigid frame via reflected waves. *Journal of Applied Physics*. 2003;**94**:7914-7922
- [22] Fellah ZEA, Ogam E, Wirgin A, Fellah M, Depollier C, Lauriks W. Ultrasonic characterization of porous materials: Inverse problem. *Journal of Sound and Vibration*. 2007;**302**: 746-759
- [23] Leclaire P, Kelders L, Lauriks W, Glorieux C, Thoen J. Determination of the viscous characteristic length in air-filled porous materials by ultrasonic attenuation measurements. *The Journal of the Acoustical Society of America*. 1996;**99**:1944
- [24] Leclaire P, Kelders L, Lauriks W, Brown NR, Melon M, Castagnède B. Determination of viscous and thermal characteristic lengths of plastic foams by ultrasonic measurements in helium and air. *Journal of Applied Physics*. 1996;**80**:2009
- [25] Fellah ZEA, Depollier C, Berger S, Lauriks W, Trompette P, Chapelon JY. Determination of transport parameters in air saturated porous materials via ultrasonic reflected waves. *The Journal of the Acoustical Society of America*. 2003;**113**(5):2561-2569
- [26] Fellah ZEA, Berger S, Lauriks W, Depollier C, Chapelon JY. Inverse problem in air-saturated porous media via reflected waves. *Review of Scientific Instruments*. 2003;**74**(5): 2871
- [27] Fellah ZEA, Berger S, Lauriks W, Depollier C, Aristégui C, Chapelon JY. Measuring the porosity and the tortuosity of porous materials via reflected waves at oblique incidence. *The Journal of the Acoustical Society of America*. 2003;**113**(5):2424
- [28] Fellah ZEA, Berger S, Lauriks W, Depollier C, Trompette P, Chapelon JY. Ultrasonic measuring of the porosity and tortuosity of air- saturated random packings of beads. *Journal of Applied Physics*. 2003;**93**:9352
- [29] Fellah ZEA, Mitri FG, Depollier D, Berger S, Lauriks W, Chapelon JY. Characterization of porous materials having a rigid frame via reflected waves. *Journal of Applied Physics*. 2003;**94**:7914
- [30] Fellah ZEA, Berger S, Lauriks W, Depollier C, Fellah M. Measurement of the porosity of porous materials having a rigid frame via reflected waves: A time domain analysis with fractional derivatives. *Journal of Applied Physics*. 2003;**93**:296
- [31] Fellah ZEA, Mitri FG, Fellah M, Ogam E, Depollier C. Ultrasonic characterization of porous absorbing materials: Inverse problem. *Journal of Sound and Vibration*. 2007;**302**: 746-759

Unsteady Magnetohydrodynamic Flow of Jeffrey Fluid through a Porous Oscillating Rectangular Duct

Amir Khan, Gul Zaman and Obaid Algahtani

Additional information is available at the end of the chapter

<http://dx.doi.org/10.5772/intechopen.70891>

Abstract

This chapter presents some new exact solutions corresponding to unsteady magnetohydrodynamic (MHD) flow of Jeffrey fluid in a long porous rectangular duct oscillating parallel to its length. The exact solutions are established by means of the double finite Fourier sine transform (DFST) and discrete Laplace transform (LT). The series solution of velocity field, associated shear stress and volume flow rate in terms of Fox H-functions, satisfying all imposed initial and boundary conditions, have been obtained. Also, the obtained results are analyzed graphically through various pertinent parameter.

Keywords: porous medium, Jeffrey fluid, oscillating rectangular duct, Fox H-function, MSC (2010): 76A05, 76A10

1. Introduction

Considerable progress has been made in studying flows of non-Newtonian fluids throughout the last few decades. Due to their viscoelastic nature non-Newtonian fluids, such as oils, paints, ketchup, liquid polymers and asphalt exhibit some remarkable phenomena. Amplifying interest of many researchers has shown that these flows are imperative in industry, manufacturing of food and paper, polymer processing and technology. Dissimilar to the Newtonian fluid, the flows of non-Newtonian fluids cannot be explained by a single constitutive model. In general the rheological properties of fluids are specified by their so-called constitutive equations. Exact recent solutions for constitutive equations of viscoelastic fluids are given by Rajagopal and Bhatnagar [1], Tan and Masuoka [2, 3], Khadrawi et al. [4] and Chen et al. [5] etc. Among non-Newtonian fluids the Jeffrey model is considered to be one of the simplest type of model which best explain the rheological effects of viscoelastic fluids. The Jeffrey model is a relatively simple linear model using the time derivatives instead of convected derivatives. Nadeem et al. [6] obtained analytic solutions for stagnation flow of Jeffrey fluid over a shrinking sheet. Khan [7] investigated partial slip effects on the oscillatory flows of fractional Jeffrey fluid in a porous medium. Hayat et al. [8]

examined oscillatory rotating flows of a fractional Jeffrey fluid filling a porous medium. Khan et al. [9] discussed unsteady flows of Jeffrey fluid between two side walls over a plane wall.

Much attention has been given to the flows of rectangular duct because of its wide range applications in industries. Gardner and Gardner [10] discussed magnetohydrodynamic (MHD) duct flow of two-dimensional bi-cubic B-spline finite element. Fetecau and Fetecau [11] investigated the flows of Oldroyd-B fluid in a channel of rectangular cross-section. Nazar et al. [12] examined oscillating flow passing through rectangular duct for Maxwell fluid using integral transforms. Unsteady magnetohydrodynamic flow of Maxwell fluid passing through porous rectangular duct was studied by Sultan et al. [13]. Tsangaris and Vlachakis [14] discussed analytic solution of oscillating flow in a duct of Navier-Stokes equations.

In the last few decades the study of fluid motions through porous medium have received much attention due to its importance not only to the field of academic but also to the industry. Such motions have many applications in many industrial and biological processes such as food industry, irrigation problems, oil exploitation, motion of blood in the cardiovascular system, chemistry and bio-engineering, soap and cellulose solutions and in biophysical sciences where the human lungs are considered as a porous layer. Unsteady MHD flows of viscoelastic fluids passing through porous space are of considerable interest. In the last few years a lot of work has been done on MHD flow, see [15–19] and reference therein.

According to the authors information up to yet no study has been done on the MHD flow of Jeffrey fluid passing through a long porous rectangular duct oscillating parallel to its length. Hence, our main objective in this note is to make a contribution in this regard. The obtained solutions, expressed under series form in terms of Fox H-functions, are established by means of double finite Fourier sine transform (DFFST) and Laplace transform (LT). Finally, the obtained results are analyzed graphically through various pertinent parameter.

2. Governing equations

The equation of continuity and momentum of MHD flow passing through porous space is given by [7]

$$\nabla \cdot \mathbf{V} = 0, \rho \left(\frac{d\mathbf{V}}{dt} \right) = \text{div} \mathbf{T} + \mathbf{J} \times \mathbf{B} + \mathbf{R}, \quad (1)$$

where velocity is represented by \mathbf{V} , density by ρ , Cauchy stress tensor by \mathbf{T} , magnetic body force by $\mathbf{J} \times \mathbf{B}$, current density by \mathbf{J} , magnetic field by \mathbf{B} , and Darcy's resistance in the porous medium by \mathbf{R} .

For an incompressible and unsteady Jeffrey fluid the Cauchy stress tensor is defined as [9]

$$\mathbf{T} = -p\mathbf{I} + \mathbf{S}, \quad \mathbf{S} = \frac{\mu}{1 + \lambda} \left[\mathbf{A} + \theta \left(\frac{\partial \mathbf{A}}{\partial t} + (\mathbf{V} \cdot \nabla) \mathbf{A} \right) \right], \quad (2)$$

where \mathbf{S} and $p\mathbf{I}$ represents the extra stress tensor and the indeterminate spherical stress, the dynamic viscosity is denoted by μ , $\mathbf{A} = \mathbf{L} + \mathbf{L}^T$ is the first Rivlin-Ericksen tensor, \mathbf{L} is the velocity gradient, λ is relaxation time and θ is retardation time. The Lorentz force due to magnetic field is

$$\mathbf{J} \times \mathbf{B} = -\sigma\beta_o^2\mathbf{V}, \quad (3)$$

where σ represents electrical conductivity and β_o the strength of magnetic field. For the Jeffrey fluid the Darcy's resistance satisfies the following equation

$$\mathbf{R} = -\frac{\mu\phi}{\kappa(1+\lambda)}\left(1 + \theta\frac{\partial}{\partial t}\right)\mathbf{V}, \quad (4)$$

where $\kappa(>0)$ and $\phi(0<\phi<1)$ are the permeability and the porosity of the porous medium.

In the following problem we consider a velocity field and extra stress of the form

$$\mathbf{V} = (0, 0, w(x, y, t)), \mathbf{S} = \mathbf{S}(x, y, t) \quad (5)$$

where w is the velocity in the z -direction. The continuity equation for such flows is automatically satisfied. Also, at $t=0$, the fluid being at rest is given by

$$\mathbf{S}(x, y, 0) = \mathbf{0}, \quad (6)$$

therefore from Eqs. (2), (5) and (6), it results that $S_{xx}=S_{yy}=S_{yz}=S_{zz}=0$ and the relevant equations

$$\tau_1 = \frac{\mu}{(1+\lambda)}\left(1 + \theta\frac{\partial}{\partial t}\right)\partial_x w(x, y, t), \quad \tau_2 = \frac{\mu}{(1+\lambda)}\left(1 + \theta\frac{\partial}{\partial t}\right)\partial_y w(x, y, t), \quad (7)$$

where $\tau_1=S_{xy}$ and $\tau_2=S_{xz}$ are the tangential stresses. In the absence of pressure gradient in the flow direction, the governing equation leads to

$$(1+\lambda)\partial_t w(x, y, t) = \nu\left(1 + \theta\frac{\partial}{\partial t}\right)(\partial_x^2 + \partial_y^2)w(x, y, t) - \nu K\left(1 + \theta\frac{\partial}{\partial t}\right)w(x, y, t) - H(1+\lambda)w(x, y, t), \quad (8)$$

where $H = \frac{\sigma B_o^2}{\rho}$ is the magnetic parameter, $K = \frac{\phi}{\kappa}$ is the porosity parameter and $\nu = \mu/\rho$ is the kinematic viscosity.

3. Statement of the problem

We take an incompressible flow of Jeffrey fluid in a porous rectangular duct under an imposed transverse magnetic field whose sides are at $x=0$, $x=d$, $y=0$, and $y=h$. At time $t=0^+$ the duct begins to oscillate along z -axis. Its velocity is of the form of Eq. (5) and the governing equation is given by Eq. (8). The associated initial and boundary conditions are

$$w(x, y, 0) = \partial_t w(x, y, 0) = 0, \quad (9)$$

$$w(0, y, t) = w(x, 0, t) = w(d, y, t) = w(x, h, t) = U \cos(\omega t), \quad (10)$$

or

$$w(0, y, t) = w(x, 0, t) = w(d, y, t) = w(x, h, t) = U \sin(\omega t), \quad (11)$$

$$t > 0, 0 < x < d \text{ and } 0 < y < h.$$

The solutions of problems (8)–(10) and (8), (9), (11) are denoted by $u(x, y, t)$ and $v(x, y, t)$ respectively. We define the complex velocity field

$$F(x, y, t) = u(x, y, t) + iv(x, y, t), \quad (12)$$

which is the solution of the problem

$$(1 + \lambda) \partial_t F(x, y, t) = \nu \left(1 + \theta \frac{\partial}{\partial t} \right) (\partial_x^2 + \partial_y^2) F(x, y, t) - \nu K \left(1 + \theta \frac{\partial}{\partial t} \right) F(x, y, t) - H(1 + \lambda) F(x, y, t), \quad (13)$$

$$F(x, y, 0) = \partial_t F(x, y, 0) = 0, \quad (14)$$

$$F(0, y, t) = F(d, y, t) = F(x, 0, t) = F(x, h, t) = U e^{i\omega t}, \quad (15)$$

$$t > 0, 0 < x < d \text{ and } 0 < y < h.$$

The solution of the problem (13)–(15) will be obtained by means of the DFFST and LT.

The DFFST of function $F(x, y, t)$ is denoted by

$$F_{mn}(t) = \int_0^d \int_0^h \sin\left(\frac{m\pi x}{d}\right) \sin\left(\frac{n\pi y}{h}\right) F(x, y, t) dx dy, \quad m, n = 1, 2, 3, \dots \quad (16)$$

4. Calculation of the velocity field

Multiplying both sides of Eq. (13) by $\sin\left(\frac{m\pi x}{d}\right)$ and $\sin\left(\frac{n\pi y}{h}\right)$, integrating w.r.t x and y over $[0, d] \times [0, h]$ and using Eq. (16), we get

$$\begin{aligned} (1 + \lambda) \frac{\partial F_{mn}(t)}{\partial t} + \nu \lambda_{mn} \left(1 + \theta \frac{\partial}{\partial t} \right) F_{mn}(t) + H(1 + \lambda) F_{mn}(t) + \nu K \left(1 + \theta \frac{\partial}{\partial t} \right) F_{mn}(t) \\ = \nu \lambda_{mn} U \frac{[1 - (-1)^m][1 - (-1)^n]}{\zeta_m \lambda_n} (1 + i\omega\theta) e^{i\omega t}, \end{aligned} \quad (17)$$

where

$$\zeta_m = \frac{m\pi}{d}, \lambda_n = \frac{n\pi}{h} \text{ and } \lambda_{mn} = \zeta_m^2 + \lambda_n^2.$$

The Fourier transform $F_{mn}(t)$ have to satisfy the initial conditions

$$F_{mn}(0) = \partial_t F_{mn}(0) = 0. \quad (18)$$

We apply LT to Eq. (17) and using initial conditions (18) to get

$$\bar{F}_{mn}(s) = \frac{v\lambda_{mn}U[1 - (-1)^m][1 + iw\theta][1 - (-1)^n]}{\zeta_m\lambda_n(s - iw)[(1 + \lambda)(s + H) + v(1 + \theta s)(\lambda_{mn} + K)]}. \quad (19)$$

We will apply the discrete inverse LT technique [20] to obtain analytic solution for the velocity fields and to avoid difficult calculations of residues and contour integrals, but first we express Eq. (19) in series form as

$$\begin{aligned} \bar{F}_{mn}(s) &= \frac{v\lambda_{mn}U[1 - (-1)^m][1 + iw\theta][1 - (-1)^n]}{\zeta_m\lambda_n(s - iw)} \sum_{p=0}^{\infty} \sum_{q=0}^{\infty} \sum_{r=0}^{\infty} \sum_{s=0}^{\infty} \sum_{l=0}^{\infty} \\ &\times \frac{v^{p+1}\lambda^s\theta^q K^{p-r}H^l(\lambda_{mn})^{r+1}\Gamma(q-p)\Gamma(r-p)\Gamma(s+p+1)\Gamma(l+p+1)}{(-1)^{-(p+q+r+s+l)}q!r!s!!\Gamma(p)\Gamma(p)\Gamma(1+p)\Gamma(1+p)s^{l-q+p+1}}. \end{aligned} \quad (20)$$

We apply the discrete inverse LT to Eq. (20), to obtain

$$\begin{aligned} F_{mn}(t) &= \frac{e^{iwt}U[1 - (-1)^m][1 - (-1)^n]v\lambda_{mn}(1 + iw\theta)}{\zeta_m\lambda_n} \sum_{p=0}^{\infty} \sum_{q=0}^{\infty} \sum_{r=0}^{\infty} \sum_{s=0}^{\infty} \sum_{l=0}^{\infty} \\ &\times \frac{v^{p+1}\lambda^s\theta^q K^{p-r}H^l(\lambda_{mn})^{r+1}\Gamma(q-p)\Gamma(r-p)\Gamma(s+p+1)\Gamma(l+p+1)t^{l-q+p}}{(-1)^{-(p+q+r+s+l)}q!r!s!!\Gamma(p)\Gamma(p)\Gamma(1+p)\Gamma(1+p)\Gamma l - q + p + 1}. \end{aligned} \quad (21)$$

Taking the inverse Fourier sine transform we get the analytic solution of the velocity field

$$\begin{aligned} F(x, y, t) &= \frac{4}{dh} \sum_{m=1}^{\infty} \sum_{n=1}^{\infty} \sin(\zeta_m x) \sin(\lambda_n y) F_{mn}(x, y, t) \\ &= \frac{4e^{iwt}U(1 + iw\theta)}{dh} \sum_{m=1}^{\infty} \sum_{n=1}^{\infty} \frac{[1 - (-1)^m][1 - (-1)^n] \sin(\zeta_m x) \sin(\lambda_n y)}{\zeta_m\lambda_n} \\ &\times \sum_{p=0}^{\infty} \sum_{q=0}^{\infty} \sum_{r=0}^{\infty} \sum_{s=0}^{\infty} \sum_{l=0}^{\infty} \frac{v^{p+1}\lambda^s\theta^q K^{p-r}H^l(\lambda_{mn})^{r+1}t^{l-q+p}}{(-1)^{-(p+q+r+s+l)}q!r!s!!} \\ &\times \frac{\Gamma(q-p)\Gamma(r-p)\Gamma(s+p+1)\Gamma(l+p+1)}{\Gamma(p)\Gamma(p)\Gamma(1+p)\Gamma(1+p)\Gamma l - q + p + 1}. \end{aligned} \quad (22)$$

To obtain a more compact form of velocity field we write Eq. (22) in terms of Fox H-function,

$$\begin{aligned}
 F(x, y, t) = & \frac{4e^{iwt}U(1+iw\theta)}{dh} \sum_{m=1}^{\infty} \sum_{n=1}^{\infty} \frac{\sin(\zeta_m x) \sin(\lambda_n y) [1 - (-1)^m][1 - (-1)^n]}{\zeta_m \lambda_n} \\
 & \times \sum_{p=0}^{\infty} \sum_{q=0}^{\infty} \sum_{r=0}^{\infty} \sum_{s=0}^{\infty} \frac{(-1)^{p+q+r+s} \nu^{p+1} \lambda^s \theta^q K^{p-r} (\lambda_{mn})^{r+1} t^{-q+p}}{q!r!s!} \\
 & \times H_{4,6}^{1,4} \left[Ht \left| \begin{array}{c} (1-q+p, 0), (1-r+p, 0), (-s-p, 0), (-p, 1) \\ (0, 1), (1-p, 0), (1-p, 0), (-p, 0), (-p, 0), (q-p, 1) \end{array} \right. \right].
 \end{aligned} \tag{23}$$

or

$$\begin{aligned}
 F(x, y, t) = & \frac{16e^{iwt}U(1+iw\theta)}{dh} \sum_{c=0}^{\infty} \sum_{e=0}^{\infty} \frac{\sin(\zeta_c x) \sin(\lambda_e y)}{\zeta_c \lambda_e} \\
 & \times \sum_{p=0}^{\infty} \sum_{q=0}^{\infty} \sum_{r=0}^{\infty} \sum_{s=0}^{\infty} \frac{(-1)^{p+q+r+s} \nu^{p+1} \lambda^s \theta^q K^{p-r} (\lambda_{ce})^{r+1} t^{-q+p}}{q!r!s!} \\
 & \times H_{4,6}^{1,4} \left[Ht \left| \begin{array}{c} (1-q+p, 0), (1-r+p, 0), (1-s-p, 0), (-p, 1) \\ (0, 1), (1-p, 0), (1-p, 0), (-p, 0), (-p, 0), (q-p, 1) \end{array} \right. \right],
 \end{aligned} \tag{24}$$

where

$$\zeta_c = (2m+1) \frac{\pi}{d}, \lambda_e = (2n+1) \frac{\pi}{h}, c = 2m+1, e = 2n+1.$$

From Eq. (24), we obtain the velocity field due to cosine oscillations of the duct

$$\begin{aligned}
 u(x, y, t) = & \frac{16U(\cos(wt) - w\theta \sin(wt))}{dh} \sum_{c=0}^{\infty} \sum_{e=0}^{\infty} \frac{\sin(\zeta_c x) \sin(\lambda_e y)}{\zeta_c \lambda_e} \\
 & \times \sum_{p=0}^{\infty} \sum_{q=0}^{\infty} \sum_{r=0}^{\infty} \sum_{s=0}^{\infty} \frac{(-1)^{p+q+r+s} \nu^{p+1} \lambda^s \theta^q K^{p-r} (\lambda_{ce})^{r+1} t^{-q+p}}{q!r!s!} \\
 & \times H_{4,6}^{1,4} \left[Ht \left| \begin{array}{c} (1-q+p, 0), (1-r+p, 0), (1-s-p, 0), (-p, 1) \\ (0, 1), (1-p, 0), (1-p, 0), (-p, 0), (-p, 0), (q-p, 1) \end{array} \right. \right],
 \end{aligned} \tag{25}$$

and the velocity field due to sine oscillations of the duct

$$\begin{aligned}
 v(x, y, t) = & \frac{16U(\sin(wt) - w\theta \cos(wt))}{dh} \sum_{c=0}^{\infty} \sum_{e=0}^{\infty} \frac{\sin(\zeta_c x) \sin(\lambda_e y)}{\zeta_c \lambda_e} \\
 & \times \sum_{p=0}^{\infty} \sum_{q=0}^{\infty} \sum_{r=0}^{\infty} \sum_{s=0}^{\infty} \frac{(-1)^{p+q+r+s} \nu^{p+1} \lambda^s \theta^q K^{p-r} (\lambda_{ce})^{r+1} t^{-q+p}}{q!r!s!} \\
 & \times H_{4,6}^{1,4} \left[Ht \left| \begin{array}{c} (1-q+p, 0), (1-r+p, 0), (1-s-p, 0), (-p, 1) \\ (0, 1), (1-p, 0), (1-p, 0), (-p, 0), (-p, 0), (q-p, 1) \end{array} \right. \right].
 \end{aligned} \tag{26}$$

We use the following property of the Fox H-function [21] in the above equation

$$H_{p,q+1}^{1,p} \left[-\chi \left| \begin{matrix} (1-a_1, A_1), (1-a_2, A_2), \dots, (1-a_p, A_p) \\ (1, 0), (1-b_1, B_1), \dots, (1-b_q, B_q) \end{matrix} \right. \right] \\ = \sum_{k=0}^{\infty} \frac{\Gamma(a_1 + A_1 k) \dots \Gamma(a_p + A_p k)}{k! \Gamma(b_1 + B_1 k) \dots \Gamma(b_q + B_q k)} \chi^k.$$

5. Calculation of the shear stress

We denote the tangential tensions for the cosine oscillations of the duct by $\tau_{1c}(x, y, t)$, $\tau_{2c}(x, y, t)$ and for sine oscillations by $\tau_{1s}(x, y, t)$, $\tau_{2s}(x, y, t)$.

If we introduce

$$\tau_1(x, y, t) = \tau_{1c}(x, y, t) + i\tau_{1s}(x, y, t), \quad (27)$$

$$\tau_2(x, y, t) = \tau_{2c}(x, y, t) + i\tau_{2s}(x, y, t), \quad (28)$$

in Eq. (7), we get

$$\tau_1(x, y, t) = \frac{\mu}{(1+\lambda)} \left(1 + \theta \frac{\partial}{\partial t} \right) \partial_x F(x, y, t), \quad (29)$$

$$\tau_2(x, y, t) = \frac{\mu}{(1+\lambda)} \left(1 + \theta \frac{\partial}{\partial t} \right) \partial_y F(x, y, t). \quad (30)$$

We apply LT to Eqs. (29) and (30), to obtain

$$\bar{\tau}_1(x, y, s) = \frac{\mu(1+\theta s)}{1+\lambda} \partial_x \bar{F}(x, y, s), \quad (31)$$

$$\bar{\tau}_2(x, y, s) = \frac{\mu(1+\theta s)}{1+\lambda} \partial_y \bar{F}(x, y, s). \quad (32)$$

Taking the inverse Fourier transform of Eq. (19) to get $\bar{F}(x, y, s)$ and then by putting it into Eq. (31), we get

$$\bar{\tau}_1(x, y, s) = \frac{4\mu(1+\theta s)}{dh(1+\lambda)} \sum_{m=1}^{\infty} \sum_{n=1}^{\infty} \frac{\cos(\zeta_m x) \sin(\lambda_n y) [1 - (-1)^m][1 - (-1)^n]}{[(1+\lambda)(s+H) + \nu(1+\theta s)(\lambda_{mn} + K)]} \\ \times \frac{U\nu\lambda_{mn}(1+iw\theta)}{\lambda_n(s-iw)}, \quad (33)$$

or

$$\bar{\tau}_1(x, y, s) = \frac{16\mu(1+\theta s)}{dh(1+\lambda)} \sum_{c=0}^{\infty} \sum_{e=0}^{\infty} \frac{\cos(\zeta_c x) \sin(\lambda_e y) U\nu\lambda_{ce}(1+iw\theta)}{\lambda_e(s-iw)[(1+\lambda)(s+H) + \nu(1+\theta s)(\lambda_{ce} + K)]}, \quad (34)$$

where

$$\zeta_c = (2m+1)\frac{\pi}{d}, \lambda_e = (2n+1)\frac{\pi}{h}, c = 2m+1, e = 2n+1.$$

We express Eq. (34) in series form in order to obtain a more suitable form of τ_1 ,

$$\begin{aligned} \bar{\tau}_1(x, y, s) &= \frac{16\mu U(1+iw\theta)}{dh(s-iw)} \sum_{c=0}^{\infty} \sum_{e=0}^{\infty} \frac{\cos(\zeta_c x) \sin(\lambda_e y)}{\lambda_e} \sum_{p=0}^{\infty} \sum_{q=0}^{\infty} \sum_{r=0}^{\infty} \sum_{s=0}^{\infty} \sum_{l=0}^{\infty} \\ &\times \frac{\nu^{p+1} \lambda^s \theta^q K^{p-r} H^l(\lambda_{ce})^{r+1} \Gamma(q-p-1) \Gamma(r-p) \Gamma(s+p+2) \Gamma(l+p+1)}{(-1)^{-(p+q+r+s+l)} q! r! s! l! \Gamma(p) \Gamma(p+1) \Gamma(2+p) \Gamma(1+p) s^{l-q+p+1}}. \end{aligned} \quad (35)$$

Using the inverse LT of the last equation, we obtain

$$\begin{aligned} \tau_1(x, y, t) &= \frac{16\mu e^{iwt} U(1+iw\theta)}{dh} \sum_{c=0}^{\infty} \sum_{e=0}^{\infty} \frac{\cos(\zeta_c x) \sin(\lambda_e y)}{\lambda_e} \sum_{p=0}^{\infty} \sum_{q=0}^{\infty} \sum_{r=0}^{\infty} \sum_{s=0}^{\infty} \\ &\times \sum_{l=0}^{\infty} \frac{\nu^{p+1} \lambda^s \theta^q K^{p-r} H^l(\lambda_{ce})^{r+1} t^{l-q+p} \Gamma(q-p-1) \Gamma(s+p+2)}{(-1)^{-(p+q+r+s+l)} q! r! s! l! \Gamma(p) \Gamma(p+1) \Gamma(2+p) \Gamma(1+p)} \\ &\times \frac{\Gamma(l+p+1)}{\Gamma(l-q+p+1)}. \end{aligned} \quad (36)$$

Lastly, we write the stress field in a more compact form by using Fox H-function

$$\begin{aligned} \tau_1(x, y, t) &= \frac{16\mu e^{iwt} U(1+iw\theta)}{dh} \sum_{c=0}^{\infty} \sum_{e=0}^{\infty} \frac{\cos(\zeta_c x) \sin(\lambda_e y)}{\lambda_e} \sum_{p=0}^{\infty} \\ &\times \sum_{q=0}^{\infty} \sum_{r=0}^{\infty} \sum_{s=0}^{\infty} \frac{\nu^{p+1} \lambda^s \theta^q K^{p-r} (\lambda_{mm})^{r+1} t^{-q+p}}{(-1)^{-(p+q+r+s)} q! r! s!} \\ &\times H_{4,6}^{1,4} \left[Ht \left| \begin{array}{l} (2-q+p, 0), (1-r+p, 0), (-1-s-p, 0), (-p, 1) \\ (0, 1), (-p, 0), (-1-p, 0), (-p, 0), (-p, 0), (q-p, 1) \end{array} \right. \right]. \end{aligned} \quad (37)$$

From Eq. (37), we obtain the tangential tension due to cosine oscillations of the duct

$$\begin{aligned} \tau_{1c}(x, y, t) &= \frac{16U\mu(\cos(wt) - w\theta \sin(wt))}{dh} \sum_{c=0}^{\infty} \sum_{e=0}^{\infty} \frac{\cos(\zeta_c x) \sin(\lambda_e y)}{\lambda_e} \\ &\times \sum_{p=0}^{\infty} \sum_{q=0}^{\infty} \sum_{r=0}^{\infty} \sum_{s=0}^{\infty} \frac{(-1)^{p+q+r+s} \nu^{p+1} \lambda^s \theta^q K^{p-r} (\lambda_{mm})^{r+1} t^{-q+p}}{q! r! s!} \\ &\times H_{4,6}^{1,4} \left[Ht \left| \begin{array}{l} (2-q+p, 0), (1-r+p, 0), (-1-s-p, 0), (-p, 1) \\ (0, 1), (-p, 0), (-1-p, 0), (-p, 0), (-p, 0), (q-p, 1) \end{array} \right. \right], \end{aligned} \quad (38)$$

and the tangential tension corresponding to sine oscillations of the duct

$$\begin{aligned} \tau_{1s}(x, y, t) = & \frac{16U\mu(\sin(wt) - w\theta \cos(wt))}{dh} \sum_{c=0}^{\infty} \sum_{e=0}^{\infty} \frac{\cos(\zeta_c x) \sin(\lambda_e y)}{\lambda_e} \sum_{p=0}^{\infty} \\ & \times \sum_{q=0}^{\infty} \sum_{r=0}^{\infty} \sum_{s=0}^{\infty} \frac{(-1)^{p+q+r+s} \nu^{p+1} \lambda^s \theta^q K^{p-r} (\lambda_{mn})^{r+1} t^{-q+p}}{q!r!s!} \\ & \times H_{4,6}^{1,4} \left[Ht \left| \begin{matrix} (2-q+p, 0), (1-r+p, 0), (-1-s-p, 0), (-p, 1) \\ (0, 1), (-p, 0), (-1-p, 0), (-p, 0), (-p, 0), (q-p, 1) \end{matrix} \right. \right]. \end{aligned} \quad (39)$$

In the similar fashion we can find $\tau_{2c}(x, y, t)$ and $\tau_{2s}(x, y, t)$ from Eqs. (19) and (32).

6. Volume flux

The volume flux due to cosine oscillations is given by

$$Q_c(x, y, t) = \int_0^d \int_0^h u(x, y, t) dx dy, \quad (40)$$

putting $u(x, y, t)$ from Eq. (25) into the above equation, we obtain the volume flux of the rectangular duct due to cosine oscillations

$$\begin{aligned} u(x, y, t) = & \frac{64U(\cos(wt) - w\theta \sin(wt))}{dh} \sum_{c=0}^{\infty} \sum_{e=0}^{\infty} \frac{1}{(\zeta_c \lambda_e)^2} \\ & \times \sum_{p=0}^{\infty} \sum_{q=0}^{\infty} \sum_{r=0}^{\infty} \sum_{s=0}^{\infty} \frac{\nu^{p+1} \lambda^s \theta^q K^{p-r} (\lambda_{ce})^{r+1} t^{-q+p}}{(-1)^{-(p+q+r+s)} q!r!s!} \\ & \times H_{4,6}^{1,4} \left[Ht \left| \begin{matrix} (1-q+p, 0), (1-r+p, 0), (1-s-p, 0), (-p, 1) \\ (0, 1), (1-p, 0), (1-p, 0), (-p, 0), (-p, 0), (q-p, 1) \end{matrix} \right. \right]. \end{aligned} \quad (41)$$

Similarly, we obtain the volume flux of the rectangular duct due to the sine oscillations

$$\begin{aligned} v(x, y, t) = & \frac{64U(\sin(wt) - w\theta \cos(wt))}{dh} \sum_{c=0}^{\infty} \sum_{e=0}^{\infty} \frac{1}{(\zeta_c \lambda_e)^2} \\ & \times \sum_{p=0}^{\infty} \sum_{q=0}^{\infty} \sum_{r=0}^{\infty} \sum_{s=0}^{\infty} \frac{\nu^{p+1} \lambda^s \theta^q K^{p-r} (\lambda_{ce})^{r+1} t^{-q+p}}{(-1)^{-(p+q+r+s)} q!r!s!} \\ & \times H_{4,6}^{1,4} \left[Ht \left| \begin{matrix} (1-q+p, 0), (1-r+p, 0), (1-s-p, 0), (-p, 1) \\ (0, 1), (1-p, 0), (1-p, 0), (-p, 0), (-p, 0), (q-p, 1) \end{matrix} \right. \right]. \end{aligned} \quad (42)$$

7. Numerical results and discussion

We have presented flow problem of MHD Jeffrey fluid passing through a porous rectangular duct. Exact analytical solutions are established for such flow problem using DFFST and LT

technique. The obtained solutions are expressed in series form using Fox H-functions. Several graphs are presented here for the analysis of some important physical aspects of the obtained solutions. The numerical results show the profiles of velocity and the adequate shear stress for the flow. We analyze these results by varying different parameters of interest.

The effects of relaxation time λ of the model are important for us to be discuss. In **Figure 1** we depict the profiles of velocity and shear stress for three different values of λ . It is observed from these figures that the flow velocity as well as the shear stress decreases with increasing λ , which corresponds to the shear thickening phenomenon. **Figure 2** are sketched to show the velocity and the shear stress profiles at different values of retardation time θ . It is noticeable that velocity as well as the shear stress decreases by increasing θ . In order to study the effect of frequency of oscillation ω , we have plotted **Figure 3**, where it appears that the velocity is also a strong function of ω of the Jeffrey fluid. The effect of frequency of oscillation on the velocity profile for cosine oscillation is same as that of the retardation time θ . The effect of magnetic parameter H of the model is important for us to be discussed. In **Figure 4**,

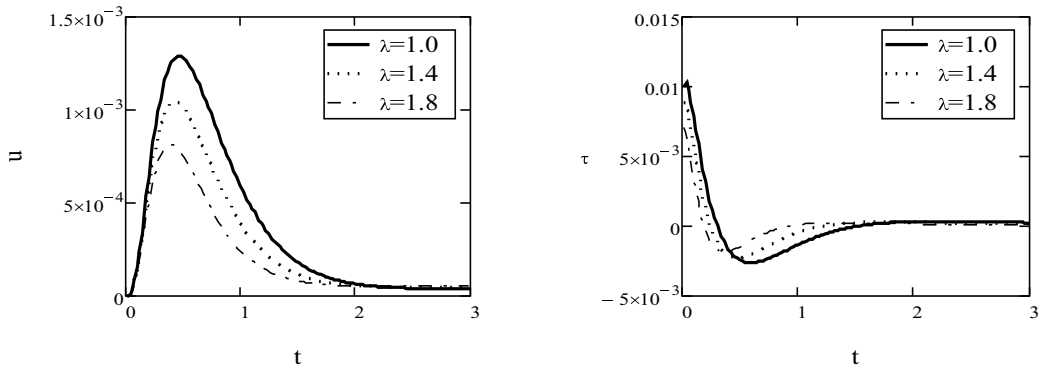


Figure 1. Velocity and shear stress profiles corresponding to the cosine oscillations of the duct for different values of λ . Other parameters are taken as $x = 0.5$, $y = 0.3$, $U = 0.2$, $H = 0.5$, $K = 0.6$, $d = 1$, $h = 2$, $\theta = 0.6$, $\omega = 0.5$ and $\nu = 0.1$.

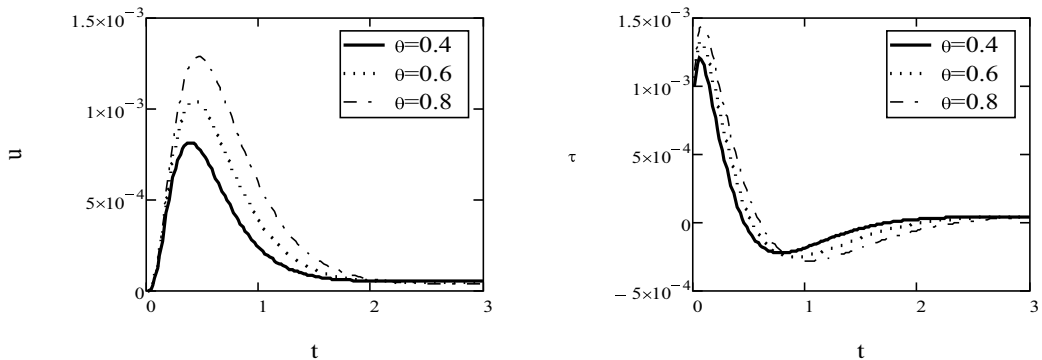


Figure 2. Velocity and shear stress profiles corresponding to the cosine oscillations of the duct for different values of θ . Other parameters are taken as $x = 0.5$, $y = 0.3$, $U = 0.2$, $H = 0.5$, $K = 0.6$, $d = 1$, $h = 2$, $\lambda = 1.4$, $\omega = 0.5$ and $\nu = 0.1$.

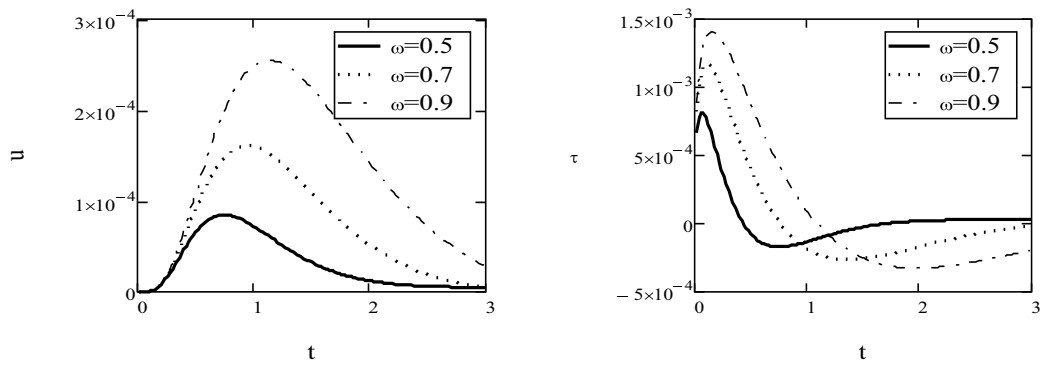


Figure 3. Velocity and shear stress profiles corresponding to the cosine oscillations of the duct for different values of ω . Other parameters are taken as $x = 0.5$, $y = 0.3$, $U = 0.2$, $H = 0.5$, $K = 0.6$, $d = 1$, $h = 2$, $\theta = 0.6$, $\lambda = 1.4$ and $\nu = 0.1$.

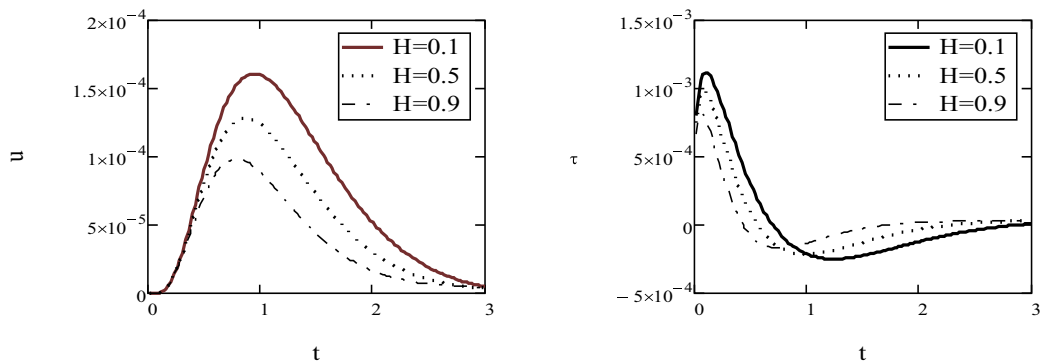


Figure 4. Velocity and shear stress profiles corresponding to the cosine oscillations of the duct for different values of H . Other parameters are taken as $x = 0.5$, $y = 0.3$, $U = 0.2$, $\lambda = 1.4$, $K = 0.6$, $d = 1$, $h = 2$, $\theta = 0.6$, $\omega = 0.5$ and $\nu = 0.1$.

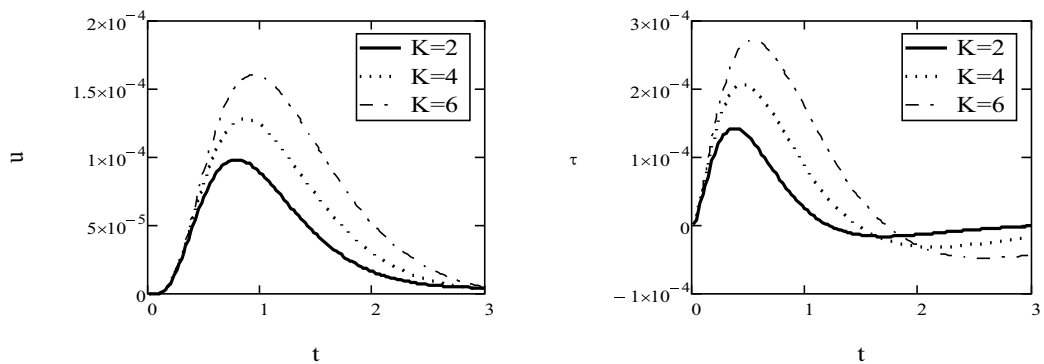


Figure 5. Velocity and shear stress profiles corresponding to the cosine oscillations of the duct for different values of K . Other parameters are taken as $x = 0.5$, $y = 0.3$, $U = 0.2$, $H = 0.5$, $\lambda = 1.4$, $d = 1$, $h = 2$, $\theta = 0.6$, $\omega = 0.5$ and $\nu = 0.1$.

we depict the profiles of velocity and shear stress for three different values of H . It is observed from these figures that the flow velocity as well as the shear stress decreases with increasing H , which corresponds to the shear thickening phenomenon. **Figure 5** is sketched to show the velocity and the shear stress profiles at different values of K . It is noticeable that velocity as well as the shear stress increases by increasing K . In order to study the effects of t , we have plotted **Figure 6**, where it appears that the velocity is also a strong function of t of the Jeffrey fluid. It can be observed that the increase of t acts as an increase of the magnitude of velocity components near the plate, and this corresponds to the shear-thinning behavior of the examined non-Newtonian fluid. **Figure 7** presents the velocity field and the shear stress profiles at different values of y . It is noticeable that velocity and shear stress both decreases by increasing y .

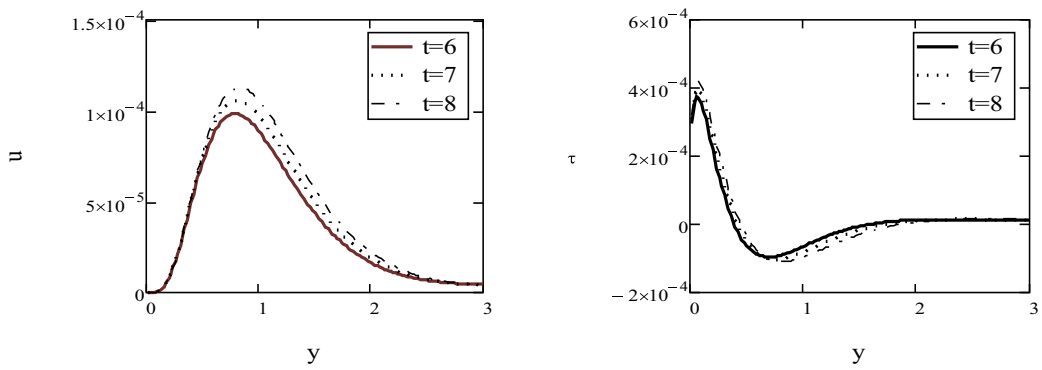


Figure 6. Velocity and shear stress profiles corresponding to the cosine oscillations of the duct for different values of t . Other parameters are taken as $\alpha = 0.5$, $\lambda = 1.4$, $U = 0.2$, $H = 0.5$, $K = 0.6$, $d = 1$, $h = 2$, $\theta = 0.6$, $\omega = 0.5$ and $\nu = 0.1$.

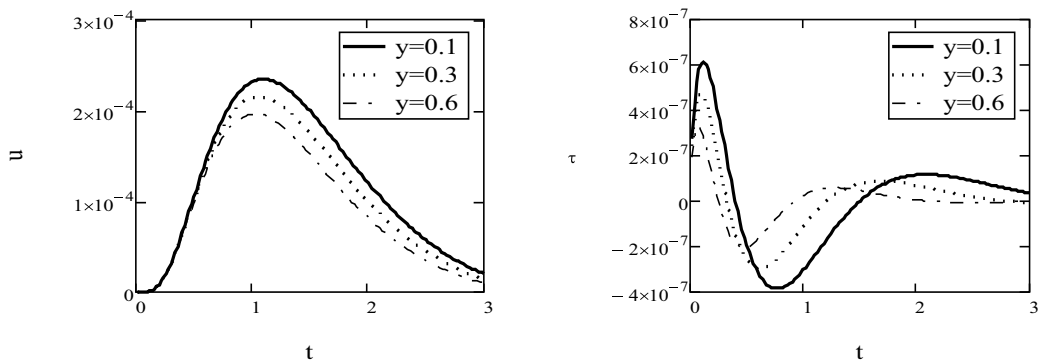


Figure 7. Velocity and shear stress profiles corresponding to the cosine oscillations of the duct for different values of y . Other parameters are taken as $\alpha = 0.5$, $\lambda = 1.4$, $U = 0.2$, $H = 0.5$, $K = 0.6$, $d = 1$, $h = 2$, $\theta = 0.6$, $\omega = 0.5$ and $\nu = 0.1$.

Author details

Amir Khan^{1,2*}, Gul Zaman¹ and Obaid Algahtani³

*Address all correspondence to: amir.maths@gmail.com

1 Department of Mathematics, University of Malakand, Chakdara, Dir (Lower), Khyber Pakhtunkhwa, Pakistan

2 Department of Mathematics and Statistics, University of Swat, Khyber Pakhtunkhwa, Pakistan

3 Department of Mathematics, Science College, King Saud University, Saudi Arabia

References

- [1] Rajagopal KR, Srinivasa A. Exact solutions for some simple flows of an Oldroyd-B fluid. *Acta Mechanica*. 1995;**113**:233-239
- [2] Tan WC, Masuoka T. Stoke's first problem for second grade fluid in a porous half space. *International Journal of Non-Linear Mechanics*. 2005;**40**:515-522
- [3] Tan WC, Masuoka T. Stoke's first problem for an Oldroyd-B fluid in a porous half space. *Physics of Fluids*. 2005;**17**:023101
- [4] Khadrawi AF, Al-Nimr MA, Othman A. Basic viscoelastic fluid problems using the Jeffreys model. *Chemical Engineering Science*. 2005;**60**:7131-7136
- [5] Chen CI, Chen CK, Yang YT. Unsteady unidirectional flow of an Oldroyd-B fluid in a circular duct with different given volume flow rate. *International Journal of Heat and Mass Transfer*. 2004;**40**:203-209
- [6] Nadeem S, Hussain A, Khan M. Stagnation flow of a Jeffrey fluid over a shrinking sheet. *Zeitschrift für Naturforschung*. 2010;**65a**:540-548
- [7] Khan M. Partial slip effects on the oscillatory flows of a fractional Jeffrey fluid in a porous medium. *Journal of Porous Media*. 2007;**10**:473-487
- [8] Hayat T, Khan M, Fakhar K, Amin N. Oscillatory rotating flows of a fractional Jeffrey fluid filling a porous medium. *Journal of Porous Media*. 2010;**13**(1):29-38
- [9] Khan M, Iftikhar F, Anjum A. Some unsteady flows of a Jeffrey fluid between two side walls over a plane wall. *Zeitschrift für Naturforschung*. 2011;**66**(a):745-752
- [10] Gardner LRT, Gardner GA. A two-dimensional bi-cubic B-spline finite element used in a study of MHD duct flow. *Computer Methods in Applied Mechanics and Engineering*. 1995;**124**:365-375

- [11] Fetecau C, Fetecau C. Unsteady flows of Oldroyd-B fluids in a channel of rectangular cross-section. *International Journal of Non-Linear Mechanics*. 2005;**40**:1214-1219
- [12] Nazar M, Shahid F, Akram S, Sultan Q. Flow on oscillating rectangular duct for Maxwell fluid. *Applied Mathematics and Mechanics (English Edition)*. 2012;**33**:717-730
- [13] Sultan Q, Nazar M, Akhtar W, Ali U. Unsteady flow of a Maxwell fluid in a porous rectangular duct. *Scientific International Journal*. 2013;**25**(2):181-194
- [14] Tsangaris S, Vlachakis NW. Exact solution of the Navier-Stokes equations for the oscillating flow in a duct of a cross-section of right-angled isosceles triangle. *Zeitschrift für Angewandte Mathematik und Physik*. 2003;**54**:1094-1100
- [15] Vajravelu K. Hydromagnetic flow and heat transfer over a continuous moving porous flat surface. *Acta Mechanica*. 1986;**64**:179-185
- [16] Amakiri ARC, Ogulu A. The effect of viscous dissipative heat and uniform magnetic field on the free convective flow through a porous medium with heat generation/absorption. *European Journal of Scientific Research*. 2006;**15**(4):436-445
- [17] Singh KD. Exact solution of an oscillatory MHD flow in a channel filled with porous medium. *International Journal of Applied Mechanics and Engineering*. 2011;**16**:277-283
- [18] Samiulhaq, Fetecau, Khan I, Ali F, Shafie S. Radiation and porosity effects on the magnetohydrodynamic flow past an oscillating vertical plate with uniform heat flux. *Zeitschrift für Naturforschung*. 2012;**67**(a):572-580
- [19] Khan I, Fakhar K, Shafie S. Magnetohydrodynamic free convection flow past an oscillating plate embedded in a porous medium. *Journal of the Physical Society of Japan*. 2011;**80**:104-110
- [20] Sneddon IN. *Fourier Transforms*. New York: McGraw-Hill; 1951
- [21] Mathai AM, Saxena RK, Haubold HJ. *The H-functions: Theory and Applications*. New York: Springer; 2010

Porosity Effect on the Materials Properties

Porous Structures in Heat Pipes

Patrik Nemec

Additional information is available at the end of the chapter

<http://dx.doi.org/10.5772/intechopen.71763>

Abstract

This work deals with heat pipes with porous wick structures and experiments depending on the wick structure porosity, because the porosity is one of the wick structure properties which has effect on the heat transport ability of the heat pipe. The work describes manufacturing porous wick structures for wick heat pipe by sintering of copper metal powders with various powder grain size; manufacturing porous wick structures for loop heat pipe by sintering of copper and nickel metal powders with various powder grain size; influence of manufacturing technology on the wick structure porosity by microscopic analysis of the porous structure; design and construction of wick heat pipe and loop heat pipes; experimental determination influence of the wick structure porosity on the heat transport ability of loop heat pipes at various conditions; and experimental and mathematical determination influence of the wick structure porosity on the heat transport ability of wick heat pipes at various conditions.

Keywords: wick heat pipe, loop heat pipe, wick structure, porosity, sintering, copper powder, nickel powder, heat transfer, thermal performance, mathematical calculation

1. Introduction

Two-phase heat transfer systems with capillary-driven offer important advantages over traditional single-phase systems. The most significant advantage associated with the phase change of a working fluid is higher heat transfer coefficient that results in enhanced heat transfer. Comparing with the single-phase liquid system, smaller mass flow rates are required to transport equivalent heat flux amounts for a given temperature range. Better thermal characteristics and lower mass flow rates offer the two-phase system benefit of smaller and lighter construction and increased performance. Single-phase system requires a high temperature gradient or a high mass flow rate to transfer high amount of heat flux, because thermal capacity of a single-phase system depends on the temperature change of the working fluid. The two-phase system provides essentially isothermal operation regardless of the heat load.

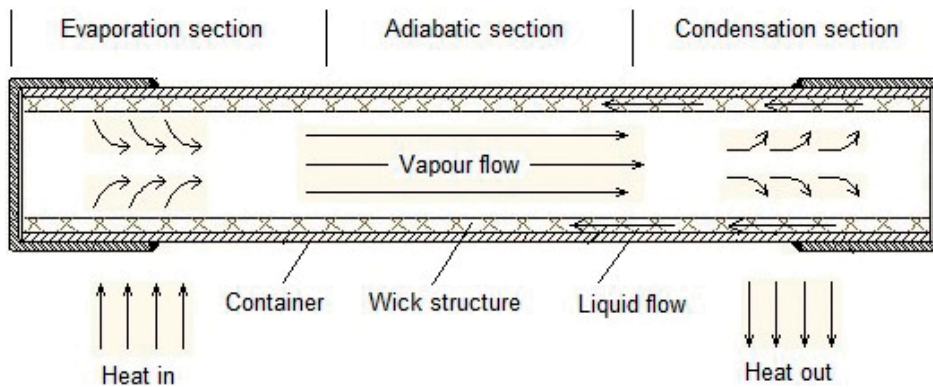


Figure 1. Schema of heat pipe.

Additionally, the single-phase systems need to working fluid circulation mechanical pumps or fans, while in the capillary-driven two-phase systems the working fluid circulate without any additional mechanical devices, which make such systems more reliable and free of electric power. The best known capillary-driven two-phase system is heat pipe and its schema is shown in **Figure 1**. The concept of the heat pipe was first suggested by Gaugler in 1944 [1] and by Trefethen [2] but was not widely publicized until serious development work by Grover and his co-worker in Los Alamos laboratory [3]. Heat pipes are passive heat transfer devices that transport heat from one point (heat source) to another (heat sink) with extremely high thermal conductance due the latent heat of vaporization of a working fluid. As shown in **Figure 1**, it consists of container, working fluid, wick structure and has three sections (an evaporator section, an adiabatic section, and a condenser section) [4].

Since one of the most important parts of the heat pipe HP and loop heat pipe LHP is the porous wick structure, this work is focused on experiments influencing porous wick structure on the heat transport ability of the heat pipe and loop heat pipe.

2. Heat pipe

The heat pipe is heat transfer device using the phase-change of working fluid to transfer heat from a heat source to heat sink and capillary forces generated in the wick structure to working fluid circulation. The heat pipe consists of hermetically closed container with wick structure on the inner surface and working fluid near its saturation temperature. Heat absorbed through the container to the liquid in the evaporator causes liquid evaporation and vapor flow through the open core of the heat pipe evaporator. The vapor flows out of the evaporator through the adiabatic section into the condenser. There the vapor condenses and released heat is transfer through wick structure and container wall into condenser ambient. Condensed liquid saturates the wick structure and creates capillary pressure; thus the liquid is pumped back into the evaporator. The operation of the heat pipe depends mainly on the parameters of container, working fluid and wick structure. Proper selection and design of the main heat pipe parts influence its operational characteristics defined by the heat transfer limitations, effective

thermal conductivity, and axial temperature difference. The two-phase heat transfer of the working fluid makes a heat pipe ideal for transferring heat over long distances with a very small temperature drop due the temperature stabilization of the almost isothermal surface created during the operation. Almost isothermal condition of the heat pipe operation are related to working fluid operation in thermodynamic saturated state when the heat is transported using the latent heat of vaporization instead of sensible heat or conduction. Heat transported using the latent heat of vaporization is several times greater than heat transported by sensible heat for a geometrically equivalent system. The two-phase capillary-driven working fluid system allows efficiently to transfer large amounts of heat without additional mechanical pumping systems, decreasing the heat transfer area and thus saving the material, cost and weight. Wide range of the usable working fluid, high efficiencies, low dimensions and weights, and the absence of external pumps make heat pipes attractive options in a wide range of heat transfer applications [4].

2.1. Heat pipe construction

The heat pipe may have several basic parts depending on its type. During the heat pipe development, the main components and materials remained the same. The simplest type of heat pipe consists of two basic parts, the body (container) and the working medium. A capillary structure (wick) can be placed inside the heat pipe body to allow the condensed liquid phase of the working fluid wicking against the vapor flow due the capillary action. Such a heat pipe is called a wick heat pipe. The heat pipe without capillary structure, is called gravitational heat pipe because it returns the liquid phase from the condenser part to the evaporator part which is due to gravity [5].

2.1.1. Container

The container of the heat pipe can have different shapes for different applications, but the most often is in the form of a closed pipe of a circular, flat or triangular cross-section. The main function of the heat pipe container is to isolate the working fluid from the outside environment. The container of the heat pipe should be strong enough to prevent internal dimension and internal pressure in case of compression or bending. The choice of the container material depends on many properties and should have the most appropriate combination (working fluid and environment compatibility, strength-to-weight ratio, thermal conductivity, porosity, wettability, machinability, formability, weldability or bondability). The container material should have a high thermal conductivity, solid and tough but easily machined, formable and easily soldered and welded. The surface of the material should be well-wetted, but at least as porous as possible to avoid gas diffusion. The materials of heat pipes are most commonly made of steel, copper, aluminum and their alloys. Various coatings of steel materials are also used [6].

2.1.2. Working fluid

Since the operation of the heat pipe is based on evaporation and condensation of the working fluid, its selection is an important factor in the design and manufacture of the heat pipe. The working fluid is chosen in particular according to the working temperature range of the heat pipe. Therefore, when selecting a working fluid, it is necessary to be careful if the operating temperature

range of the working fluid lies in the operating temperature range of the heat pipe. The heat pipe can operate at any temperature that is in the range between the triple and the critical point of the working fluid. The decision criterion at working fluid selection, in case of working fluids with the same operating temperature, is an appropriate combination of working fluid thermodynamics properties. The recommended features that working fluid should have are compatibility with the capillary structure material and the heat pipe container, good thermal stability, wettability of the capillary structure and heat pipe container, vapor pressure in the operating temperature range, high surface tension, low viscosity of the liquid and vapor phase, high thermal conductivity, high latent heat of vaporization, acceptable melting point and solidification point [6]. **Table 1** shows typical heat pipes working fluids sorted by operating temperature range.

2.1.3. Wick structures

The wick structure and working fluid generate the capillary forces that are required to pump liquid from the condenser to the evaporator and keep liquid evenly distributed in the wicking material. Heat pipe wicks can be classified as either homogeneous wicks or composite wicks. Homogeneous wicks are composed of a single material and configuration. The most common types of homogeneous wicks are wrapped screen, sintered metal and axial groove. Composite wicks are composed of two or more materials and configurations. The most common types of composite wicks are variable screen mesh, screen-covered groove, screen slab with grooves, and screen tunnel with grooves. Regardless of the wick configuration, the desired material properties and structural characteristics of heat pipe wick structures are a high thermal conductivity, high wick porosity, small capillary radius, and high wick permeability [6].

Working fluid	Melting point at atmospheric pressure (°C)	Boiling point at atmospheric pressure (°C)	Latent heat of vaporization (kJ kg ⁻¹)	Useful range (°C)
Helium	-271	-269	21	-271 to -269
Nitrogen	-210	-196	198	-203 to -160
Ammonia	-78	-33	1360	-60 to 100
Acetone	-95	57	518	0 to 120
Methanol	-98	64	1093	10 to 130
Ethanol	-112	78	850	0 to 130
Water	0	100	2260	30 to 200
Mercury	-39	361	298	250 to 650
Caesium	29	670	490	450 to 900
Potassium	62	774	1938	500 to 1000
Sodium	98	895	3913	600 to 1200
Lithium	179	1340	19,700	1000 to 1800
Silver	960	2212	2350	1800 to 2300

Table 1. Typical heat pipe working fluids.

2.2. Operation of heat pipe

In order of the heat pipe operation, the maximum capillary pressure must be greater than the total pressure drop in heat pipe.

Total pressure drop in heat pipe consist of three sections:

1. ΔP_l is pressure drop in the wick structure necessary to return the liquid from the condenser to the evaporator.
2. ΔP_v is pressure drop in the vapor core necessary to vapor flow from the evaporator to the condenser.
3. ΔP_g is pressure drop due gravity, depending on the heat pipe inclination that may be zero, positive or negative.

The correct operation of heat pipe must meet condition of:

$$\Delta P_{c, \max} \geq \Delta P_l + \Delta P_v + \Delta P_g \quad (1)$$

If heat pipe does not meet this condition, it will not operate due to the dry out of the wick in the evaporator section. This condition is referred as the capillary limit which determines the maximum heat flux of majority heat pipe operating range. The vapor velocity of liquid metal heat pipes may reach sonic values at start-up and with certain high-temperature. Then, heat pipe performance is limited by speed of sound, and compressibility effects must be taken into account in the calculation of the vapor pressure drop. Other most important limitations are the vapor pressure or viscous limit which occur at heat pipe stat-up when the heat pipe operates at low temperature. However the condenser pressure cannot be less than zero, the low vapor pressure of the liquid in the evaporator cause that the vapor pressure difference between evaporator and condenser of the heat pipe is insufficient to overcome viscous and gravitational forces. When the heat pipe operates at high heat fluxes, vapor flow may entrain liquid returning to the evaporator and cause dry out of the evaporator. This condition is referred as an entrainment limitation. Above mentioned limitations of the heat pipe relate to axial flow. During the heat pipe operation, temperature difference of radial heat flux is relatively small. When the heat flux reaches a critical value, the vapor blankets surface of evaporator wall results in an increase in temperature difference in evaporator. Limitation related to the radial flow of the heat pipe is referred as a boiling limit [7].

If stable liquid properties along the pipe, uniform wick structure along the pipe and neglect of pressure drop due to vapor flow are assumed, the total heat flux of heat pipe is given by

$$Q = \dot{m}_{\max} \cdot L. \quad (2)$$

$$\dot{m}_{\max} = \left[\frac{\rho_l \cdot \sigma_l}{\mu_l} \right] \cdot \left[\frac{K \cdot A}{l} \right] \cdot \left[\frac{2}{r_e} - \frac{\rho_l \cdot g \cdot l}{\sigma_l} \cdot \sin \theta \right] \quad (3)$$

3. Loop heat pipe

Loop heat pipe was developed to overcome the inherent problem of incorporating a long wick with small pore radius in conventional heat pipe by Gerasimov and Maydanik in 1972. LHP is a two-phase heat transfer device that utilizes the evaporation and condensation of a working fluid to remove heat and the capillary forces developed in fine porous wicks to circulate the fluid. **Figure 2** shows schema of LHP. It consists of an evaporator with wick structure, a compensation chamber, a condenser, and a liquid and vapor line. Wick structure is only in the evaporator and the compensation chamber. The rest parts of the LHP are made of smooth wall pipe. The wick structure of the evaporator has fine pores to create a capillary pressure and ensure working fluid circulation in the loop. The wick structure of the compensation chamber has larger pores for the purpose to transport working fluid to the evaporator. Heat applied to the evaporator causes that working fluid to start to evaporate and the vapor is pushed through the vapor line to the condenser due the capillary forces in the evaporator wick. Vapor condenses in the condenser and the liquid flows through the liquid line to the compensation chamber. The function of the compensation chamber is to store excess liquid and to control the operating temperature of the loop heat pipe. Thus, working fluid circulates without external pump in the loop [8, 9].

LHP can operate only if the capillary pressure developed in the evaporator wick is greater than the total pressure drop in the loop. The total pressure drop in the loop heat pipe is the sum of frictional pressure drops in the evaporator grooves, the vapor line, the condenser, the liquid line, the evaporator wick, and static pressure drop due to gravity:

$$\Delta P_{total} = \Delta P_{grove} + \Delta P_{vap} + \Delta P_{con} + \Delta P_{liq} + \Delta P_w + \Delta P_g \quad (4)$$

The capillary pressure of the evaporator wick is given by expression

$$\Delta P_{cap} = \frac{2\sigma \cdot \cos \theta}{R} \quad (5)$$

where, σ is the surface tension of the working fluid, θ is the contact angle between the liquid and the wick, and R is the radius of curvature of the meniscus in the wick. Increasing the heat load to the evaporator increases the mass flow rate and the total pressure drop in the system. The reaction to it, is the decrease of radius of curvature of the meniscus so that a capillary pressure will be higher than the pressure drop of total system. Increasing the heat load will decrease radius of curvature of the meniscus until the pore radius of the wick. The maximum capillary pumping capability of the wick is given by expression.

$$\Delta P_{cap, max} = \frac{2\sigma \cdot \cos \theta}{R_v} \quad (6)$$

Further increase of the heat load will lead to vapor penetration through the wick and system deprime. Thus, under normal operation, the following condition must be satisfied at all times [10]:

$$\Delta P_{total} \leq \Delta P_{cap} \quad (7)$$

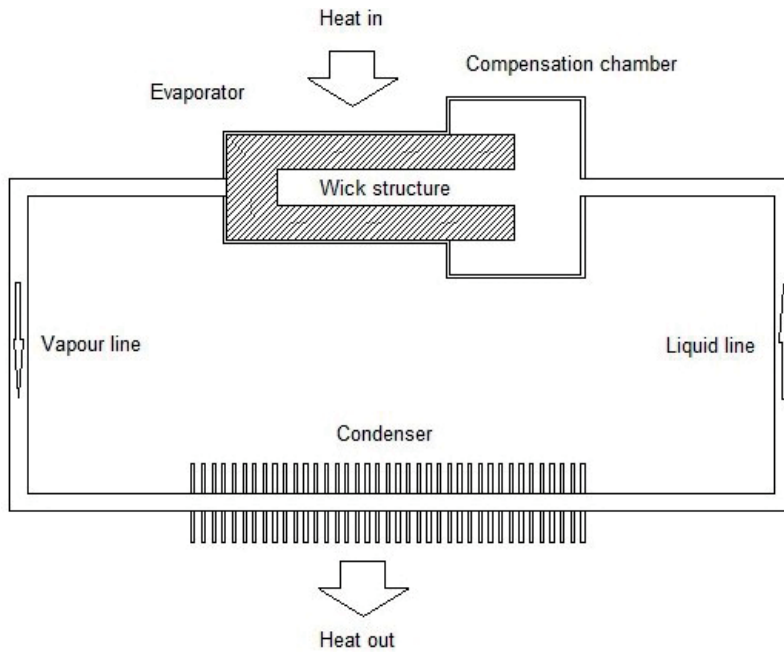


Figure 2. Schema of loop heat pipe.

Williams and Harris [11] investigated the in-plane and cross-plane properties of step-graded metal felt wicks for heat pipe applications. Porosity, effective pore radius, and liquid permeability were determined using imbibition, capillary flow porometry, and pressure-flow rate data, respectively. The authors determined that many of the correlations in the literature for pore size and permeability are too general in nature, echoing the conclusions of Bonnefoy and Ochterbeck [12] in regard to effective thermal conductivity.

Holley and Faghri [13] outlined methods for permeability and effective pore radius measurements based on the rate-of-rise test.

Typically, the rate-of-rise test requires observing the liquid front as it rises in a dry wick partially immersed in a liquid pool. As the precise location of this front can be difficult to detect, the authors devised a method using mass uptake rather than the meniscus front to determine the rate-of-rise of liquid in the wick. By analyzing the climbing meniscus, the authors developed a series of equations which could be used to numerically reduce the mass uptake data to yield permeability and pore size results.

Several relationships for permeability can be found, the most common is the Blake-Kozeny equation [14, 15], which gives the permeability of a bed of packed spheres as

$$K = \frac{r_p^2 \epsilon^3}{37.5(1 - \epsilon)^2} \quad (8)$$

where, K is permeability, r_p is pore radius, and ϵ is porosity.

Ren and Wu [16] modeled the effect of wick effective thermal conductivity in LHP evaporators; a two-dimensional axisymmetric model was developed yielding results in agreement with the literature in some respects, namely the position of the liquid front in relation to a heated fin [17, 18].

Zhao and Liao [18] presented temperature profiles indicating decreasing heat leak for increasing heat flux in a bed of packed spheres.

Iverson et al. [19] studied heat and mass transport in sintered copper wick structures. Wick samples were mounted vertically with the lower section immersed in a pool of water. A heater mounted to the back face of the wick applied power to the sample and the resulting temperature gradients were measured along with the mass flow rate of working fluid.

The majority of heat load is used in vaporization on the outer surface of wick [20]. The rest of heat input (called "heat leak") is conducted across the wick and is proportional to the effective thermal conductivity (ETC) of the capillary wicks [21]. Lower thermal conductivity of the porous wick ensures lesser heat conduction to the liquid inside the wick inner surface and maintains the operating temperature and thus the thermal resistance of the whole LHP.

Ku [10] and Furukawa [22] developed simplest LHP heat leak model that utilizes conductance parameter which varies with geometry and operating conditions.

$$Q_{e,cc} = G_{e,cc}(T_e - T_{cc}) \quad (9)$$

where Q is power, G is conductance parameter, and T is temperature of the evaporator and compensation chamber.

In steady state operation, the heat leak to the compensation chamber must be offset by the liquid returning from the condenser; Eq. (7) results, where ΔT represents the subcooling of the returning fluid

$$Q_{e,cc} = \dot{m}c_p\Delta T \quad (10)$$

where m is mass flow and c_p is specific heat.

Chuang [23] developed a steady state LHP model which breaks the overall heat leak into two separate components: axially from the evaporator to the compensation chamber and radially from the heat source to the evaporator core. These two effects are related in that the formation of vapor bubbles in the evaporator core due to radial leak reduces the overall heat flow path back to the compensation chamber, increasing axial leak [10].

Chuang derived the following expressions for the axial and radial heat leak, respectively:

$$Q_{leak,a} = k_{eff}A\left(\frac{T_e - T_{cc}}{L}\right) + (Nuk_f\pi L)\left(\frac{T_e - T_{cc}}{2}\right) \quad (11)$$

$$Q_{leak,r} = \frac{2\pi k_{eff}L\zeta}{\left(\frac{r_o}{r_i}\right)^{(\zeta-1)}}\Delta T_W \quad (12)$$

where Q_{leak} is heat leak power, k_{eff} is effective thermal conductivity, A is area, L is characteristic length, Nu is Nusselt number, k_f is fluid thermal conductivity, and ς represents a non-dimensional ratio of advection and conduction given by

$$\varsigma = \frac{\dot{m}c_p}{2\pi k_{\text{eff}}L} \quad (13)$$

In his analysis and experiment, Chuang assumed this parameter to be zero, i.e., pure conduction. For the low power cases studied, this assumption was valid and resulted in low error; however, for high power levels or low wick conductivity, this assumption loses validity.

3.1. LHP wick structure

Wick structure is one of the main parts of loop heat pipe. To achieve good heat transfer ability of the LHP, wick structure with high porosity and permeability and fine pore radius is expected. The most frequently used wick structures in loop heat pipe are made of sintered metals, such as copper, nickel, stainless steel, titanium or polymers (polypropylene, polyethylene, PTFE) [24–26].

Reimbrechta et al. used a tap powder sintering technique by using a graphite matrix, to manufacture Ni wicks for capillary pump applications [27]. It shows that the graphite has low interaction with nickel by sintering the nickel powders at common sintering temperatures. Combination of two different methods, the cold-pressing sintering and the direct loose sintering, was used by Gongming et al. [28], for development of Ni and Ni-Cu (90% nickel and 10% copper) wicks for loop heat pipes. They found that using direct loose sintering technique with mean pore radii of 0.54 μm , an optimal Ni-Cu wick structure is prepared. Huang and Franchi [29] used copper screen mesh and two powder materials (nickel filamentary powder and spherical copper powder) to manufacture of bimodal wick structure. But it showed that these wicks may be produced with failures. Samanta et al. [30] developed metal injection molding Ni wick structures and performed study on its physical characteristic depending on sintering time (30, 60, and 90 min) and temperature (900, 930, and 950°C). Gernert et al. [31] developed fine pore wick structure for LPH. Wu et al. [32] discussed about the effect of sintering temperature curve in wick structure manufactured for LHP. Launay et al. referred a porosity, pore diameter, and permeability as the main parameters of wick structure in the work [20]. There is the optimal porosity of sintered wick referred between 30 and 75%, and the optimal permeability referred between 10^{-14} and $3 \times 10^{-13} \text{ m}^2$. The porosity of the wick structure decreases when the sintering temperature or the forming pressure increases. Majority of the sintered porous materials has pore diameters between 1 and 20 μm , except copper, which has pore diameters between 20 and 1000 μm .

In Ref. [33], the optimal capillary wick was found to be sintered at 650°C for 30 min, using direct loose sintering technique, with 90% nickel and 10% copper. The wick reaches the porosity of 70% and a mean pore diameter of 1.8 μm . In Ref. [10], biporous nickel wicks were fabricated. A porosity of 77.4% was achieved using cold pressure sintering method, at a temperature of 700°C, with a pore former content of 30% in volume.

4. Loop heat pipe experiments

The next experiment was performed in frame scientific research of porous structures suitable for LHP and finding possibility of heat removal produced by IGBT. The knowledge gained from the IGBT cooling by LHP has given us the information necessary to know how much heat flux LHP is able remove from heat source. This information will be in the future useful in the design of cooling devices working with the LHP.

4.1. Characterization of sintered structures

According to above-mentioned experiences with sintered structures for LHP, we decided to make wick structures from nickel and copper powder. At first, we do analysis of several sintered structures depending on grain size, sintering temperature, and sintering time on porosity, pore size, and strength. In an electric furnace, etalons were sintered from copper powders with grain sizes 50 and 100 μm and nickel powders with grain sizes 10 and 25 μm . The copper powders were sintered at temperature 800 and 950°C for time 30 and 90 min, and nickel powders were sintered at temperature 600°C for time 30 and 90 min.

4.1.1. Porosity measuring

The porosity of a wick structure describes the fraction of void space in the material, where the void may contain working fluid [34]. For the porosity measuring, the weight method was used. At first, the sample was weighed in dry state. Secondly, the sample was soaked with distilled water ($\rho = 0.998 \text{ g cm}^{-3}$ at 20°C). The weight of absorbed water was estimated by the difference between both values, and then a deduction of the “empty space” (thus the total pore volume) and the porosity.

$$\varepsilon = \frac{M_{ss} - M_{ds}}{V_{total} - \rho_w} \quad (14)$$

where ε is wick structure porosity, M_{ss} is weight of porous soaked sample, M_{ds} is weight of porous dry sample, V_{total} is pore volume of the porous sample, and ρ_w is density of absorbed liquid (water).

The results of porosity measuring are shown in **Tables 2–5**.

Grain size (μm)	50	50	50	50
Sintering temperature (°C)	800	800	950	950
Sintering time (min)	30	90	30	90
Porosity (%)	55	54	52	50

Table 2. Porosity of sintered structures from copper powder with grain size 50 μm .

Grain size (μm)	100	100	100	100
Sintering temperature ($^{\circ}\text{C}$)	800	800	950	950
Sintering time (min)	30	90	30	90
Porosity (%)	58	56	55	52

Table 3. Porosity of sintered structures from copper powder with grain size 100 μm .

Grain size (μm)	10	10
Sintering temperature ($^{\circ}\text{C}$)	600	600
Sintering time (min)	30	90
Porosity (%)	69	67

Table 4. Porosity of sintered structures from nickel powder with grain size 10 μm .

Grain size (μm)	25	25
Sintering temperature ($^{\circ}\text{C}$)	600	600
Sintering time (min)	30	90
Porosity (%)	72	70

Table 5. Porosity of sintered structures from nickel powder with grain size 25 μm .

4.1.2. Microscopic analysis of pore size

Investigation of etalons sintered structures by microscopic analysis shown, how influent is the sintering temperature and time on the pore size and on the ratio of the grain size to pore size of each structures. **Figures 3–8** of etalons were created by 100 time's zoom of porous structures sintered from copper powder grain size 50 and 100 μm . **Figures 3** and **6** show that the structures sintered at temperature 800 $^{\circ}\text{C}$ have two times bigger pore than powder grain. Comparison of etalons sintered at temperatures 800 and 950 $^{\circ}\text{C}$ shows that the etalons sintered at temperature 800 $^{\circ}\text{C}$ have so much bigger pore size than at temperature 950 $^{\circ}\text{C}$. It means that pore sizes have so much width to create capillary action in structure. Comparison of etalons sintered at same temperature and various time intervals observed that the time of sintering at temperature nearest the melting temperature of sintering material is not decisive. Comparison of etalons at the same sintering temperature and time interval observed that the grain size of sintered material has impact on pore size. According to microscopic analysis of sintered structures, which clarifies their shape and profile, it can be concluded that the main influencing factors of pore size are grain size, sintering temperature, and not so much sintering time.

Next **Figures 9–12** were created by 500 times zoom of porous structures sintered from nickel powder grain size 10 and 25 μm . Comparison of etalons sintered from nickel powder led to the

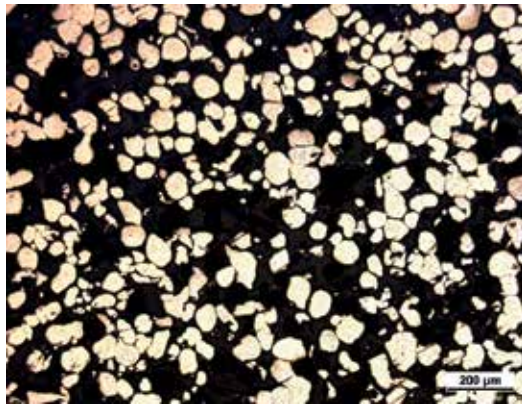


Figure 3. Grain size 50 μm, sintering temperature 800°C, sintering time 30 min.

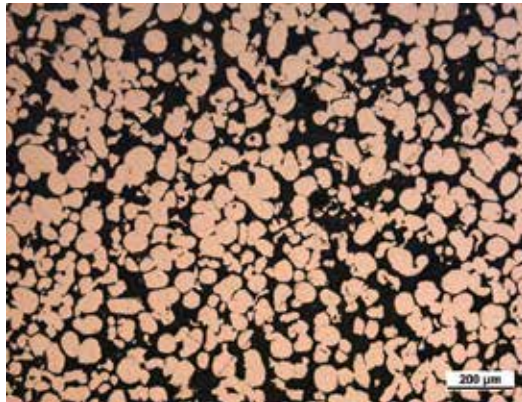


Figure 4. Grain size 50 μm, sintering temperature 950°C, sintering time 30 min.

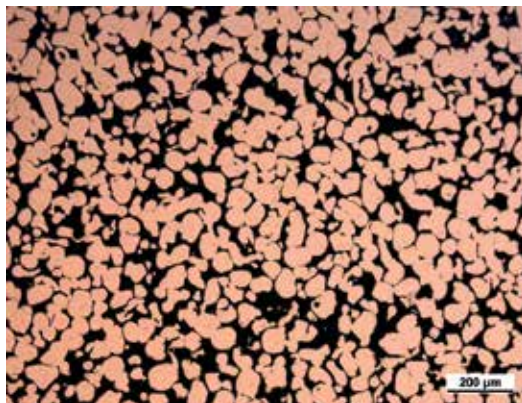


Figure 5. Grain size 50 μm, sintering temperature 950°C, sintering time 90 min.

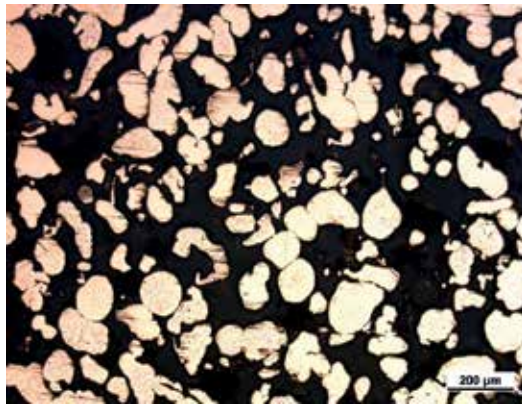


Figure 6. Grain size 100 μm , sintering temperature 800°C, sintering time 30 min.



Figure 7. Grain size 100 μm , sintering temperature 950°C, sintering time 30 min.

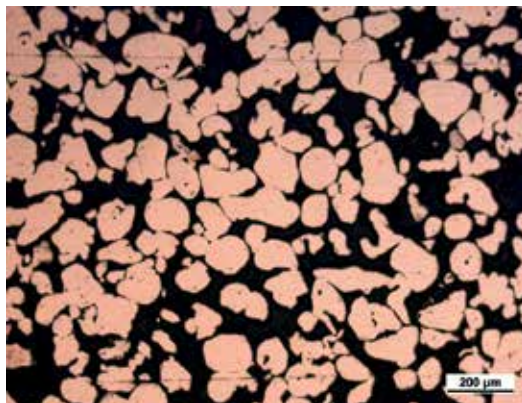


Figure 8. Grain size 100 μm , sintering temperature 950°C, sintering time 90 min.

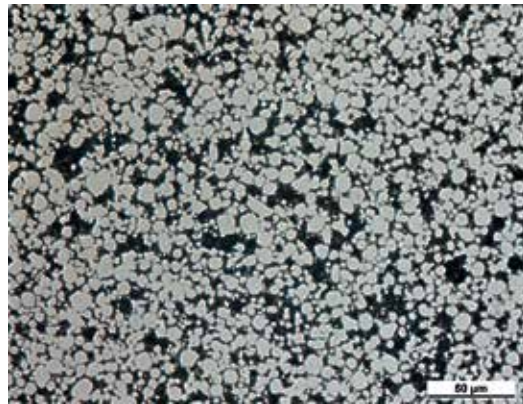


Figure 9. Grain size 10 μm, sintering temperature 600°C, sintering time 30 min.

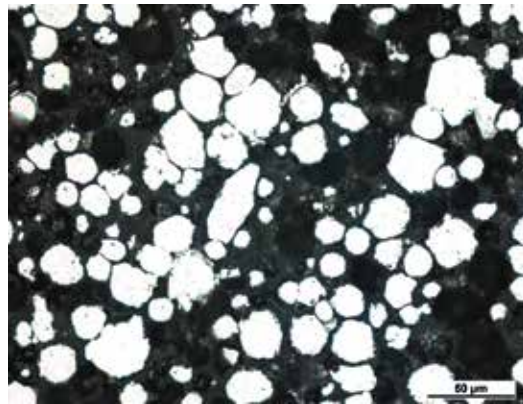


Figure 10. Grain size 25 μm, sintering temperature 600°C, sintering time 30 min.

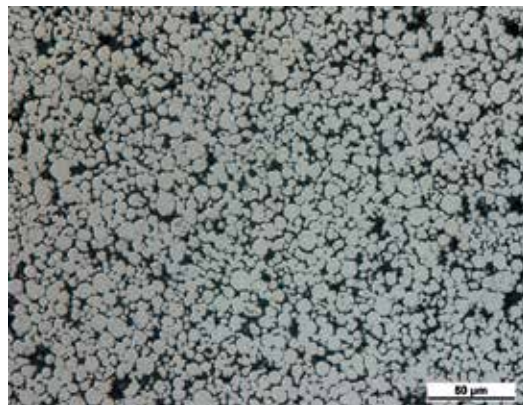


Figure 11. Grain size 10 μm, sintering temperature 600°C, sintering time 90 min.

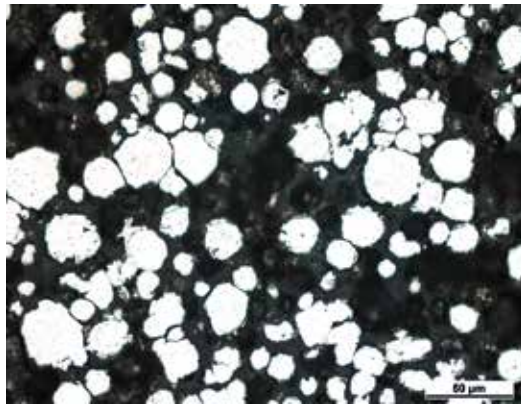


Figure 12. Grain size 25 μm , sintering temperature 600°C, sintering time 90 min.

same conclusion findings with etalons sintered copper powder. On the pore size, the formation of sintered structure does not affect sintering time but grain size.

4.2. Wick structure manufacture

From the results, porosity measurement and microscopic analysis were chosen for wick structure of LHP two copper etalons and two nickel etalons. The first structure was made of copper grain size 50 μm and sintered at temperature 950°C for 30 min (**Figure 13**). Second structure was made of copper grain size 100 μm and sintered at temperature 950°C for 30 min. Third structure was made of nickel grain size 10 μm and sintered at temperature 600°C for 90 min (**Figure 14**). The fourth structure was made of nickel grain size 25 μm and sintered at temperature 600°C for 90 min. The wick structures were sintered in send form (mold) and manufactured according to model of required shape in muffle furnace.

4.3. Loop heat pipe design

The experiments' goal was to determine the influence of various dependencies such as kind of wick structure, kind of working fluid, and amount of working fluid on LHP cooling efficiency. Therefore, special experimental LHP was designed with aluminum block mounted on the evaporator part to fix insulated gate bipolar transistor (IGBT). All parts of LHP (evaporator,



Figure 13. Porous sintered wick structures: a—Copper, b—Nickel.

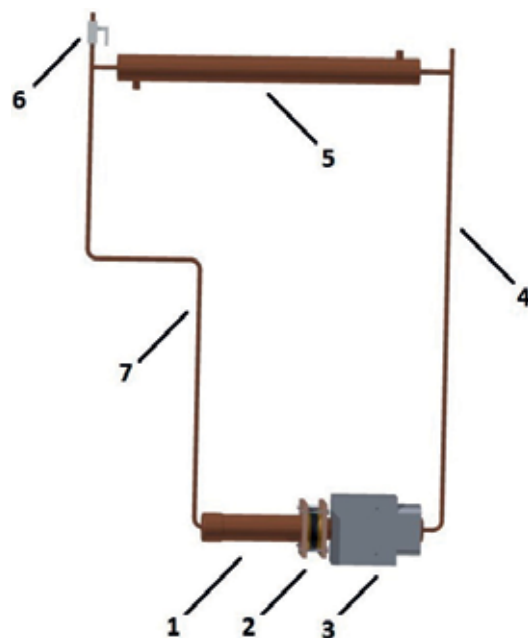


Figure 14. LHP model: 1—compensation chamber; 2—rubber seal; 3—evaporator; 4—vapor line; 5—condenser; 6—filling valve; 7—liquid line.

compensation chamber, vapor and liquid line) were made from copper pipes. As a working fluid, distilled water and acetone were used. Inside the evaporator, wick structure made by sintering metal powder was inserted. To avoid heat loss (it is also called heat leak) into the compensation chamber, a brass flange with rubber seal was inserted between the evaporator and the compensation chamber. In **Figure 15**, the model of LHP design is shown, and the main parameters of LHP design are given in **Table 6**.

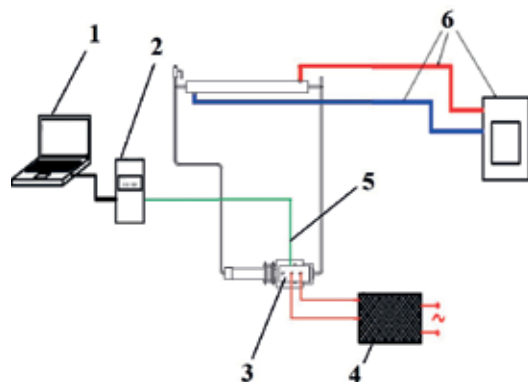


Figure 15. Schema of measuring unit: 1—PC; 2—data logger; 3—IGBT; 4—electric power supply; 5—thermocouple; 6—thermostat.

Evaporator		Compensation chamber	
Total length (mm)	130	Outer/inner diameter (mm)	35/33
Active length (mm)	86	Length (mm)	110
Outer/inner diameter (mm)	28/26	Charge mass	
Material	Copper	Distilled water	60%
Saddle		Vapor line	
Size (length/high/wide)	118/89/40	Length (mm)	670
Material	Alumina	Outer/inner diameter (mm)	6/4
Sintered copper powder		Liquid line	
Number of vapor grooves	6	Length (mm)	820
Porosity (%)	52–55	Outer/inner diameter (mm)	6/4
Outer/inner diameter (mm)	26/8	Condenser	
Sintered nickel powder		Length (mm)	420
Number of vapor grooves	6	Outer/ inner diameter (mm)	6/4
Porosity (%)	67–70		
Outer/inner diameter (mm)	26/8		

Table 6. Main design parameters of the LHP.

4.4. Determination of loop heat pipe cooling efficiency

Determination of the LHP cooling efficiency was performed on the experimental measuring unit, which is shown in **Figure 15**. Fixed IGBT on the evaporator of LHP was loaded by electric power. Produced heat by IGBT on the evaporator of LHP was removed by working fluid to the condenser of LHP. The condenser of LHP was made as tube heat exchanger and the cooling circle of heat exchanger was regulated by the thermostat at constant temperature 20°C. The gist of the LHP cooling efficiency determination is on measuring IGBT temperature with gradually increasing loaded heat by IGBT in steps 50 W from 100 W till the IGBT reaches permissible temperature 100°C. The temperature of the IGBT was measured by thermocouple inserted under IGBT. For better heat transport, thermal conductive paste was applied on the connection between IGBT and aluminum block and between aluminum block and the evaporator.

At first, measurements of influence of the working fluid amount on LHP cooling efficiency were performed. Four amounts 40, 50, 60, 80% of total LHP volume in LHP with working fluid water were investigated. In **Figure 16**, the influence of working fluid amount in dependencies on LHP cooling efficiency with working fluid water depending on loaded heat is shown. It is seen that the LHP with working fluid volume is 60% and the best operating LHP is in range of 150–350 W.

Next, the measurement of influence of wick structures on LHP ability to remove heat from IGBT was performed. The measurement was performed on LHP with the working fluid of water and amount of 60% total LHP volume. In **Figure 17**, the results of the influence of the wick structure on LHP cooling efficiency depending on loaded heat are shown. Two wick

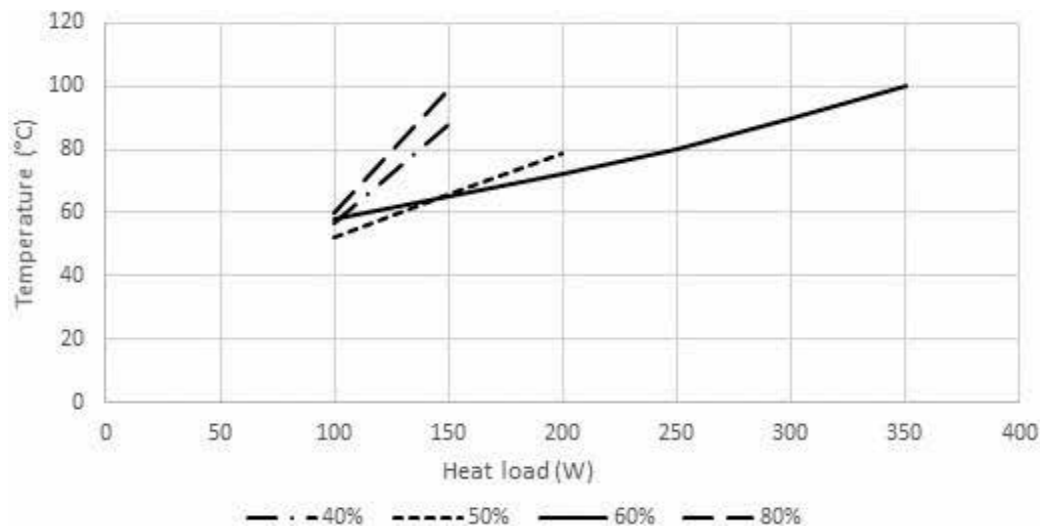


Figure 16. Influence of working fluid amount on LHP operation.

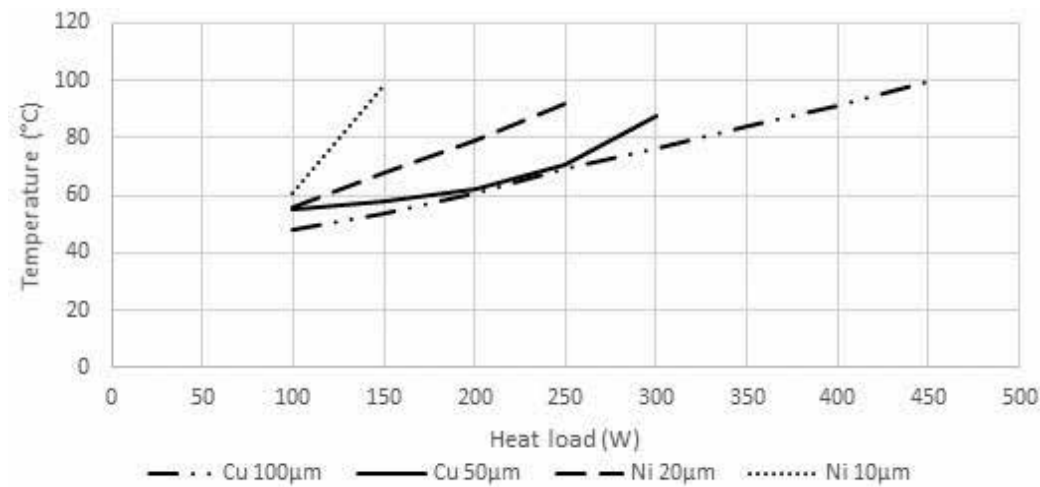


Figure 17. Influence of the wick structure on LHP cooling efficiency with working fluid water depending on loaded heat.

structures made form Cu powder with grain size 50 µm and 100 µm and two wick structures made from Ni powder grain size 20 µm and 10 µm were compared.

Comparing the results of dependence of temperature on input power of IGBT cooled by LHP with variants of sintered wick structure, the LHP with nickel wick structure does not show so good properties of heat removal than LHP with copper wick structure. Comparing the temperature curves of the LHP with first wick structure (made of Cu powder 50 µm) and LHP with second wick structure (made of Cu powder 100 µm), it is seen that both LHP have almost the same results at heat load of up to 200 W. At higher input power than 200 W loaded in to IGBT is

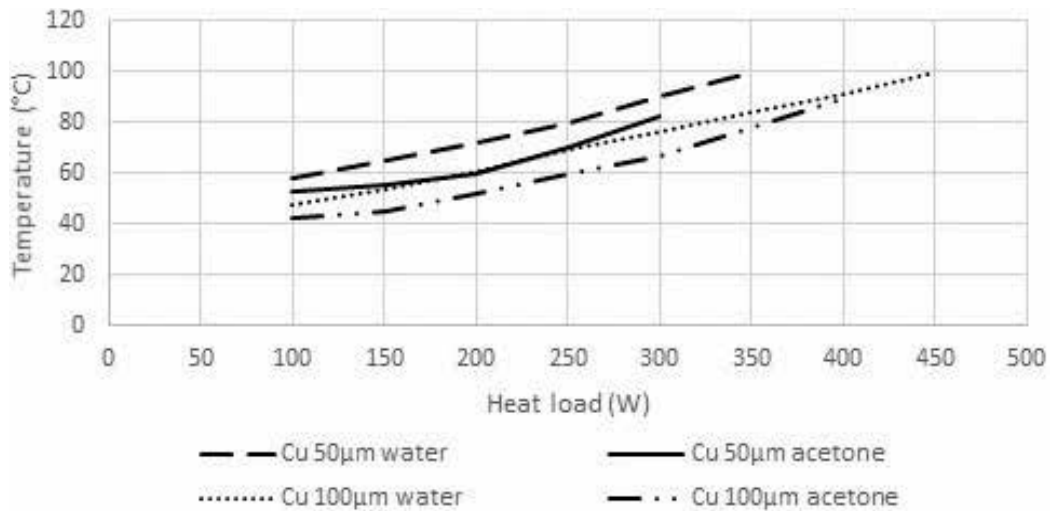


Figure 18. Influence of the working fluid on LHP cooling efficiency with wick structure made from Cu powder 100 μm and 50 μm depending on loaded heat.

seen that the LHP with first structure did not heat remove from IGBT and the temperature of IGBT exceed 100°C . The LHP with second wick structure is able to cool the IGBT under temperature 100°C until the IGBT input power 450 W. Comparing the temperature curves of the LHP with third wick structure (made of Ni powder 10 μm) and LHP with fourth wick structure (made of Ni powder 20 μm), it is seen that IGBT temperature cooled by LHP with third structure rapidly increases, already, at an input power 150 W. The LHP with fourth wick structure is able cool the IGBT under temperature 100°C until the IGBT input power 250 W.

At third, measurement impact of working fluid in LHP with wick structure made from Cu powder 100 μm and 50 μm and amount 60% of total LHP volume with an ability to remove heat from IGBT was performed. **Figure 18** shows the result of influence of the working fluid on LHP cooling efficiency depending on loaded heat. This experiment shows that the LHP with working fluid acetone better removes heat from the IGBT at lower heat load in range of 100–300 W. At higher heat loads is the better working LHP with the working fluid water.

5. Heat pipe experiments

The next experiments were performed in frame scientific research of porous wick heat pipes, where the ability of heat transfer depending on wick structure and working fluid is investigated. The popularity of porous wick heat pipe and lack of experiments performed with them were the reason to realize experiment which deals with heat pipes with sintered wick structures made from copper powders. This section describes manufacturing process of wick heat pipe, experimental measurement of heat transfer ability of heat pipe, and mathematical calculation of heat transport limitation of heat pipes.

5.1. Heat pipe manufacture processes

The main requirements on the heat pipe production are the high purity of the material of the individual parts and the working substance, as well as their mutual compatibility.

The basis of the heat pipe construction is the pipe body and the working fluid. The production of a heat pipe primarily consists in selecting a suitable material of the pipe and the working fluid. The working fluid is selected according to the temperature conditions in which the heat pipe will be used, because heat flux transferred by the heat pipe depends on the material of the pipe, the working fluid, and their mutual compatibility. An important part of the wick heat pipe is the wick structure, which also has a large impact on the amount of transferred heat flux.

The main components of heat pipe are:

- Pipe body (container)
- Working fluid
- Wick structure
- End caps
- Filling pipe

The heat pipe body may be of any cross-section, for example, circular or square, may include mounting flanges for ease of assembly, and may be bent into various shapes. The wick structure can be formed by grooves extruded into a pipe body or fine mesh screen, porous material and artery inserted into the heat pipe body [35]. In **Figure 19**, a schema of the wick heat pipe construction is shown.

The most common shape of the heat pipe is cylinder, because in addition of easily available product (wide assortment of material and the size of the pipe cross-sections), it provides certain advantages also in terms of strength and thermomechanical parameters. The advantage of producing a cylindrical shaped heat pipe is in the ease handling with the cylindrical material. In practice, heat pipes with a flat rectangular, triangular or other cross sections are also used. The most common heat pipes are manufactured with an inner diameter of 8–25 mm and an internal diameter of 2–5 mm—the so-called micro-heat pipes. The production process

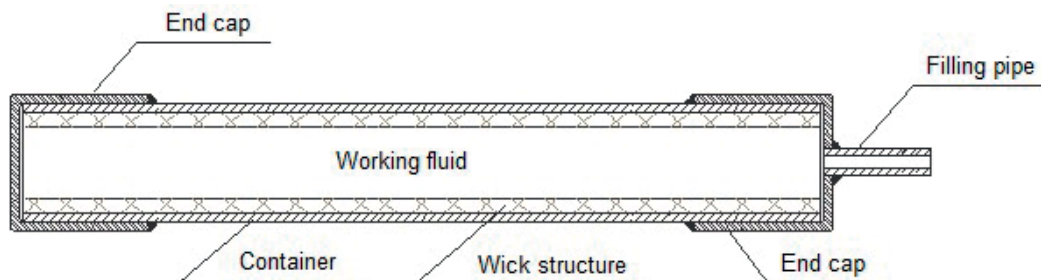


Figure 19. Schema of the wick heat pipe construction.

of the heat pipe can be divided into several sub-processes involving mechanical and chemical treatment of materials.

Technological process of the heat pipe production cycle:

- Body production and end caps.
- Production of wick structure.
- Cleaning of components.
- End caps closure by impervious joints (welding, soldering).
- Mechanical verification of body strength and tightness.
- Vacuuming of inner space and filling with the working fluid.
- Sealing the filling pipe (welding, soldering).

Before heat pipe production, it is necessary to thoroughly clean all components of the heat pipe to avoid any undesirable influence, which could ultimately have an effect on the heat transfer ability reduction. In cleaning process, first, mechanical impurities and rust from the body of the pipe are removed manually and then followed by chemical cleaning of the body, wick structure, end caps, and filling pipe [36].

5.1.1. Mechanical part of heat pipe manufacture

In the mechanical part of the production, the individual components of the heat pipe are first prepared: the body, the filling pipe, the wick structure, and the end caps. All components are then joined together by welding or soldering. In the case of wick heat pipe production, a wick structure is placed in the internal space of the body before to heat pipe closure. The closure of the heat pipe is the connection of the body with the end caps. In **Figure 20**, the standard types of the heat pipe closure by end caps are shown. The filling pipe is connected to one of the end caps due to the inner space vacuuming. After vacuuming, the heat pipe is filled with the working fluid,

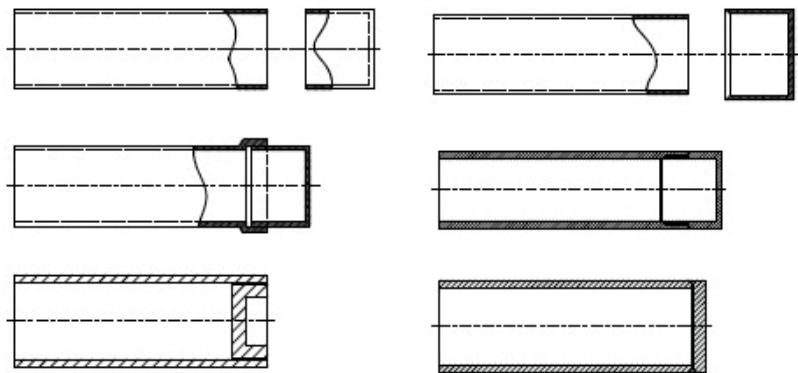


Figure 20. Types of the heat pipe closure by end caps.

filling pipe is pressed, and after disconnection from the vacuuming pump, filling pipe is sealed by soldering.

5.1.2. Chemical part of heat pipe manufacture

In the chemical part of the production, mechanical impurities and rust from the body of the heat pipe are first removed. This is followed by wet cleaning of the heat pipe components including cleaning with solutions, acids, and basic acids which are precisely determined for each type of material. The ultrasound cleaning, vacuuming, degassing, and passivation are processes that guarantee a high purity of the heat pipe material and thus contribute to long-lasting failure free operation. Generally, two important goals are achieved by cleaning. The first goal is to ensure good wetting material of the heat pipe well by working. The second goal is to remove all particles of dirt because the presence of impurities in solid, liquid or gaseous form may have an adverse effect on the heat transfer ability of heat pipe. Small particles can inhibit the formation of capillary pressure in the wick structure. Machining or human hand grease may reduce the wettability of the wick structure. Oxides formed on the walls of the wick structure may also reduce the ability of the working fluid to wet the surface. It is also highly advisable to use an ultrasonic cleaner to clean the heat pipe material, as the ultrasound breaks down impurities firmly absorbed on the surface of metallic particles that cannot be removed in any other way. The cleaning of the heat pipe is repeated immediately before filling with the working fluid, after connecting the body with the end caps and the filling tube. After cleaning, the tube is degassed by heating to a higher temperature and vacuuming the interior. In the case of a wick heat pipe, it is necessary to remove the oxide layers from the wick structure by chemical cleaning (e.g., solvents).

5.1.3. Filling the heat pipe with the working fluid

The working fluid added into the heat pipe must be completely clean, free from all mechanical impurities and gases, as their trace residues can also react with the body material of the heat pipe and the formation of undesirable elements. Clean substances can be purchased without any problems at special chemical stores. However, even in pure liquids and solids, an incompressible gas may be present. These gases can be removed by repeated freezing and thawing cycles. The working fluid in the filling bottle can freeze using the liquid nitrogen or dry ice.

Filling process of each type of working fluid is happening under other conditions. The characteristic of the filling process depends on the state of the working fluid at ambient temperature. If the working fluid is at the room temperature in the gaseous state (cryogenic), the filling can be carried out via a gas container of high quality. Filling and closing process of liquid-metal heat pipes is appropriate to do in the vacuum chamber [37].

The filling of low-temperature heat pipes can be carried out at room temperature without the use of any protective atmosphere. Before filling the heat pipe, it is advisable sucking the air from it to ensure the removal of undesirable components contained in the materials which could be later shown as non-condensing components. In addition, under pressure, the working fluid naturally enters into the heat pipe, and thus the equilibrium state of the pure vapor and liquid phases at a lower pressure than atmospheric will be achieved [38].

5.2. Heat pipe manufacture

Although the production of the porous wick structure is most difficult from all types of wick structures, it is one of the three most used wick structures in the heat pipe, because it is able to create a large capillary pressure that allows the heat pipe to transfer a high heat flux in the antigravity position. One method of making a porous wick structure is to sinter a copper powder uniformly poured around a coaxially centered steel mandrel located inside the copper pipe at a temperature close to melting the powder material in a high temperature electric furnace. By sintering copper powders is possible made wick structure with the high thermal conductivity, high wick porosity, small capillary radius, and high wick permeability what are the main which the wick structure have to ensure supplies evaporator with the condensed liquid. The high thermal conductivity of copper ensures that the wick structure will not have high thermal resistance, which is one of the expecting properties of wick structure too. The formation of a suitable porous structure by sintering the metallic powder depends, in addition to the sintering temperature, both on the time of sintering and the grain size of the powder. Copper powders with a particle size of 30–100 μm or copper fibbers of 2–3 mm in length and a diameter of 20–100 μm are used for the production of porous sintering structure.

The most important part of the heat pipe is wick structure. This experiment deal with heat pipes with sintered wick structure made from copper powder with granularity of 100, 63 and 35 μm by sintering in the high thermal electric oven using powder metallurgy. By sintering the copper powder on the inner wall of the heat pipe container, 1.5 mm thick wick structures were created. The sintering process of the wick structure was approx. at temperature of 1000°C and time of 30 min. Seeing that the pore size of the wick structure depends on the grain size of the copper powder, sintering the copper powder of various grain size creates the wick structure of various pore size. The overall length of the heat pipes is 0.5 m.

In **Figure 21**, copper powders are shown, and in **Figure 22**, manufactured porous wick structure are shown.

The other important part of the heat pipe design depends on factors related to the properties of the working fluid. The working fluid must have good thermal stability in relation to the specific working temperature and pressure. The most important requirements that the working fluid must have are the following: compatibility with the capillary system and with the material of the pipe, high thermal stability, high state of heat, high thermal conductivity, low

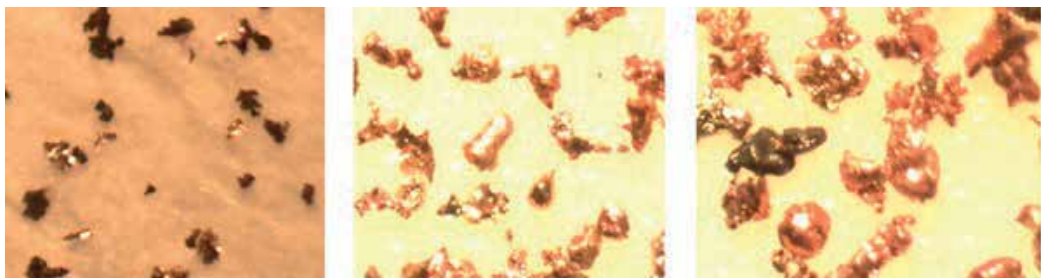


Figure 21. Copper powders (35, 63, and 100 μm).



Figure 22. Sintered porous wick structures.

viscosity of the liquid and vapor phase, high surface tension, and acceptable freezing point. For this experiment, a working fluid water and ethanol were chosen.

The amount of the working fluid in heat pipes is other alchemy of the heat pipe manufacturing. There are some recommendations of working fluid amount in heat pipe. Lack of working fluid may lead to drying of evaporator part of heat pipe. Surplus working fluid can lead to congestion of the condensation part of the heat pipe. One of the recommendation about the working fluid amount in heat pipe is that the working fluid has to fill-up at least 50% of evaporator part of the heat pipe. In general, the quantity of the working fluid is determined in the range of 15–30% of the total heat pipe volume [35]. In this experiment, heat pipes was filled with working fluid of 20% total heat pipe volume.

And finally, the process of the vacuuming, filling and closing the heat pipe are the other important part of the heat pipe manufacture. There are some methods on how to perform this process. Each of these methods has a precise plan of filing and vacuuming processes. In **Figure 23**, schema of filling and vacuuming process used in heat pipe manufacturing is shown. Working fluid was injected into the pipe via connecting capillary tube by syringe. Heat pipe container with working fluid was connected to vacuum system and by vacuum pump, air from heat pipe container was sucked off. Before connecting pipe to vacuum system, the working fluid was cooled by the immersion of pipe into the cooling medium, because during

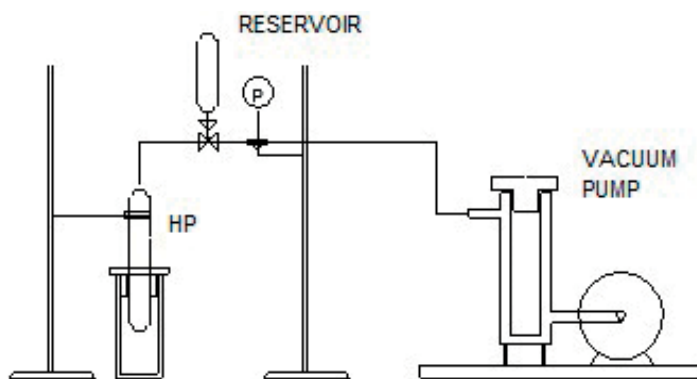


Figure 23. Schema of heat pipe filling and vacuuming process.

vacuuming of the pipe, pressure drop occurs and this may cause evaporation of working fluid. As a cooling medium, dry ice or liquid nitrogen may be used. After vacuuming, capillary tube connected was crimped, disconnected from vacuuming system and free-end soldered.

5.3. Heat transfer ability of the heat pipe

The main goal of the experiments is the determination of influence of the porous wick structure on the amount of thermal performance transferred by heat pipe. To determinate the amount of thermal performance transferred by heat pipe, measuring unit consisting of measuring apparatus (thermostat, data logger, ultrasonic flowmeter, power supply) shown in **Figure 24** was proposed. Evaporator section of heat pipe was electrically heated by connecting to the laboratory power supply. Condensation section of heat pipe is placed into the heat exchanger where transferred heat from the evaporator is dissipated. Heat transferred by heat pipe is evaluated by calorimetric method emanating from calorimetric equation, where known mass flow, specific heat capacity, input and output temperature of cooling medium are flowing in the heat exchanger.

$$Q = \dot{m} \cdot c \cdot \Delta t \quad (15)$$

$$\Delta t = t_2 - t_1 \quad (16)$$

where Δt [°C]—temperature difference, t_1 [°C]—input temperature, t_2 [°C]—output temperature, \dot{m} [J kg⁻¹ K⁻¹]—mass flow of liquid, and c [J kg s⁻¹]—special thermal capacities of liquid.

In **Figure 25**, results of the experimental determination of influence of porous wick structure and working fluid on the heat pipe heat transfer ability at horizontal position and heat source 80°C are shown. It is seen that the heat pipe with working fluid water is able to transfer highest thermal performance in range 150–200 W. The best working wick structure in the water heat pipe is porous wick structure made from Cu powder with grain size 63 μm. On the other side, the porous wick structure made from Cu powder with grain size 35 μm is better for the heat pipes with working fluids such as acetone and ethanol that are able to transfer thermal performance

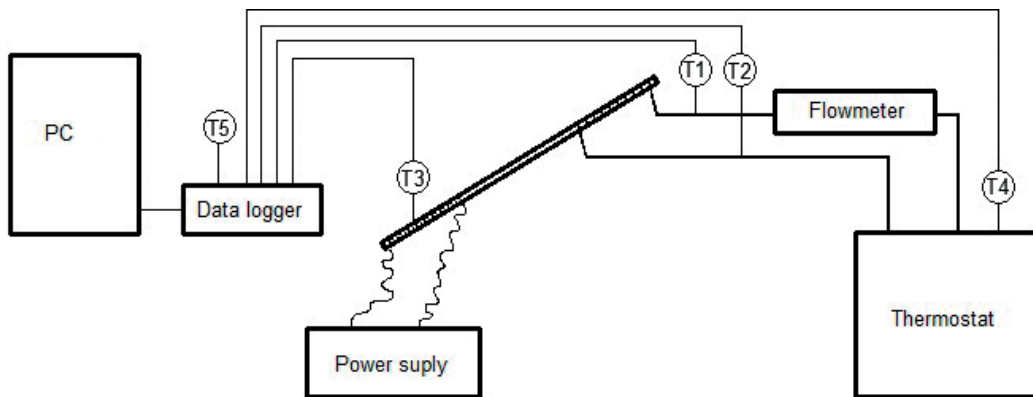


Figure 24. Scheme of measuring unit.

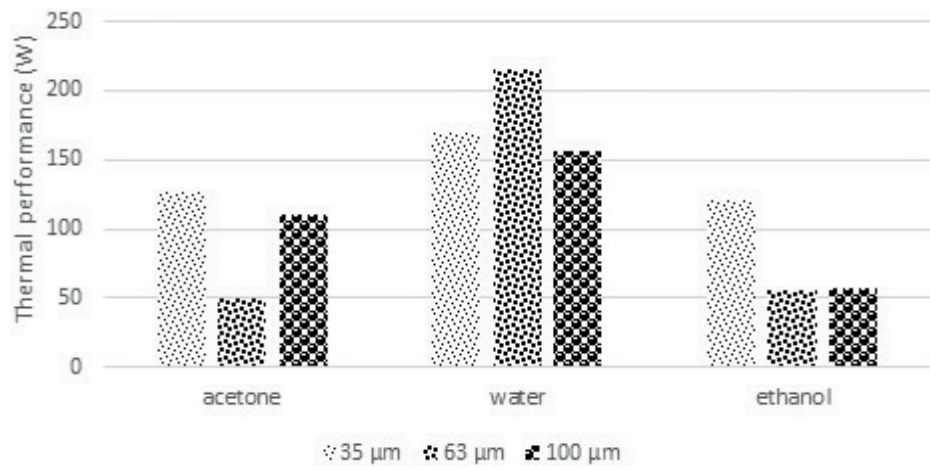


Figure 25. Influence of wick structure on the heat pipe heat transfer ability at heat source 80°C.

around 120 W. The experiment did not show the best one porous wick structure for selected working fluids, because each porous structure has various porosity and pore size which depend on the manufacturing process and each working fluid has different physical properties. There did not exist only one the best heat pipe with the best wick structure or the best working fluid because each heat pipe with various combination of the porous structure and working fluid is unique due its different properties.

In **Figure 26**, influence working position on the heat transfer ability of wick heat pipe with various porous wick structures is shown. Working position of heat pipe can be divided into three

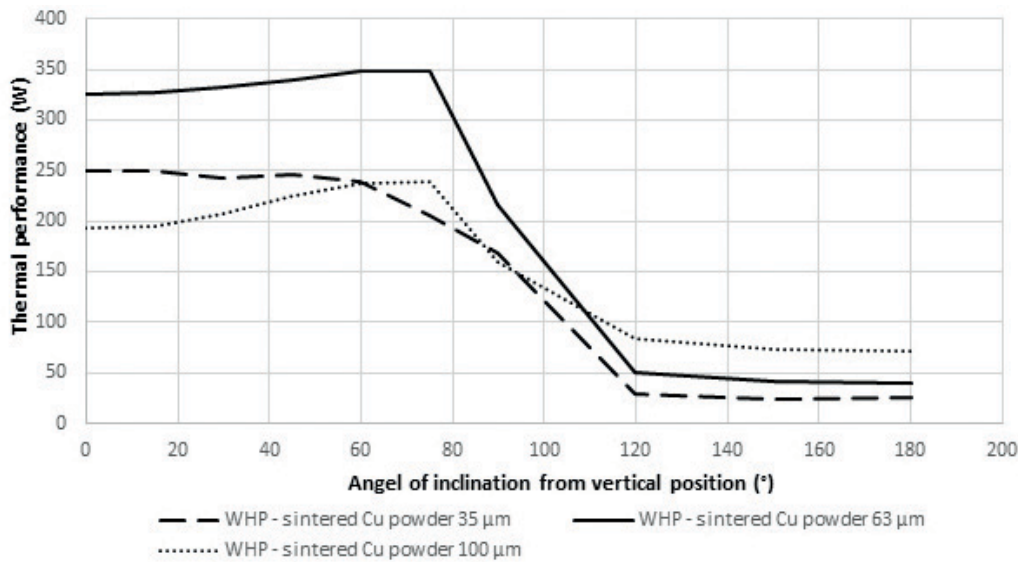


Figure 26. Dependence thermal performance on working position of wick heat pipes with various wick structures.

areas. Positive gravity action zone is represented by angle of inclination from vertical position $0-75^\circ$, zero gravity action zone (horizontal position) is represented by angle of inclination from vertical position 90° , and negative gravity action zone is represented by angle of inclination from vertical position $105-180^\circ$. There is seen that all wick heat pipe has good ability heat transfer in all zones. The best working wick heat pipe in positive and zero gravity action zone is heat pipe with wick structure made from Cu powder $63\ \mu\text{m}$. The best working heat pipe in zone with negative gravity action is wick heat pipe with wick structure made from Cu powder $100\ \mu\text{m}$.

5.4. Calculation of heat transfer limitation of the heat pipe

The heat flux transferred through the heat pipe depends mainly on the temperature difference and the corresponding thermal resistances. The real transferred heat is affected by the hydrodynamic and thermal processes that take place in the heat pipe at the various operating conditions. The heat flux transferred by the heat pipe can reach limit values that depend on these processes. There are five known limitations that limit the overall heat transfer in different parts of the heat pipe depending on the working temperature. In **Figure 27**, an ideal model of all heat transfer limitations that define area of maximum heat flux transferred by heat pipe depending on operating temperature is shown [4].

The mathematical model consists of calculation of the heat pipe heat transfer limitations. Heat pipe heat transfer limitations depend on the working fluid, the wick structure, the dimensions of the heat pipe, and the heat pipe operation temperature. Each heat transfer limitation expresses part of total heat flux heat pipe, which is influenced by hydrodynamic and thermal processes occurring in the heat pipe. Each of limitations exists alone and they are oneself non-influence together. To design mathematical model for the calculation of heat flux transferred by heat pipe,

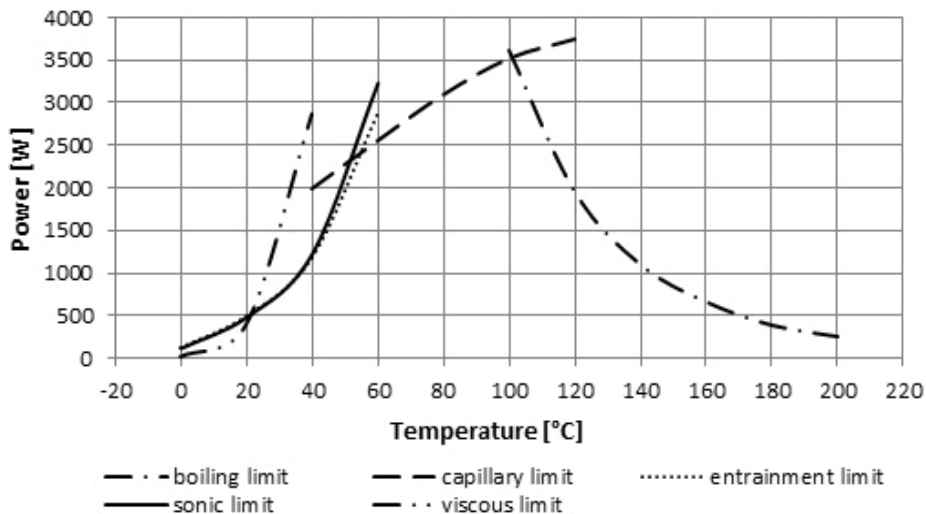


Figure 27. Heat transfer limitations of water wick heat pipe with sintered wick structure (heat pipe inner diameter 20 mm, total length 2 m, axial orientation 90° , sphere diameter of copper powder $0.85\ \mu\text{m}$, porosity 0.55, and width of wick structure 6 mm).

it is necessary to know basic and derived parameters of the heat pipe and its wick structure and physical properties of the working fluid liquid and vapor phase.

5.4.1. Capillary limitation

Capillary limitation involves a limitation that affects the wick heat pipe operation, which results from the capillary pressure acting on the condensed working fluid in the capillary structure. At the contact of liquid and wick structure surface, the capillary pressure is formed. This causes the liquid phase of the working fluid to flow from the condenser to the evaporator. Decreasing the pores of the capillary structure increases the capillary pressure as well as hydraulic resistance. The capillary limit occurs when the capillary forces at the interface of the liquid and vapor phases in the evaporator and condenser section of the heat pipe are not large enough to overcome the pressure losses generated by the friction. If the capillary pressure in the heat pipe during the operation is insufficient to provide the necessary condensate flow from the condenser to the evaporator, the capillary structure in the evaporator is dried and thus the further evaporation of the working substance is stopped. In general, the capillary limit is the primary limit that influences the heat pipe performance and is expressed by the relationship [39].

$$\dot{Q}_c = \frac{\sigma_l \rho_l l_v}{\mu_l} \cdot \frac{K A_w}{l_{eff}} \left(\frac{2}{r_{eff}} - \frac{\rho_l g l_t \cos \Psi}{\sigma_l} \right) \quad (17)$$

where A_w is the wick cross-sectional area (m^2), K is the wick permeability (m^2), μ_l is the liquid viscosity ($N \cdot s/m^2$), ρ_l is the liquid density (kg/m^3), g is the acceleration due to gravity (9.8 m/s^2), r_{eff} is the wick capillary radius in the evaporator (m), and l_t is the total length of the pipe (m) [7].

Furthermore, if the heat pipe has properly operated, the maximum capillary pressure has to be greater than the total pressure loss in the heat pipe and it is expressed by the relationship

$$(\Delta P_c)_{\max} \geq \Delta P_{\text{tot}} \quad (18)$$

The maximum capillary pressure ΔP_c developed in wick structure of the heat pipe is defined by the Laplace-Young equation.

$$\Delta P_c = \frac{2\sigma}{r_{eff}} \cdot \cos \theta \quad (19)$$

where r_{eff} is the effective pores radius of the wick structure and θ is contact angle liquid phase of the working fluid in wick structure, where $\theta = 0^\circ$ is the best wetting contact angle [4].

5.4.2. Viscous limitation

When the heat pipe operates at low operating temperatures, the saturated vapor pressure may be very small and has the same range as the required pressure drop necessary for the vapor to flow from the evaporator to the condenser of the heat pipe. This results in a condition expressed by the viscous limit about balance of the vapor pressure and viscous forces in the

capillary structure in the low-velocity vapor flow. The most frequent cases of exceeding the boundary of the viscous limit occur when the heat pipe operates at temperature close to the solidification of the working fluid. In this case, working fluid evaporation in the evaporator and heat transfer in the form of vapor flow through the adiabatic section into the condenser of the heat pipe did not occur. It is assumed that the vapor is isothermal ideal gas, the water vapor pressure on the end of the condenser is equal to zero, which provides the absolute limit for the pressure in the condenser. The viscous limit is referred as the condition of the vapor phase flow at low velocity and is expressed by the relationship

$$Q_e = A_v l_v \left(\frac{\rho_v \sigma_l}{2 P_{v,e} \mu_v} \right)^{0.5} \quad (20)$$

where l_v is the latent heat of vaporization (J/kg), r_v is the cross-sectional radius of the vapor core (m), l_{eff} is the effective length of the heat pipe (m), μ_v is the vapor viscosity in the evaporator (N s/m²), P_v (Pa) is the vapor pressure, and ρ_v (kg/m³) is the density at the end of the heat pipe evaporator [4].

In cases when the viscous limit is reached for many conditions, the condenser pressure could not be a zero. Then the following expression is applied:

$$Q_b = \frac{4\pi l_{\text{eff}} A_{\text{eff}} T_v \sigma_l}{l_v \rho_v \ln \frac{r_i}{r_e}} \left(\frac{1}{r_i} - \frac{1}{r_{\text{eff}}} \right) \quad (21)$$

where $P_{v,c}$ is the vapor pressure in the condenser [40].

5.4.3. Sonic limitation

The sonic limit characterizes the state in which the velocity of the evaporated vapor flow at the outlet of the evaporator reaches the sound velocity. Generally, this phenomenon occurs on the start of heat pipe operation at a low vapor pressure of the working fluid. Assuming that the vapor of the working fluid is the ideal gas and the vapor flow at the sound velocity throughout the heat pipe cross section is uniform, the sonic limit is determined by the relationship (22). The sonic limit does not depend on the heat pipe orientation and type of the heat pipe, and the same formula is applied for the gravity and wick heat pipe. The most difficult in the sonic limit determination is determining quantities of vapor density and pressure on inlet to the condenser [41].

$$Q_s = 0,474 A_v l_v (\rho_v P_v)^{0.5} \quad (22)$$

where ρ_v (kg/m³) is the vapor density, P_v (Pa) is pressure at the end of heat pipe evaporator, and A_v is the cross-sectional area of the vapor core (m²).

The sonic limit is mainly associated with liquid metal heat pipe startup or low-temperature heat pipe operation due to very low vapor densities that occur in these cases. For the low temperature or cryogenic temperatures, the sonic limit is not a typically factor, except for heat

pipes with very small vapor channel diameters. The sonic limitation is referred as an upper limit of the axial heat transport capacity and does not necessarily result in dry out of the wick structure in heat pipe evaporator or total heat pipe failure [4].

5.4.4. Entrainment limitation

Increasing the heat flux transferred by heat pipe increases the vapor flow velocity of the working fluid too and this results in a more pronounced interaction of the vapor and liquid phase inside the heat pipe. The interfacial surface becomes unstable and the viscous force on the surface of the liquid overcomes the forces of the surface tension. The waves are created on the liquid phase surface at first from which the droplets gradually tears off. At a certain vapor flow velocity, the liquid flow interruption into the evaporator section occurs. The condenser section of heat pipe is overfilled by vapor and liquid phase and the evaporator is overheated due to lack of the working fluid. The limit value of the heat flux, when the heat pipe condenser is overfilled by vapor and liquid, corresponds to interaction limit [42]. Entrainment limitation of the wick heat pipe is related to the condition when the vapor flows against the liquid flow in the wick structure, which may result in insufficient liquid flow in the wick structure [43]. Entrainment limitation of the wick heat pipe is expressed by relationship:

$$Q_e = A_v \cdot l_v \cdot \left(\frac{\rho_v \cdot \sigma_l}{2 \cdot r_{c,ave}} \right)^{0.5} \quad (23)$$

where $r_{c,ave}$ is the average capillary radius of the wick structure and, in many cases, it is approximated to r_{eff} and σ_l is the liquid surface tension (N/m) [4].

5.4.5. Boiling limitation

When heating the surface of the heat pipe wall with a layer of liquid in the saturation boundary, a three basic heat transfer regimes can occur. At low temperature difference of the heated surface and interfacial surface of the liquid, a natural convection and evaporation from the liquid surface occur. When increasing the temperature difference, a bubble boiling and gradual transformation to the film boiling occur. In heat pipe, a surface evaporation at low heat flux densities and bubble boiling at higher densities occur. Although the heat transfer intensity is greatest in the bubble boiling, for most types of wick heat pipes, the bubble boiling is not desired because it interferes with the liquid wicking into the wick structure. On the other hand, in a heat pipe with a grooved capillary structure, a gravity heat pipe with bubble boiling is favorable [44]. The heat flux in which the bubble boiling occurs in the wick heat pipes and the film boiling occurs in the gravity heat pipe is referred as the boiling limit. The gravity heat pipe is expressed by the relationship [45]:

$$Q_b = 0,16 \cdot A_v \cdot l_v \cdot \sqrt{\sigma_l \cdot g \cdot \rho_v^2 (\rho_l - \rho_v)} \quad (24)$$

Determination of the boiling limit of the wick heat pipe is problematic, because it depends on a number of technological and operating conditions. The most reliable determination of the boiling limit is experimental determination for the particular wick structure and working fluid.

Approximate determination of the boiling limitation for the wick heat pipe is expressed by the relationship [46]

$$Q_b = 0.16 \cdot A_v \cdot l_v \sqrt[4]{\sigma_l \cdot g \cdot \rho_v^2 (\rho_l - \rho_v)} \quad (25)$$

where λ_{eff} is the effective thermal conductivity of the wick structure which is composed of the wick thermal conductivity and working fluid thermal conductivity (W/m K), T_v is temperature of vapor saturation (K), r_v is the vapor core radius, r_i is the inner container radius (m), and r_n is the bubble nucleation radius in range from 0.1 to 25.0 μm for conventional metallic heat pipe container materials [4].

5.4.6. Heat pipe parameters

To calculate heat pipe heat transport limitations, it is necessary to know thermophysical properties of working fluid in heat pipe, basic heat pipe parameters, thermal conductivity of heat pipe material, working temperature of heat pipe, axial orientation of heat pipe, and other heat pipe parameters calculated from basic heat pipe parameters.

$$l_t = l_e + l_{ad} + l_c \quad (26)$$

$$l_{\text{eff}} = 0.5(l_e + l_c) + l_{ad} \quad (27)$$

$$A_v = \pi r_v^2 \quad (28)$$

$$A_w = \pi (r_i^2 - (r_i - h)^2) \quad (29)$$

where l_t is total length of heat pipe [m], l_e is evaporation length of heat pipe [m], l_{ad} adiabatic length of heat pipe [m], l_c is condensation length of heat pipe [m], l_{eff} is effective length of heat pipe [m], A_v is cross-sectional area of the vapor core [m²], A_w is wick cross-sectional area [m²], r_v is cross-sectional radius of vapor core [m], r_i is inner container radius [m], and h is wick structure width [m].

The other parameters needed to calculate heat pipe heat transport limitations are basic parameters of sintered wick structure and other parameters calculated from basic parameters of wick structure.

$$r_{\text{eff}} = 0.21 \cdot d_s \quad (30)$$

$$K = \frac{d^2 \cdot \varepsilon^3}{150 \cdot (1 - \varepsilon)^2} \quad (31)$$

$$\lambda_{\text{eff}} = \lambda_l \frac{2 \cdot \lambda_l + \lambda_m - 2 \cdot (1 - \varepsilon) \cdot (\lambda_l - \lambda_m)}{2 \cdot \lambda_l + \lambda_m + (1 - \varepsilon) \cdot (\lambda_l - \lambda_m)} \quad (32)$$

where K is permeability [m²], d is sphere diameter [m], ε is porosity [–], r_{eff} is effective radius of wick structure [m], λ_{eff} is effective thermal conductivity, λ_l is thermal conductivity of working fluid liquid, and λ_m is thermal conductivity of wick material [47].

5.5. Verification of mathematical model

The mathematical model was created according to above equations of limitations and input heat pipe parameters. Result of mathematical model is graphic dependencies of heat transport limitations on heat pipe working temperature. Mathematical model results of heat transport limitations of specific types of heat pipes were compare with results from measurement of heat pipe performance at temperatures 50°C and 70°C. In **Figure 28**, graphic comparison results of heat transport limitations determining total performance of heat pipe from mathematical model with measured performance of ethanol wick heat pipe with sintered wick structure and sphere diameter of copper powder 0.1 mm are shown. Dotted line creates boundary of heat pipe performance by capillary limitation and dashed line is boiling limitation. The full line is measured results of heat pipe thermal performance at temperature 50°C and 70°C. **Figure 29**

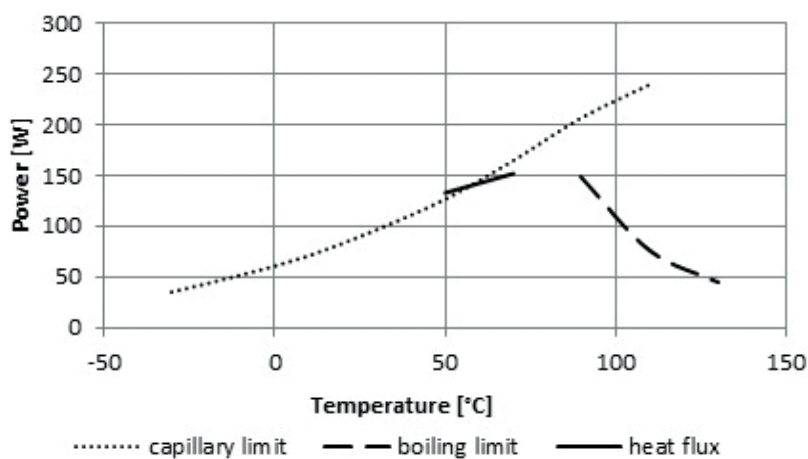


Figure 28. Verification of mathematical model by measuring of heat pipe performance (ethanol wick heat pipe with sintered wick structure and sphere diameter of copper powder 0.1 mm and axial orientation of heat pipe ψ 180°).

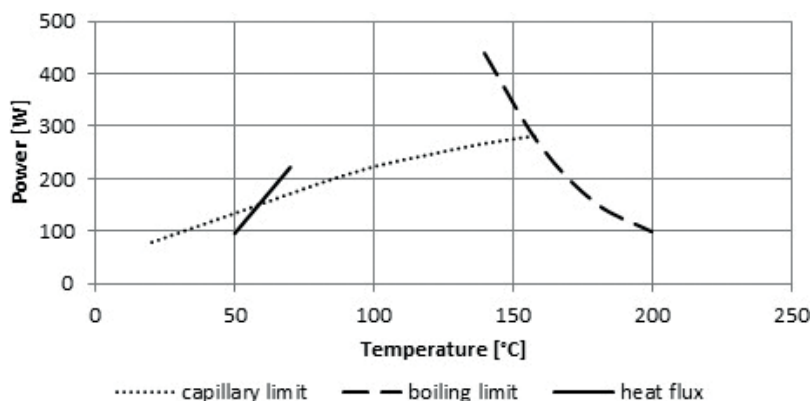


Figure 29. Verification of mathematical model by measuring of heat pipe performance (water wick heat pipe with sintered wick structure and sphere diameter of copper powder 0.63 mm axial orientation of heat pipe ψ 180°).

confirms the verification of mathematical model, where it is seen that the measured values of the transferred heat flux by heat pipe with sintered wick structure at temperatures 50°C and 70°C, are in approximately the same area as a calculated values of capillary limitation by mathematical model. In **Figures 28** and **29**, it is seen that the dotted line and full line are approximately in the same region at temperatures 50°C and 70°C.

5.6. Results of the mathematical model

Results of the heat pipe calculation are some interesting graphs of the maximal heat flux transferred by heat pipe depending on the wick structure parameters. It could be used in design optimization of the heat pipe wick structure. The curves present an area of maximal heat flux transferred by heat pipe depending on operating temperature.

Next graphic dependencies of heat pipe performance are created from mathematical model for ethanol wick heat pipe with sintered wick structure and various porosity, sphere diameter of copper powder, and wick structure width. In **Figure 30**, the influence of porosity on heat pipe performance is shown. Porosity of wick structure can change by adding some additives to sintered technology. There is clearly seen a rise in heat pipe performance with increasing porosity of wick structure. Heat pipe with the higher permeability of the wick structure can transfer higher heat flux. But with increasing permeability of wick structure, entrainment of liquid flow to evaporator by vapor flow can occur. This may cause dry out of heat pipe evaporation section and decrease total heat pipe performance.

In **Figure 31**, the influence of sphere diameter copper powder on sintered wick structure is shown. Using the bigger sphere diameter of copper powder to sintered technology, higher porosity wick structure is created. It can be said that increasing porosity is directly proportional to sphere dimension of copper powder, and to make more porosity wick structures, adding additives to sintered technology is not needed. In this case, an increase of heat pipe performance with used bigger sphere dimension of copper powder is seen.

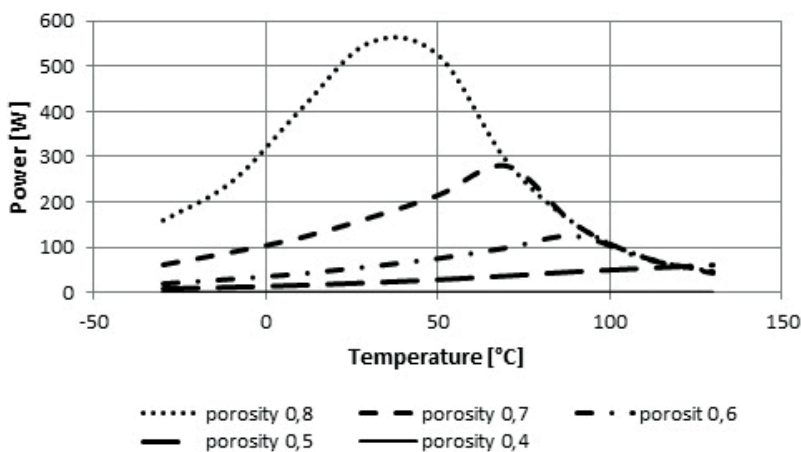


Figure 30. Dependence of heat pipe performance from wick structure porosity of the sintered wick heat pipe.

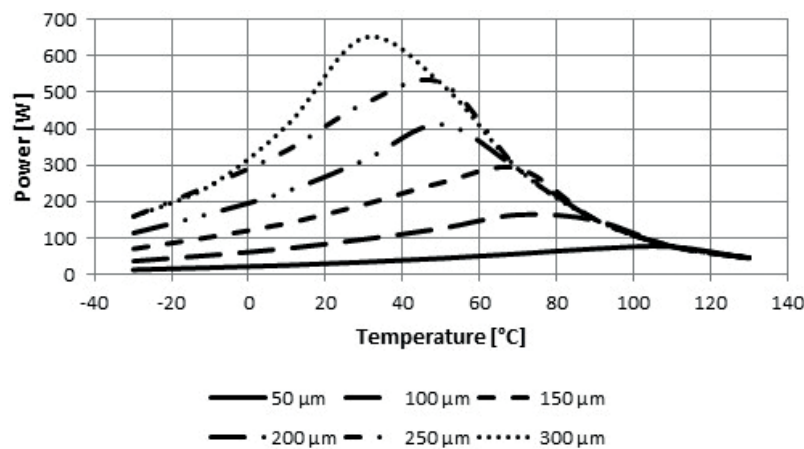


Figure 31. Dependence of heat pipe performance from sphere diameter of the copper powder in sintered wick heat pipe.

In **Figure 32**, the influence of wick structure width on heat pipe performance is shown. Wick structure width is an important factor, which influences heat pipe performance. It is seen that the heat pipe performance increases with the wick structure thickness in operating temperature region of -30 to 60°C . The capillary limitation is a main limitation for this region. On the other way, an increase of the wick structure thickness decreases the heat pipe performance in the operating temperature region of 80 – 130°C . It may be caused by bubble nucleation in wick structure, when the returning liquid from the condenser section to evaporator section of heat pipe evaporates. In this case, the main limitation is boiling limitation.

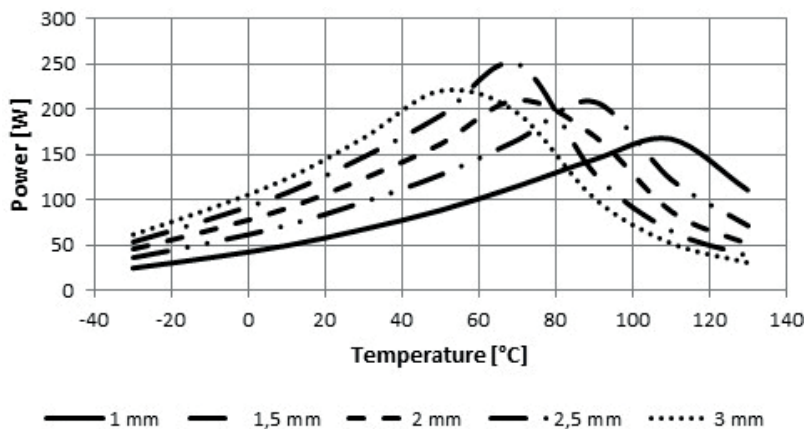


Figure 32. Dependence of heat pipe performance from wick structure width of the sintered wick heat pipe.

6. Conclusion

The experiments performed with the heat pipes in this work give several conclusions about the influence of porous wick structures on their heat transfer ability, where the porosity and pore size play main role. Experiments' influence of manufacturing technology on the wick structure porosity show that the sintering time and temperature of the metal powders are not influencing the wick structure porosity. Other finding of the influence of manufacturing technology on the porous wick structure by the metal powders sintering is that main influencing factors of the wick structure pore size are grain size, sintering temperature, and not so much sintering time.

The experiments' influence of working fluid amount, kind of wick structure and working fluid on heat transfer ability of loop heat pipe show that the optimal amount of the working fluid in LHP is in range 50–60%. In view of influence of the wick structure on the LHP operation, we can conclude that the porosity and pore size of the wick structure have influence on heat transfer ability, when the LHP with porous structure with 50% porosity has better effect on heat removal from IGBT than with 70% and LHP with porous structure with bigger pore size has better effect on heat removal from IGBT than with smaller pore size. Generally, the smallest pore size could cause the low capillary pressure in sintered wick structures against total pressure in whole LHP system. Experimental influence of working fluid on the LHP heat transfer ability shows that the LHP with working fluid acetone better removes heat from the IGBT at lower heat load in range of 100–300 W and LHP with the working fluid water better works at higher heat loads of LHP up to 450 W.

The experiments' influence of the wick structure and working fluid on heat transfer ability of the heat pipe did not show the best one combination of porous wick structure and working fluid. This experiment shows that the heat pipes with porous wick structure are able to transfer heat in range 100–200 W in the horizontal position. It depends on the wick structure parameters and kind of working fluid, because each heat pipe with various combination of these factors is unique due its different properties.

The mathematical calculation of the heat pipe heat transport limitations shows that the critical limitations influencing heat transfer ability of wick heat pipe are entrainment limitation, capillary limitation, and boiling limitation. These limitations depend on thermophysical properties, wick, and heat pipe parameters. The thermophysical properties of each working fluid are stable in temperature range and they cannot change. Changing the dimensions of wick structure is possible to optimize total heat flux transferred by heat pipe, because capillary pressure made in the wick structure depends mainly on the wick structure permeability. When the wick structure is designed, it is necessary to be careful because the increase in pore dimension increases permeability but decreases capillary pressure which manages the working fluid circulation in heat pipe. Therefore, the capillary limitation is the main heat transport limitation in wick heat pipe.

Acknowledgements

This article was created within the frame of projects APVV—15-0778 “Limits of radiative and convective cooling through the phase changes of working fluid in loop thermosyphon” and 042ŽU—4/2016 “Cooling on the basis of physical and chemical processes.”

Author details

Patrik Nemec

Address all correspondence to: patrik.nemec@fstroj.uniza.sk

University of Zilina, Zilina, Slovakia

References

- [1] Gaugler RS. Heat transfer devices. U.S. patent 2,350,348. 1944
- [2] Trefethen L. On the surface tension pumping of liquids or a possible role of the candle-wick in space exploration. In: GE Tech. Int. Ser. No G15-D114. NY: General Electric Co.; 1962
- [3] Grover GM, Cotter TP, Erikson GF. Structures of very high thermal conductivity. *Journal of Applied Physics*. 1964;**35**:1190-1191
- [4] Ochterbeck JM. Heat Pipes, in *Heat Transfer Handbook*. 1st ed. Editors Bejan A, Kraus AD. Hoboken, New Jersey: John Wiley & Sons, Inc.; 2003
- [5] Cernecky J, Koniar J, Brodnianska Z. The effect of heat transfer area roughness on heat transfer enhancement by forced convection. *Journal of Heat Transfer*. April 2014;**136**(4) Article number 4025920
- [6] Swanson LW. In: Kreith F, editor. *Heat Pipe, Heat and Mass Transfer, Mechanical Engineering Handbook*. Boca Raton: CRC Press LLC; 1999
- [7] Reay D, Kew P. *Heat Pipes Theory, Design and Applications*. 5th ed. Oxford, UK: Elsevier; 2006
- [8] Kaya T, Ku J. Thermal operational characteristics of a small-loop heat pipe. *Journal of Thermophysics and Heat Transfer*. 2003;**17**(4):464-470
- [9] Cheung KH, Hoang TT, Ku J, Kaya T. Thermal Performance and Operational Characteristics of Loop Heat Pipe (NRL LHP), SAE Technical Paper, No. 981813, 1998

- [10] Ku J. Operating characteristics of loop heat pipes. In: 29th International Conference on Environmental System, July 12–15, 1999, Denver, Colorado
- [11] Williams RR, Harris DK. Cross-plane and in-plane porous properties measurements of thin metal felts, applications in heat pipes. *Experimental Thermal and Fluid Science*. 2003;**27**:227-235
- [12] Bonnefoy M, Ochterbeck JM. Effective thermal conductivity of saturated sintered nickel loop heat pipe wicks. In: 37th Thermophysics Conference, American Institute of Aeronautics and Astronautics, June 28-July 1, 2004, Portland, Oregon. pp. 1-10
- [13] Holley B, Faghri A. Permeability and effective pore radius measurements for heat pipe and fuel cell applications. *Applied Thermal Engineering*. 2006;**26**:448-462
- [14] Chi SW. *Heat Pipe Theory and Practice: A Sourcebook*. New York: Hemisphere Publishing Corp; 1976
- [15] Čarnogurská M, Příhoda M, Brestovič T, Molínek J, Pyszko R. Determination of permeability and inertial resistance coefficient of filter inserts used in the cleaning of natural gas. *Journal of Mechanical Science and Technology*. 2012;**26**(1):103-111
- [16] Ren C, Wu Q. Heat transfer in loop heat pipes capillary wick, effect effective thermal conductivity. *Journal of Thermophysics and Heat Transfer*. 2007;**21**:134-140
- [17] Khrustalev D, Faghri A. Heat transfer in the inverted meniscus type evaporator at high heat fluxes. *International Journal of Heat and Mass Transfer*. 1995;**38**:3091-3101
- [18] Zhao TS, Liao Q. On capillary-driven flow and phase change heat transfer in a porous structure heated by a finned surface: Measurements and modelling. *International Journal of Heat and Mass Transfer*. 2000;**43**:1141-1155
- [19] Iverson BD, Davis TW, Garimella SV, North MT, Kang SS. Heat and mass transport in heat pipe wick structures. *Journal of Thermophysics and Heat Transfer*. 2007;**21**:392-404
- [20] Launay S, Sartre V, Bonjour J. Parametric analysis of loop heat pipe operation: A literature review. *International Journal of Thermal Sciences*. 2007;**46**:621-636
- [21] Gongming X, Kehang C, Yong Z, Lin C. Reduction of effective thermal conductivity for sintered LHP wicks. *International Journal of Heat and Mass Transfer*. 2010;**53**:2932-2934
- [22] Furukawa M. Model-based method of theoretical design analysis of a loop heat pipe. *Journal of Thermophysics and Heat Transfer*. 2006;**20**:111-121
- [23] Chuang PYA. *An Improved Steady-State Model of Loop Heat Pipes Based on Experimental and Theoretical Analyses [PhD Thesis]*. The Pennsylvania State University; 2003
- [24] Li J, Zou Y, Cheng L, Singh R, Akbarzadeh A. Effect of fabricating parameters on properties of sintered porous wick for loop heat pipe. *Power Technology*. 2010;**204**(2–3):241-248
- [25] Maydanik YF. Loop heat pipes. *Applied Thermal Engineering*. 2005;**25**:635-657

- [26] Patukhov V, Maidanik YF, Vershinin C. Miniature loop heat pipes for electronic cooling. *Applied Thermal Engineering*. 2003;**23**(9):1125-1135
- [27] Reimbrechta EG, Fredel MC, Bazzo E, Pereira FM. Manufacturing and microstructural characterization of sintered nickel wicks for capillary pumps. *Material Research*. 1999;**2**(3):225-229
- [28] Gongming X, Kehang C, Yong Z, Lin C. Development of sintered Ni-Cu wicks for loop heat pipes. *Science in China Series E: Technological Sciences*. 2009;**52**(6):1607-1612
- [29] Huang X, Franchi G. Design and fabrication of hybrid bimodal wick structure for heat pipe application. *Journal Porous Mater*. 2008;**15**:635-664
- [30] Samanta SK, Sharma BB, Das P, Lohar AK. Development of tubular Ni wicks used in LHP for space applications. *Frontiers in Heat Pipes (FHP)*. 2011;**2**. DOI: 043004
- [31] Gernert NJ, Baldassarre GJ, Gottschlich JM. Fine pore loop heat pipe wick structure development, SAE Technical Paper, No. 961319, 1996
- [32] Wu SC, Lo KC, Chen JR, Chung CY, Lin WJ, Su SJ. Effect of sintering temperature curve in wick manufactured for loop heat pipe. *Applied Mechanics and Materials*. 2014;**595**:24-29
- [33] Xin G, Cui K, Zou Y, Cheng L. Development of sintered Ni-Cu wicks for loop heat pipes. *Science in China Series E-Technological Sciences*. 2009;**52**(6):1607-1612
- [34] Orman LJ. Possibility of the application of microstructures in heating and ventilation systems. *Structure and Environment*. 2010;**2**(1):41-45
- [35] Zohuri B. *Heat Pipe Design and Technology: A Practical Approach*. Hillsborough, CA, USA: Galaxy Advanced Engineering; 2011
- [36] Peterson GP. *An Introduction to Heat Pipes: Modelling, Testing and Applications*. Atlanta: Wiley-Interscience; 1994
- [37] Silverstein C. *Design and Technology of Heat Pipes for Cooling and Heat Exchange*. Boca Raton: CRC Press; 1992
- [38] Faghri A. *Heat Pipe Science and Technology*, Washington, DC. Taylor & Francis; 1995
- [39] Chi SW. *Heat Pipe Theory and Practice*. Washington, DC: Hemisphere Publishing; 1976
- [40] Busse CA. Theory of the ultimate transfer of cylindrical heat pipes. *International Journal Heat Mass Transfer*. 1973;**16**:169-186
- [41] Ivanovskii MN, Sorokin VP, Yagodkin IV. *The Physical Properties of Heat Pipes*. Oxford: Clarendon Press; 1982
- [42] Busse CA, Kemme JE. Dry—Out phenomena in gravity— Assist heat pipes with capillary flow. *International Journal Heat Mass Transfer*. 1980;**23**:643-654
- [43] Cotter TP. Heat pipe startup dynamics. *Proceeding of SAE Thermionic Conversion Specialist Conference*, Palo Alto, CA; 1967

- [44] Marcu BD. On the Operation of Heat Pipes, Report 9895-6001-TU-000. Redondo Beach, CA: TRW; 1965
- [45] Dunn PD, Reay DA. Heat Pipes. 3rd ed. New York: Pergamon Press; 1982
- [46] Brennan PJ, Kroliczek EJ. Heat Pipe Design Handbook, NASA Contract Report NAS5-23406, 1979
- [47] Hlavačka V, Polášek F, Štulc P, Zbořil V. Tepelné trubice v elektrotechnice. Praha: STNL - Nakladatelství technické literatury; 1990

High-Porosity Metal Foams: Potentials, Applications, and Formulations

Ahmed Niameh Mehdy Alhusseney,
Adel Gharib Nasser and Nabeel M J Al-zurf

Additional information is available at the end of the chapter

<http://dx.doi.org/10.5772/intechopen.70451>

Abstract

This chapter is aimed as a concise review, but well-focused on the potentials of what is known as “High-porosity metal foams,” and hence, the practical applications where such promising media have been/can be employed successfully, particularly in the field of managing, recovering, dissipating, or enhancing heat transfer. Furthermore, an extensive comparison is conducted between the formulations presented so far for the geometrical and thermal characteristics concerning the heat and fluid flow in open-cell metal foams.

Keywords: high porosity, open cell, metal foam, fluid flow, thermal transport

1. Introduction

A porous medium can be defined as a material composed of a solid matrix consisting of interconnected voids. This solid matrix is usually assumed to be rigid, but sometimes it may undergo limited deformations. The interconnected pores allow for a single type of fluid or more to flow through the material. There are many examples of these permeable materials available in nature such as sand beds, limestone, sponges, wood, and so on.

Porous media have become one of the most important materials used in insulating, transferring, storing, and dissipating thermal energy. The benefits these characteristics confer have led to porous materials being widely used in practical applications such as thermal insulation, geothermal applications, cooling systems, recuperative/regenerative heat exchangers, and solar energy collection systems, in addition to chemical and nuclear engineering. Thus, convective flows in porous materials have been investigated widely over recent decades and various aspects have been considered for different applications so far.

High-porosity metal foams are usually porous media with low density and novel structural and thermal properties. This sort of media is mainly formed from multi-struts interconnected to each other at joint nodes to shape pores and cells (see the SEM image in **Figure 1**) (Liu et al. [1]). They offer very high porosity ($\epsilon \geq 0.89$), light weight, high rigidity and strength, and a large surface area, which make them able to recycle energy efficiently. This capacity to transport a large amount of heat is attributed to their superior thermal conductivity compared to ordinary fluids and high surface-area density (surface area per a given volume of metal foam) as well as enhanced convective transport (flow mixing) due to the tortuous flow paths existing within them, as shown in **Figure 1** (Zhao [2]). Also, their open-cell structure makes them even less resistant to the fluids flowing through them, and hence, the pressure drop across them is much less than it is in the case of fluid flow via packed beds or granular porous materials.

Open-cell metal foams were first invented by the ERG Materials and Aerospace Corp. in 1967, and since then, they have been continuously developed. This invention was patented to Walz [3], where the manufacturing processes were based on an organic preformation cast. However, this invention was originally intended for only classified military and aerospace applications. Accordingly, nonclassified applications had not made use of this technology until the mid of 1990s, when it has become generally available for industrial applications. Since then, other manufacturers have joined the global competition in this industry. To name a few, M-Pore GmbH in Germany, the French company Alveotec, and Constellium from Netherlands are currently making open-cell metal foams on a large scale for a wide range of applications.

The traditional way of casting open-cell metal foams is still adopted by ERG Materials and Aerospace [4] as well as M-Pore GmbH [5], where the foams are cast with an investment process based on polyurethane preformation. As the fabrication process is affected by gravity, the foams resulted will be shaped from oval rather than spherical cells, as illustrated in **Figure 2** (De Schampheleire et al. [6]). Alveotec [7] and Constellium, on the other hand, use a different way called leachable bed casting, in which metal is cast over a stack of soluble spheres to shape out the interconnecting open-cells desired. The spheres used are usually made out of either salt

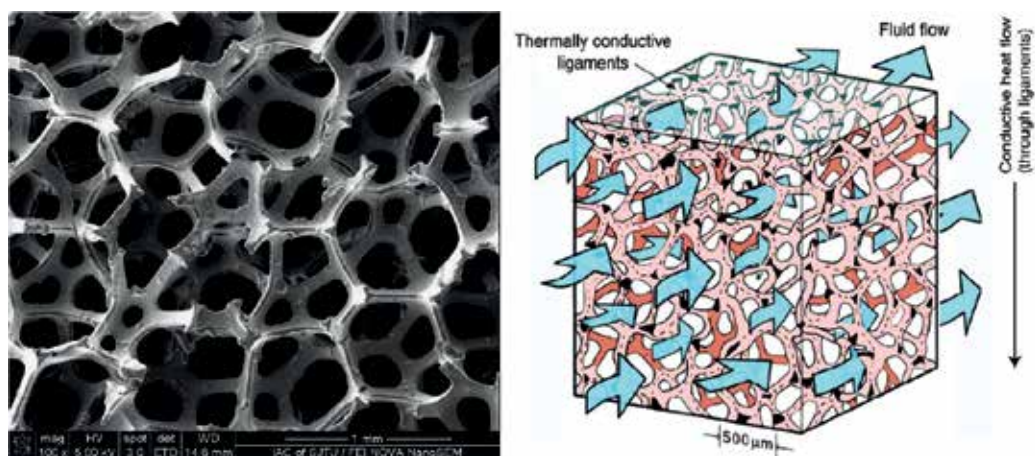


Figure 1. Open-cell metal foams: SEM image of the structure (left); mechanism of flow mixing (right).

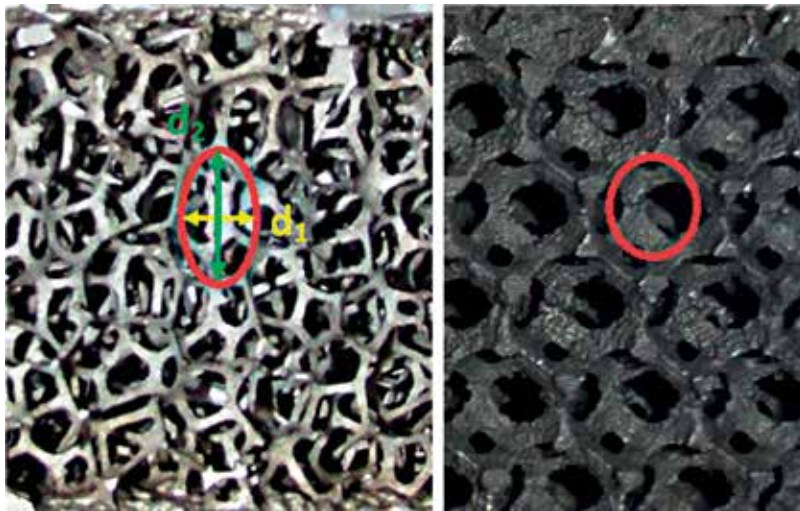


Figure 2. Open-cell metal foams formed by: Investment casting (left); (b) leachable bed casting (right).

or sand plus a polymer bonding agent. After metal solidification, the spheres are dissolved through washing them simply with water. Using this casting technique results in foams having more uniformly spherical-shaped cells unlike those formed by the investment casting, as shown in **Figure 2** (De Schampheleire et al. [6]).

2. Potentials

Open-cell metal foams possess unique characteristics, making them a promising candidate for plenty of practical and engineering applications. Among these potentials are the following:

1. Very high porosity, ranges usually from 80% and up to 97.5%.
2. The open-core structure makes them attractive for applications where lightweight is a crucial requirement.
3. The open-cell nature makes them even less resistant to the fluids flowing through them, resulting in a significant saving in the pressure drop resulted.
4. Very high effective thermal conductivity.
5. High surface-area density, roughly from 1000 to 3000 m²/m³. Therefore, exceptional heat transfer area per a given volume of metal foam is offered. The surface area density can be further increased through compressing them in a particular direction, where the specific surface area of such a compressed metal foam can reach up to 8000 m²/m³ [2].
6. The tortuous flow paths existing within them considerably enhance the convective transport (flow mixing).
7. They are efficient sound-absorption materials [8].

8. They have the potential to be used for radiation shielding [9].
9. Good-impact energy absorption [10], where the structure of metal foam makes it possible to ensure a constant stress throughout the deformation.
10. Have attractive stiffness/strength properties and can be processed in large quantity at low cost via the metal sintering route.

3. Applications

Due to their uniquely promising potentials, high-porosity metal foams have been increasingly utilized in a variety of engineering and industrial applications. Such applications are diversely increasing day by day, making it quite hard to categorize them into particular groups. Thus, it is aimed herein to present an overview of their most recent applications without intensely going into details.

Their ability to meet the increasing daily demands to effectively transfer, exchange, or dissipate heat has attracted researchers and manufacturers to utilize them as a successful alternative to traditional heat transport media. For example, the experiments conducted by Boomsma et al. [11] showed that the thermal performance offered by the compressed open-cell aluminum foam heat exchangers is usually two to three times higher than that achieved through the commercially available heat exchangers, while they require comparable pumping power. Similarly, Mahjoob and Vafai [12] pointed out that despite the potential increase in pressure loss, utilizing metal foams in heat exchangers leads to a substantial enhancement in heat transfer, which can compensate the increase in pressure drop.

Therefore, metal foam heat exchangers have emerged recently in various practical sectors. Among them, metal foams were used as alternative to find extended surfaces utilized in removing heat from geothermal power plants, where metal foam heat exchangers offer superior thermal performance compared to conventional finned surfaces, at no extra cost resulting from the pressure drop and/or material weight [13]. In this regard, wrapping a thin layer of foam around the surfaces of tubes was proposed to enhance the heat transferred from/to them with little increase in the pressure drop produced [14–16]. Despite the higher pressure loss resulted from the increase in foam layer thickness, it was observed that the exterior convective resistance is reduced significantly, and hence, a considerable transfer enhancement is achieved. Also, the overall performance attained through using the foam-covered tubes was comparable to that achieved by the helically finned tubes at the low levels of inlet velocities and far superior at the higher velocities.

In the context of HVAC&R applications, metal foams have been presented as a promising candidate to replace the conventionally finned heat exchangers. Dai et al. [17] compared the heat transfer performance of a flat-tube, louvered-fin heat exchanger with that obtained using an identical foam heat exchanger. The analytical results revealed that for the same fan power and heat transfer performance, the metal foam heat exchanger is significantly more economical in both size and weight for a wide range of design requirements. In another comparison study

[18], it was observed that the heat transfer rate offered by metal-foam heat exchangers is up to six times better than that in the case of the bare-tube bundle with no extra fan power. Also, it was found that if the dimensions of the foamed heat exchanger are not fixed, that is, the frontal area can be manipulated, metal-foam heat exchangers outperform the louvered-fin heat exchanger. In other words, a smaller metal-foam heat exchanger can be used for the same thermal duty, and hence, a smaller fan can perform what is required.

Employing high-porosity metal foams to improve the thermal effectiveness of counterflow double-pipe heat exchangers has been the subject of increasing interest recently. Xu et al. [19] pointed out that to achieve high thermal effectiveness, that is, greater than 0.8, porosity and pore density should be in the range of ($\varepsilon < 0.9$) and ($\omega > 10$ PPI), respectively. Furthermore, Chen et al. [20] observed that despite the increase occurred in the pressure drop, using metal foams results in a remarkable heat transfer enhancement (by as much as 11 times), which leads to a considerable improvement in the comprehensive performance, that is, up to 700%. More recently, an innovative double-pipe heat exchanger was proposed [21, 22] through using rotating metal foam guiding vanes fixed obliquely to force fluid particles to flow over the conducting surface while rotation. Furthermore, the conducting surface itself was covered with a metal foam layer to improve the heat conductance across it. To optimize the performance achieved, an overall performance system factor, that is, *OSP*, was introduced as the ratio of the heat exchanged to the total pumping power required. Overall, the negligibly small pumping power required compared to the amount of heat exchanged makes the overall performance of such heat exchangers incomparable, that is, $OSP = O(10^2)$ (Figure 3) (Alhuseny et al. [22]). It was also observed that while increasing the temperature difference from 30 to 300°C, the overall performance achieved can be improved up to 200–300% depending on the Re^* value. This outcome indicates the promising prospects to utilize the proposed configuration as a recuperator in gas turbine systems.

Now, utilizing metal foam can offer as more as twice the cooling effectiveness obtained by the traditional finned heat exchangers. Thus, such a sort of heat exchangers is widely employed today in medical and medicinal products, defense systems, industrial power generation plants,

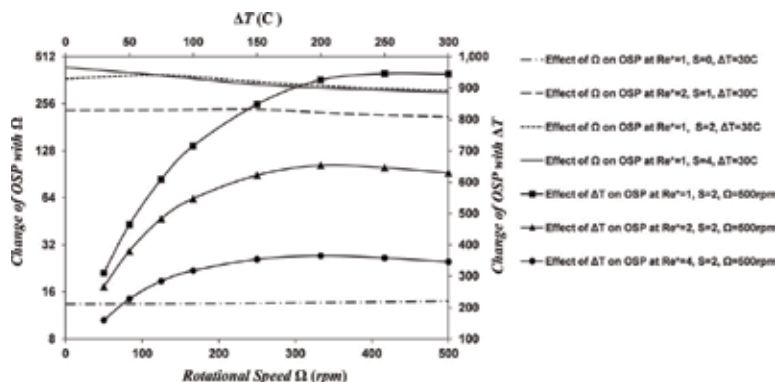


Figure 3. The change of the overall system performance *OSP* with the rotational speed Ω and characteristic temperature difference ΔT for $\varepsilon = 0.9$ and $\omega = 10$ PPI.

semiconductor, manufacturing, and aerospace manned flight [4]. Similarly, they have been proposed as an effective way to enhance the heat dissipated from heavy-duty electrical generators through filling their rotating cooling passages either fully or partially with open-cell metal foams [23–25]. The value of this proposal was inspected by introducing an enhancement factor as the ratio of heat transported to the pumping power required, that is, $\frac{Nu}{Re(p_{in}-p_e)/\rho u_{in}^2}$, and comparing it with the corresponding values from a previous work regarding turbulent flow in a rotating clear channel [26], as shown in **Figure 4** [25], where it was confirmed that the proposed enhancement is practically justified and efficient.

They have also been utilized effectively in electronic cooling, where various configurations of metal foam heat sinks have been suggested [27–33] as an effective alternative to the traditional heat sinks incorporated in electronic devices.

In similar context, utilizing metal foams to improve internal cooling of turbine blades is of increasing interest. Filling a radially rotating serpentine channel with open-cell aluminum foam is proposed as an effective way to improve the overall efficiency of the cooling process [34]. Recently, heat transport enhancement along a 180° round channel was proposed through placing multiple aluminum foam blocks alternately along the flow path [35]. It was found that using discrete foam blocks increases the heat transported by 74–140% compared to what the empty channel yields. In addition, it was observed that staggering the foam blocks vertically is more desirable for improving the overall system performance.

Due to their capability to transport heat effectively, metal foams are shaped into rings placed between the combustor and the turbine section of a jet engine in order to homogenize the temperature profiles of the gases leaving the combustor and, hence, to improve the overall efficiency of turbojet engines [36]. To provide a stable isothermalized platform for the airborne laser communication systems, ERG Materials & Aerospace [4] have fabricated aluminum foam

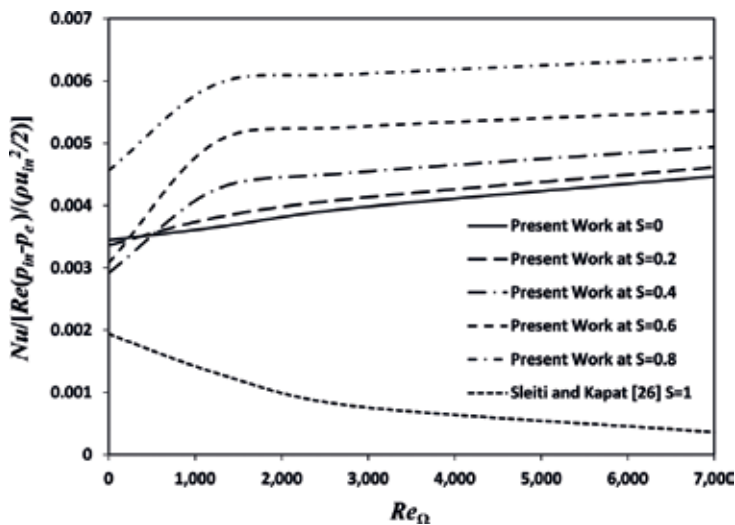


Figure 4. Influence of ΔT on the overall system performance; at $S = 2$, $\Omega = 500$ rpm, and $T_{cl} = 20^\circ\text{C}$.

composite opticals having the ability to allow unprecedented heat transfer. In the experiments conducted by Williams et al. [37], a porous insert material (PIM) formed of high porosity foam was proposed to improve the swirl stabilization in LPM combustion systems. It was found that using a reticulated foam insert results in mitigating the thermoacoustic instability effectively as well as reducing the combustion noise over the entire frequency range for a wide range of the design parameters considered.

As most of the phase change materials (PCMs) used for latent heat thermal energy storage (LHTES) possess poor thermal conductivity, the charging/discharging rate achieved will be quite modest. To overcome this deficit, high porosity metal foams have been suggested by Zhao et al. [38] as an effective means to improve the PCMs' overall thermal conductivity, leading to enhance the heat transported and, hence, promote the PCM melting and solidification, as can be seen in **Figure 5** (Alhusseny et al. [39]). This concept has been extensively investigated later to further improve the performance achieved, to name a few, the works presented for low-temperature [40–42] and high-temperature LHTES systems [43–45].

Open-cell aluminum foams are considered as promising lightweight materials for γ -ray and thermal neutron shielding materials. The data collected experimentally by Xu et al. [46] reveal that filling the foam with water results in improving the mass attenuation coefficients compared to the nonfilled samples. Overall, following such a proposal to achieve high shielding performance is still in progress [47, 48] and requires further optimizations.

Overall, there is a variety of applications where high-porosity metal foam can be utilized successfully. For further applications, ERG Materials & Aerospace [4] lists diverse sorts of applications whether in daily life or military industries. For example, open-cell metal

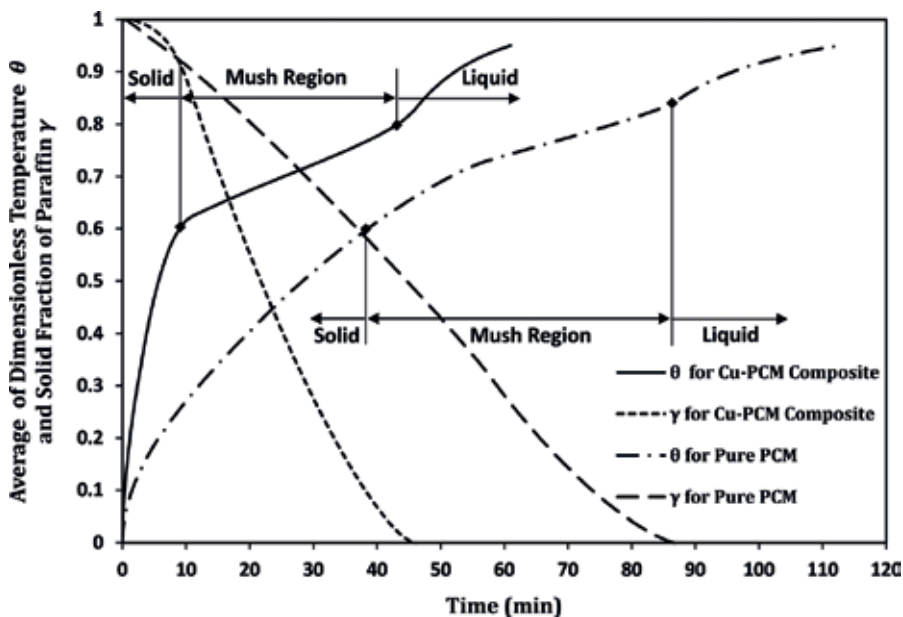


Figure 5. Time development of charging process of paraffin-copper foam composite vs. pure paraffin.

foams are commonly used as energy absorber in aerospace and military applications, air/oil separators in aircraft engine gearboxes, baffles to prevent sudden surges in liquids while being penetrated by solid frames, and breather plugs in applications requiring fast equalization of pressure changes. Also, they are utilized in electrodes, fuel cells, bone researches, micrometeorite shields, optics/mirrors, windscreens and so on. Manufacturers' data and the open literature can be further dug for much more applications where high-porosity metal foams have outperformed and/or achieved considerable savings in the expenses required.

4. Formulations

Open-cell metal foams are classified as high-porosity materials that consist of irregularly shaped and tortuous flow passages. Pressure drop and heat transfer through such media are significantly affected by their geometrical characteristics, namely the foam porosity ε , fiber size d_f , pore diameter d_p , pore density ω , and cell shape. Therefore, most aspects regarding granular porous media and packed beds need to be adjusted for metal foams [11].

4.1. Estimation of fiber and pore diameter

In practice, the ligament size, or in other words fiber diameter, is usually measured using a microscope. Alternatively, the mean pore diameter can be estimated by counting the number of pores that exist in a particular length of foam, which is usually provided by the manufacturer in terms of pore density (PPI), that is, number of pores per inch. Depending on the representative unit cell used (**Figure 6**), various models were proposed. Among them is the model proposed by Fourie and Du Plessis [49] for pore size estimation as a function of the width of a cubic representative unit cell and tortuosity (Eq. (1)). Another model was developed by Calmidi [50] to estimate the fiber- to pore-diameter ratio as a function of the porosity and shape function, $G = 1 - e^{-(1 - \varepsilon)/0.04}$, for both the cubic unit cell (Eq. (2)) and the three-dimensional structure of a dodecahedron unit cell (Eq. (3)).

Fourie and Du Plessis [49]:

$$d_p = d \frac{2}{(3 - \chi)}, \quad d = d_p + d_f \quad (1)$$

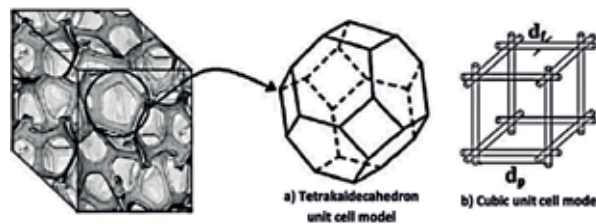


Figure 6. Models used to represent microstructural unit cells in metal foams.

Calmidi [50]:

$$\frac{d_f}{d_p} = 2\sqrt{\frac{(1-\varepsilon)}{3\pi}} \frac{1}{G} \quad (2)$$

$$\frac{d_f}{d_p} = 1.18\sqrt{\frac{(1-\varepsilon)}{3\pi}} \frac{1}{G} \quad (3)$$

4.2. Models developed for predicting tortuosity of high-porosity metal foams

The tortuosity, defined as the total tortuous pore length within a linear length scale divided by the linear length scale in the porous medium [49], was modeled by Du Plessis et al. [51] as a function of porosity only (Eq. (4)). However, experiments conducted by Bhattacharya et al. [52] indicated that the accuracy of tortuosity model proposed by Du Plessis et al. [51] is limited for higher levels of pore density; hence, a tortuosity formulation that accurately covers a wider range of porosity and pore densities was established in terms of porosity and shape function G (Eq. (5)). Recently, an analytical model was proposed by Yang et al. [53] (Eq. (6)), as a simple function of both foam porosity and a pore shape factor. The shape factor β is defined as the ratio of the representative pore perimeter to the perimeter of a typical reference circle with an area equal to that of the representative pore.

Du Plessis et al. [51]:

$$\frac{1}{\chi} = \frac{3}{4\varepsilon} + \frac{\sqrt{9-8\varepsilon}}{2\varepsilon} \cos \left\{ \frac{4\pi}{3} + \frac{1}{3} \cos^{-1} \left[\frac{8\varepsilon^2 - 36\varepsilon + 27}{(9-8\varepsilon)^{3/2}} \right] \right\} \quad (4)$$

Bhattacharya et al. [52]:

$$\frac{1}{\chi} = \frac{\pi}{4\varepsilon} \left\{ 1 - \left(1.18\sqrt{\frac{(1-\varepsilon)}{3\pi}} \frac{1}{G} \right)^2 \right\} \quad (5)$$

Yang et al. [53]:

$$\chi = \frac{\beta\varepsilon}{1 - (1-\varepsilon)^{1/3}} \quad (6)$$

4.3. Models developed for estimating pressure drop across open-cell metal foams

With regard to predicting the pressure drop produced in fluid flows across high-porosity metal foams, a variety of models have been developed, which can be classified into two main categories. The first encompasses those investigations interested in estimating the pressure drop by means of the foam friction factor. Among them is the model presented by Paek et al. [54] for the friction factor as a function of pore Reynolds number (Eq. (7)). Also, the empirical correlations established by Liu et al. [55] offer friction factor estimation for airflow via aluminum foams for a wide range of porosity and various flow regimes (Eq. (8)).

Paek et al. [54]:

$$f = \frac{1}{\text{Re}_K} + 0.105 \quad f = \frac{(\Delta P/L)\sqrt{K}}{\rho u^2}, \text{ and } \text{Re}_K = \frac{\rho u \sqrt{K}}{\mu} \quad (7)$$

Liu et al. [55]:

$$\left. \begin{aligned} 30 < \text{Re}_{D_p} < 300 : f &= \frac{22(1-\varepsilon)}{\text{Re}_{D_p}} + 0.22 \\ \text{Re}_{D_p} \gg 300 : f &= 0.22 \end{aligned} \right\} \quad (8)$$

$$f = \frac{(\Delta P/L)D_p}{\rho u^2} \frac{\varepsilon^3}{1-\varepsilon}, \text{ and } \text{Re}_{D_p} = \frac{\rho u \sqrt{K}}{\mu}$$

The other category of pressure drop models consists of those concerned with estimating the permeability and inertial coefficient according to Darcy–Forchheimer’s equation:

$$\frac{dp}{dx} = \frac{\mu}{K}u + \frac{\rho F}{\sqrt{K}}u^2 \quad (9)$$

Based on a cubic representative unit cell, a theoretical model for predicting permeability and inertial coefficient was derived by Du Plessis et al. [51] (Eqs. (10) and (11)), as functions of porosity, tortuosity, and the width of cubic representative unit cell. In the study conducted by Calmidi [50], mathematical models were developed for both permeability and inertial coefficient as functions of the fiber and pore diameters as well as the foam porosity (Eqs. (12) and (13)). A correlation was established by Bhattacharya et al. [52] for predicting the inertial coefficient (Eq. (14)), in terms of tortuosity, porosity, shape function, and form drag coefficient $C_D(\varepsilon)$. Based on Ergun’s law $\left(\frac{\Delta p}{L} = \alpha \frac{(1-\varepsilon)^2}{\varepsilon^3 d^2} \mu u + \beta \frac{(1-\varepsilon)}{\varepsilon^3 d} \rho u^2\right)$, Tadrist et al. [56] developed an empirical model for estimating permeability and inertial coefficient as functions of foam porosity and fiber size (Eqs. (15) and (16)). In the experiments conducted by Dukhan [57], the pressure drop resulting from airflow across aluminum foam was correlated into a model predicting the permeability and inertial coefficient as functions of porosity only (Eqs. (17) and (18)). Recently, an analytical model for estimating the permeability of metal foams (Eq. (19)) was established by Yang et al. [53] according to the cubic representative unit cell. This model offers the capability of estimating the permeability for a wide range of foam porosities $\varepsilon = 0.55 \sim 0.98$ and pore densities $\omega = 5 \sim 100$ PPI.

Du Plessis et al. [51]:

$$K = \frac{\varepsilon^2 d^2}{36\chi(\chi-1)} \quad (10)$$

$$F = \frac{2.05\chi(\chi-1)\sqrt{K}}{\varepsilon^2(3-\chi)} \frac{1}{d} \quad (11)$$

Calmidi [50]:

$$K = 0.00073 d_p^2 (1 - \varepsilon)^{-0.224} \left(\frac{d_f}{d_p} \right)^{-1.11} \quad (12)$$

$$F = 0.00212 (1 - \varepsilon)^{-0.132} \left(\frac{d_f}{d_p} \right)^{-1.63} \quad (13)$$

Bhattacharya et al. [52]:

$$F = 0.095 \frac{C_{D(\varepsilon=0.85)}}{12} G^{0.2} \sqrt{\frac{\varepsilon}{3(\chi - 1)}} \left(1.18 \sqrt{\frac{(1 - \varepsilon)}{3\pi}} \frac{1}{G} \right)^{-1} \quad (14)$$

$$\left. \begin{array}{l} 0.85 < \varepsilon < 0.97 : \quad G = 1 - e^{-(1-\varepsilon)/0.04} \\ \varepsilon \geq 0.97 : \quad G = 0.5831 \end{array} \right\}, \text{ and, } C_{D(\varepsilon=0.85)} = 1.2$$

Tadrist et al. [56]:

$$K = \frac{\varepsilon^3 d_f^2}{\alpha (1 - \varepsilon)^2}, \quad \alpha : 100 \sim 865 \quad (15)$$

$$F = \frac{\beta (1 - \varepsilon)}{\varepsilon^3} \frac{\sqrt{K}}{d_f}, \quad \beta : 0.65 \sim 2.6 \quad (16)$$

Dukhan [57]:

$$K = a_1 e^{b_1 \varepsilon} \quad (17)$$

$$F = (a_2 \varepsilon + b_2) \sqrt{K} \quad (18)$$

a_1, a_2, b_1 , and b_2 are all constants

Yang et al. [53]:

$$\frac{K}{d^2} = \frac{\varepsilon \left(1 - (1 - \varepsilon)^{1/3} \right)^2}{36\beta \left[(1 - \varepsilon)^{1/3} - (1 - \beta\varepsilon) \right]} \quad (19)$$

4.4. Effective thermal conductivity models for high-porosity metal foams

Many investigations have been conducted to evaluate the effective thermal conductivity k_e as a key factor in the thermal analysis of such systems. Among them is the model established by Paek et al. [54] based on one-dimensional heat conduction through a cubic unit cell (Eq. (20)). This model indicates that foam porosity has a direct impact on the overall thermal conductivity unlike the pore size, which was found to have a marginal influence.

The theoretical model derived by Calmidi and Mahajan [58] for the effective thermal conductivity as a function of the foam porosity (Eq. (21)) was found to match well with the experiments for both air and water as fluid phase. Similarly, Bhattacharya et al. [52] examined a two-dimensional unit cell shaped as a hexagonal honey comb to estimate the effective thermal conductivity, but taking into account circular nodes at each intersection joint rather than the square nodes considered earlier by Calmidi and Mahajan [58]. Although this model showed excellent agreement with the experimental data obtained and its formulations detailed in Eq. (22) look mathematically simpler than that derived by Calmidi and Mahajan [58], it is in fact more complicated because this model is valid only for a limited case when the intersection size R approaches zero, which implies that $r \rightarrow \infty$.

A tetrakaidecahedron unit cell was adopted by Boomsma and Poulikakos [59] to estimate the effective thermal conductivity. Despite the fact that taking tetrakaidecahedron topology into account can provide a better estimation, it leads to more complex formulae, detailed in Eq. (23). Moreover, it was found that this model includes some aspects need to be adjusted as found by Dai et al. [60] (Eq. (24)). Based on the tetrakaidecahedron unit cell as well but with assuming one-dimensional heat conduction along the highly tortuous ligaments, a quite simplistic model (Eq. (25)) was recently derived by Yang et al. [61] for effective thermal conductivity of metal foams saturated with low conducting fluids, for example, air. However, this model is limited to highly conducting foams, where heat conduction is assumed to occur only along the tortuous ligaments ignoring the heat conduction through the fluid phase. More recently, the 3D tetrakaidecahedron unit cell was considered by Yao et al. [62] to establish a more realistic formulation for effective thermal conductivity (Eq. (26)) through taking into account the concavity and orientation of the tri-prism ligaments and for four pyramids nodes. In addition to including no empirical parameters, this model has outperformed, in terms of accuracy, what were reported earlier in the literature [62].

Paek et al. [54]:

$$k_e = k_f(1-t)^2 + k_s t^2 + \frac{2t(1-t)k_f k_s}{k_f t + k_s(1-t)}, \quad t = \frac{1}{2} + \cos \left(\frac{1}{3} \cos^{-1}(2\varepsilon - 1) + \frac{4\pi}{3} \right) \quad (20)$$

Calmidi and Mahajan [58]:

$$k_e = \left\{ \frac{2}{\sqrt{3}} \left[\frac{r(\frac{b}{L})}{k_f + (1 + \frac{b}{L})\frac{(k_s - k_f)}{3}} + \frac{(1-r)(\frac{b}{L})}{k_f + \frac{2}{3}(\frac{b}{L})(k_s - k_f)} + \frac{\frac{\sqrt{3}}{2} - \frac{b}{L}}{k_f + \frac{4r}{3\sqrt{3}}(\frac{b}{L})(k_s - k_f)} \right] \right\}^{-1} \quad (21)$$

$$\frac{b}{L} = \frac{-r + \sqrt{r^2 + \frac{2}{\sqrt{3}}(1-\varepsilon) \left[2 - r \left(1 + \frac{4}{\sqrt{3}} \right) \right]}}{\frac{2}{3} \left[2 - r \left(1 + \frac{4}{\sqrt{3}} \right) \right]}, \quad \text{and, } r = 0.09$$

Bhattacharya et al. [52]:

$$k_e = \left\{ \frac{2}{\sqrt{3}} \left[\frac{\frac{t}{L}}{k_f + \frac{(k_s - k_f)}{3}} + \frac{\frac{\sqrt{3} - t}{2}}{k_f} \right] \right\}^{-1}, \quad \frac{t}{L} = \frac{-\sqrt{3} - \sqrt{3 + (1 - \varepsilon)(\sqrt{3} - 5)}}{1 + \frac{1}{\sqrt{3}} - \frac{8}{3}} \quad (22)$$

Boomsma and Poulikakos [59]:

$$\left. \begin{aligned} k_e &= \frac{\sqrt{2}}{(R_A + R_B + R_C + R_D)} \\ R_A &= \frac{4d}{[2e^2 + \pi d(1 - e)]k_s + [4 - 2e^2 - \pi d(1 - e)]k_f} \\ R_B &= \frac{(e - 2d)^2}{(e - 2d)e^2k_s + [2e - 4d - (e - 2d)e^2]k_f} \\ R_C &= \frac{(\sqrt{2} - 2e)^2}{2\pi d^2(1 - 2e\sqrt{2})k_s + 2[\sqrt{2} - 2e - \pi d^2(1 - 2e\sqrt{2})]k_f} \\ R_D &= \frac{2e}{e^2k_s + (4 - e^2)k_f} \\ d &= \sqrt{\frac{\sqrt{2}[2 - (5/8)e^3\sqrt{2} - 2\varepsilon]}{\pi(3 - 4e\sqrt{2} - e)}}, \text{ and, } e = 0.339 \end{aligned} \right\} \quad (23)$$

Dai et al. [60]:

$$\left. \begin{aligned} R_C &= \frac{\sqrt{2} - 2e}{\sqrt{2}\pi d^2k_s + (2 - \sqrt{2}\pi d^2)k_f} \\ d &= \sqrt{\frac{\sqrt{2}[2 - (3/4)e^3\sqrt{2} - 2\varepsilon]}{\pi(3 - 2e\sqrt{2} - e)}}, \text{ and, } e = 0.198 \end{aligned} \right\} \quad (24)$$

Yang et al. [61]:

$$k_e = \frac{1}{3}(1 - \varepsilon)k_s \quad (25)$$

Yao et al. [62]:

$$\left. \begin{aligned}
k_e &= \frac{1}{(\lambda/k_A) + ((1 - 2\lambda)/k_B) + (\lambda/k_C)} \\
k_A &= \frac{\sqrt{2}}{6} \pi \lambda (3 - 4\lambda) \frac{1 + a_1^2}{a_1^2} k_s + \left[1 - \frac{\sqrt{2}}{6} \pi \lambda (3 - 4\lambda) \frac{1 + a_1^2}{a_1^2} \right] k_f \\
k_B &= \frac{\sqrt{2}}{2} \pi \lambda^2 \frac{1 + a_1^2}{a_1^2} k_s + \left(1 - \sqrt{2} \pi \lambda^2 \frac{1 + a_1^2}{a_1^2} \right) k_f \\
k_C &= \frac{\sqrt{2}}{6} \pi \lambda^2 \frac{1 + a_1^2}{a_1^2} k_s + \left(1 - \frac{\sqrt{2}}{6} \pi \lambda^2 \frac{1 + a_1^2}{a_1^2} \right) k_f \\
\varepsilon &= 1 - \frac{\sqrt{2}}{2} \pi \lambda^2 (3 - 5\lambda) \frac{1 + a_1^2}{a_1^2}, \text{ and, } a_1 = 2.01
\end{aligned} \right\} \quad (26)$$

4.5. Solid–fluid interstitial thermal exchange within open-cell metal foams

The condition of local thermal equilibrium (LTE) often occurs between the fluid and solid phases when a fluid flows across a permeable medium formed of comparably thermally conductive material. This makes the temperature difference between the two phases negligibly small. However, when the solid thermal conductivity is much higher than the corresponding value for the fluid phase, for example, metal foams, the assumption of LTE is no longer valid and usually results in an overestimation of the heat transported between the two phases. Hence, taking into account the local thermal nonequilibrium (LTNE) between the two phases becomes indispensable in metal foams, where two energy equations are coupled together to predict heat transfer in each phase separately.

Three principal heat transfer modes take place when a low conductive fluid flows across the ligaments of highly conductive foam: convection between the solid and fluid phases besides conduction via each one of the two phases. Thus, the three key parameters required for applying the LTNE approach are the effective thermal conductivity of the fluid k_{fe} and solid k_{se} phases in addition to the interstitial specific heat transfer rate between the two phases ($a_{sf} h_{sf}$), which depends on the foam structure and the flow regime across it.

The interstitial heat exchange rate depends on two individual quantities: the interfacial specific surface area a_{sf} and the solid-to-fluid interfacial heat transfer coefficient h_{sf} . By utilizing the dodecahedral structure of open-cell foams and taking into account the noncircular fiber cross section, the solid-to-fluid interfacial specific surface area a_{sf} was modeled by Calmidi and Mahajan [63] for arrays of cylinders that intersect in three mutually perpendicular directions (Eq. (27)), while Fourie and Du Plessis [49] established another model based on the cubic unit-cell representation (Eq. (28)). However, Schampheleire et al. [6] observed that the a_{sf} values estimated using Eq. (27) by Calmidi and Mahajan [63] deviates seriously from those obtained experimentally through a μCT scan with differences up to 233%, while the model of Fourie and Du Plessis [49] performs much better with up to 22% deviation from the experimental data of the full μCT scan.

Calmidi and Mahajan [63]:

$$a_{sf} = \frac{3\pi d_f}{(0.59d_p)^2} \left[1 - e^{-(1-\varepsilon)/0.04} \right] \quad (27)$$

Fourie and Du Plessis [49]:

$$a_{sf} = \frac{3}{d} (3 - \chi)(\chi - 1) \quad (28)$$

With regard to estimating the solid–fluid interfacial heat transfer coefficient in high-porosity metal foams, Calmidi and Mahajan [63] proposed a correlation for interfacial Nusselt number as a function of both the foam porosity and fiber diameter (Eq. (29)). Another model was established by Shih et al. [28] for Nusselt number as a function of the foam porosity and pore diameter (Eq. (30)), where a and b are constants depending on the geometrical characteristics of the foam samples used in the experiments conducted. The correlations developed by Zukauskas [64] for staggered cylinders are widely used as a model to predict the interfacial Nusselt number as a function of the foam porosity, fiber diameter, and the value of Reynolds number (Eq. (31)), which makes it more general than the one proposed by Calmidi and Mahajan [63] as it is valid for a limited range of Reynolds numbers (40–1000).

Calmidi and Mahajan [63]:

$$Nu_{sf} = \frac{h_{sf} d_f}{k_f} = C_T Re_{df}^{0.5} Pr^{0.37} = 0.52 \sqrt{\frac{u d_f}{\varepsilon v}} Pr^{0.37} \quad (29)$$

Shih et al. [28]:

$$Nu_{Dp} = \frac{h D_p}{k_{se}} = a Re_{Dp}^b = a \left(\frac{\rho u D_p}{\mu} \right)^b \quad (30)$$

Zukauskas [64]:

$$Nu_{sf} = \frac{h_{sf} d}{k_f} = \left\{ \begin{array}{ll} 0.76 Re_d^{0.4} Pr^{0.37}, & (1 \leq Re_d \leq 40) \\ 0.52 Re_d^{0.5} Pr^{0.37}, & (40 \leq Re_d \leq 10^3) \\ 0.26 Re_d^{0.6} Pr^{0.37}, & (10^3 \leq Re_d \leq 2 \times 10^5) \end{array} \right\} \quad (31)$$

$$d = (1 - e^{-(1-\varepsilon)/0.04}) d_f$$

Author details

Ahmed Niameh Mehdy Alhusseney^{1,2*}, Adel Gharib Nasser² and Nabeel M J Al-zurf¹

*Address all correspondence to: ahmedn.alhusseini@uokufa.edu.iq

1 Mechanical Engineering Department, Faculty of Engineering, University of Kufa, Iraq

2 School of Mechanical, Aerospace and Civil Engineering, University of Manchester, UK

References

- [1] Liu Z, Yao Y, Wu H. Numerical modeling for solid-liquid phase change phenomena in porous media: Shell-and-tube type latent heat thermal energy storage. *Applied Energy*. 2013;**112**:1222-1232
- [2] Zhao CY. Review on thermal transport in high porosity cellular metal foams with open cells. *International Journal of Heat and Mass Transfer*. 2012;**55**:3618-3632
- [3] Walz DD. *Reticulated Foam Structure*. Oakland: Energy Research & Generation Inc.; 1976
- [4] ERG Materials & Aerospace. ERG Duocel® Foam [Internet]. Available from: <http://www.ergaerospace.com/index.html> [Accessed: 19-06-2017]
- [5] MAYSER®. Foam Technology & Moulding [Internet]. Available from: <http://www.mayser.com/en/foamtechnology-and-moulding> [Accessed: 24-06-2017]
- [6] De Schampheleire S, De Jaeger P, De Kerpel K, Ameel B, Huisseune H, De Paepe M. How to study thermal applications of open-cell metal foam: Experiments and computational fluid dynamics. *Materials*. 2016;**9**(2):1-27/94
- [7] Alveotec. The Metal Foam by Alvéotec or Honeycomb Casting Process [Internet]. Available from: <http://www.alveotec.fr/en/innovation.html> [Accessed: 26-06-2017]
- [8] Xu C, Mao Y, Hu Z. Tonal and broadband noise control of an axial flow fan with metal foams: Design and experimental validation. In: 22nd AIAA/CEAS Aeroacoustics Conference, Aeroacoustics Conferences, (AIAA 2016–3062); 30 May–1 June; Lyon, France. AIAA; 2016
- [9] Dixit T, Ghosh I. Radiation heat transfer in high porosity open-cell metal foams for cryogenic applications. *Applied Thermal Engineering*. 2016;**102**:942-951
- [10] Borovinšek M, Ren Z. Computational modelling of irregular open-cell foam behaviour under impact loading. *Materials Science & Engineering Technology*. 2008;**39**(2):114-120
- [11] Boomsma K, Poulikakos D, Zwick F. Metal foams as compact high performance heat exchangers. *Mechanics of Materials*. 2003;**35**:1161-1176
- [12] Mahjoob S, Vafai K. A synthesis of fluid and thermal transport models for metal foam heat exchangers. *International Journal of Heat and Mass Transfer*. 2008;**51**:3701-3711
- [13] Ejlali A, Ejlali A, Hooman K, Gurgenci H. Application of high porosity metal foams as air-cooled heat exchangers to high heat load removal systems. *International Communications in Heat and Mass Transfer*. 2009;**36**:674-679
- [14] Straatman AG, Gallego NC, Thompson BE, Hangan H. Thermal characterization of porous carbon foam-convection in parallel flow. *International Journal of Heat and Mass Transfer*. 2006;**49**:1991-1998
- [15] T'Joel C, De Jaeger P, Huisseune H, Van Herzeele S, Vorst N, De Paepe M. Thermo-hydraulic study of a single row heat exchanger consisting of metal foam covered round tubes. *International Journal of Heat and Mass Transfer*. 2010;**53**:3262-3274

- [16] Odabae M, Hooman K. Metal foam heat exchangers for heat transfer augmentation from a tube bank. *Applied Thermal Engineering*. 2012;**36**:456-463
- [17] Dai Z, Nawaz K, Park Y, Chen Q, Jacobi AM. A comparison of metal-foam heat exchangers to compact multi-louver designs for air-side heat transfer applications. *Heat Transfer Engineering*. 2012;**33**:21-30
- [18] Huisseune H, De Schampheleire S, Ameel B, De Paepe M. Comparison of metal foam heat exchangers to a finned heat exchanger for low Reynolds number applications. *International Journal of Heat and Mass Transfer*. 2015;**89**:1-9
- [19] Xu HJ, Qu ZG, Tao WQ. Numerical investigation on self-coupling heat transfer in a counter-flow double-pipe heat exchanger filled with metallic foams. *Applied Thermal Engineering*. 2014;**66**:43-54
- [20] Chen X, Tavakkoli F, Vafai K. Analysis and characterization of metal foam-filled double-pipe heat exchangers. *Numerical Heat Transfer, Part A: Applications*. 2015;**68**:1031-1049
- [21] Alhusseny A, Turan A, Nasser A, Al-zurfi N. Performance improvement of a counter-flowing double-pipe heat exchanger partially filled with a metal foam and rotating coaxially. In: 12th International Conference on Heat Transfer, Fluid Mechanics and Thermodynamics; 11–13 July; Costa del Sol, Malaga. 2016. pp. 1368-1377
- [22] Alhusseny A, Turan A, Nasser A. Rotating metal foam structures for performance enhancement of double-pipe heat exchangers. *International Journal of Heat and Mass Transfer*. 2017;**105**:124-139
- [23] Alhusseny A, Turan A. Effects of centrifugal buoyancy on developing convective laminar flow in a square channel occupied with a high porosity fibrous medium. *International Journal of Heat and Mass Transfer*. 2015;**82**:335-347
- [24] Alhusseny A, Turan A, Nasser A, Hidri F. Hydrodynamically and thermally developing flow in a rectangular channel filled with a high porosity fiber and rotating about a parallel axis. *International Communications in Heat and Mass Transfer*. 2015;**67**:114-123
- [25] Alhusseny A, Turan A, Nasser A. Developing convective flow in a square channel partially filled with a high porosity metal foam and rotating in a parallel-mode. *International Journal of Heat and Mass Transfer*. 2015;**90**:578-590
- [26] Sleiti AK, Kapat JS. Heat transfer in channels in parallel-mode rotation at high rotation numbers. *Journal of Thermophysics and Heat Transfer*. 2006;**20**:748-753
- [27] Kuo SM, Tien CL. Heat transfer augmentation in a foam-material filled duct with discrete heat sources. In: Intersociety Conference on IEEE Thermal Phenomena in the Fabrication and Operation of Electronic Components (I-THERM '88); 11–13 May. Los Angeles, CA. 1988. pp. 87-91
- [28] Shih WH, Chiu WC, Hsieh WH. Height effect on heat-transfer characteristics of aluminium-foam heat sinks. *Journal of Heat Transfer*. 2006;**128**:530-537

- [29] Bhattacharya A, Mahajan RL. Metal foam and finned metal foam heat sinks for electronics cooling in buoyancy-induced convection. *Journal of Electronic Packaging*. 2006;**128**: 259-266
- [30] CT DG, Straatman AG, Betchen LJ. Modeling forced convection in finned metal foam heat sinks. *Journal of Electronic Packaging*. 2009;**131**:1-10/021001
- [31] Kuang JJ, Kim T, Xu ML, Lu TJ. Ultralightweight compact heat sinks with metal foams under axial fan flow impingement. *Heat Transfer Engineering*. 2012;**33**(7):642-650
- [32] Krishnan S, Hernon D, Hodes M, Mullins J, Lyons AM. Design of complex structured monolithic heat sinks for enhanced air cooling. *IEEE Transactions on Components, Packaging and Manufacturing Technology*. 2012;**2**(2):266-277
- [33] Feng SS, Kuang JJ, Lu TJ, Ichimiya K. Heat transfer and pressure drop characteristics of finned metal foam heat sinks under uniform impinging flow. *Journal of Electronic Packaging*. 2015;**137**:1-12/021014
- [34] Tzeng S-C, Soong C-Y, Wong S-C. Heat transfer in rotating channel with open cell porous aluminium foam. *International Communications in Heat and Mass Transfer*. 2004;**31**:261-272
- [35] Jeng T-M, Tzeng S-C, Xu R. Experimental study of heat transfer characteristics in a 180-deg round turned channel with discrete aluminium-foam blocks. *International Journal of Heat and Mass Transfer*. 2014;**71**:133-141
- [36] Azzi W, Roberts WL, Rabiei A. A study on pressure drop and heat transfer in open cell metal foams for jet engine applications. *Materials & Design*. 2007;**28**:569-574
- [37] Williams LJ, Meadows J, Agrawal AK. Passive control of thermoacoustic instabilities in swirl stabilized combustion at elevated pressures. *International Journal of Spray and Combustion Dynamics*. 2016;**8**:173-182
- [38] Zhao CY, Lu W, Tian Y. Heat transfer enhancement for thermal energy storage using metal foams embedded within phase change materials (PCMs). *Solar Energy*. 2010;**84**: 1402-1412
- [39] Alhusseny A, Nasser A, Al-Fatlawi A. Metal foams as an effective means to improve the performance of PCM thermal storage systems. In: 7th International Symposium on Energy; 13–17 August. Manchester, UK; 2017
- [40] Li WQ, Qu ZG, He YL, Tao WQ. Experimental and numerical studies on melting phase change heat transfer in open-cell metallic foams filled with paraffin. *Applied Thermal Engineering*. 2012;**37**:1-9
- [41] Chen Z, Gao D, Shi J. Experimental and numerical study on melting of phase change materials in metal foams at pore scale. *International Journal of Heat and Mass Transfer*. 2014;**72**:646-655
- [42] Yang J, Yang L, Xu C, Du X. Experimental study on enhancement of thermal energy storage with phase-change material. *Applied Energy*. 2016;**169**:164-176

- [43] Zhao CY, Wu ZG. Heat transfer enhancement of high temperature thermal energy storage using metal foams and expanded graphite. *Solar Energy Materials & Solar Cells*. 2011;**95**:636-643
- [44] Wu ZG, Zhao CY. Experimental investigations of porous materials in high temperature thermal energy storage systems. *Solar Energy*. 2011;**85**:1371-1380
- [45] Yang J, Du X, Yang L, Yang Y. Numerical analysis on the thermal behaviour of high temperature latent heat thermal energy storage system. *Solar Energy*. 2013;**98**:543-552
- [46] Xu S, Bourham M, Rabiei A. A novel ultra-light structure for radiation shielding. *Materials and Design*. 2010;**31**:2140-2146
- [47] Chen S, Bourham M, Rabiei A. Novel light-weight materials for shielding gamma ray. *Radiation Physics and Chemistry*. 2014;**96**:27-37
- [48] Chen S, Bourham M, Rabiei A. Neutrons attenuation on composite metal foams and hybrid open-cell al foam. *Radiation Physics and Chemistry*. 2015;**109**:27-39
- [49] Fourie JG, Du Plessis JP. Pressure drop modelling in cellular metallic foams. *Chemical Engineering Science*. 2002;**57**:2781-2789
- [50] Calmidi VV. Transport Phenomena in High Porosity Metal Foams [Thesis]. University of Colorado: UMI; 1998
- [51] Du Plessis P, Montillet A, Comiti J, Legrand J. Pressure drop prediction for flow through high porosity metallic foams. *Chemical Engineering Science*. 1994;**49**:3545-3553
- [52] Bhattacharya A, Calmidi VV, Mahajan RL. Thermophysical properties of high porosity metal foams. *International Journal of Heat and Mass Transfer*. 2002;**45**:1017-1031
- [53] Yang X, Bai J, Lu T. A simplistic analytical model of permeability for open-cell metallic foams. *Chinese Journal of Theoretical and Applied Mechanics*. 2014;**46**:682-686
- [54] Paek JW, Kang BH, Kim SY, Hyun JM. Effective thermal conductivity and permeability of aluminium foam materials. *International Journal of Thermophysics*. 2000;**21**(2):453-464
- [55] Liu JF, Wu WT, Chiu WC, Hsieh WH. Measurement and correlation of friction characteristic of flow through foam matrixes. *Experimental Thermal and Fluid Science*. 2006;**30**:329-336
- [56] Tadrist L, Miscevic M, Rahli O, Topin F. About the use of fibrous materials in compact heat exchangers. *Experimental Thermal and Fluid Science*. 2004;**28**:193-199
- [57] Dukhan N. Correlations for the pressure drop for flow through metal foam. *Experiments in Fluids*. 2006;**41**:665-672
- [58] Calmidi VV, Mahajan RL. The effective thermal conductivity of high porosity fibrous metal foams. *Journal of Heat Transfer*. 1999;**121**:466-471
- [59] Boomsma K, Poulikakos D. On the effective thermal conductivity of a three- dimensionally structured fluid-saturated metal foam. *International Journal of Heat and Mass Transfer*. 2001;**44**:827-836

- [60] Dai Z, Nawaz K, Park YG, Bock J, Jacobi AM. Correcting and extending the Boomsma-Poulikakos effective thermal conductivity model for three-dimensional, fluid-saturated metal foams. *International Communications in Heat and Mass Transfer*. 2010;**37**:575-580
- [61] Yang XH, Kuang JJ, Lu TJ, Han FS, Kim T. A simplistic analytical unit cell based model for the effective thermal conductivity of high porosity open-cell metal foams. *Journal of Physics D: Applied Physics*. 2013;**46**:1-6/255302
- [62] Yao Y, Wu H, Liu Z. A new prediction model for the effective thermal conductivity of high porosity open-cell metal foams. *International Journal of Thermal Sciences*. 2015;**97**:56-67
- [63] Calmidi VV, Mahajan RL. Forced convection in high porosity metal foams. *Journal of Heat Transfer*. 2000;**122**:557-565
- [64] Zukauskas AA. Convective heat transfer in cross-flow. In: Kakac S, Shah RK, Aung W, editors. *Handbook of Single-Phase Convective Heat Transfer*. New York: Wiley; 1987

Porosity Evolution during Chemo-Mechanical Compaction

Anders Nermoen

Additional information is available at the end of the chapter

<http://dx.doi.org/10.5772/intechopen.72795>

Abstract

This chapter presents the constitutive equations necessary to interpret laboratory and field data when both solid and pore volume evolve through time due to chemical and mechanical processes. The equations for the porosity evolution that are developed are generic, but the examples presented are acquired from chalk core studies. The processes at play when porosity is subject to change due to volumetric compaction and fluid-rock interactions when porous chalks are continuously flooded are presented here. As the overall solid mass is a conserved quantity, the void space is not. Constitutive equations are therefore required to estimate the time-evolution of the porosity. Laboratory triaxial tests were performed on high-porosity outcrop chalks from Obourg, Liège, and Mons (Belgium). These tests are being compacted and continuously flooded with MgCl_2 brine at elevated temperature and at high stresses. As calcite is replaced by magnesite, the overall mass and solid density change, thereby changing the volume of the solid. At the same time, the bulk volume is changing. Taking both effects into consideration, the pore volume evolution can be determined. We find that the porosity changes in nonintuitive ways as the relative importance of bulk compaction and chemical interaction may vary over time.

Keywords: dynamic porosity, chalk, dissolution, precipitation, deformation, compaction

1. Introduction

Understanding how chemically reactive and mechanically deformable rock-fluid systems consisting of solids and voids evolve is very important to several fields in the Earth sciences. Examples include the lithification of sedimentary strata [1] and long-term creep behavior of crustal rocks [2]. In addition, a range of industrial processes are affected by chemo-mechanical interactions, including, e.g., pharmaceutical and food processing industries, and geotechnical engineering concerning roadwork construction, mass transportation, and slope stability.

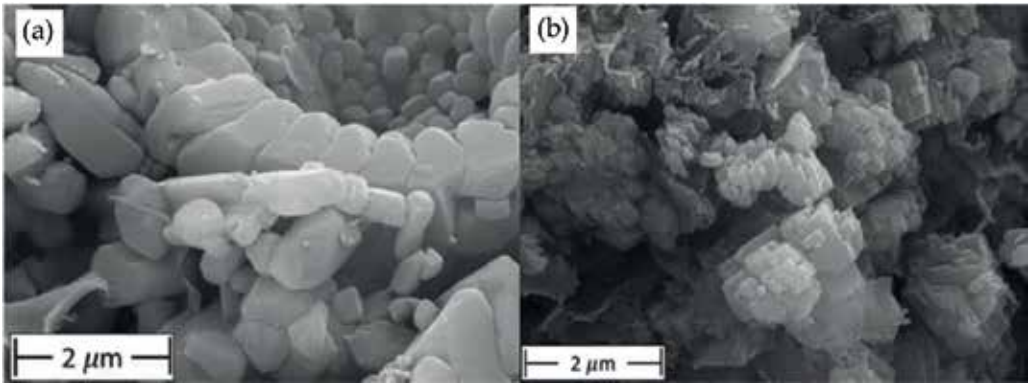


Figure 1. (a) SEM image of an unaltered chalk (Liegè, Belgium [3]). Calcite grains partially organized in coccolith rings and foraminifers. (b) Reworked Liegè chalk from the same core as (a) after 1090 days of continuous mechanical compaction and flow of reactive 0.219 M MgCl₂ brine at 130°C (Table 1).

The pore volume fraction, the pore size distribution, and the mineral surfaces are key parameters to ensure safe disposal of radioactive waste and captured CO₂, and to understand how ores' deposit evolves with time. In petroleum sciences, chemo-mechanical processes are important to accurately predict the porosity since it is inside the pores where hydrocarbons are stored, and it is through the pores, the hydrocarbons are being produced by miscible and immiscible fluid migration across reactive mineral surfaces that again are subject to change. Both pore volume and production rate are crucial to determine the recoverable hydrocarbon potential.

Reactive pore fluids in nonequilibrium with their host rocks lead to dissolution and precipitation transforming the mineral assembly into another, see for example, [3–5]. Dissolution and

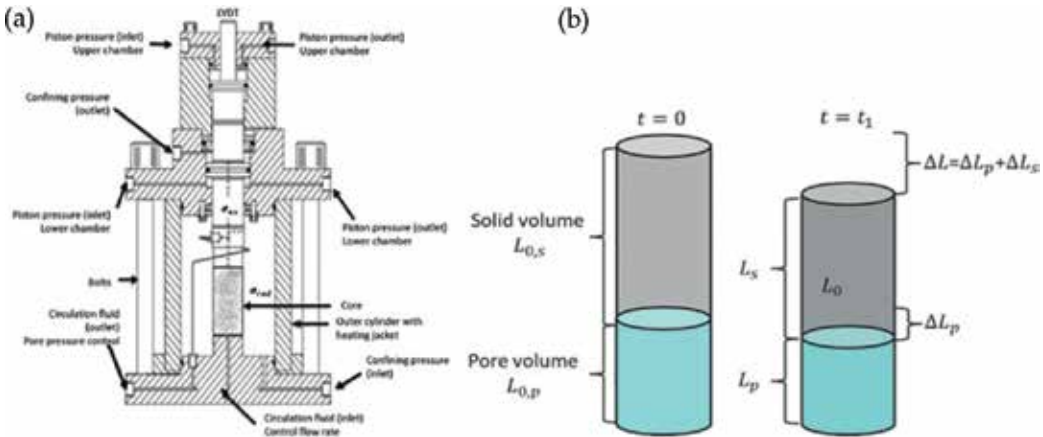


Figure 2. (a) Triaxial cell setup controlling axial and radial stress, the pore pressure, flow rate, and temperature. (b) Additive partitioning of the total bulk strain into a pore and solid volume component. Here, uniaxial strain is assumed (constant diameter) such that lengths relate to volumes.

precipitation lead to changes to grain texture and morphology, and the mineral surface's affinity to oil and water. These are factors, together with porosity, that dictate not only the flow property of the porous rock but also the mechanical parameters that control the stiffness, strength, and the rate at which compaction by grain reorganization and pore collapse occurs. The general processes that are described here is applied to understand how the porosity of chalks develops (**Figure 1a, b** display unaltered and altered chalks) dynamically in a controlled triaxial cell experiments (**Figure 2a**), with control of temperature, pore pressure, side stress, and overburden stress of cylindrical samples (**Figure 2b**).

This chapter deals with some of the constitutive relations that are used to describe the evolution of porous bodies. We incorporate a discussion of how rock-fluid chemistry may impact the grain volume, and review the ways in which total volume reduction may be facilitated in compressive systems. The discussion summarized in the development of a porosity evolution equation in which all effects are included. The usage of the porosity evolution equation is exemplified with references to already published experimental results.

2. Constitutive equations for porosity evolution

The basic equations that are used to quantify the porosity evolution through time are presented. The analysis is based on the work presented in Nermoen, et al. [3]. The overall bulk volume of a bi-phase material equals the sum of the solid volume and pore volume

$$V_b = V_s + V_p \quad (1)$$

Any changes in solid volume and pore volume lead to changes in the bulk

$$\Delta V_b = \Delta V_s + \Delta V_p \quad (2)$$

The pore volume, and hence the porosity, itself is not a conserved quantity. In that case, the bulk volume (size of the object of study) and the solid volume evolution have to be used. Since the volumes are additive by nature, the changes in pore volume can be calculated

$$\Delta V_p = \Delta V_b + \Delta V_s \quad (3)$$

At any given time through dynamic porosity evolution, the porosity is given by

$$\phi = \frac{V_p}{V_b} = 1 - \frac{V_s}{V_b} \quad (4)$$

When both the bulk volume and the pore volume change dynamically from known measurements before the experiment starts ($V_{b,0}$ and $V_{p,0}$ are known), then the time-evolution of the porosity is given by

$$\phi(t) = \frac{V_{p,0} + \Delta V_p(t)}{V_{b,0} + \Delta V_b(t)} \quad (5)$$

Using Eq. (3) enables the determination of the porosity from known quantities

$$\phi(t) = \frac{V_{p,0} + \Delta V_b(t) - \Delta V_s(t)}{V_{b,0} + \Delta V_b(t)} \quad (6)$$

This equation is useful when determining pore volume evolution when considering mechanical and chemical processes that occur at reactive rock-fluid systems exposed to elevated stresses. To simplify the porosity evolution equation further, the volumetric strain and the initial porosity before chemo-mechanical processes occur are introduced

$$\varepsilon_{vol}(t) = -\frac{\Delta V_b(t)}{V_{b,0}} \text{ and } \phi_0 = \frac{V_{p,0}}{V_{b,0}} \quad (7)$$

The minus sign in the volumetric strain here are in line with the definition in geotechnical engineering that inward deformation is positive, often different from other fields of sciences. Dividing by the initial bulk volume and employing the definitions Eq. (6) become

$$\phi(t) = \frac{\phi_0 - \varepsilon_{vol} - \Delta V_s(t)/V_{b,0}}{1 - \varepsilon_{vol}} \quad (8)$$

Eq. 8 is used to analyze how the pore volume fraction changes as the overall volume and the solid volume changes through time. Typically, it is easier to quantify the changes in the solid volume and total volume because of conservation of mass, but this does not generally apply. In other cases, when the pore volume and solid volume are known, the porosity can be calculated from

$$\phi(t) = \frac{V_{p,0} + \Delta V_p(t)}{V_{p,0} + V_{s,0} + \Delta V_p(t) + \Delta V_s(t)}. \quad (9)$$

This equation could be used when the volumes of injected and produced fluid volumes are monitored and solid volume change can be back-calculated from ion chromatography (IC) of produced fluids. If, however, the bulk volume (e.g., 4D seismic) and the pore volume were obtained from monitoring the injected and produced fluid *volumes*, the porosity is as follows:

$$\phi(t) = \frac{V_{p,0} + \Delta V_p(t)}{V_{b,0} + \Delta V_b(t)}. \quad (10)$$

3. Volumetric strain by imposed stress

In compressive hydrostatic systems, the porous rocks deform by reducing its bulk volume. This may affect the porosity through, for example, Eq. (8). In closed systems, in which the mass and density of the minerals are conserved, the bulk volume reduction equals the pore volume reduction. This is facilitated by grains moving relative to each other, and/or by pressure solution (dissolution of stressed grain contacts and precipitation in unstressed parts of the

mineral framework [6]). In open systems subjected reactive flow, both mass and density of the core material may change because of mineral reactions. To evaluate the relative importance of how evolution mechanisms of the solid volume and pore volume dictate the porosity in real systems, a rigorous definition of stresses and strains are required. The aim is to pave the way for quantitative analyses of how stresses impact strains, and how strains impact the porosity chemo-mechanical compaction.

3.1. The stress tensor in porous materials

The stress tensor describes the stresses (force per unit area) in a solid porous body. For cylindrical core plug, it is convenient to express the stress tensor σ as

$$\sigma_{ij} = \begin{bmatrix} \sigma_{zz} & \tau_{zr} & \tau_{z\theta} \\ \tau_{rz} & \sigma_{rr} & \tau_{r\theta} \\ \tau_{\theta z} & \tau_{\theta r} & \sigma_{\theta\theta} \end{bmatrix}. \quad (11)$$

Shear and normal components are abbreviated τ_{ij} and σ_{ij} , respectively, with $ij = \{z, r, \theta\}$ denoting the axial (z), radial (r), and tangential (θ) direction. Compressive stresses and inward deformation are defined positive. When there is no net translational or rotational force acting in the solid body (i.e., $\tau_{zr} = \tau_{rz}$, $\tau_{z\theta} = \tau_{\theta z}$, and $\tau_{r\theta} = \tau_{\theta r}$), only six independent stress tensor components apply. For a cylindrical core plug stressed in a triaxial cell, the tangential stress equals the radial, and the principal stress directions coincide with the imposed z and r directed stress such that the shear stresses are zero. The stress tensor may, therefore, be expressed through the orthogonal principal stresses vector with two components

$$\begin{bmatrix} \sigma_z \\ \sigma_r \end{bmatrix} \quad (12)$$

In reservoir systems, however, all stress components may apply, and as such, the off-diagonal elements of the stress tensor are nonzero. However, in these cases, the stress tensor can be rotated such that the principal stress notation can be obtained. It is customary procedure to arrange the first, second, and third principal stress directions as $\sigma_1 > \sigma_2 > \sigma_3$, where σ_1 is typically in the vertical direction (weight dominated), and, consequently, the σ_2 and σ_3 are horizontal (often abbreviated σ_H as the highest horizontal stress and σ_h is the least horizontal stress). σ_h and σ_H depend upon Poisson ratio and tectonic regional stresses.

3.2. Effective stress

In porous rocks, it is the effective stresses introduced by [7] that drive deformation. The external load applied onto a material that consists of solids and voids is balanced by the interparticle contacts in force networks (material framework) and a fraction α of the pore pressure. Drained conditions apply to the cases where fluids are allowed to escape to keep the pore pressure constant (hence constant effective stress), differ from undrained conditions in which the pore pressure increases because of compaction (thereby reducing the effective stress).

Simultaneously, seepage forces arising from differences in fluid pressure expose a net force onto the solid framework (see **Figure 3**). In partially consolidated systems, in which the cross

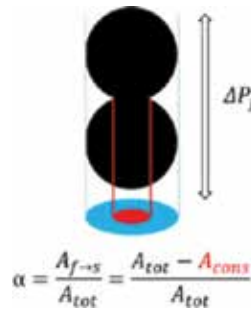


Figure 3. Fluid pressure differences (ΔP_f) impart forces onto the solid framework through the fluid-to-solid contact areas, which covers only a fraction α of the cross-section ($A_{f-s} = A_{tot} - A_{cons}$).

area is given by the sum of the consolidated area (solid–solid area) and the area of the fluid-to-solid contact area ($A_{tot} = A_{fs} + A_{ss}$), the force from the fluid pressure differences (ΔP_f) to the solids is given as $F_{fs} = \Delta P_f \alpha A_{tot}$, where the fraction total area is termed as the Biot coefficient, and can be expressed as $\alpha = A_{fs} / A_{tot}$. In addition, other definitions of the Biot coefficient may also apply. In weight-dominated reservoir systems of fluid saturated rocks, the solid stress increases with the lithostatic weight. The net effective stress, that is, the stress that drive deformation is given by the differences between lithostatic pressure and the fraction α (the Biot coefficient) of the pore pressure

$$\sigma'_v = \sigma_v - \alpha P_f \text{ which is greater than } \sigma'_H = \sigma_H - \alpha P_f > \sigma'_h = \sigma_h - \alpha P_f \quad (13)$$

Here, the largest and smallest horizontal stress is abbreviated with an index H and h , respectively.

In core scale experiments, the directions perpendicular to the z -axis are equal, $\sigma_r = \sigma_\theta$, implying that full description of the effective stress state of a cylindrical core experiment are given by two effective stresses, $\sigma'_r = \sigma_r - \alpha P_f$ and $\sigma'_z = \sigma_z - \alpha P_f$. The stress exerted onto the core in the radial direction is in many (not all) rock mechanical experiments performed by increasing the hydraulic confining pressure of oil surrounding the core encapsulated by a rubber or plastic sleeve while a piston placed on top of the core controls the axial stress.

3.3. Defining strain

The most commonly used definition of strain, applicable to small finite deformations, is presented here. It is acknowledged that other definitions of strain also exist in the scientific literature. The strain at any time is given by the ratio of elongation divided by the initial length

$$\varepsilon(t) = -\frac{L(t) - L_0}{L_0} = -\frac{\Delta L}{L_0} \text{ and } \varepsilon_{vol} = -\frac{\Delta V}{V_0} \quad (14)$$

Stresses may deform Earth materials so that two initially orthogonal directions change by an angle Ψ . This change in angle is related to the shear strain Γ as

$$\Gamma = \frac{1}{2} \tan \Psi. \quad (15)$$

In three dimensions (cylindrical coordinates), the pairs of shear and normal strains are organized in the strain tensor

$$\begin{bmatrix} \varepsilon_{zz} & \Gamma_{zr} & \Gamma_{z\theta} \\ \Gamma_{rz} & \varepsilon_{rr} & \Gamma_{r\theta} \\ \Gamma_{\theta z} & \Gamma_{\theta r} & \varepsilon_{\theta\theta} \end{bmatrix} \quad (16)$$

Similar to the stress tensor, the shear strains balance each other ($\Gamma_{rz} = \Gamma_{zr}$, $\Gamma_{\theta z} = \Gamma_{z\theta}$, $\Gamma_{\theta r} = \Gamma_{r\theta}$), thereby, reducing the number of parameters to fully describe the deformation of a volume element in 3D from nine to six parameters. In addition, for isotropic materials, the principal strains can also be found by rotating the strain matrix, the same way as the stress matrix, such that the off-diagonal elements vanish ($\Gamma_{ij} = 0$). In addition, the radial and tangential strains are equal, such that the strain vector for cylindrical cores:

$$\begin{bmatrix} \varepsilon_z \\ \varepsilon_r \end{bmatrix} \quad (17)$$

To estimate the porosity evolution, bulk volumetric strain has to be used. The volumetric strain equals the change in volume divided by the initial volume, which is the first strain invariant, given by $\varepsilon_{vol} = -\Delta V/V_0 = \text{Tr}(\varepsilon_{ij})$. The volume strain remains unchanged upon coordinate change (i.e., the volume is the same irrespective of which coordinate system is used). Depending upon the geometry of the setup, the way in which strain measurements and hence the strain tensor components will vary. For cylindrical geometries, in which the volume of a cylinder is given by $V = \pi D^2 L/4$, where D is the diameter and L is the length, the volumetric strain can be calculated from the radial and axial strains

$$\varepsilon_{vol} = \varepsilon_z + 2\varepsilon_r + 2\varepsilon_z\varepsilon_r + \varepsilon_r^2 + \varepsilon_z\varepsilon_r^2 \quad (18)$$

If the length and diameter of cylindrical cores are being measured continuously, then the volumetric strain can be estimated. Typically, for small strains, the second and third order terms can be omitted, hence, $\varepsilon_{vol} \simeq \varepsilon_z + 2\varepsilon_r$.

4. Partitioning time-independent and time-dependent deformation

The volumetric strain can be split into an immediate strain, occurring when the effective stress is being changed, and time-dependent deformation. The two cases are presented briefly in the following sections, even though this is a large area of research. For the time-independent case, Hooke's law is described before nonlinear models are presented, followed by a short note on plasticity and other failure mechanisms before time-dependent models are described.

4.1. Elastic strain: linear elasticity

Hooke's law is the simplest relation to describe the relation between the stress-strain tensors. It assumes that the deformation is immediate, linear, and reversible. In continuous media, for small stress and strain increments in the linear limit, the ε_{ij} and σ_{ij} are described by the compliance (stiffness) fourth order tensor c_{ijkl} . In 3D systems, it consists of 81 real numbers, and the tensorial equation attains the compact form $\sigma_{ij} = c_{ijkl}\varepsilon_{kl}$, where the indexes i, j, k, l represent the three spatial dimensions $[x, y, z]$ in Cartesian co-ordinate systems, and $[z, r, \theta]$ in cylindrical systems. In the case, when the rotational forces balances, which applies to most continuum mechanical cases, the number of stiffness parameters describing the stress-strain relation reduces to 27. In the case of isotropic materials, the number of elastic parameters that describe the stress-strain relation of a volume element along the principal directions is further reduced to the Young's modulus (E) and Poisson's ratio (ν) via the matrix equation

$$\begin{bmatrix} \varepsilon_z \\ \varepsilon_r \\ \varepsilon_\theta \end{bmatrix} = \frac{1}{E} \begin{bmatrix} 1 & -\nu & -\nu \\ -\nu & 1 & -\nu \\ -\nu & -\nu & 1 \end{bmatrix} \begin{bmatrix} \sigma'_z \\ \sigma'_r \\ \sigma'_\theta \end{bmatrix} \quad (19)$$

By adding up the three equations expressed in the matrix form earlier

$$(\varepsilon_z + \varepsilon_r + \varepsilon_\theta)E = (1 - 2\nu)(\sigma'_z + \sigma'_r + \sigma'_\theta), \quad (20)$$

we may use this equation to define the bulk modulus in hydrostatic tests. When omitting higher order terms in the volumetric strain (Eq. (18)), the left hand side of Eq. (20) equals the volumetric strain. For hydrostatic tests, in which the stresses in all spatial directions equal, $\sigma'_z = \sigma'_r = \sigma'_\theta = \sigma'_p$, then Eq. (20) simplifies to

$$\frac{E}{1 - 2\nu} \varepsilon_{vol} = \sigma'_p \rightarrow K \varepsilon_{vol} = \sigma'_p \quad (21)$$

In Eq. (21), the bulk modulus (K) is defined. σ'_p is frequently used to define the hydrostatic effective stress. For nonhydrostatic triaxial tests, where $\sigma_z > \sigma_r$, and $\sigma'_r = \sigma'_\theta$ and $\varepsilon_r = \varepsilon_\theta$ Hooke's law in Eq. (19) simplifies to

$$\begin{aligned} E\varepsilon_r &= (1 - \nu)\sigma'_r - \nu\sigma'_z \\ E\varepsilon_z &= \sigma'_z - 2\nu\sigma'_r \end{aligned} \quad (22)$$

4.2. The effective stress changes that drive deformation

Within the elastic domain, any change in the effective stress drive deformation in the sample, from here on abbreviated with the δ -symbol used to rewrite Hooke's law at quasistatic changes. The δ -symbol is used to identify the variables that are changing during for example, a loading sequence

$$\begin{aligned} E\delta\varepsilon_r &= (1 - \nu)\delta\sigma'_r - \nu\delta\sigma'_z \\ E\delta\varepsilon_z &= \delta\sigma'_z - 2\nu\delta\sigma'_r \end{aligned} \quad (23)$$

In Eq. (23), the underlying assumption is that Young's modulus and Poisson ratio remain fixed. Furthermore, when pore pressure is included, the effective stress changes due to both axial and radial stress and pore pressure

$$\sigma'_r = \delta\sigma_r - \alpha\delta P_f \text{ and } \delta\sigma'_z = \delta\sigma_z - \alpha\delta P_f \quad (24)$$

It is assumed that the Biot stress coefficient remains fixed during loading. Using these definitions into Eq. (32) enables us to fully describe the relation between the stress, pore pressure, and strain in Hooke's law

$$\begin{aligned} E\delta\varepsilon_r &= (1 - \nu)\delta\sigma_r - \nu\delta\sigma_z + (2\nu - 1)\alpha\delta P_f \\ E\delta\varepsilon_z &= \delta\sigma_z - 2\nu\delta\sigma_r + (2\nu - 1)\alpha\delta P_f \end{aligned} \quad (25)$$

4.3. Plasticity and irreversible deformation

For a highly porous chalk, a nonzero component of the observed strain is always irreversible when the load is released as exemplified by [8] and [9] where irreversible plasticity is seen also within the 'elastic' phase of the QP -plot (Figure 4). As such, loading and unloading may display history dependence in the elastic parameters. This may be caused by the way in which the porous material is being held together and the relative importance of the different forces responsible for determining the stiffness of the chalk. Now, at increasing stresses beyond 'elasticity', the type of irreversible deformation that develops, depend on the state of stress, as illustrated in Figure 4. Here, the mean effective stress is plotted on the horizontal axis and the deviatoric stress along the vertical axis. Considering cylindrical cases, the deviatoric stress equals $Q = \sigma_z - \sigma_r$ and the mean effective stress is $P = (\sigma_z + 2\sigma_r)/3 - \alpha P_f$. Since both Q and

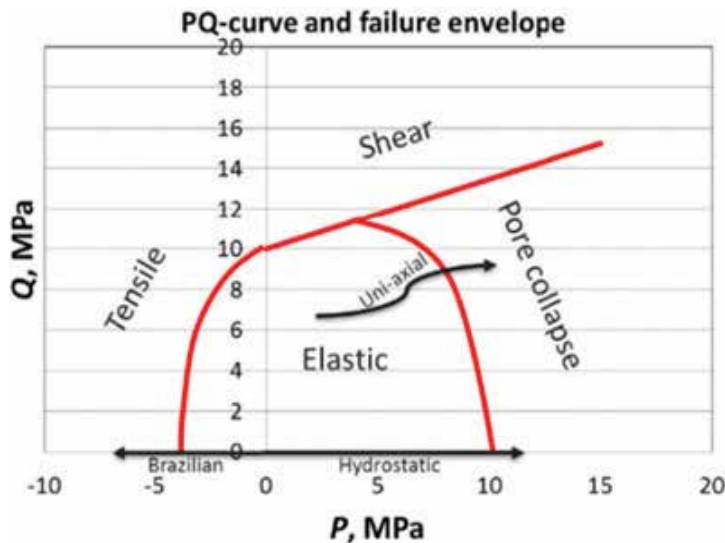


Figure 4. The failure envelope (solid line) shows that at which stresses plasticity and irreversible deformation occur (numbers are not applicable). Mean effective stress (P) and Q is the deviatoric stress, hence the end cap depends solely upon the material and not the geometry.

P are invariant, the results of core data can be used at any case in which the material is the same: (1) for hydrostatic systems, $Q = 0$, and pore collapse occurs when the mean effective stress exceeds a certain threshold; (2) tensile fractures develop at negative values of P which can be found for high fluid pressures, or in Brazilian tests; and (3) shear failure occurs when the deviatoric stress exceeds a certain value. For frictional materials, it is typical to observe that the deviatoric stress required to induce shear failure is increasing with increasing mean effective stress. For Coulomb materials, this relation is proportional, and the slope is related to the frictional coefficient. Chalks have been found to be satisfactorily described with such a frictional coefficient, while clays behave differently. The way in which the irreversible deformation affects the porosity evolution differs from case to case. Within shear zones, the porosity may both increase, because of dilation and de-compaction when tightly packed grains reorganize or reduce because of grain crushing when the imposed forces exceed a certain level.

5. Time-dependent pore volume reduction processes and compaction

To understand how the mechanical and chemical processes affect the porosity during pore collapse, it is important to take a closer look at how the observed bulk strain can be partitioned. In this section, we consider the simplest possible partition (below) in which the overall strain is partitioned additively into a solid volume and a pore volume component. The relative importance of these mechanisms may be found by the analysis of quantitative measurements of the bulk volume change and the change in the solid volume due to the dissolution/precipitation as the mineral mass and density change over time, while grains reorganize, crush, and solid contacts evolve. In this case, the observed volumetric change can be partitioned additively via

$$\varepsilon_{vol} = \varepsilon_{pore} + \varepsilon_{solid} \quad (26)$$

This does not imply that cross terms do not exist in which: (a) the rate of pore volume reduction is sensitive to the reduction in solid volume and (b) how the solid volume rate may depend on how grains reorganize to change the flow pattern and potentially expose new fresh mineral surfaces to the reactive brine. It is likely to assume that based on the accelerated strain presented in [10] minute changes to the solid volume increase the rate of pore collapse (also seen in [4]).

Given the simple partitioning above, a model can be developed to describe the observed creep curve with a few physical parameters (see Eqs. (20)–(23) in [10]). In this model, overall volumetric strain is additively partitioned into a pore and solid volume component in which the pore volume equals, $V_p = \phi V_b$. Extending the rate of change in bulk volume is by the pore volume change (via using the product rule) and the solid volume change rate

$$\frac{dV_b}{dt} = \frac{dV_p}{dt} + \frac{dV_s}{dt} = \phi \frac{dV_b}{dt} + V_b \frac{d\phi}{dt} - \beta \quad (27)$$

The solid volume rate is assumed to be constant (β , in cm^3/day determined from ion chromatography data). For Mons chalk at 130°C and 92°C at 1 PV/day of 0.219 MgCl_2 brine, the solid

volume changes approximately by 0.01 and 0.005 cm³/day, respectively. The porosity reduction rate can be proportional to porosity

$$\frac{d\phi}{dt} = -\xi(\phi - \phi_c)^n \quad (28)$$

where ξ is the proportionality constant, ϕ_c is a terminal porosity (grain reorganization cannot continue until zero porosity), and the power n is used to model nonlinear behavior. For simplicity, if we assume $n = 1$ and $\phi_c = 0$, the volumetric strain is explicitly given as

$$\varepsilon_{vol}(t) = \frac{(1 - \phi_0)e^{\xi t}}{e^{\xi t} - \phi_0} - \frac{\beta t}{V_{b,0}(1 - e^{-\xi t})} - 1 \quad (29)$$

This model takes the initial porosity (ϕ_0) and bulk volume ($V_{b,0}$), while the porosity rate constant ξ is a free variable.

The mathematical models aimed to match observed creep data have a long history, and several, more or less physically based models were reported. Generally, these models do not consider the underlying solid and pore volume contribution, but may still satisfactorily match the observed strains. Three models that have been used are:

Power law with cut-off:

$$\varepsilon_P = At^B e^{-t/t_0} \quad (30a)$$

De Waal [11]:

$$\varepsilon_{dW} = A \log(Bt + 1) \quad (30b)$$

Griggs [12]:

$$\varepsilon_G = A \log(t + 1) + Bt \quad (30c)$$

The model parameters (A, B and t_0) are found when the residual strain $RES = \frac{1}{N} \sum_n |\varepsilon_{exp} - \varepsilon_{model}|$ is minimized.

5.1. Pore collapse and grain reorganization: the constant solid volume case

The movement of grains relative to each other at high-mean effective pressures causes pore volumes to collapse. It has been experimentally verified that for chalks, the rate of compaction may sometimes accelerate when the fluid composition change, a process termed water weakening. Water weakening has been used to understand reservoir processes [13–15] and to interpret core experiments as exemplified in **Figure 5**, where an additional strain of ~1% is seen at the first days of seawater (SSW) flow (approximately 2 pore volumes). This process cannot be attributed to chemical reactions leading to solid volume changes, since the ions in the produced effluent water are inadequate to cause any solid volume change from the mass loss and increased density often seen in these cases when chemical reactions occur. As such, the additional bulk strain is caused by pore collapse. This does not exclude how long-term

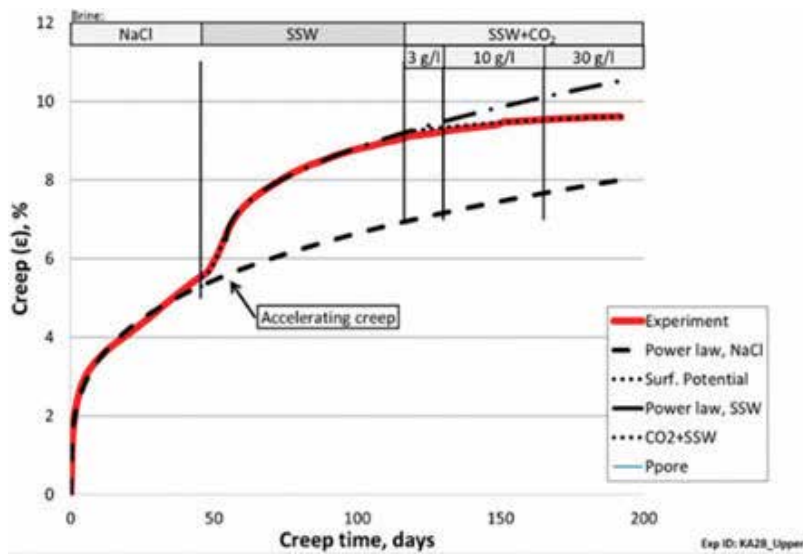


Figure 5. Axial creep strain over time at uniaxial strain condition performed on a Kansas chalk sample. The injection of seawater (SSW) leads to accelerated creep. The accelerated creep period is associated with the loss of sulfate ions in the effluent samples. Mixing CO₂ into the SSW from 120 days and onwards does not induce additional strain (from [20]).

chemical reactions can weaken rocks over longer time periods when porous chalk cores are continuously flooded.

To understand the immediate additional deformation (i.e., 1–2 days corresponding to a flow of 1–2 pore volumes as seen here), a grain-level approach is required. The grain-grain friction controls and cement bonds binding neighboring grains together control the relative movement of grains. Friction between grains is given by the frictional coefficient times the normal force, $F_{fric} = \mu F_N$. The normal force arises from the externally imposed load and the attractive Van der Waal forces that induce the cohesive forces grains. This has been shown to be reduced by negative disjoining pressures in the overlapping double layer between adjacent mineral grains when surface-active divalent ions adsorb onto the charged chalk surfaces [16–19].

5.2. Pressure solution and other grain-reorganization mechanisms

Pressure and temperature are the state variables that control the Gibbs chemical potential [21]. During diagenesis and burial, the chemical stability of mineral phases is altered as the temperature, hydrostatic and lithostatic pressure increases. Pressure solution of stressed grain contacts, and precipitation in unstressed parts of the rock framework, have been used as one of the primary rock-forming mechanisms during diagenesis. Pressure solution can occur in closed systems, in which the overall mass and density remain fixed. For high Biot coefficients, the local stress at particle contacts may become significant (see Figure 7 in [10]), and thus, a stress-dependent production of Ca-ions is observed where more Ca-production for high stress than low stress (see Figure 6 acquired from [10]).

It has been a long-standing discussion how to mathematically describe the relevant thermodynamic pressure for accurate determination of the chemical potential from the stress tensor.

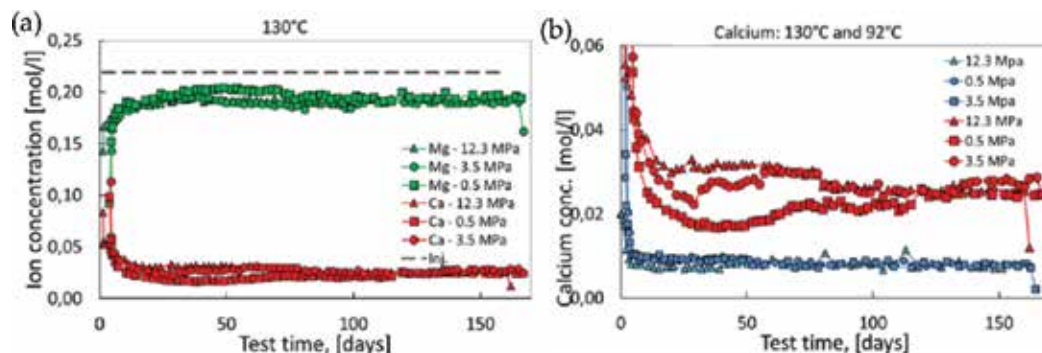


Figure 6. (a) Outlet cation concentration of 0.219 M MgCl_2 (dashed line, same ion strength as seawater) flooded through chalk from the Obourg saint vast formation (Mons, Belgium) at 130°C for 0.5, 3.5, and 12.3 MPa effective stress. (b) Calcium production at varying stresses at 130°C and 92°C. The amount of Ca ions in the produced effluent depends on time, temperature, and stress (acquired from Figure 6 in [10]).

Several candidates coexist. The stress tensor in reservoir systems (and core scale experiments) depends on the weight of the overburden (lithostatic weight), side stress (tectonic forces), pore pressure, and the Biot coefficient. The simplest of determining the thermodynamic pressure is using the pore pressure. This way of thinking may seem reasonable at first glance since it is at the interface between the solid and the fluid where the chemical reactions occur. Simultaneously, at the rock-fluid interface, the stresses through the solid framework could also play a role in determining chemical solubility. In that case, the continuum mechanics provide a range of choices for calculating the thermodynamic pressure: (1) the average compressive stress (i.e., the first invariant of the solid framework stress tensor), (2) the principal stresses, thereby leading to different solubility in the different spatial directions. In sedimentary systems, this would often lead to enhanced solubility in the vertical direction as the first principal stress direction is vertical. This may explain the formation of the horizontal stylolites that are sometimes found in calcitic, carbonate, and limestone rocks [6]. (3) The relevant thermodynamic pressure could be related to the stress gradients that have been observed throughout porous materials, termed force chains. At grain-grain contacts, through which the externally imposed loads are being carried, the stresses can be significantly higher than the average. In these regions, the solid-solid stress is given by $\sigma'_{ss} = \sigma' / (1 - \alpha)$, where σ' is the effective stress and α is the Biot stress coefficient. As such, for unconsolidated sands and calcitic mudstone, in which $\alpha > 0.9$, this fraction is significant and may be responsible for additional calcite dissolution [10]. As has been shown previously (in e.g., [18, 22] and also before that), the contact area ratio is linked to the Biot stress coefficient (α).

Even though pressure solution is a process of chemical nature, it does not necessarily change the solid volume since the mass can be conserved (closed system, i.e., no larger scale mass flow) and the same mineral phase is precipitated as the one dissolved (i.e., same density). In that sense, pressure solution contributes to pore volume reduction rather than the solid volume in the strain partitioning presented here. Hence, pressure solution may fall under mechanical compaction even though the underlying mechanisms of pressure solution are chemically driven.

6. Time-dependent solid volume evolution mechanisms

In open, nonequilibrium systems with rock-fluid interactions, the solid volume is subject to change. It has been shown in a range of experiments how additional strain is accumulated during compaction at constant stress conditions when reactive brines are injected [4, 23]. The solid volume varies when solid mass (M_s) and mineralogical density (ρ_s) change

$$V_s = \frac{M_s}{\rho_s} \quad (31)$$

The change in solid volume may be evaluated by

$$\Delta V_s(t) = \frac{M_s(t)}{\rho_s(t)} - \frac{M_{s,0}}{\rho_{s,0}} \quad (32)$$

Here, the solid volume change is given by the difference between the ratio of the mass and density at a given time and the values before chemo-mechanical processes initiated. The evolution of the solid mass over time is given by the difference between the chemical mass flux in and out of the system, and density changes as new minerals precipitate.

6.1. Mass transfer in open systems

When fluids continuously flow and react with the rock, the mass (and hence the solid volume) changes. The chemical flux can be monitored by evaluating the effluent concentration through difference between the ion concentrations in and out of the volume element (**Figure 6a, b**). This volume element may, in some cases, be between an injector and a producer in an oil field, or a core scale experiment in the laboratory [3]. The concentration of ions can be measured using ion chromatography, and over a time interval δt the difference in mass is given by

$$\frac{\delta M_s}{\delta t} = \sum_j (c_{in,j} - c_{out,j}) q m_j \quad (33)$$

In Eq. (33), the factor $(c_{in,j} - c_{out,j})$ is the difference in the ion concentration of chemical species j (mole/L), q is the flow rate (L/day), and m_j is the molar mass of species j (g/mole). Hence, the term $\delta M_s / \delta t$ is given in g/day. The overall mass is estimated by summing over all measured ions in the chemical interaction, giving a unit (g/day), which can be used further. The total mass evolution of each species is determined by integration. Assessing rock-fluid interactions to real cases, for example during, seawater flooding of the Ekofisk field (North Sea, Norway), chemical reactions have been observed. Here, dissolution of 1–2 wt. % is anticipated from the analysis of the produced water [24–26].

6.2. Method to quantify the solid volume evolution

In Eq. (32), the change in solid volume depends on the change in both mass and in density as the minerals dissolve and precipitate. The overall mineral density, as n minerals dissolve/precipitate in time is given by

$$\begin{aligned}\rho_s &= c_1\rho_1 + c_2\rho_2 + \dots + c_n\rho_n \\ 1 &= c_1 + c_2 + \dots + c_n\end{aligned}\quad (34)$$

As the concentrations of different minerals vary, the changes to ρ_s can be estimated.

It is not always the case that a detailed kinetic chemical model exist tuned to take into account how different mineral mixtures react with fluids in each different case. If the overall density before ($\rho_{s,0}$) and after ($\rho_{s,f}$) the chemical experiment are known (from e.g., pycnometry) a reduced mass parameter (\tilde{m}) ranging from 0 to 1 can be defined from the initial and final mass using mineral k ($M_{k,0}$ and $M_{k,f}$, respectively)

$$\tilde{m}(t) = \frac{M_k(t) - M_{k,0}}{M_{k,f} - M_{k,0}} \quad (35)$$

Then, the density at any given time may be estimated using

$$\rho_s(t) = \tilde{m}(t)\rho_{s,f} + (1 - \tilde{m}(t))\rho_{s,0} \quad (36)$$

7. Predicting dynamic porosity evolution: an illustrative example

An example of a dynamic porosity development analysis is presented here based on material published in 2015 [3]. The results of an experiment performed over 1090 days where a Liegè (Belgium) chalk sample was exposed to hydrostatic stress (11.1 MPa, approximately 5 MPa above yield) and continuous flow of 0.219 M MgCl₂ (33 and 99 cm³/day, pore pressure 0.7 MPa and 130°C). Basic sample measurements were performed of dry/saturated mass, pore volume, solid and bulk volume and hence porosity before and after test, hence the mineral density estimated and confirmed using He-pycnometry (**Table 1**). The bulk core volume was reduced more than 15% and mineral mass is reduced by more than 18% while the density is increased from 2.7 to 2.9 g/cm³. The stresses are sufficient to induce pore collapse for these chalks, and the 0.219 M MgCl₂-brine (with equal ion strength as seawater) induced dissolution of the calcium carbonate and precipitation of denser Mg-bearing carbonates (e.g., magnesite and dolomite).

	Before test	After test (1090 days)	Change
Dry mass (on scale)	125.57 g	102.64 g	−22.93 g
Wet weight (saturated)	158.56 g	126.34 g	−32.22 g
Pore volume	32.99 cm ³	23.71 cm ³	−9.28 cm ³
Solid volume	46.85 cm ³	35.53 cm ³	−11.32 cm ³
Bulk volume	79.84 cm ³	59.23 cm ³	−20.61 cm ³
Mineral density (saturation and pycnometer)	2.68 and 2.70 g/cm ³	2.89 and 2.90 g/cm ³	0.21 and 0.20 g/cm ³
Porosity (saturation and pycnometer)	41.3 and 41.7%	40.0 and 40.1%	−1.3 and −1.6%

Table 1. Basic measurements of the core before and after the 1090 days long-term test [3]. **Figure 1** displays SEM images of the core material before and after the flow-through test.

During the test, the axial deformation and the ion concentration of the effluent fluids were measured. In **Figure 7a**, the Mg and Ca ion concentrations are measured through time. These measurements can be used to find the production rate in g/day using Eq. (33), seen in **Figure 7b**. A trebling of the inlet flow rate leads to more than a doubling in the calcite dissolution. The mass evolution is used to estimate the dynamic change in density using Eq. (36), and is then combined to estimate the solid volume as function of time as seen by the dotted line in **Figure 7c** plotted together with the bulk volume, estimated from the axial strain. Thus, the pore volume can be estimated (dashed line in **Figure 7c**). As can be seen, the pore volume is reduced when bulk compaction dominate the overall process until 200 days. A typical observation from primary creep experiments is that the overall creep rate decreases with time. After 200 days, when the compaction rate has reduced, the flow rate was increased thereby increasing the rate at which dissolution/precipitation occurs, see Eq. (33) where the flow-rate dependency is explicitly shown. At this point of time, the overall porosity dynamics change. In the initial compaction-dominated regime, the overall porosity reduced to a value of as low as 33%, and afterwards it starts increasing (solid line in **Figure 7d**). At approximately 400 days, the flow rate is then reduced again and the rate of change in porosity is changing accordingly.

From 900 days and onwards, the Ca that was initially found within the core had been produced, after the solid volume was interpreted to be constant and the bulk compaction is facilitated by pore volume reduction, and hence the porosity is decreased to 40.1%.

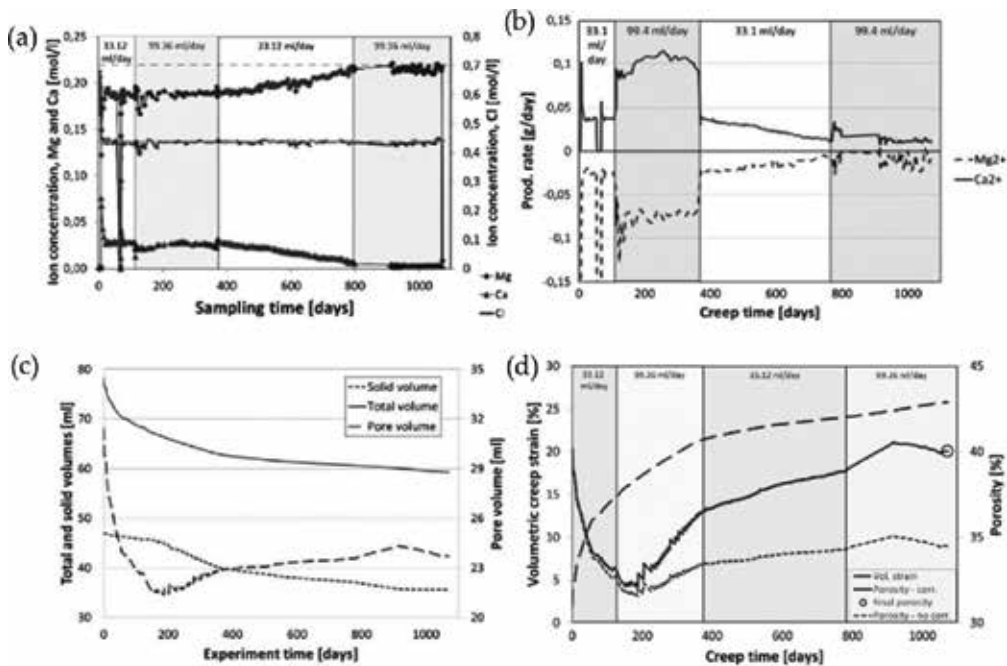


Figure 7. (a) Ion chromatography of the produced ion concentration of mg and Ca throughout the test. Mg is retained in the core while Ca is produced. (b) Calculated production rate of mg (solid) and Ca (dashed) using Eq. (32), (33) and (36), while (c) displays the total, pore, and solid volume evolution. (d) Observed volumetric creep (dashed line) and estimated porosity evolution as the relative importance of bulk compaction and dissolution/precipitation change.

In the experiment presented here, both pore and solid volume are subject to change. Since only the bulk volume or the solid volume could be determined from axial strain IC data, respectively, the pore volume was determined. As is exemplified in the presented experiment, the porosity evolution dynamics display a complex behavior because of the reduction in pore volume and solid volume. Their rate depends upon stress, the way in which deformation is accumulated and the rate of dissolution/precipitation.

8. Summary

Porosity is an important parameter for understanding the diagenetic processes and petrophysical reservoir systems. Its importance to the mechanical stiffness and strength of porous rocks, and to the resource potential, and rate of hydrocarbons produced from reservoirs is evident. The porosity is a dynamic parameter from the strain and chemical reactions from injection of fluids out of equilibrium with the host rock (e.g., seawater brines at elevated temperature in chalks) that induce additional deformation over time. The adsorption of surface-active ions leads to alterations in the forces binding grains together, leading to instantaneous additional deformation.

To understand quantitatively how porosity changes dynamically through time, there are series of processes that needs to be incorporated. This chapter presents some of the ways in which the bulk strain can be partitioned into elastic/plastic components, time-dependent, and time-independent components, and solid volume and pore volume processes. For chalks, the dynamic porosity evolution depends on the relative importance of the different processes at play, that again are functions of the stress, strain, temperature, flow rate, and fluid chemistry.

The methods presented here do not cover all possibilities for porosity evolution determination depending upon measurements that are available. When the bulk volume strain and chemical composition of the effluent fluids are known, the following porosity evolution model applies

$$\phi(t) = \frac{\phi_0 - \varepsilon_{vol}(t) - \left(\frac{M_s(t)}{\rho_s(t)} - \frac{M_{s,0}}{\rho_{s,0}} \right) / V_{b,0}}{1 - \varepsilon_{vol}(t)} \quad (37)$$

Author details

Anders Nermoen^{1,2,3*}

*Address all correspondence to: anders.nermoen@iris.no

1 Institute of Energy Resources, University of Stavanger, Stavanger, Norway

2 International Research Institute of Stavanger (IRIS AS), Stavanger, Norway

3 National IOR Centre of Norway, University of Stavanger, Norway

References

- [1] Fabricius IL. Burial stress and elastic strain of carbonate rocks. *Geophysical Prospecting*. 2014;**62**:1327-1336. DOI: 10.111/1365-2478.12184
- [2] Amitrano D, Helmstetter A. Brittle creep, damage and time to failure in rocks. *Journal of Geophysical Research—Solid Earth*. 2006;**111**:B11. DOI: 10.1029/2005JB004252
- [3] Nermoen A, Korsnes RI, Hiorth A, Madland MV. Porosity and permeability development in compacting chalks during flooding of nonequilibrium brines: Insights from long-term experiments. *Journal of Geophysical Research—Solid Earth*. 2015;**120**. DOI: 10.1002/2014JB011631
- [4] Madland MV, Hiorth A, Omdal E, Megawati M, Hildebrand-Habel T, Korsnes RI, Evje S, Cathles LM. Chemical alterations induced by rock-fluid interactions when injecting brines in high porosity chalks. *Transport in Porous Media*. 2011;**87**(3):679-702
- [5] Megawati M, Madland MV, Hiorth A. Mechanical and physical behavior of high-porosity chalks exposed to chemical perturbation. *Journal of Petroleum Science and Engineering*. 2015;**133**:313-327
- [6] Croize D, Renard F, Bjørlykke K, Dysthe DK. Experimental calcite dissolution under stress: Evolution of grain contact microstructure during pressure solution creep. *Journal of Geophysical Research—Solid Earth*. 2010;**115**:B09207
- [7] Biot MA. General theory of three-dimensional consolidation. *Journal of Applied Physics*. 1941;**12**:155-164
- [8] Sachdeva JS, Nermoen A, Madland MV, Korsnes RI. Elastic and plastic partitioning of chalks at deviatoric stress conditions: Experiments performed with four different brines. In: *IOR Norway 2017—19th European Symposium on Improved Oil Recovery*; Stavanger. 2017
- [9] Voake T, Nermoen A, Korsnes RI, Fabricius IL. Induced shear failure by temperature reduction at uni-axial strain conditions. *IOR Norway 2017—19th European Symposium on Improved Oil Recovery*; Stavanger. 2017
- [10] Nermoen A, Korsnes RI, Aursjø O, Madland MV, Carslen Kjørslevik T, Østensen G. How do stress and temperature conditions affect the rock fluid chemistry and deformation for high porosity chalk. *Frontiers in Physics*. 2016;**4**:1-19
- [11] de Waal JA. *On the Rate Type Compaction Behavior on Sandstone Reservoir Rock* [PhD]. Amsterdam; 1986
- [12] Griggs D. Creep of rocks. *Journal of Geology*. 1939;**47**:225-251
- [13] Nagel NB. Compaction and subsidence issues within the petroleum industry: From Wilmington to Ekofisk and beyond. *Physics and Chemistry of the Earth, Part A*. 2001;**26**:3-14
- [14] Hermansen H, Landa GH, Sylte JE, Thomas LK. Experiences after 10 years of water-flooding the Ekofisk field, Norway. *Journal of Petroleum Science and Engineering*. 2000;**26**:11-18

- [15] Sylte JE, Thomas LK, Rhett DW, Bruning DD, Nagel NB. Water induced compaction and the Ekofisk field. In: SPE Annual Technical Conference and Exhibition, SPE 56426; Houston. 1999
- [16] Megawati M, Hiorth A, Madland MV. The impact of surface charge on the mechanical behaviour of high-porosity chalk. *Rock Mechanical Engineering*. 2013;**46**:1073-1090
- [17] Huang YC, Fowkes FM, Lloyd TB, Sanders ND. Adsorption of calcium ions from calcite chloride solutions onto calcium carbonate particles. *Langmuir*. 1991;**7**:1742-1748
- [18] Nermoen A, Korsnes RI, Vika Storm E, Stødle T, Madland MV, Fabricius IL. Incorporating electrostatic effects into the effective stress relation—Insights from chalk experiments. *Geophysics*. Accepted, 2018
- [19] Stipp S. Toward a conceptual model of the calcite surface: Hydration, hydrolysis and surface potential. *Geochimica et Cosmochimica Acta*. 1999;**63**:3121-3131
- [20] Nermoen A, Korsnes RI, Aloysius Haug S, Hiorth A, Madland MV. The dynamic stability of chalks during flooding of non-equilibrium brines and CO₂. In: 4th EAGE-CO₂ Geological Storage Workshop. DOI: 10.3997/2214-4909.20140092; Stavanger. 2014
- [21] Hellmann R, Renders PJN, Gratier JP, Guiguet R. Experimental pressure solution compaction of chalk in aqueous solutions. Part 1. Deformation behavior and chemistry. Water-rock interactions, ore deposits and environmental geochemistry: A tribute to David a. Crerar. In: The Geochemical Society, Special Publication. Vol. 7. 2002. pp. 129-152
- [22] Nermoen A, Korsnes RI, Christensen HF, Trads N, Hiorth A, Madland MV. Measuring the biot stress coefficients and its implications on the effective stress estimate. In: ARMA 13–282; San Francisco. 2014
- [23] Wang W, Madland MV, Zimmermann U, Nermoen A, Korsnes RI, Bertolino SRA, Hildebrand-Habel T. Evaluation of porosity change during chemo-mechanical compaction in flooding experiments on Liegè outcrop chalk. In: Reservoir Quality of Clastic and Carbonate Rocks: Analysis, Modelling and Prediction. Geological Society of London, Special Publications. Vol. 435; London. 2016. <http://doi.org/10.1144/SP435.10>
- [24] Hiorth A, Bache Ø, Jettestuen E, Cathles LM, Moe RW, Omdal E, Korsnes RI, Madland MV. A simplified approach to translate chemical alteration in core experiments to field conditions. In: International Symposium of the Society of Core Analysts. Paper #A053; 18–21 September; Austin. 2011
- [25] Hiorth A, Jettestuen E, Vinningland J-L, Cathles LM, Madland MV. Thermo-chemistry reservoir simulation for better EOR prediction. In: IEA EOR 34th Annual Symposium; Stavanger. 2013
- [26] Hiorth A, Sagen J, Lohne A, Nossen A, Vinningland J-L, Jettestuen E, Sira T. IORSim—A simulator for fast and accurate simulation of multi-phase geochemical interactions at the field scale. In: ECMOR XV—Proceedings of 15h European Conference on the Mathematics of Oil Recovery—EAGE; 29 August–1 September; Amsterdam. 2016. ISBN: 978–94–6282-193-4

Role of Interparticle Space in Hollow Spheres of Silica-Based Solid Acids on Their Acidic Properties and Activity for Hydrolytic Dehydrogenation of Ammonia Borane

Tetsuo Umegaki, Toyama Naoki and
Yoshiyuki Kojima

Additional information is available at the end of the chapter

<http://dx.doi.org/10.5772/intechopen.71307>

Abstract

Porous materials with micropores and mesopores have attracted much attention as materials potentially applied in various fields such as absorbents, catalysts, energy storage, and so on. The kind of materials showed intrinsic properties compared with other types of materials such as fine particles. This chapter reviewed our recent research about hollow silica-alumina composite spheres for the hydrolytic dehydrogenation of ammonia borane. This chapter has mainly discussed about the role of interparticle space in the hollow spheres on their acidic properties and activity for the hydrolytic dehydrogenation of ammonia borane.

Keywords: hollow spheres, interparticle space, silica-alumina, composite, hydrolytic dehydrogenation of ammonia borane

1. Introduction

The ability to generate highly defined, hierarchically structured materials that range in size from a few nanometers to several micrometers is a key prerequisite for the fabrication of highly functional materials. Such structured materials have potential applications in the fields of energy conversion, energy storage, catalysis, and separation [1–4]. Bottom-up approaches that rely on the self-assembly of molecular or colloidal building blocks into superstructures of defined length scales and symmetries have been used to obtain these structures [5, 6]. The size and shape of these building blocks translate directly into the

assembled superstructure [7, 8]. A small space made from pores or hollow structures leads to special properties such as the micropore filling of a pore for gas adsorption applications. If a special property were initiated into a solid-state material, a new possibility of material design would become available. Both porosity and hollow structures are very attractive for material functionalization.

Several papers have reported that mesoporous silica (MCM-41) itself acts as a typical acid catalyst for several reactions, including acetalization [9, 10], isomerization [11], and debenzoylation [12]. Although the wall of mesoporous silica is made of amorphous silica and is generally believed to be neutral or slightly acidic, acetalization is generally believed to require strong or intermediate acids, such as HCl or proton zeolites, as catalysts [13–15]. These findings regarding the acidity of mesoporous silica [9–11, 16–21] raise important questions about how the surface of the material becomes acidic.

Hollow spheres have attracted much research and industrial interest due to their special shape, low density, and large fraction of voids. Hollow spheres possess a series of advantages such as tunable void volume, excellent flow performance, and large surface area. The large internal volume provides a storage space or artificial reaction cells that can serve many functions [22, 23]. The controlled synthesis of inorganic materials with well-designed structures at the nano-size level is extremely important in materials science. In particular, the preparation of hollow inorganic spheres with a defined structure has received increasing attention because of their broad potential applications ranging from drug delivery [24–26], ion exchange [27–29], sensors [30, 31], electro-optics [32, 33], and microreactors [34–36] to building block of photonic crystals [37]. Recently, this field has been advanced to the fabrication of hollow microspheres with holes on the shell wall, namely porous hollow microspheres. Because of their high specific surface area, low density, adsorption capacity, and ability to encapsulate actives, such materials are very useful in catalysis [38, 39], bioseparation [40, 41], tissue engineering [42–44], solar cells [45], and reaction separation [46].

In this chapter, we review our previous works of hollow silica-alumina composite spheres. In our previous study, we investigated fabrication and morphology control of the hollow spheres and functionality of the hollow spheres. First, we discussed intrinsic properties of the hollow spheres compared with the conventional fine particles and their morphological effects on their acidic properties and activity for hydrolytic dehydrogenation of ammonia borane. Second, we also discussed the influence of dispersion of active sites on activity of the hollow spheres for hydrolytic dehydrogenation of ammonia borane. Four-coordinated aluminum species substituting silicon atom in silica lattice was assigned as Brønsted acid sites, and the sites were active species for hydrolysis dehydrogenation of ammonia borane. Thus, the increase of their dispersion is expected to improve the activity of silica-alumina composite particles. From the above two points of view, we reviewed our previous works on hollow silica-alumina composite spheres.

2. Typical experimental procedures

2.1. Preparation of composites

Hollow silica-alumina composite spheres were fabricated through the PS template method. Monodisperse PS particles were prepared by emulsifier-free emulsion polymerization using the following procedure. Styrene (9.0 mL; Kanto Chem. Co., >99.0%), poly(vinyl pyrrolidone) K30 (1.5 g; Fluka, $M_w \approx 40,000$), and the cationic initiator 2,2'-azobis(2-methylpropionamide) dihydrochloride (0.26 g; Wako Pure Chemical, >97.0%) were dissolved in ion exchanged water (100 mL) inside a 250-mL three-necked flask. The flask was equipped with a mechanical stirrer, a thermometer with a temperature controller, a nitrogen gas inlet, and a Graham condenser, and it was placed in an oil bath for heating. The reaction solution was deoxygenated by bubbling nitrogen gas at room temperature for 1 h and heated at 343 K for 24 h under stirring at 250 rpm. The final PS suspension was centrifuged at 6000 rpm for 5 min and washed three times with ethanol (30 mL; Kanto Chem. Co., >99.5%). The PS contents could be tailored through the addition of ethanol. Aluminum isopropoxide (0.0057 g; Aldrich, >98.0%), aqueous ammonia solution (3 mL; 28 wt.%, Kanto Chem. Co.), ethanol (40 mL), and tetraethoxysilane (0.1551 mL; TEOS, Kanto Chem. Co., >99.9%) were added to the PS suspension (15 g). The sol-gel reaction was carried out at 323 K for 1.5 h. The composite was dried overnight in a desiccator. Then, the composites were calcined in air at 873 K at a heating rate of 0.5 K min^{-1} and cooling down immediately after the designated temperature was reached. Fine silica-alumina composite particles were prepared by sol-gel method without the PS template particles. Aluminum isopropoxide (0.0057 g), aqueous ammonia solution (3 mL), and TEOS (0.1551 mL) were added to ethanol (40 mL). The sol-gel reaction was carried out at 323 K for 1.5 h. The composite was dried overnight in a desiccator. Then, the composite was calcined under the same conditions used for the hollow spheres.

2.2. Characterization

Morphology of the composite was identified by a transmission electron microscopy (TEM) using a Hitachi FE-2000 system operating at an acceleration voltage of 200 kV. Temperature-programmed desorption of ammonia (NH_3 -TPD) was carried out on a BELCAT-B instrument. The analysis was performed by loading 50 mg of the composites into a quartz reactor and drying them under a flow of pure He at 783 K for 1 h followed by purging with pure He at the same temperature for 1 h. The composites were allowed to cool to 373 K under the He flow and then exposed to NH_3 -He gas mixture (95 vol.% He) at 373 K for 1 h to allow NH_3 adsorption. The composites were then purged using pure He to allow for the accurate detection of the desorbed NH_3 . The NH_3 -TPD measurements were conducted by heating the composites from 373 to 773 K at a rate of 10 K min^{-1} under a flow of pure He. The desorbed NH_3 molecules were detected by a thermal conductivity detector (TCD).

2.3. Activity tests for hydrolytic dehydrogenation of NH_3BH_3

The composites were placed in a two-necked round-bottomed flask under air at room temperature. One of the necks was connected to a gas burette and the other was connected to an addition funnel. The reaction was initiated by adding aqueous NH_3BH_3 solution (3.5 mL, 0.14 wt.%; Aldrich, 90%) from the addition funnel to the composites. The evolution of gas from the reaction was monitored using the gas burette.

3. Results and discussion

3.1. Influence of the morphology on the activity for hydrolytic dehydrogenation of ammonia borane

Homogeneous hollow spheres of silica-alumina composite particles were obtained by adjusting some factors such as calcination temperature and soaking time [47]. **Figure 1a** shows TEM images of typical hollow silica-alumina composite spheres. Homogeneous hollow spheres with the shell thickness of ca. 6 nm and the particle size of ca. 220 nm were observed in the TEM image. The sample was prepared with PS templates with the diameter of ca. 200 nm; thus, the size of the hollow voids of the hollow spheres reflected the size of PS templates. The shell thickness and particle size were also controlled by adjusting ratios of silica-alumina composite to the amount of PS templates and particle size of PS templates, respectively [48–50]. **Figure 1b** shows the TEM image of the fine particles prepared with similar method for preparation of the hollow spheres without PS templates. The sample consists of fine particles with the particle size of ca. 13 nm. Particle agglomeration was observed in some parts of this composite. The specific surface areas of the hollow spheres and the fine particles were found to be 393 and 295 $\text{m}^2 \text{g}^{-1}$, respectively, indicating that the specific surface areas do not significantly differ from each other, and the primary particles including the hollow spheres were slightly small compared with the particle size of the fine particles. On the other hand, both the hollow spheres and the fine particles consisted of a typical amorphous silica-alumina from the results of powder XRD measurements [51, 52].

The hollow silica-alumina composite spheres show unexpected high activity for hydrolytic dehydrogenation of ammonia borane compared with the silica-alumina composite

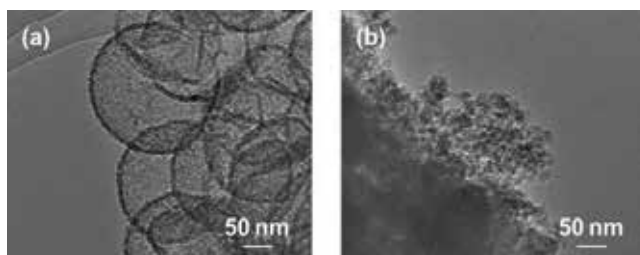
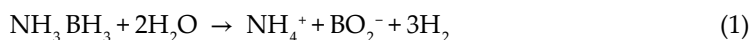


Figure 1. TEM images of (a) hollow silica-alumina composite spheres and (b) silica-alumina composite fine particles [52].

fine particles. The amount of evolved hydrogen from aqueous ammonia borane solution in the presence of the hollow spheres was 10 mL with the completion of the reaction in 12 min, while the evolution 2.5 mL of hydrogen with the completion of the reaction in 12 and 2 min, respectively. The molar ratios of the hydrolytically evolved hydrogen to the initial ammonia borane were 2.6 and 0.6 in the presence of the hollow spheres and the fine particles, respectively. These results indicate that the amount of hydrogen evolved in the presence of the hollow spheres was significantly higher than the amount of hydrogen evolved in the presence of the fine particles. It has been reported that the acidic protons on Brønsted acid sites promote the dissociation of the B–N bond and the hydrolysis of BH_3 species to produce borate ion species along with the hydrogen release Eq. (1) [47, 51, 53].



However, the hydrolytic dehydrogenation of ammonia borane in the presence of the hollow spheres was incomplete. It is suggested that the H_3BO_3 produced from the reaction of BO_2^- with the acidic protons on Brønsted acid sites shift the reaction shown in Eq. (2) to the right side [53].



To determine the recycle ability of the composites, the activity of the recycled composites was compared. The recycled hollow spheres evolved 1.5 mL of hydrogen with the completion of the reaction in 2 min. On the other hand, the recycled fine particles showed no activity. The recycled hollow spheres were much lower amount of hydrogen evolution than the original hollow spheres because the acidic protons might be exchange into ammonium ion on the Brønsted acid sites of the hollow spheres during hydrolytic dehydrogenation of ammonia borane. Then, the recycled hollow spheres were calcined at 723 K at heating rate of 0.5 K min^{-1} and cooling down immediately after the designated temperature was reached. The recycled hollow spheres after calcination showed the same activity as the recycled hollow spheres. These results suggest that almost all the acidic protons on Brønsted acid sites of the hollow spheres were consumed by the hydrolytic dehydrogenation reaction. The acidic properties of the silica-alumina composites were measured using NH_3 -TPD. **Figure 2** shows NH_3 -TPD profiles of the hollow spheres and the fine particles. The NH_3 desorption from the hollow spheres showed two peaks: first peak at around 420 K (low-temperature peak) and a broad peak at around 580 K (high-temperature peak), whereas the NH_3 desorption from the fine particles showed peaks at around 420 and 430 K (low-temperature peaks), respectively. The low-temperature peaks can be attributed to Brønsted acid sites with weakly adsorbed NH_3 (weak Brønsted acid sites), whereas the high-temperature peak observed for the hollow spheres can be attributed to Brønsted acid sites with strongly adsorbed NH_3 (strong Brønsted acid sites) [54–56]. These results indicate that the hollow spheres possess both weak and strong Brønsted acid sites, while the fine particles possess only weak Brønsted acid sites. The amount of Brønsted acid sites calculated from the areas under the peak in the temperature range 400–600 K [57–59] for the hollow spheres and the fine particles was 0.18 and 0.10 mmol g^{-1} , respectively. The result indicates that the amount of Brønsted acid sites

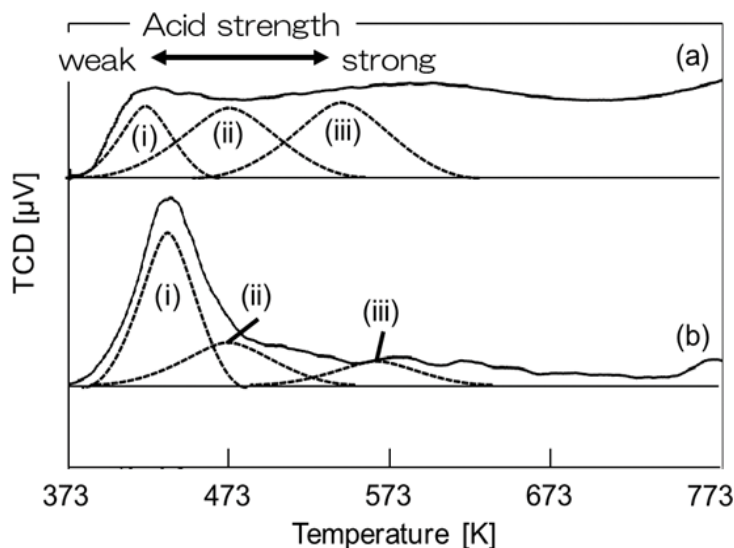


Figure 2. NH_3 -TPD profiles of (a) hollow silica-alumina composite spheres and (b) silica-alumina composite fine particles [52].

in the silica-alumina composites depends on their morphology. According to the result, the amount of hydrogen evolution increases with the increase of the amount of Brønsted acid sites. The total amount of Brønsted acid sites in the hollow spheres is found to be 1.8 times higher than those in the fine particles. Moreover, the amount of hydrogen evolved in the presence of the hollow spheres is more than four times higher than that in the presence of the fine particles. Consequently, it is indicated that the morphology of silica-alumina composites influences their acidic properties and that the strong Brønsted acid sites are more effective for hydrolytic dehydrogenation of ammonia borane than the weak Brønsted acid sites. In addition, it is also suggested that the primary particles consisting of the shell of the hollow spheres formed micro- and/or meso-interparticles spacing, and the integrated surface acid sites showed unexpectedly strong acid property.

3.2. Improvement of dispersion of active species of hollow silica-alumina composite spheres

As described in the previous section, Brønsted acid sites are main active sites for hydrolytic dehydrogenation of ammonia borane. The acid sites can generally increase with the increase of four-coordinated aluminum species, which are well-dispersed active species. We investigated the influence of various preparation conditions such as promoters of sol-gel reaction for the formation of the shell of the hollow spheres, alcohol solvents, aluminum precursors, and so on, on the dispersion of the active aluminum species of hollow silica-alumina composite spheres and their activity for hydrolytic dehydrogenation of ammonia borane [60–62]. In the conditions, aluminum precursors significantly influenced on the dispersion and the activity. In this session, we especially introduce the investigation of the effects of aluminum precursors.

All the hollow silica-alumina composite spheres prepared using various aluminum precursors possessed similar morphology as shown in **Figure 3**. The shell thickness and diameter of all the hollow spheres were approximately 25 and 260 nm, respectively. The specific surface areas of the hollow spheres prepared using various aluminum precursors measured through nitrogen sorption using the Brunauer-Emmett-Teller (BET) methods were 436, 476, 483, and 523 m² g⁻¹, respectively, indicating that the specific surface area does not significantly depend on the kind of aluminum precursors. On the other hand, the coordination numbers of the hollow spheres prepared using various aluminum precursors were quite different, and the ratio of four-coordinated aluminum species to all the aluminum species of the hollow spheres prepared using aluminum ethoxide, aluminum iso-propoxide, aluminum n-butoxide, and aluminum sec-butoxide calculated from the results of ²⁷Al MAS NMR spectra were 0.10, 0.33, 0.12, and 0.44, respectively [62]. The result indicates that the hollow spheres prepared using aluminum precursors with the branched alkyl groups exhibit larger proportion of four-coordinated aluminum species than those prepared using aluminum precursors with the normal alkyl groups. The dispersion of aluminum species increases with increase of the ratio of four-coordinated aluminum species [63]. The result indicates that the aluminum species of the hollow spheres prepared using aluminum precursors with the branched alkyl groups were well dispersed in the silica matrix. The acidic properties of the hollow spheres were measured using NH₃-TPD. **Figure 4** shows NH₃-TPD profiles of the hollow spheres prepared using various aluminum precursors. The assignment of NH₃ desorption peaks in this figure was same in Section 3.1, and the number of Brønsted acid sites was calculated using the area of the NH₃ desorption peaks of the hollow spheres. The number of Brønsted acid sites in the hollow spheres prepared using aluminum ethoxide, aluminum iso-propoxide, aluminum n-butoxide, and aluminum sec-butoxide were 0.08, 0.30, 0.12, and

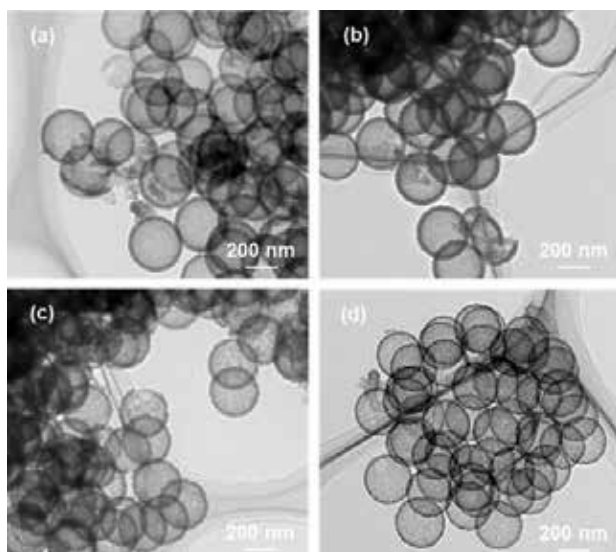


Figure 3. TEM images of hollow silica-alumina composite spheres prepared using (a) aluminum ethoxide, (b) aluminum iso-propoxide, (c) aluminum n-butoxide, and (d) aluminum sec-butoxide [62].

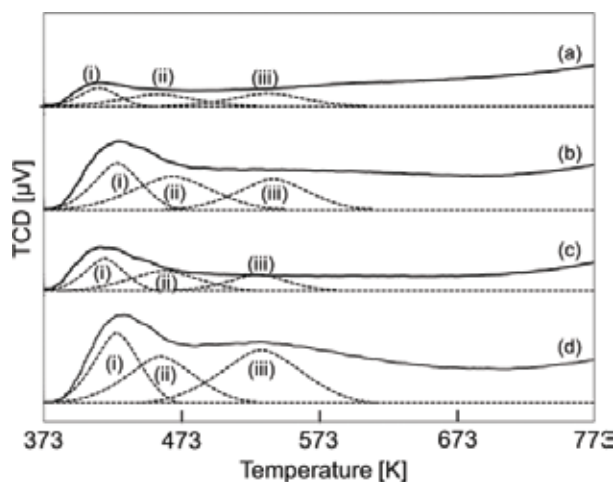


Figure 4. NH_3 -TPD profiles of hollow silica-alumina composite spheres prepared using (a) aluminum ethoxide, (b) aluminum iso-propoxide, (c) aluminum n-butoxide, and (d) aluminum sec-butoxide [62].

0.34 mmol g^{-1} , respectively. From the result, the hollow spheres prepared using aluminum precursors with the branched alkyl groups exhibit more Brønsted acid sites than those prepared using aluminum precursors with the normal alkyl groups. The result indicates that the number of Brønsted acid sites depends on the kind of aluminum precursors. In addition, the surface concentrations of Brønsted acid sites in the hollow spheres prepared using aluminum ethoxide, aluminum iso-propoxide, aluminum n-butoxide, and aluminum sec-butoxide was 0.18 , 0.63 , 0.25 , and 0.65 mmol m^2 , respectively. From the result, the hollow spheres prepared using aluminum precursors with the branched alkyl groups exhibit more surface concentration of Brønsted acid sites than those prepared using aluminum precursors with the normal alkyl groups. The result suggests that the aluminum species of the hollow spheres prepared using aluminum precursors with the branched alkyl groups were well dispersed in the silica matrix.

The activities of the hollow spheres prepared using various aluminum precursors for hydrolytic dehydrogenation of ammonia borane were compared. The hydrogen evolution of 5.0 , 10.5 , 6.0 , and 11.5 mL was occurred in 40 , 45 , 45 , and 35 min , respectively, in the presence of the hollow spheres prepared using aluminum ethoxide, aluminum iso-propoxide, aluminum n-butoxide, and aluminum sec-butoxide, respectively. The molar ratios of the hydrolytically evolved hydrogen to introduced ammonia borane were 1.3 , 2.8 , 1.5 , and 3.0 in the presence of the hollow spheres prepared using aluminum ethoxide, aluminum iso-propoxide, aluminum n-butoxide, and aluminum sec-butoxide, respectively. The hollow spheres prepared using aluminum precursors with the branched alkyl groups exhibit more hydrogen evolution than those prepared using aluminum precursors with the normal alkyl groups. It has been reported that the branched alkyl groups exhibit lower sol-gel reaction in silicon precursors rate than the normal alkyl groups because of steric effects [64]. Consequently, the amount of hydrogen evolution increases as the sol-gel reaction rate decreases. The result indicates that the amount of hydrogen evolution depends on the kind

of aluminum precursors. Hydrogen evolution of 1.0 mL was occurred in 3 min in the presence of the recycled hollow spheres prepared using aluminum sec-butoxide, indicating that the recycled hollow spheres exhibit much less hydrogen evolution than the fresh hollow spheres. The recycled hollow spheres prepared using aluminum ethoxide, aluminum isopropoxide, and aluminum n-butoxide exhibit similar results. Hydrogen evolution rate of the hollow spheres prepared using aluminum ethoxide, aluminum isopropoxide, aluminum n-butoxide, and aluminum sec-butoxide calculated using data from the first 50% of the reaction was 1.5, 2.0, 1.5, 2.0, and 0.3 mL min⁻¹, respectively, indicating that the rate of hydrogen evolution of all the hollow spheres was similar because they possess similar pore size distribution calculated from the results of nitrogen sorption measurement.

In order to evaluate the effect of the morphology and the dispersion of active aluminum species in the hollow spheres, the relation between the ratios of four-coordinated aluminum species and the activity for hydrogen evolution amount from aqueous solutions in the presence of various silica-aluminum composite particles. The relation calculated from some of our previous studies [52, 61, 62] was shown in **Figure 5**. From this figure, the hollow spheres showed unexpected high activity as compared with the fine particles, although the ratio of four-coordinated aluminum species in the hollow spheres was not significantly higher than the ratio of the fine particles. As described in Section 3.1, the larger amount of more effective strong Brønsted acid sites for hydrogen evolution from aqueous ammonia borane solution are in the hollow spheres than that in the fine particles. The micro- and/or meso-interparticles spacing formed by the primary particles in the shell of the hollow spheres in which the integrated surface acid sites showed unexpectedly strong acid property were included. On the other hand, the dispersion of aluminum species included in the hollow spheres was controlled by adjusting the preparation conditions and the activity for hydrogen evolution from aqueous ammonia borane solution linearly depended on the dispersion as shown in **Figure 5**.

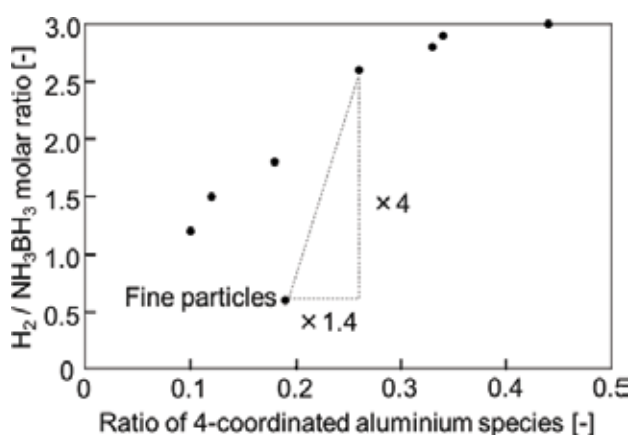


Figure 5. Relation between ratio of four-coordinated aluminum species and hydrogen evolution amount from aqueous ammonia borane solution in the presence of various silica-alumina composite particles [52, 61, 62].

4. Conclusions

In this chapter, we reviewed our previous works of fabrication and morphology control of the hollow spheres and functionality of the hollow spheres. The hollow silica-alumina composite spheres show unexpected high activity for hydrolytic dehydrogenation of ammonia borane compared with the silica-alumina composite fine particles though the ratio of active four-coordinated aluminum species of the hollow spheres was not significantly high compared with that of the fine particles. From the result of NH_3 -TPD, the hollow spheres possessed higher number of strong Brønsted acid sites, which are effective for hydrolytic dehydrogenation of ammonia borane, than the fine particles. It possibly depends on micro- and/or meso-interparticles spacing, which was formed by the primary particles consisting of the shell of the hollow spheres, and it is suggested that the integrated surface acid sites showed unexpectedly strong acid property.

The activity of the hollow spheres for hydrolytic dehydrogenation of ammonia borane improved with increasing dispersion of active aluminum species and increasing four-coordinated aluminum species. We previously investigated the influence of various preparation conditions of the hollow spheres to improve the dispersion of the aluminum species and the activity for hydrolytic dehydrogenation of ammonia borane and aluminum precursor that significantly influence both on the dispersion and the activity. The number of Brønsted acid sites and ratio of four-coordinated aluminum species of the hollow spheres prepared using aluminum precursors with the branched alkyl groups was significantly higher than those of the hollow spheres prepared using aluminum precursors with the normal alkyl groups, and then the activity of the hollow spheres prepared using aluminum precursors with the branched alkyl groups was significantly higher than those of the hollow spheres prepared using aluminum precursors with the normal alkyl groups. These results indicate that the hollow spheres with well-ordered pore structure and well-dispersed active aluminum species are expected to show significantly high activity for the hydrogen evolution reaction.

Author details

Tetsuo Umegaki*, Toyama Naoki and Yoshiyuki Kojima

*Address all correspondence to: umegaki.tetsuo@nihon-u.ac.jp

College of Science and Technology, Nihon University, Tokyo, Japan

References

- [1] Choi H, Sofranko AC, Dionysiou DD. Nanocrystalline TiO_2 Photocatalytic membranes with a hierarchical mesoporous multilayer structure: Synthesis, characterization, and multifunction. *Advanced Functional Materials*. 2006;**16**:1067-1074

- [2] Rhee DK, Jung B, Kim YH, Yeo SJ, Choi SJ, Rauf A, Han S, Yi GR, Lee D, Yoo PJ. Particle-nested inverse opal structures as hierarchically structured large-scale membranes with tunable separation properties. *ACS Applied Materials & Interfaces*. 2014;**6**:9950-9954
- [3] Su BL, Sanchez C, Yang XY. *Hierarchically Structured Porous Materials: From Nanoscience to Catalysis, Separation, Optics, Energy, and Life Science*. Weinheim: Wiley-VCH Verlag GmbH & Co. KGaA; 2011. ISSN: 978-3-527-32788-1
- [4] Cho CY, Moon JH. Hierarchical twin-scale inverse opal TiO₂ electrodes for dye-sensitized solar cells. *Langmuir*. 2012;**28**:9372-9377
- [5] Wang DY, Möhwald H. Template-directed colloidal self-assembly – The route to ‘top-down’ nanochemical engineering. *Journal of Materials Chemistry*. 2004;**14**:459-468
- [6] von Freymann G, Kitaev V, Lotsch BV, Ozin GA. Bottom-up assembly of photonic crystals. *Chemical Society Reviews*. 2013;**42**:2528-2554
- [7] Vogel N, Retsch M, Fustin CA, Del Campo A, Jonas U. Advances in colloidal assembly: The design of structure and hierarchy in two and three dimensions. *Chemical Reviews*. 2015;**115**:6265-6311
- [8] Gröschel AH, Walther A, Löbbling TI, Schacher FH, Schmalz H, Müller AHE. Guided hierarchical co-assembly of soft patchy nanoparticles. *Nature*. 2013;**503**:247-251
- [9] Tanaka Y, Sawamura N, Iwamoto M. Highly effective acetalization of aldehydes and ketones with methanol on siliceous mesoporous material. *Tetrahedron Letters*. 1998;**39**:9457-9460
- [10] Iwamoto M, Tanaka Y, Sawamura N, Namba S. Remarkable effect of pore size on the catalytic activity of mesoporous silica for the acetalization of cyclohexanone with methanol. *Journal of American Chemical Society*. 2003;**125**:13032-13033
- [11] Yamamoto T, Tanaka T, Funabiki T, Yoshida S. Acidic property of FSM-16. *Journal of Physical Chemistry B*. 1998;**102**:5830-5839
- [12] Itoh A, Kodama T, Maeda S, Masaki Y. Selective acceleration for deprotection of benzyl ethers with Ti-HMS. *Tetrahedron Letters*. December, 1998;**39**:9461-9464 ISSN 0040-4039
- [13] Greene TW, Wuts PGM. *Protective Groups in Organic Synthesis*. 2nd ed. New York: John Wiley & Sons; 1991. p. 178
- [14] Strukul G. Lewis acid behavior of cationic complexes of palladium(II) and platinum(II): Some examples of catalytic applications. *Topics in Catalysis*. 2002;**19**:33-42
- [15] Urabe H, Sato F. In: Yamamoto H, editor. *Lewis Acids in Organic Synthesis*. Wiley-VCH: Weinheim; 2000. p. 653
- [16] Thomas JM, Terasaki O, Gai PL, Zhou W, Gonzalez-Calbet J. Structural elucidation of microporous and Mesoporous catalysts and molecular sieves by high-resolution electron microscopy. *Account of Chemical Research*. 2001;**34**:583-594
- [17] Trikalitis PN, Rangan KK, Bakas T, Kanatzidis MG. Varied pore organization in meso-structured semiconductors based on the [SnSe₄]⁴⁻ anion. *Nature*. 2001;**410**:671-675

- [18] On DT, Desplantier-Giscard D, Danumah C, Kaliaguine S. Perspectives in catalytic applications of mesostructured materials. *Applied Catalysis A*. 2001;**222**:299-357
- [19] Lei C, Shin Y, Liu J, Ackerman EJ. Entrapping enzyme in a functionalized Nanoporous support. *Journal of American Chemical Society*. 2002;**124**:11242-11243
- [20] Inagaki S, Guan S, Ohsuna T, Terasaki O. An ordered mesoporous organosilica hybrid material with a crystal-like wall structure. *Nature*. 2002;**416**:304-307
- [21] Kageyama K, Tamazawa J, Aida T. Extrusion polymerization: Catalyzed synthesis of crystalline linear polyethylene nanofibers within a mesoporous silica. *Science*. 1999;**285**:2113-2115
- [22] Meier W. Polymer nanocapsules. *Chemical Society Reviews*. 2000;**29**:295-303
- [23] Caruso F. Hollow capsule processing through colloidal templating and self-assembly. *Chemistry–European Journal*. 2000;**6**:413-419
- [24] Wei W, Ma GH, Hu G, Yu D, Mcleis T, ZG S, Shen ZY. Preparation of hierarchical hollow CaCO_3 particles and the application as anticancer drug carrier. *Journal of American Chemical Society*. 2008;**130**:15808-15810
- [25] Moon SK, Oh MJ, Paik DH, Ryu TK, Park K, Kim SE, Park JH, Kim JH, Choi SW. A facile method for the preparation of monodisperse beads with uniform pore sizes for cell culture. *Macromolecular Rapid Communication*. 2013;**34**:399-405
- [26] Zhu Y, Ikoma T, Hanagata N, Kaskel S. Rattle-type $\text{Fe}_3\text{O}_4@ \text{SiO}_2$ hollow mesoporous spheres as carriers for drug delivery. *Small*. 2010;**6**:471-478
- [27] Lou XW, Wang Y, Yuan C, Lee JY, Archer LA. Template-free synthesis of SnO_2 hollow nanostructures with high lithium storage capacity. *Advanced Materials*. 2006;**18**:2325-2329
- [28] Cao AM, JS H, Liang HP, Wan LJ. Self-assembled vanadium pentoxide (V_2O_5) hollow microspheres from nanorods and their application in lithium-ion batteries. *Angewandte Chemie International Edition*. 2005;**44**:4391-4395
- [29] Lee KT, Jung YS, Oh SM. Synthesis of tin-encapsulated spherical hollow carbon for anode material in lithium secondary batteries. *Journal of American Chemical Society*. 2003;**125**:5652-5653
- [30] Gyger F, Hübner M, Feldmann C, Barsan N, Weimar U. Nanoscale SnO_2 hollow spheres and their application as a gas-sensing material. *Chemistry of Materials*. 2010;**22**:4821-4827
- [31] Zhang J, Liu X, Wu S, Xu M, Guo X, Wang S. Au nanoparticle-decorated porous SnO_2 hollow spheres: A new model for a chemical sensor. *Journal of Materials Chemistry*. 2010;**20**:6453-6459
- [32] Jiang Y, Sun Q, Zhang L, Jiang Z. Capsules-in-bead scaffold: A rational architecture for spatially separated multienzyme cascade system. *Journal of Materials Chemistry* 2009;**19**:9068-9074
- [33] Wang Z, Wu L, Chen M, Zhou S. Facile synthesis of superparamagnetic fluorescent $\text{Fe}_3\text{O}_4/\text{ZnS}$ hollow nanospheres. *Journal of American Chemical Society*. 2009;**131**:11276-11277

- [34] Hyun DC, Lu P, Choi SI, Jeong U, Xia Y. Microscale polymer bottles corked with a phase-change material for temperature controlled release. *Angewandte Chemie International Edition*. 2013;**52**:10468-10471
- [35] Li M, Xue J. Facile route to synthesize polyurethane hollow microspheres with size-tunable single holes. *Langmuir*. 2011;**27**:3229-3232
- [36] Im SH, Jeong U, Xia Y. Polymer hollow particles with controllable holes in their surfaces. *Nature Material*. 2005;**4**:671-675
- [37] Xu X, Asher SA. Synthesis and utilization of monodisperse hollow polymeric particles in photonic crystals. *Journal of American Chemical Society*. 2004;**126**:7940-7945
- [38] Tian G, Chen Y, Zhou W, Pan K, Dong Y, Tian C, Fu H. Facile solvothermal synthesis of hierarchical flower-like Bi_2MoO_6 hollow spheres as high performance visible-light driven photocatalysts. *Journal of Materials Chemistry*. 2011;**21**:887-892
- [39] Chen Q, Bahnemann DW. Reduction of carbon dioxide by magnetite: Implications for the primordial synthesis of organic molecules. *Journal of American Chemical Society*. 2000;**122**:970-971
- [40] Kirkland J, Truszkowski F, Dilks Jr C, Engel G. Superficially porous silica microspheres for fast high-performance liquid chromatography of macromolecules. *Journal Chromatography A*. 2000;**890**:3-13
- [41] Qu JB, Wan XZ, Zhai YQ, Zhou WQ, Su ZG, Ma GH. A novel stationary phase derivatized from hydrophilic gigaporous polystyrene-based microspheres for high-speed protein chromatography. *Journal of Chromatography A*. 2009;**1216**:6511-6516
- [42] Kim SE, Park JH, Cho YW, Chung H, Jeong SY, Lee EB, Kwon IC. Porous chitosan scaffold containing microspheres loaded with transforming growth factor- β 1: Implications for cartilage tissue engineering. *Journal of Controlled Release*. 2003;**91**:365-374
- [43] Langer R, Tirrell DA. Designing materials for biology and medicine. *Nature*. 2004;**428**:487-492
- [44] Hollister SJ. Porous scaffold design for tissue engineering. *Nature Material*. 2005;**4**:518-524
- [45] Bach U, Lupo D, Comte P, Moser J, Weissörtel F, Salbeck J, Spreitzer H, Grätzel M. Solid-state dye-sensitized mesoporous TiO_2 solar cells with high photon-to-electron conversion efficiencies. *Nature*. 1998;**395**:583-585
- [46] Fan JB, Huang C, Jiang L, Wang S. Nanoporous microspheres: From controllable synthesis to healthcare applications. *Journal of Materials Chemistry B*. 2013;**1**:2222-2235
- [47] Toyama N, Umegaki T, Kojima Y. Fabrication of hollow silica-alumina composite spheres and their activity for hydrolytic dehydrogenation of ammonia borane. *International Journal of Hydrogen Energy*. 2014;**39**:17136-17143
- [48] Toyama N, Umegaki T, Xu Q, Kojima Y. Control of shell thickness of hollow silica-alumina composite spheres and their activity for hydrolytic dehydrogenation of ammonia borane. *Key Engineering Materials*. 2014;**617**:166-169

- [49] Toyama N, Umegaki T, Xu Q, Kojima Y. Control of particle size of hollow silica-alumina composite spheres and their activity for hydrolytic dehydrogenation of ammonia Borane. *Journal of Japan Institute of Energy*. 2014;**93**:511-516
- [50] Toyama N, Kamada K, Umegaki T, Kojima Y. Control of particle size of hollow silica-alumina composite spheres prepared using L(+)-arginine and their activity for hydrolytic dehydrogenation of ammonia borane. *Transactions of Materials Research Society of Japan*. 2015; **40**:81-84
- [51] Toyama N, Umegaki T, Kojima Y. Influence of Si/Al molar ratio of hollow silica-alumina composite spheres on their activity for hydrogenation dehydrogenation of ammonia borane. *International Journal of Hydrogen Energy*. 2015;**40**:6151-6157
- [52] Toyama N, Ohki S, Tansho M, Shimizu T, Umegaki T, Kojima Y. Influence of morphology of silica-alumina composites on their activity for hydrolytic dehydrogenation of ammonia Borane. *Journal of Japan Institute of Energy*. 2016;**95**:480-486
- [53] Chandra M, Xu Q. Dissociation and hydrolysis of ammonia-borane with solid acids and carbon dioxide: An efficient hydrogen generation system. *Journal of Power Sources*. 2006;**159**:855-860
- [54] Topsøe NY, Pedersen K, Derouane E. Infrared and temperature-programmed desorption study of the acidic properties of ZSM-5-type zeolites. *Journal of Catalysis*. 1981;**70**:41-52
- [55] Hidalgo CV, Itoh H, Hattori T, Niwa M, Murakami Y. ESCA studies on silica- and alumina-supported rhenium oxide catalysts. *Journal of Catalysis*. 1984;**85**:362-369
- [56] Tonetto G, Atlas J, de Lasa H. FCC catalysts with different zeolite crystallite sizes: Acidity, structural properties and reactivity. *Applied Catalysis A*. 2004;**270**:9-25
- [57] Fang X, Liu Z, Hsieh MF, Chen M, Liu P, Chen C, Zheng N. Hollow Mesoporous Aluminosilica spheres with perpendicular pore channels as catalytic nanoreactors. *ACS Nano*. 2012;**6**:4434-4444
- [58] Sakthivel A, Dapurkar SE, Gupta NM, Kulshreshtha SK, Selvam P. The influence of aluminium sources on the acidic behaviour as well as on the catalytic activity of mesoporous H-AlMCM-41 molecular sieves. *Microporous and Mesoporous Materials*. 2003;**65**:177-187
- [59] Wang Y, Lang N, Tuel A. Nature and acidity of aluminum species in AlMCM-41 with a high aluminum content (Si/Al = 1.25). *Microporous and Mesoporous Materials*. 2006;**93**:46-54
- [60] Umegaki T, Imamura S, Toyama N, Kojima Y. Influence of preparation conditions on the morphology of hollow silica-alumina composite spheres and their activity for hydrolytic dehydrogenation of ammonia borane. *Microporous and Mesoporous Materials*. 2014;**196**:349-353
- [61] Toyama N, Ohki S, Tansho M, Shimizu T, Umegaki T, Kojima Y. Influence of alcohol solvents on morphology of hollow silica-alumina composite spheres and their activity for hydrolytic dehydrogenation of ammonia borane. *Journal of Sol-Gel Science and Technology*. 2017;**82**:92-100

- [62] Toyama N, Ohki S, Tansho M, Shimizu T, Umegaki T, Kojima Y. Influence of aluminum precursors on structure and acidic properties of hollow silica-alumina composite spheres, and their activity for hydrolytic dehydrogenation of ammonia borane. *International Journal of Hydrogen Energy*. 2017;**42**:22318-22324
- [63] Koekkoek AJJ, Rob van Veen JA, Gerritsen PB, Giltay P, Magusin PCMM, Hensen EJM. Brønsted acidity of Al/SBA-15. *Microporous and Mesoporous Materials*. 2012;**151**:34-43
- [64] Brinker CJ. Hydrolysis and condensation of silicates: Effects on structure. *Journal of Non-Crystalline Solids*. 1988;**100**:31-50



Edited by Taher Hcine Ghrib

This book discusses multiways in the porous materials. It involves materials with a large number of holes, and it highlights the synthesis, structure, and surface properties of porous materials closely related to more applications, such as support, catalyst, energy storage, chemical reactions, and optical applications. It studies the effect of the filling materials, the thermal treatments, and the porous density in the improvement of physical properties, electrical and energy efficiency, and the generation of new materials. Some synthetic process will be discussed with the effect of some parameters on the final characteristics of the prepared porous structures.

Published in London, UK

© 2018 IntechOpen

© rawpixel.com / unsplash

IntechOpen

